TECHNICAL TRANSACTIONS
CZASOPISMO TECHNICZNE

ENVIRONMENTAL ENGINEERING
ŚRODOWISKO

ISSUE 2-Ś (24)
ZESZYT 2-Ś (24)

YEAR 2015 (112)
ROK 2015 (112)

WYDAWNICTWO POLITECHNIKI KRAKOWSKIEJ

TECHNICAL TRANSACTIONS | CZASOPISMO TECHNICZNE

ENVIRONMENTAL ENGINEERING | ŚRODOWISKO

ISSUE 2-Ś (24) | ZESZYT 2-Ś (24)
YEAR 2015 (112) | ROK 2015 (112)

Basic version of each Technical Transactions magazine is its online version
Pierwotną wersją każdego zeszytu Czasopisma Technicznego jest jego wersja online
www.ejournals.eu/Czasopismo-Techniczne www.technicaltransactions.com www.czasopismotechniczne.pl

TECHNICAL TRANSACTIONS | CZASOPISMO TECHNICZNE
ENVIRONMENTAL ENGINEERING | ŚRODOWISKO
2-Ś/2015

HONORATA ADAMOWICZ*, PAWEŁ POPIELSKI

ANALYSIS OF CHANGES IN GROUNDWATER AND SOIL CONDITIONS IN A HIGHLY URBANIZED AREA DUE TO DEEP BUILDING FOUNDATIONS

ANALIZA ZMIAN WARUNKÓW WODNO-GRUNTOWYCH NA TERENIE SILNIE ZURBANIZOWANYM NA SKUTEK GŁĘBOKIEGO POSADOWIENIA

Abstract

The article describes an urban environment and the anthropogenic factors that influence groundwater and soil conditions. Deep building foundations impact on changes in both groundwater flow and soil consistency, which may occur due to filtration phenomena. Suffusion and internal erosion were described, determining the criteria applied for assessment of soil susceptibility to these phenomena. The results of numerical modelling executed with Visual Modflow software are presented. It is stated that the creation of deep building foundations in an extensively urban area may influence the groundwater and soil conditions.

Keywords: groundwater, filtration, suffusion, internal erosion, deep foundation

Streszczenie

W artykule scharakteryzowano środowisko zurbanizowane oraz opisano wpływ czynników antropogenicznych na warunki gruntowo-wodne. Uwzględniono wpływ głęboko posadowionych budynków na zmiany przepływu wód gruntowych i zmiany stanu gruntu, które mogą być wywołane przez zjawiska filtracyjne. Opisano zagadnienie sufozji i erozji wewnętrznej oraz określono, jakie kryteria są stosowane do oceny podatności gruntu na wystąpienie tego zjawiska. Przedstawiono wyniki modelowania numerycznego wykonanego w programie Visual Modflow. Stwierdzono, że realizacja głęboko posadowionych obiektów w terenie silnie zurbanizowanym może wpływać na warunki wodno-gruntowe.

Słowa kluczowe: woda gruntowa, filtracja, sufozja, erozja wewnętrzna, głębokie posadowienia

DOI: 10.4467/2353737XCT.15.222.4608

* MSc. Honorata Adamowicz, DSc. PhD. Paweł Popielski, Department Hydro-Engineering and Hydraulics, Faculty of Environmental Engineering, Warsaw University of Technology.

1. Introduction

Issues related to groundwater flow in urban areas have become a topic of growing importance over recent years. Cities currently remain home to c.a. 50% of the world's population and the population inhabiting urban areas is expected to increase by mid-century to 70% [28]. Due to dynamic city development, appropriate planning and execution of developments stand out as the key element for the balanced and safe development of the urban environment. To allow this, it is necessary to recognize and understand the natural and anthropogenic processes that form the city ecosystem, which are characteristic for urban areas. What distinguishes the hydrology of urban areas from other hydrological systems, is the frequency of occurrence of certain "elements", which influence both groundwater flow and its chemistry (Fig. 1.).

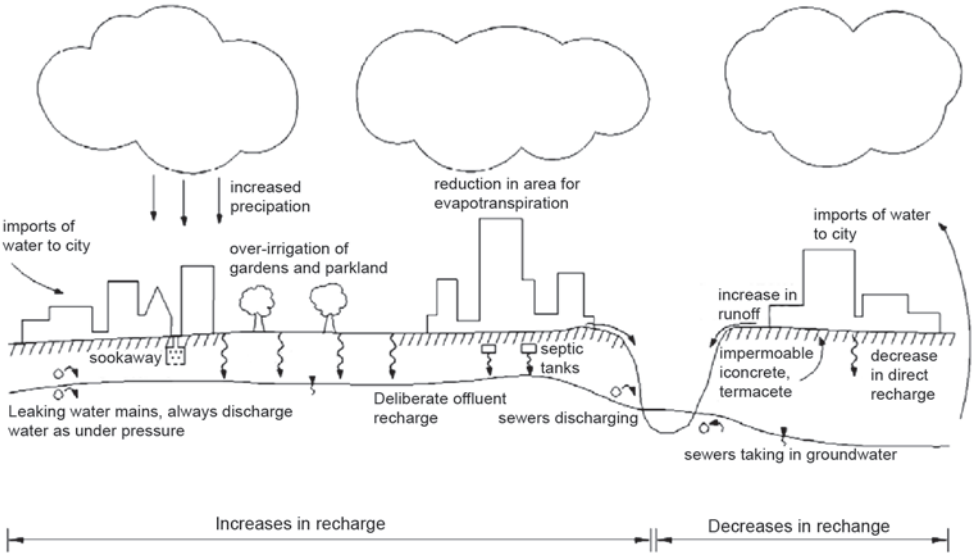

Fig. 1. Water circulation scheme in urban areas [19]

The contribution and influence of anthropogenic elements depends on many factors, such as grade of field coverage with impermeable layer, underground technical pipelines (sewage, water supply, heating, etc.) leakiness scale, or level of groundwater exploitation for communal or industrial purposes [28]. In addition to elements participating in water circulation, other elements of possible significant influence on groundwater-soil conditions also occur in urban areas. Buildings with deep foundations that partition groundwater horizons may disrupt the natural directions of groundwater flow, which can happen not only during their execution (excavation drainage, often simultaneous execution of several buildings), but also during exploitation. Thoughtless action or a lack of urban infrastructure maintenance may result in failure, varying in range and scale.

Elements that influence the groundwater-soil environment in extensively urban areas, include:

– deep foundations,
  – cavity walls,
  – tunnels (excavated using mining techniques and TBM),
– construction drainage (pumping water to and from the soil),
– leaking of underground technical pipelines (water supply, heating, etc.),
– anthropogenic bottom,
– impermeable field coverage,
– drainage systems.

The phrase "anthropogenic bottom" refers to constructional, industrial or communal waste built into the ground to fill the field depressions, e.g. to assure an appropriate construction level. In Warsaw, it was common to construct on ruins buried after the Second World War. The bottom of such material may be of hydraulic conductivity significantly higher than the surrounding material and develop a certain privileged flow pathway or, if of low permeability, may cause flow to be restricted to the groundwater bearing horizon or create a barrier that restricts the water inflow to the soil.

The extent of impermeable layers has a driving influence on the character of urban catchment. The participation of basic processes in the hydrological cycle changes with the spread of solidified (hardened) surfaces (Fig. 2.). Impermeable coverage, compared to direct

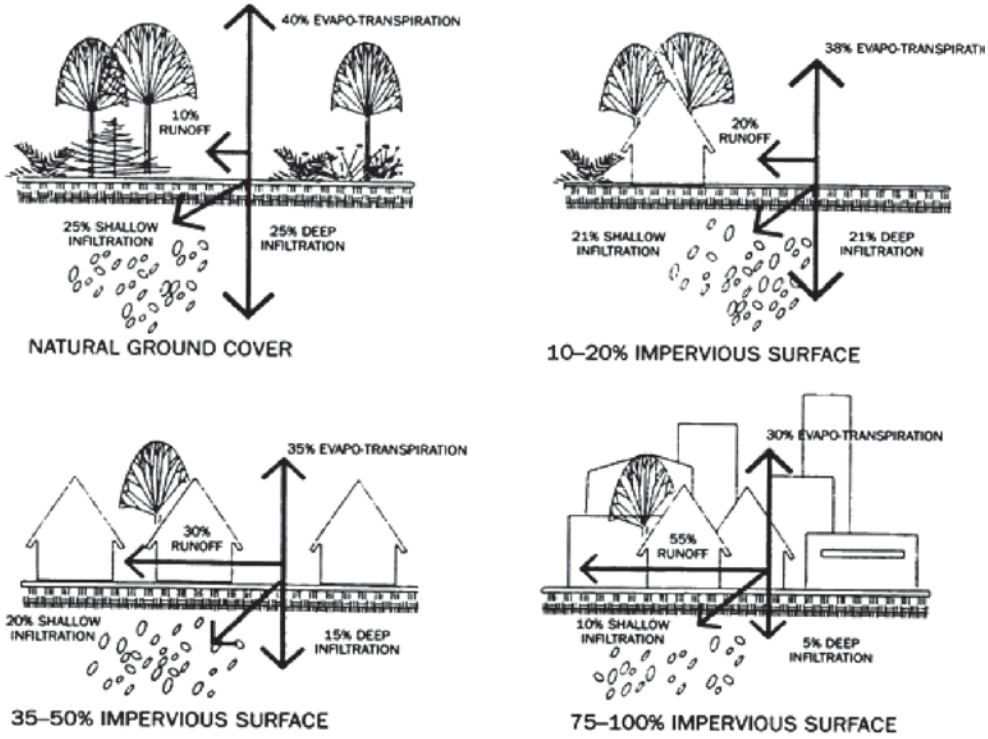

Fig. 2. Influence of degree of urbanization on the participation of basic processes in the hydrological cycle [Source: Environmental Protection Agency, Guidance Specifying Management Measures for Sources of Nonpoint Source Pollution in Coastal Waters, #840-B-92-002, 1993]

infiltration, causes a significant increase in surface runoff. However, a decreased inflow of rainwater to the soil is often compensated for by leakages from underground technical installations (e.g. water supply pipelines). In some cases, water inflow from such leakages may constitute the main source of groundwater supply. Such a situation frequently occurs in ecosystems with low annual rainfall, where water inflow from leaking pipelines can reach 90% of total inflow (e.g. Lima, Peru) [28]. Moreover, uncontrolled outflow of pressurized water, e.g. from a damaged water supply main, may lead to leach of soil and a following local field collapse.

In 2004, a heating pipeline failure occurred, resulting in the collapse of Złota Street in Warsaw. Two cars fell into a hot water filled breach in the asphalt. Another such failure occurred in 2011, when Koszykowa Street collapsed due to leach of soil by water from a damaged water supply main (Fig. 3). Similar damage occurred from infiltration of groundwater into a sewer collector under Krakowska Avenue, causing soil erosion in the collector's surroundings.

Fig. 3. Subsidence on Koszykowa Street in Warsaw (source: TVN24 publication)

Deep foundations are becoming one of the key geo-engineering problems. Urban development results in new investments, usually with a leveled basement, occurring in city centres with dense and often historical infrastructure. Such objects not only influence the surface infrastructure, but also underground facilities like subway tunnels and stations. Urban areas are characterized by high "saturation" in the underground infrastructure, which is often sensitive to displacements due to buildings with foundations at considerable depths. [30] Moreover, deep foundations influence the groundwater flow conditions by partitioning natural flow directions, or through complete change of the water regime due to water pumping from/to the soil (not only during construction, but also exploitation). Damming of water flow or its concentration in between deeply founded buildings may result in the initiation of filtration phenomena in areas of respectively high velocity and hydraulic gradient values. For the soils

susceptible to such phenomena (granulometric composition, compaction, flow direction), even a relatively low increase in the gradient may initiate leaching of fine soil grains and, as a result, an increase in soil porosity and decrease in its bearing capacity. In extreme situations, this process may lead to damage or failure of a building founded on such soil.

In some cases, the influence of external factors is so strong that soil degradation occurs regardless of its parameters. In 1998 in Moscow, a soil collapse occurred that caused damage to a two-stage building. (Fig. 4). The collapse occurred when water-saturated sand was removed to a tunnel that was excavated below (Fig. 5). The amount of soil used during repair actions necessary to fill the subsidence was estimated to be over 1000 m^3.

Fig. 4. A building destroyed due to ground uplift from under the foundation to a tunnel executed below, Moscow 1998 [15]

In 2012 in Warsaw, during execution of a tunnel connection for two parts of the subway station Warsaw-Centrum Nauki Kopernik, hydraulic heave occurred at the tunnel front, resulting in flooding and soil inflow into the station platform chamber, in the station western section [11] (Fig. 5). The executed tunnel was localized under an existing tunnel of the Wisłostrada freeway. A vein under the Wisłostrada tunnel occurred due to soil displacement into the station interior (Fig. 6), and tunnel channel constructions underwent displacement (settlement), most probably subsequently wedging at the cavity walls and in dilatations between themselves [9]. The space under the Wisłostrada filled with water to the level of c.a. 2 m under the tunnel slab bottom [24]. The loss of soil from under the Wisłostrada tunnel was estimated to be of c.a. 6500 m^3.

Groundwater related hazards linked to deep foundation execution that may lead to soil displacement are caused by changes in the groundwater table level and filtration processes in the excavation area (Fig. 7). These processes include: flow through leakages in excavation walls, filtration along the contact of wall and soil, filtration below (around) the wall, inflow from a suspended layer to the excavation, as well as changes in groundwater table level due to drainage [30].

Fig. 5. Initial phase of soil liquefaction after the heave of excavation work ceiling [11]

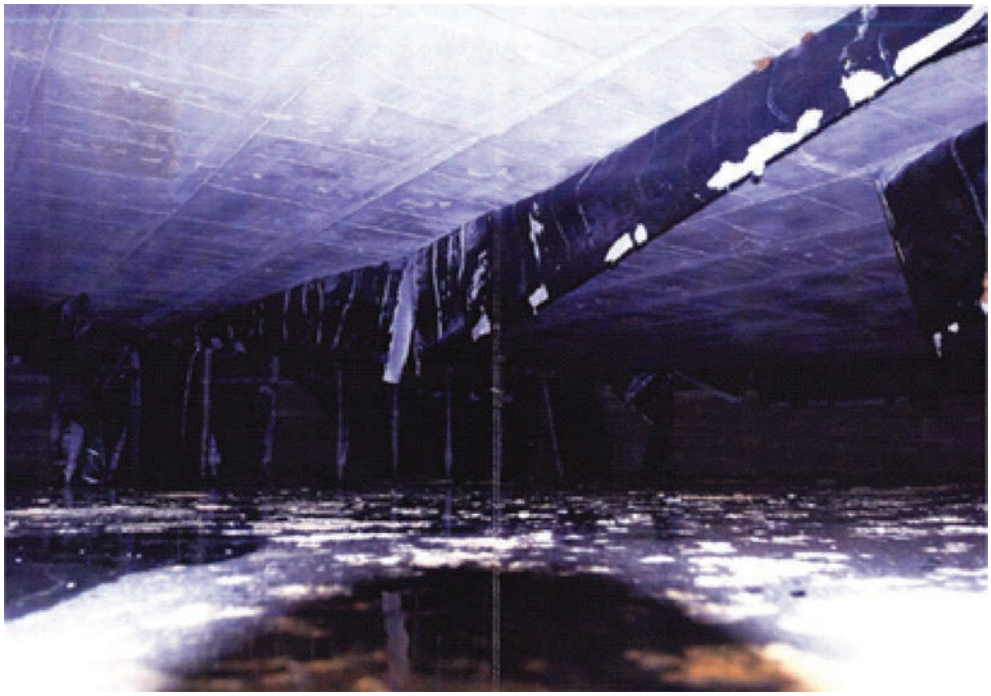

Fig. 6. A view from inside the vein under the Wisłostrada tunnel (materials of AGP) [9]

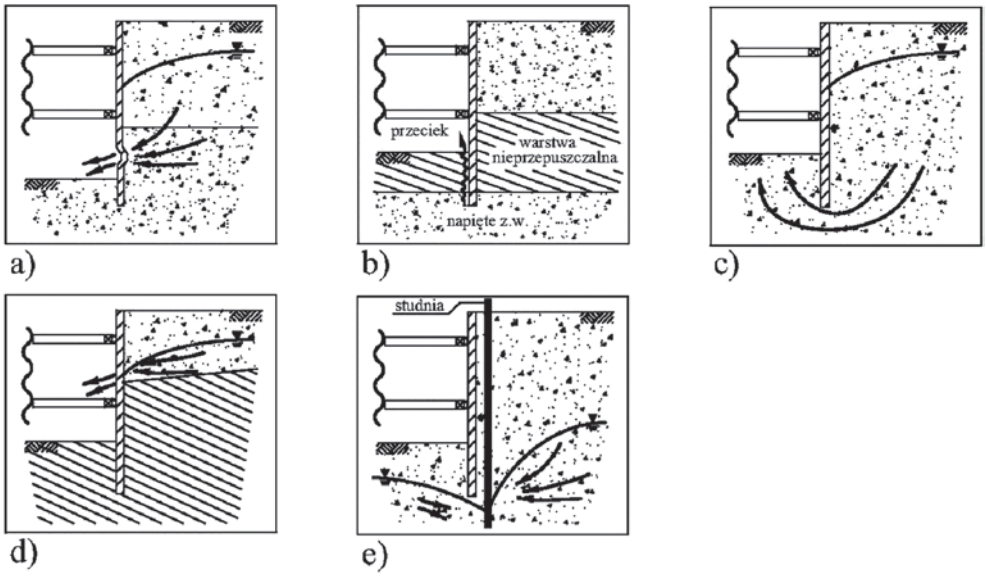

Fig. 7. Groundwater related hazard cases, which may cause changes in the bottom during execution of deep foundations [Clough G., O'Rurke T. 1990]: a) flow though wall leakages, b) flow along the wall and soil contact, c) flow below (around) the wall, d) suspended water inflow, e) drainage-caused flow [30]

The interference of deeply founded buildings with groundwater-soil conditions may result in [30]:

- change in level of groundwater table,
- change in flow direction (sometimes, local direction diversion),
- change in pressure gradient and groundwater flow velocity,
- change in soil parameters (changes of humidity, porosity, suffusion, internal and external erosion, colmatation).

To minimize the negative influence of deeply founded buildings, it is important to execute appropriate design and impact assessment on the groundwater-soil environment during both construction and further exploitation.

2. Suffusion

Suffusion is a phenomenon that belongs to the group of so called filtration deformations. It is based on finer particle or grain removal from the soil or their movement within its mineral structure, due to groundwater flow through that soil [16]. The process may be chemical or mechanical in nature.

Mechanical suffusion is a phenomenon in which soil skeleton elements are under the pressure of flowing water mass, which is referred to as seepage pressure. That pressure mechanically impacts respective elements of the soil skeleton (depending on structure, soil granulometric composition and velocity of filtrating water), causing leaching of soil grains

[5]. Enlargement of soil pores results in an increase in the filtration coefficient and flowing water velocity. The water of higher velocity may move respectively bigger soil grains, causing further development of the suffusion process. An increase in soil porosity decreases its strength and might cause sudden settlement or displacement, or occurrence of channels or hydraulic heave within.

The phenomenon of leaching fine grains from the soil skeleton can progress in various ways, depending on the place of its occurrence in the soil. Those distinguished are: internal erosion, occurring within a certain type of soil; external erosion (also known as backward erosion), occurring in the near-surface zone of bottom and at the contact surface between two different soil layers, when water flow direction is perpendicular to that contact surface; as well as contact erosion, occurring at the contact surface between two different soil types when the water flow direction is parallel to the contact surface (Fig. 8) [29].

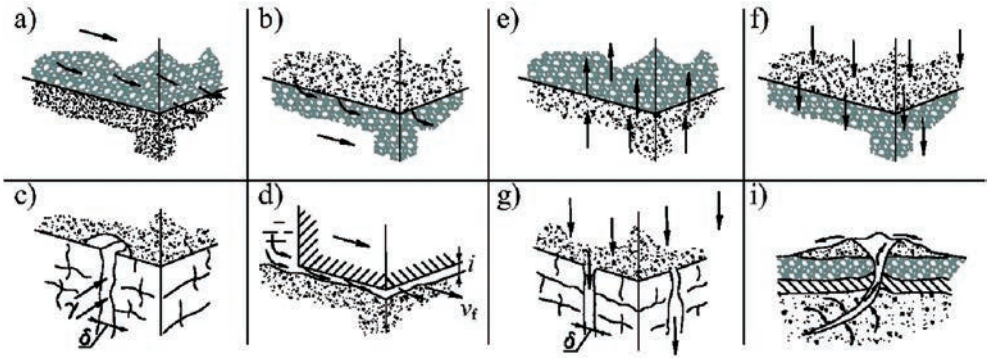

Fig. 8. Forms of soil medium destruction by filtrating water: a) b) c) d) contact erosion, e) f) g) external erosion (backward erosion), i) hydraulic heave [30]

To determine the susceptibility of soil to suffusion, geometrical or hydraulic criteria may be employed. Geometrical criteria refer to soil grain size and the granulometric composition. From the geometrical criterion perspective, two conditions must be met for suffusion to occur:

– the fine grain size in the soil must be smaller than the soil skeleton material pores (a fine soil particle/grain is understood as a grain of diameter smaller than 0.075mm and will be referred further to as such) [4], therefore soil with equal grains will not be susceptible to suffosion, as the dimensions of free spaces in between soil particles are smaller than the size of soil skeleton grains, even if distributed more loosely [7],
– the soil must contain fine particles amount smaller than is necessary to fill the spaces between the coarse, skeleton-forming particles (in the case of finer particle occurrence, the coarse particles will be “borne” in a skeleton of fine-grained soil and suffosion will not occur) [4].

Moreover, for suffusion to start, the forces causing the leach of soil particles must overbear the forces of soil resistance – the hydraulic criterion. Grain resistivity forces depend on the soil type (cohesivity), resulting mainly from their weight and interactions with other particles (granulometric composition, shape of grains, compaction). The velocity of water flowing through must reach the appropriate value (critical velocity), or an appropriately high

hydraulic gradient must occur (critical gradient). This dependence is often referred to as local (hydraulic) gradient difference, described as the critical value gradient for a given soil.

The geometrical criterion is based on soil granulometric composition analysis (grain size distribution curve). The soil is potentially unstable and susceptible to suffosion if its poorly graded or gap- graded (i.e. being of leap character – lack of medium diameter grains in the soil), or if it mainly consists of coarse grains with certain restricted percentile content of fine particles.

Many considerations on the geometrical criterion are still based on Terzaghi's criterion, applied in the design of reverse filters (securing the construction against suffusion). According to this criterion, the following dependencies must be met for erosion not to occur:

$$D_{15}/d_{85} \leq 4 \tag{1}$$

and

$$D_{15}/d_{15} \geq 4 \tag{2}$$

where:

D_{15} – grain diameter of filter soil, whose content, including finer grains, is of 15%,

d_{15}, d_{85} – grain diameter of protected soil, whose content with finer grains is respectively of 15% and 85%.

The seepage pressure refers to hydraulic gradient, which in turn is related to the hydraulic forces that cause the movement of fine soil grains [4]. Terzaghi defined a critical hydraulic gradient for vertical flow, for a scenario of seepage pressure value exceeding the watered bulk density of soil skeleton and causing loss of stability in soil [14]:

$$i_{kr} = (1-n)\cdot(1-\rho) = \frac{\rho - \rho_w}{\rho_w} \tag{3}$$

where:

n – porosity,

ρ – soil volumetric density,

ρ_w – water volumetric density.

The value of the critical hydraulic gradient defined by the equation above, is equal to 1. For this value, the soil undergoes liquefaction. However, critical hydraulic gradients related to suffusion are often lower than those determined employing the equation above [14].

3. Numerical analysis

One of the possible means to evaluate the impact of deep foundations on groundwater-soil environment and the possibility of suffusion is numerical calculations. Such analysis has been performed for a zone in between Puławska, Dolna, Konduktorska and Belgijska streets, in the area of Morskie Oko Square in Warsaw (Fig. 9). The calculations were performed

to investigate the possible influence of deep foundations on groundwater-soil conditions in the investigated area, through analysis of the changes in directions, velocities and gradients of water flowing through. The geological setting was prepared in numerical form (GIS). The model was built in the HydroGeo Builder software and subsequently the necessary parameters and boundary conditions were determined in Visual Modflow, with subsequent execution of the model.

The goal of the execution of the model was to investigate the deep foundation's influence on groundwater-soil conditions through:

- analysis of groundwater table changes,
- analysis of water flow directions,
- analysis of possible periodic humidification causes for surrounding buildings,
- analysis of groundwater gradients and flow velocities,
- identification zones of soil being potentially at risk of suffusion.

Fig. 9. The new deep foundation buildings are surrounded by a black line. The striped field depicts the area of existing buildings whose basements are damp [map source: geoportal.gov.pl]

The restriction of the model depth below ground level was assumed on the boundary of Pleistocene sediments, i.e. on the ceiling level of Pleistocene clays (on average, at 80 m b.g.l.). Quaternary deposits occurring in the investigated area are typical for continental glaciations.

The quaternary groundwater bearing horizon occurs in the whole city area. The high plain part of the investigated area breaks into the eastern and western part, from which the first is of multi-layer groundwater bearing horizon and the latter has one groundwater bearing horizon, mostly occurring in the eastern part. The two groundwater bearing horizons, locally three on the south-east, remain in hydraulic contact, with their possible transformation into one layer towards north. The quaternary groundwater bearing horizon generally lacks isolation from the surface.

To allow numerical modelling, conceptual soil conditions had to be developed, with certain assumed groundwater conditions. After analysis of the known geological cross-sections, the one near Belgijska street was selected (recommended by PGI-NRI) (Fig. 10).

As no water outflow from the scarp was observed in the investigated area (water-head area) [32, 33] it was assumed that hydraulic connection must exist between the surface and the sands overlaying the high plain, as well as these sands and the valley sands (PGI-NRI, ITB). Such a state entails the existence of hydrogeological windows, i.e. areas lacking in impermeable layers, which results in direct filtration. Moreover, a landslide occurred in the investigated area in the past, which could have led to mixing of soil layers. Therefore it was stated that permeable soils must occur in the area depicted with black line on Fig. 10.

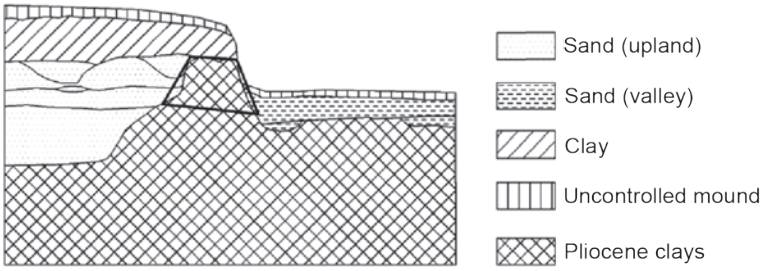

Fig. 10. A sketch geological cross-section of the investigated area [PGI,32,33]
The black line surrounds soil area of changes in filtration coefficient value, depending on the numerical calculations variant under consideration

The planar placement of permeable layers was changed in subsequent variants. An area was established at the scarp, in the contact zone of high-plain and valley sands, for which zones of changing filtration coefficient were determined (depending on calculation variant, the flow through the zone was enabled or disabled). The filtration coefficient value assumed for the permeable zones was of $1 \cdot 10^{-4}$ m/s, whereas for impermeable layers it was given at $1 \cdot 10^{-6}$ m/s.

The groundwater level was established on two model boundaries (left and right), according to the natural groundwater flow (from the scarp towards the Vistula river). Initial groundwater level was determined based on the map (Fig. 11) from PGI-NRI, depicting mean, multiannual values.

The average annual rainfall in Warsaw was taken at the level of 500mm/year. Filtration index was assumed at 0.25. On that basis, the determined amount of rainwater infiltrating to the soil was of 125mm/year.

Calculations in Visual Modflow were executed for five variants, varying in planar placement of changing filtration coefficient zone.

The building foundation depth was assumed according to the scheme in Fig. 12 below:
- new, deeply founded buildings (marked on fig. 10 with red line): 10 m b.g.l.,
- old buildings, with basements rising above the ground level: 2.5 m b.g.l. (two buildings by Ludowa Street),
- old buildings with basements below the ground level: 3.0 m b.g.l.,
- old buildings without basements: 1.5 m b.g.l.

Calculations for each variant were executed in two versions:
- Version 1 – taking deep foundation buildings into account,
- Version 2 – disregarding deep foundation buildings.

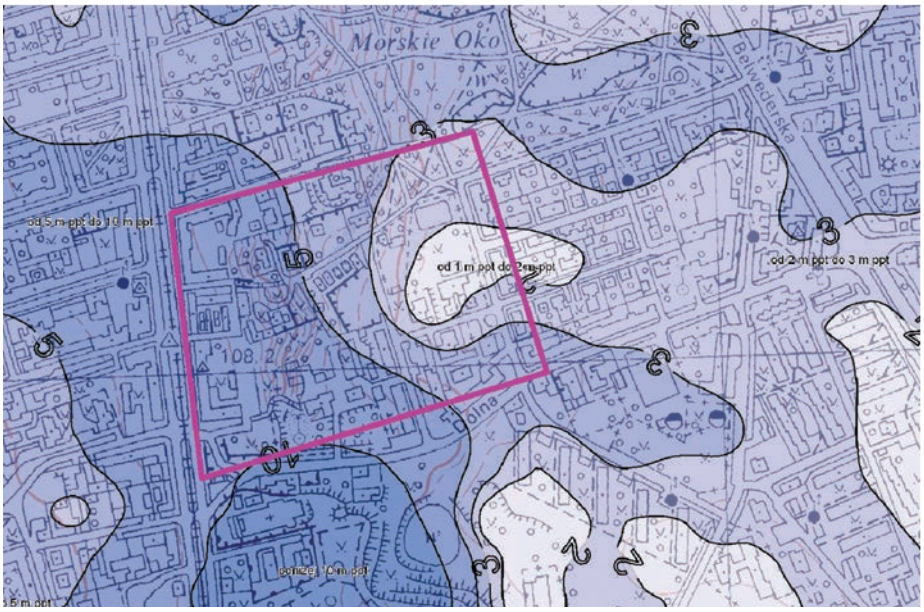

Fig. 11. The first groundwater table – multiannual average state [PGI-NRI]
The boundaries of the area investigated are marked with pink line. Isolines (black) depict the groundwater table depth below the ground level

To diversify the building foundation depth, the model space was divided in-depth into two layers. The foundations of deeply founded buildings partition the whole model height, as the cavity walls used for their construction were dipped into the upper surface of the impermeable layer, which constitutes the lower model boundary.

This paper presents the results for one variant (Fig. 14 to 16). Figures 14 and 15 represent the results for the version taking deep foundation buildings into account, whereas Fig. 16 – for the version without. The arrows visualize the velocity vectors of water flow. Also, groundwater level isolines (5m step) are marked, whereas the thick black line depicts areas of changing (depending on variant) filtration coefficient values. As can be observed, including deep foundation buildings into the model caused change in the direction of water flow. Due to the narrowed water outflow possibilities from the scarp towards the Vistula River and the partitioning of natural flow, an increase in gradients and flow velocities occurred, compared to the variant disregarding the deep foundations.

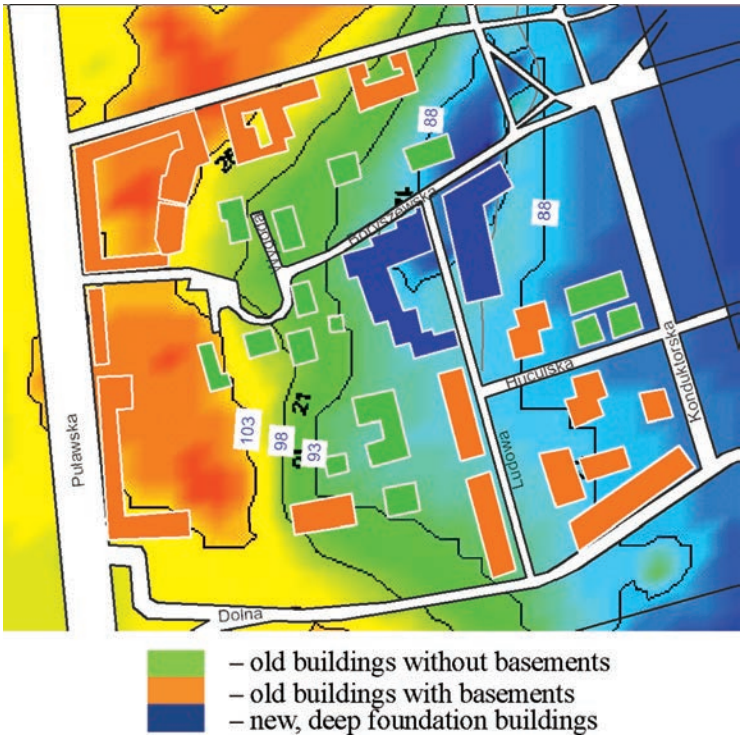

Fig. 12. Situational plan – upper model surface generated in HydroGeoBuilder software, with introduced localization of buildings and roads; levels are given in m a.s.l.

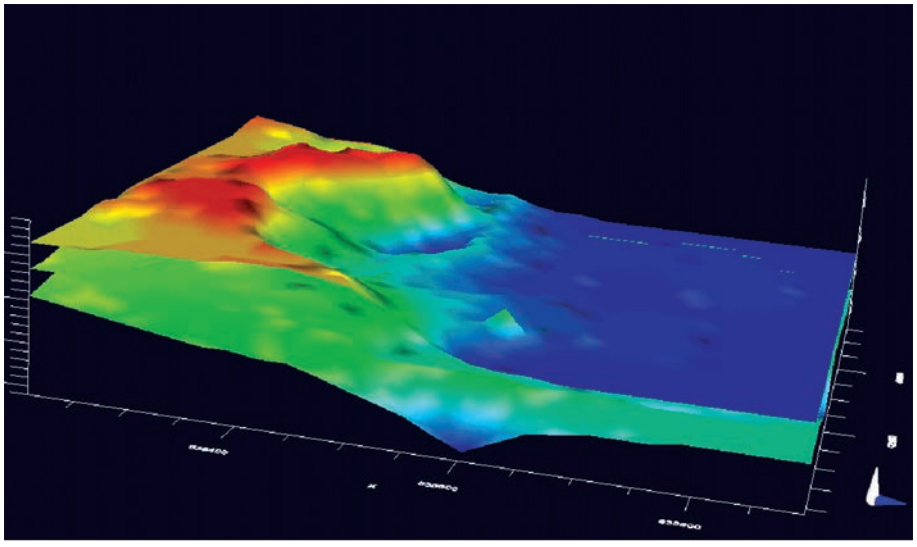

Fig. 13. A 3D view of the modeled area from Dolna Street perspective (HydroGeoBuilder)

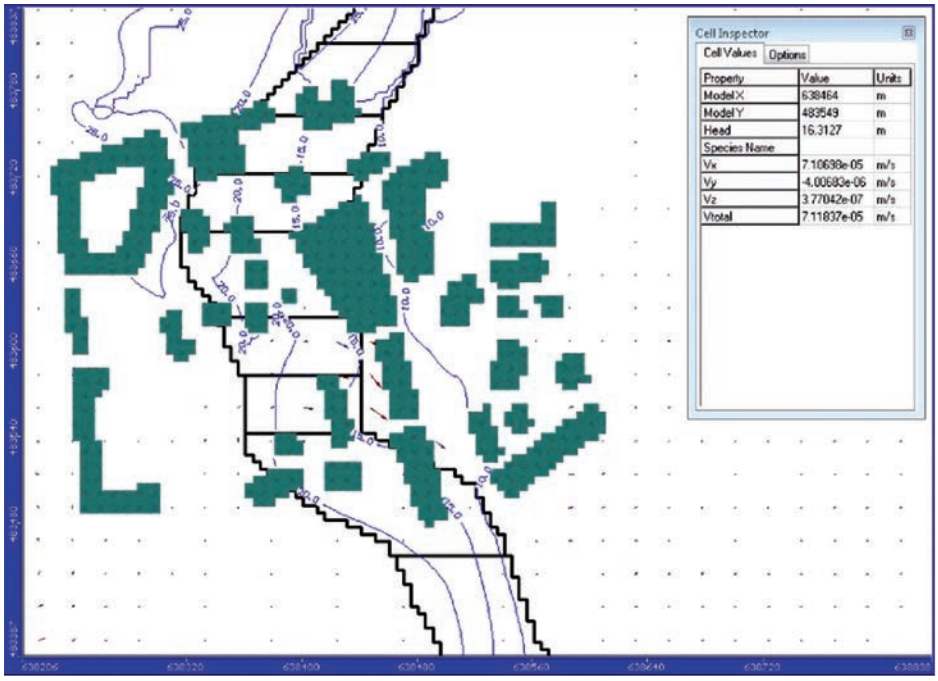

Fig. 14. Results for variant III – Version1 / Layer1

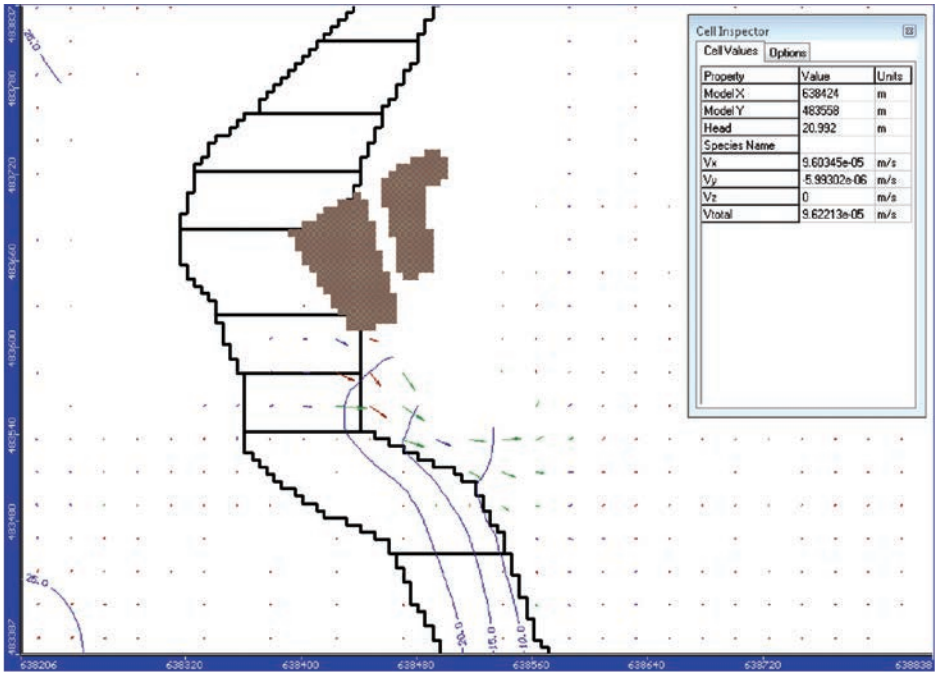

Fig. 15. Results for variant III – Version1 / Layer2

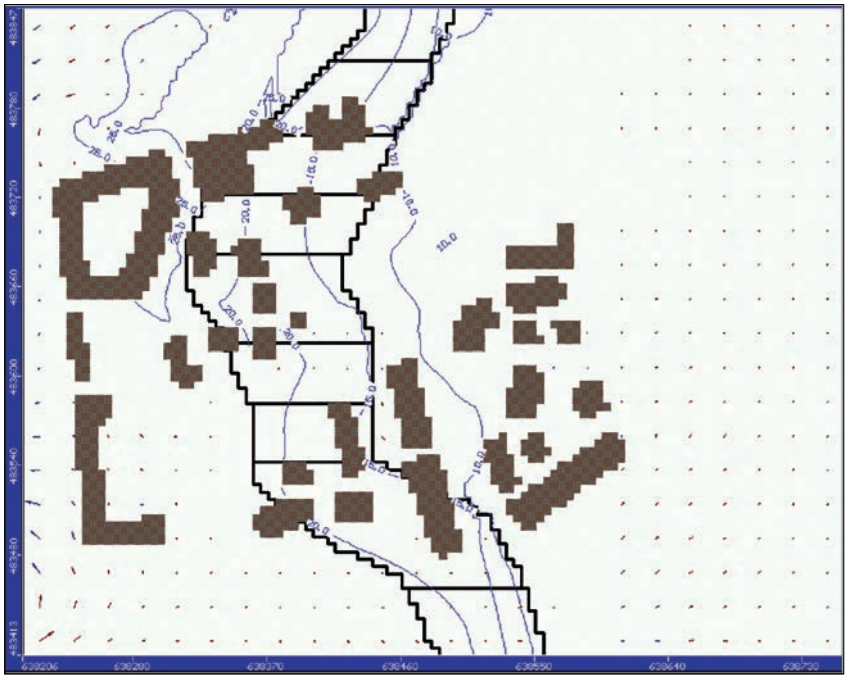

Fig. 16. Results for variant III – Version2 / Layer1

After the numerical analysis for all the variants, it was stated that there was noticeable influence of deep foundation buildings occurs on groundwater flow directions, velocity and gradient values, as well as groundwater table level. The deep foundation and narrowing of permeable space on the contact between high-plain and valley sands, caused flow concentration and uplift of the groundwater table.

In some calculation variants, the output gradients reached values considered sufficient to initiate suffusion under favourable geological conditions [14].

Following the analysis of possible causes for building basement humidification by Huculska Street, additional elements were pointed out that may contribute to periodic or constant uplift of groundwater level except rainwater infiltrating naturally in the area:

– periodic groundwater table uplift in the given area can be caused by rainwater exfiltrating from a leaking rain-pipeline or, if a field downslope occurs towards these buildings – additional water infiltrating in the area, originating from surface runoff,
– additional factor for the potential increase in basement humidification are, as mentioned above, leaking water pipelines, water from which exfiltrates to the soil constantly, supplying the groundwater bearing horizon. The condition of water and sewage infrastructure in the described area should be verified in the field,
– after the performance of numerical modelling it was observed that groundwater table uplift occurred in some variants after execution of deep foundation buildings, being additionally strengthened by narrowed groundwater outflow from the high plain towards the Vistula river. The above may be the next factor influencing the humidification of basements after rainfall, as an element causing constant uplift of the groundwater table.

4. Summary

In 1946, Terzaghi compared the importance of means to be assured by a designer to prevent external suffusion to the importance of anti-corrosion means in steel constructions, or means protective against biological degradation in wooden constructions [30].

Sufussion and external erosion issues have been addressed since 2004 by the ICOLD working group (International Commission of Large Dams). The final stage of Group work is the preparation of a report – a set of data and practical guidance to prevent internal erosion. The first part of the report was edited in 2013 [30].

In the document Eurocode 7 (PN-EN 1997-1:2008), bottom deformations that may result in loss of stability were raised up to a range of critical soil state, which justifies the necessity of in-depth analysis for that phenomenon. However, assessment criteria for suffusion of soils were not determined in the abovementioned standards. Hence, developing adequate tools and determining appropriate action schemes for soil analysis of this phenomenon are of crucial importance in the short term. Suffusion is now not only considered a marginal phenomenon occurring in the soil, but a real hazard deciding on ground stability.

Taking the aforementioned, it seems necessary that Warsaw, as a developing urban agglomeration, undergo a thoroughgoing analysis to assure construction safety not only for existing buildings, but also for objects currently planned or in construction. Performing numerical analysis for the urban part is necessary, with a set of laboratory tests aimed at determining the susceptibility of soils in Warsaw to suffusion. Based on the numerical and geotechnical research given above, adequate tools can be determined that take geometrical and hydraulic criteria for soil suffusion into account, with simultaneous consideration of effective stress influence. The research may lead to identification of areas in central Warsaw that are particularly at risk of changes in groundwater-soil conditions due to deep foundations. Establishing appropriate criteria, assisted by numerical calculations at the investment planning & design stage, would appear to be a necessary element in identifying and undertaking appropriate preventive measures to eliminate the negative impact of suffusion. Such action will ensure the sustainable and safe development of urban areas.

References

[1] Baran P., Gruchot A.T., *Metoda doboru gruntów i projektowania filtrów odwrotnych ochraniających grunty sypkie*, 1999–2003.

[2] Bonelli S., *Erosion of geomaterials*, ISTE Ltd 2012.

[3] Delleur J.W., G.T., CRC Press 2007.

[4] Fell R., Wan Ch.F., *Methods for estimating the probability of failure of embankment dams by internal erosion and piping in the foundation and from embankment to foundation*, UNICIV REPORT No. R-436, Sydney 2005.

[5] Filipowicz B., Sobkowiak J., *Zjawisko sufozji: trudne do przewidzenia czy błąd człowieka?*, Bielsko-Biała 2005.

[6] Filipowicz B., Sobkowiak J., P*rocesy sufozyjne – w jakiej sytuacji mogą wystąpić*, Bielsko-Biała 2007.

[7] Filipowicz B., Florkiewicz A., *Zjawisko i sposoby zapobiegania sufozji*, Instytut Inżynierii Lądowej Politechniki Poznańskiej, 2011.
[8] Grabowski D., *Objaśnienia do mapy osuwisk terenów zagrożonych ruchami masowymi ziemi*, PIG, Warszawa 2010.
[9] Grodecki W., Lewandowska-Siemiańska A., *Ekspertyza dotycząca określenia przyczyn awarii i metod jej usunięcia na stacji C13 odcinka centralnego II linii metra w Warszawie*, Politechnika Warszawska, Instytut Dróg i Mostów, Zakład Geotechniki i Budowli Podziemnych, 2012.
[10] Grubecki J., Sysak J., *Geologia inżynierska*, Arkady, Warszawa 1960.
[11] Grzegorzewicz K., Kłosiński B., Rychlewski P., *Ekspertyza techniczna dotycząca określenia przyczyn awarii i metod jej usunięcia na stacji C13 odcinka centralnego II linii metra w Warszawie*, IBDiM, Warszawa 2012.
[12] Howard K., Israfilov R., *Current problems of hydrogeology in urban areas, urban agglomerates and industral centres,* Kluwer Academic Publishers, 2002.
[13] ICOLD, *Internal erosion of existing dams, levees and dikes, and their foundations. Volume1: Internal erosion processes and engineering assessment*, CIGB ICOLD, 2012.
[14] Jantzer I., Knutsson S., *Critical gradients for tailing dam design*, Luleå University of Technology, Sweden.
[15] Khomenko V.P., *Suffosion hazard: Today's and tomorrow's problems for cities*, IAEG, 2006.
[16] Kowalski W.C., *Geologia inżynierska,* Wydawnictwa Geologiczne, Warszawa 1988.
[17] Kwiatek J., Frolik A., Straszewski B., Rogoż M., *Ochrona obiektów budowlanych na terenach górniczych*, Wydawnictwo Głównego Instytutu Górnictwa, Katowice 1997.
[18] Kwietniewski M., *Awaryjność infrastruktury wodociągowej i kanalizacyjnej w Polsce w świetle badań eksploatacyjnych*, XXV Konferencja Naukowo-Techniczna, Międzyzdroje 2011.
[19] Lerner D.N., *Groundwater recharge in urban areas*, IAHS Publ., no. 198, 1990.
[20] Li M., *Seepage induced instability in widely graded soils*, The University of British Colombia (Vancouver), May 2008.
[21] Łukasik S., *Warunki geotechniczne w rejonie tunelu Trasy W-Z, kościoła św. Anny i Zamku Królewskiego w Warszawie*, Prace ITB, Kwartalnik nr 3 (135) 2005.
[22] Łukasik S., *Stan Skarpy Wiślanej na odcinku Starego Miasta w Warszawie*, Miesięcznik Materiały Budowlane 2/2005.
[23] Łukasik S., *Stateczność Skarpy Zamku Królewskiego i Starego Miasta w Warszawie*, ITB, 60 lat Zakladu Geotechniki i Fundamentowania ITB, Seminarium, Warszawa 2005.
[24] Łukasik S., Godlewski T., Chada K., Kaczyński Ł., Sobiech J., *Ekspertyza techniczna dotycząca przyczyn powstania awarii na budowie stacji C13 II linii metra w Warszawie*, ITB, Warszawa 2012.
[25] Marsalek J., Jimenez-Cisneros B.E., Malmquist P.A., Karamouz M., Goldenfum J., Chocat B., *Urban water cycle processes and interactions*, Unesco/IHP 2006.
[26] Moffat R., Fannin J., Garner S.J., *Spatial and temporal progression of internal erosion in cohesionless soil*, Canadian Geotechnical Journal, March 2011.
[27] Nowicki Z., *Wody podziemne*, PIG, 2007.
[28] Pokrajec D., Howard K., *Advance simulation and modelling for urban groundwater management – UGROW*, CRC Press 2010.

[29] Popielski P., *Model sufozji mechanicznej w ujęciu metody elementów skończonych*, Warszawa 2000.
[30] Popielski P., *Oddziaływanie głębokich posadowień na otoczenie w środowisku zurbanizowanym,* Prace naukowe Politechniki Warszawskiej, Inżynieria Środowiska, Warszawa 2012.
[31] Rutschmann P., *Assessment of Risk of Internal Erosion of Water Retaining Structures: Dams, Dykes, Levees*, 2007.
[32] Sarnacka Z., *Stratygrafia utworów czwartorzędowych Warszawy i okolic*, Wydawnictwo Geologiczne, 1992.
[33] Sarnacka Z., *Objaśnienia do szczegółowej mapy geologicznej Polski, Arkusz Warszawa Wschód*, Wydawnictwo Geologiczne, 1980.
[34] Seiler K.P., Gat J.R., *Groundwater recharge from run-off, infiltration and percolation*, Springer, 2007.
[35] Semar O., Witt K.J., Fannin R.J., *Conference: International Conference on Scour and Erosion 2010: Suffosion evaluation – comparison of current approaches*, American Society of Civil Engineering.
[36] Steeb H., Diebels S., Vardoulakis I., *Conference: Geo-Denver 2007: Modeling internal erosion in porous media*, American Society of Civil Engineering.
[37] Wiłun Z., *Zarys geotechniki*, Wydawnictwa Komunikacji i Łączności Warszawa 1976, 2010.
[38] Wysokiński L., *Ocena stateczności skarp i zboczy. Zasady wyboru zabezpieczeń*, ITB, Instrukcje, wytyczne, Poradniki nr 424/2011.

TECHNICAL TRANSACTIONS | CZASOPISMO TECHNICZNE
ENVIRONMENTAL ENGINEERING | ŚRODOWISKO
2-Ś/2015

MARIUSZ BIAŁY*, SZYMON SKRZYPIEC

ANALYSIS OF INTERACTION OF PREFABRICATED REINFORCED CONCRETE TUNNEL WITH SUBSOIL

ANALIZA WSPÓŁPRACY ŻELBETOWEGO PREFABRYKOWANEGO TUNELU Z PODŁOŻEM GRUNTOWYM

Abstract

The paper presents the results of analyses of numerical interaction between a tunnel made of reinforced concrete prefabricated with backfill and stratified ground. A number of variants of foundation have been discussed: gravel cushion, on an additional concrete strip, and on a cap based on jet-grouting columns. The grounds in the simulations were described using the Coulomb-Mohr model.

Keywords: prefabricated tunnel made of reinforced concrete, numerical analysis of interaction between tunnel and subsoil and backfill

Streszczenie

W artykule zaprezentowano wyniki analiz numerycznych współpracy żelbetowego tunelu prefabrykowanego z zasypką i z uwarstwionym podłożem. Rozpatrzono kilka wariantów posadowienia: na poduszce żwirowej, na dodatkowej ławie betonowej i na oczepie opartym na kolumnach jet-grouting. Grunty w symulacjach opisano modelem Coulomba-Mohra.

Słowa kluczowe: żelbetowy tunel prefabrykowany, analizy numeryczne współpracy tunelu z podłożem i zasypką

DOI: 10.4467/2353737XCT.15.223.4609

* PhD. Mariusz Biały, MSc. Szymon Skrzypiec, Department of Geotechnics, Faculty of Civil Engineering, The Silesian University of Technology.

1. Introduction

During recent years, intensive works on the building of expressways, clearways and local roads have been carried out in Poland. These routes must overcome several obstacles which necessitate the building of a large number of engineering objects: viaducts, bridges, culverts and tunnels. The participation of the costs of these objects in total road costs is significant. It can be restricted by using, where possible, prefabricated structures. Actually, a number of systems based on prefabricated elements are used: Matiere present on the British and Irish market, and in the countries of Central-Eastern Europe mediated by ABM Europe, Tech Span delivered by the Reinforced Earth Company of the Freyssinet group and BEBO offered by Swiss BEBO International AG.

Concrete reinforced, backfilled tunnels that are based on prefabricated arches have a span from 3 to 20 m, height up to 9 m and length up to 360 m. The coat thickness changes within 200 and 350 mm, exceptionally is 520 mm. The relation of arch radius to their range rises together with an increase in the coat thickness of the initial backfill. The BEBO system uses elliptic arches, circular and "shallow arch" (flattened parabolic arches) fixed one or two parts united on the build site. The Matiere system is based on three arches made of three parts two curved walls with a shaped isolated footing and a curved ceiling element. The widening of the foundation through concreting a bracket is used. Construction of the tunnel segment in Tech Span technology comprises the following prefabricated elements: the foundation, two half-arches and a wet concrete principal beam connecting them. The task of the principal beam is to brace the tunnel construction at length without moving the bending moments where it connects with the shells.

2. Description of the analysed object

The analysed object is one of a series of arches passing above a small number of obstacles of the flyover of a national road. The designers of the flyover used the Matiere system arch of range 18.128 m and height 9.787 m.

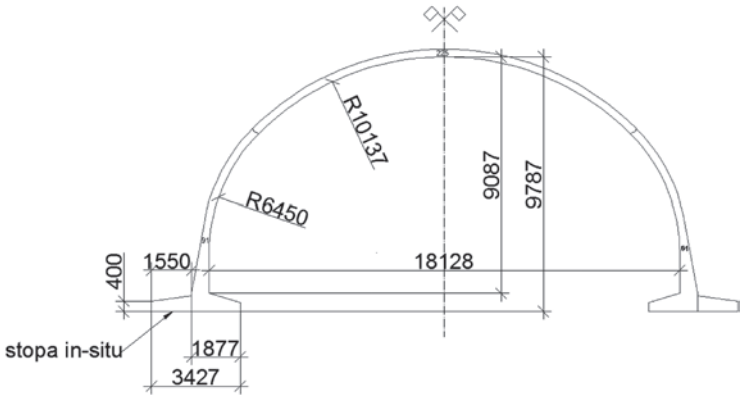

Fig. 1. Section of the prefabricated reinforced concrete element of the Matiere system arch

The geometry of this arch is presented in Fig. 1, and the method of assembling the segments for a double communication tunnel is presented in Fig. 2.

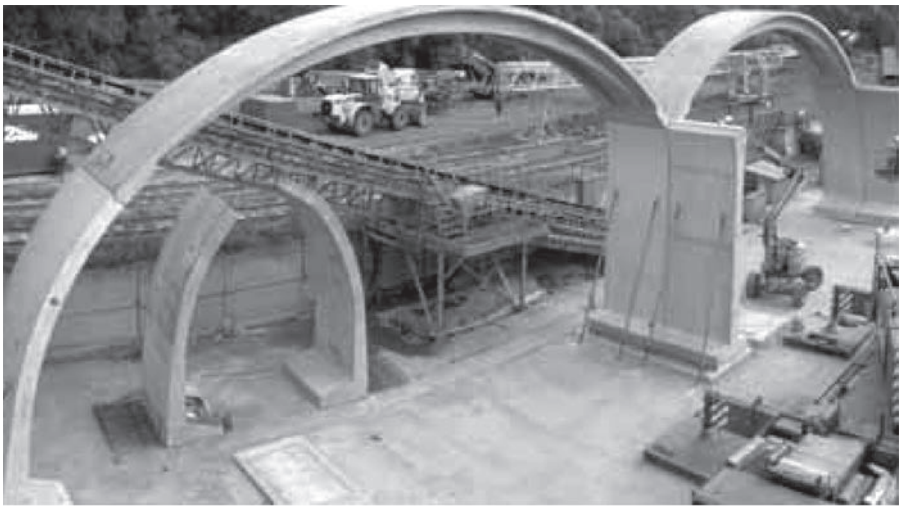

Fig. 2. Construction of the arch of Matiere system made of prefabricated elements

The foundation of the prefabricated element was widened by concreting an additional bracket 1.55 m, finally obtaining a strip width of 3.427 m. The thickness of the pod is 300 mm, and the segment length is 2.49 m. The tunnel length is is 63 m.

During creating the tunnels with prefabricated elements, the method of preparing the backfill of the integrated tunnel construction is significant. Arranging the backfill can start after setting the wet concrete. The backfill should be made of well compacted soils that have less than 10% grains, smaller than 0.05 mm, obtaining a compaction index I_s = 0.98. The compaction should be made on a layer thickness of 25 cm, at the difference of the level at both sides of the transverse section not larger than 50 cm. Within a distance not larger than 2 m from the shell edge, only manually controlled compaction is allowed.

The assembly of the prefabricated walls and ceiling arch of the individual segment of the tunnel requires high precision. The foundation of the shell should be made with an accuracy up to 3 mm on each 6 m of the length. Moreover, the requirements are changed that concern the acceptable deformation of the integrated construction on the plane of the tunnel transverse section. The maximum difference of foundations settlements of the opposite wall should not exceed 10 mm. Maximal settlements of the foundation layer of the road on the road layers and over the prefabricated construction cannot exceed 100 mm. In the engineer's practice, for estimation of the tunnels foundations settlements the Winkler model is used. The rigidity of the subsoil is determined by the elasticity coefficient K determined on the basis of pressiometric and dilatometric studies. The modification of the way of calculation of the modulus was introduced by J.Krizek, and details of the changes are given in reference [3].

3. Numerical analyses

The numerical model was generated in the Z_Soil sytem ver 11-07. The mesh was made step by step using the existence function. In the first step (initial state) the subsoil of the embankment with the road situated in the tunnel was erected. Additionally the initial stress state was calculated. The next step was the erection of the prefabricated arch with layers of backfill and the road situated in the tunnel.

Three variants of the tunnel foundations grounding are discussed:

a) on the foundation strip of width 3.43 m based on a soil cushion of width 4.0 m and thickness 1.56 m,
b) on the strip of width 4 m and height 0.92 m made under the prefabricated element and additional bracket,
c) on the strip based on the foundation supported by jet-grouting columns.

It should be pointed out that in the Matiere system, the additional concrete pad is made under the back of the prefabricated wall element which facilitates the construction leveling and concreting an additional bracket widening the tunnel foundation, hence the b) scheme was adopted.

The subsoil of the object is recognized as fine sands and sand with gravels in medium state, dense state, clay in hard-plastic, plastic and soft-plastic state. The modulus of elasticity E of soils was given from PN-81/B-03020. For the soil characteristic, the elastic, plastic ideal model of the ground with a Coulomb-Mohr plastic surface was adopted. The concrete of the shell, the pad foundation, capping beam and ground-cement material of jet-grouting columns were described using an elastic model. The discretisation of the geometric models for the presented tasks is shown in Fig. 3, 4 and 5. Jet-grouting columns were modelled with beam elements. The parameters of the material sections are presented in table 1. Between the concrete arch and soil, interfaces were generated ($\phi = 20°$, $c = 2$ kPa). The mesh of the FEM elements was created in Autodesk Auto CAD system and exported to the Z_Soil system.

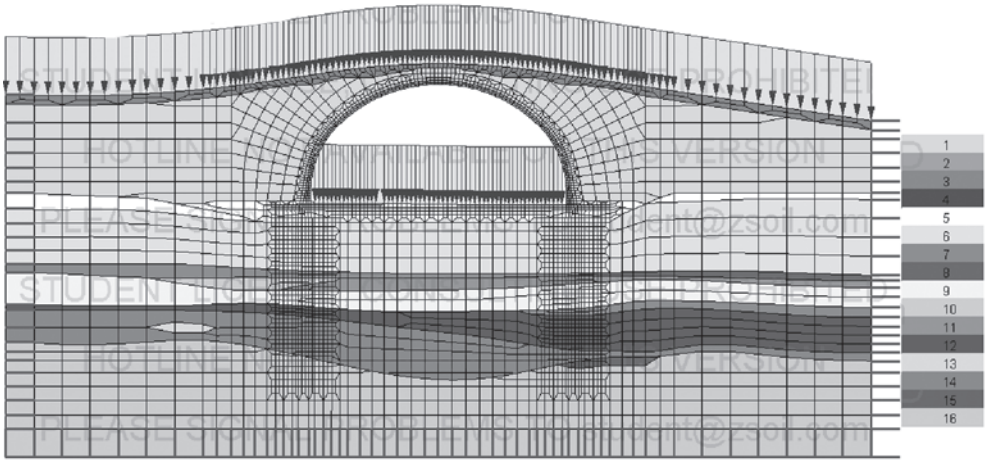

Fig. 3. Discretization of the FEM mesh of the prefabricated arch with backfill and subsoil

Table 1

Parameters of material zones of the models adopted in the numerical analyses

Lp.	Material zone	Internal friction angel [°]	Cohesion c_u [kPa]	Specific gravity γ [kN/ m^3]	Poisson ratio ν [–]	Modulus of elasticity E [MPa]
1	Backfill	35	2	18	0.25	130
2	Tunnel arch	–	–	25	0.2	37000
3	Road structure	–	–	25	0.2	550
4	Concrete bracket	–	–	25	0.2	500
5	FSa. I_D = 0,58	31	2	16.5	0.3	55
6	FSa. I_D = 0,50	30.5	2	17.5	0.3	50
7	FSa. I_D = 0,50 below water level	30.5	2	9	0.3	50
8	FSa. I_D = 0,33	30	2	8.5	0.2	35
9	grS., I_D = 0,64	39	2	11	0.25	165
10	saCl. I_L = 0,61	15	26	20.5	0.3	20
11	saCl. I_L = 0,42	18	30	21	0.25	23
12	saCl. I_L = 0,05	25	50	22	0.25	70
13	saCl. I_L = 0,21	21.5	39	22	0.25	37
14	FSa. I_D = 0,51	30.5	2	17.5	0.3	50
15	grSa. I_D = 0,77	40	2	20	0.2	190
16	saCl. I_L = 0,00	25	50	22	0.25	68
17	Jet-grouting	–	–	22	0.2	5400

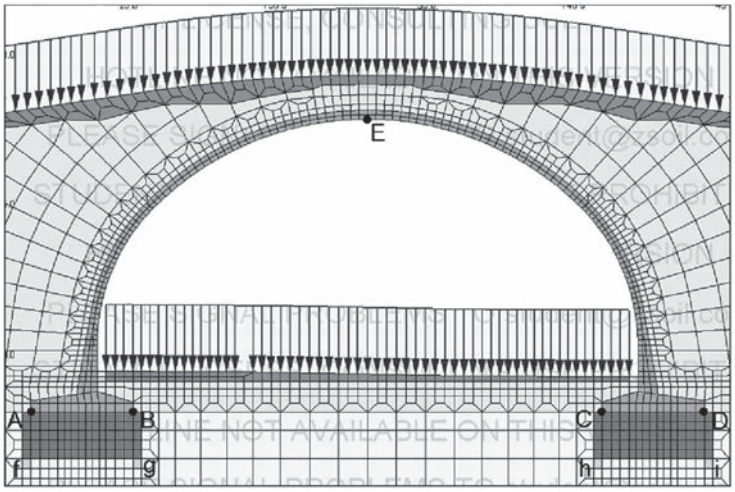

Fig. 4. Scheme of FEM mesh of the model of tunnel supported on gravelly cushions

For controlling model sensitivity, numerical analyses for different thicknesses of subsoil were carried out. Settlements of the tunnel increase with changing the thickness of analysed subsoil but the differences were small. In case of tunnel foundation on jet-grouting columns and deepened subsoil under columns up to 10 m, settlements increase to 2 mm.

The analyses were made for two schemes of road loading on the tunnel arch:

a) the load exists on the whole embankment,
b) the load exists over half of the embankment.

The parameters of the jet-grouting columns material were taken from monograph [1], and the parameters of the soil cushion were adopted on the basis of paper [4]. In the numerical analyses, the displacements of nodes marked in Figures 3 and 4 and stress in the subsoil under the gravelly cushion and the base of the jet-grouting columns were observed. The results of the analyses were given in the tables 2 and 3.

Table 2

The comparison of the tunnel construction displacements for three variants of foundation at symmetrical load

Type of foundation	Gravelly cushion	Strip foundation	Jet-grouting columns
Average settlements of the tunnel construction [mm]	49.8	49.6	29.7
Vertical displacement U_{YY} of E node (mm)	52.8	51.7	33.3
Settlements difference of the opposite foundation in the tunnel transverse section [mm]	7.4	7.3	1.8
Maximal settlements of the embankment [mm]	55.1	54.3	49.1

Table 3

The comparison of the tunnel construction displacements for three variants of foundation at nonsymmetrical load

Type of foundation	Gravelly cushion	Strip foundation	Jet-grouting columns
Average settlements of the tunnel construction [mm]	43.3	42.7	24.9
Vertical displacement U_{YY} of E node (mm)	45.5	44.6	27.4
Settlements difference of the opposite foundation in the tunnel transverse section [mm]	20.2	18.9	9.9
Maximum embankment settlement [mm]	55.7	55.1	49.2

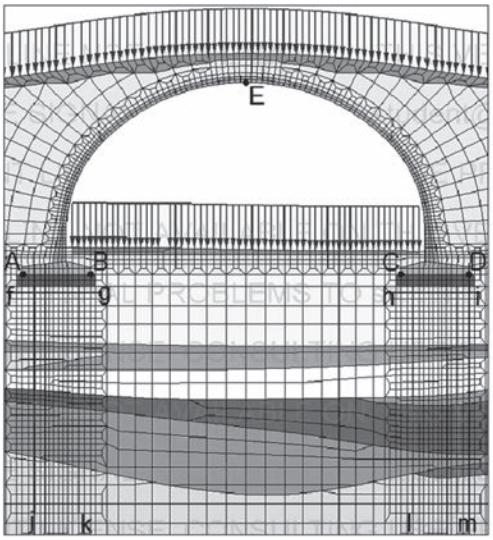

Fig. 5. Scheme of FEM mesh of the tunnel foundation on jet-grouting columns

4. Conclusions

Taking into account the results of numerical analyses, it can be concluded:

– for asymmetrical load the acceptable difference of opposite foundation in tunnels cross-section was satisfied only in the case of tunnel foundation on jet-grouting columns,
– for each case of tunnel foundation the maximum value of vertical displacements of road bed situated on the tunnel the limits were not exceeded.

In the future, for numerical analyses carrying out for interaction of prefebricated tunnel with subsoil, a soil model which describes the changes in the rigidity of the soil within very small deformations should be used. This model will improve the precision of estimating subsoil changes.

References

[1] Bzówka J., *Współpraca kolumn wykonanych techniką iniekcji strumieniowej z podłożem gruntowym*, Monografia. Wydawnictwo Politechniki Śląskiej, Gliwice 2009.
[2] Furtak K., Kędracki M., *Podstawy budowy tuneli*, Wydawnictwo Politechniki Krakowskiej im. Tadeusza Kościuszki, Kraków 2005.
[3] Krizek J., *Soil-structure interaction of integral Bridges*, Structural Engineering International" 2/2011, 169–174.
[4] Sękowski J., *Podstawy wymiarowania poduszek wzmacniających*, Zeszyty Naukowe Politechniki Śląskiej, Budownictwo z 94, 2002.
[5] *Z_Soil.PC 2011, User Manual*, ZACE Services Ltd., Lausanne 2011.

TECHNICAL TRANSACTIONS | CZASOPISMO TECHNICZNE
ENVIRONMENTAL ENGINEERING | ŚRODOWISKO
2-Ś/2015

DOMINIKA DĘBSKA*, BOGUSŁAW ZAJĄC**

CHANGES IN THE THERMAL EXPANSION COEFFICIENT OF CONCRETE DUE TO EXPOSURE TO AGGRESSIVE CHEMICAL ENVIRONMENT

WPŁYW ODDZIAŁYWANIA CHEMICZNEGO NA ROZSZERZALNOŚĆ TERMICZNĄ BETONÓW CEMENTOWYCH Z KRUSZYWA WĘGLANOWEGO

Abstract

An analysis of the impact of long-term sulphate examination conditions on the thermal expansion of ordinary cement concrete made with the use of various limestone aggregates is presented in the paper. The article contains the results of selected chemical and temperature laboratory testing. This issue is of significant value for the description of cement concrete durability under aggressive conditions in a wide range of temperatures. The experimental results can usefully be applied to predicting the sustainability of ordinary cement concrete as well as its joints working under defined aggressive conditions.

Keywords: durability, ordinary cement concrete, limestone aggregate, sulphates, CTE, coefficient of thermal expansion

Streszczenie

Przedmiotem artykułu jest analiza wpływu długoterminowego oddziaływania siarczanów na rozszerzalność termiczną betonu cementowego z kruszywem wapiennym. Opisano laboratoryjne badania chemiczne oraz termiczne. Zagadnienie to ma istotne znaczenie dla opisu pracy betonu w środowisku agresywnym w szerokim zakresie temperatury. Wyniki badań mogą być wykorzystane w zagadnieniach związanych z opisem trwałości zarówno elementów betonowych, jak i ich połączeń.

Słowa kluczowe: trwałość, beton cementowy, kruszywo wapienne, siarczany, rozszerzalność temperatura

DOI: 10.4467/2353737XCT.15.224.4610

* PhD. Dominika Dębska, Institute of Building Materials and Structures, Faculty of Civil Engineering, Cracow University of Technology.

** PhD. Bogusław Zając, Institute of Structural Mechanics, Faculty of Civil Engineering, Cracow University of Technology.

Symbols

A – surface area
l – length
T – temperature
ρ – density
α – thermal expansion coefficient
σ – normal stress
E – Young's modulus

1. Introduction

Concrete structures at service temperatures are often exposed to the harmful effects of mechanical and chemical factors, e.g. load level, changes in temperature and moisture and also the impact of various chemical agents (Fig. 1). The intensity of their negative action affects changes in the mechanical properties of structures.

The impact of temperature is connected with two different attacks. One of them describes changes caused by a cyclic freeze-thaw action in association with freezing and removal of frozen water. It is well known that these cyclic changes have a significant effect on the rate and extent of degradation [1]. The second is related to insolation and the effects of daily variable thermal changes. Thermal stresses in boundary area increase the degree of degradation due to the coefficients of thermal expansion (CTE). There are also changes observed in the value of the Young modulus [2].

Fig. 1. Example of concrete structures exposed to environmental conditions

The coefficient of thermal expansion (CTE) significantly depends on material type, moisture degree, environmental temperature, and degree of degradation due to the material's corrosion. The susceptibility of concrete to corrosion is strictly related to the aggregate (Fig. 2) and cement type, and the way it is exposed to the aggressive action [3–8].

Knowledge of all the environmental factors influencing the mechanical behaviour of the concrete allows efficient numerical analysis [9] and design to be carried out.

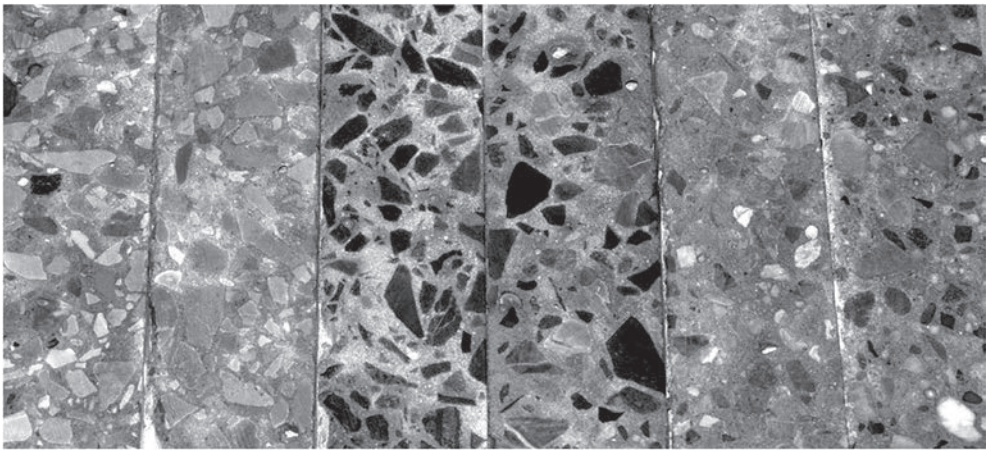

Fig. 2. Example cross-section of concrete prisms to environmental treatment

2. Experimental details

The materials used in this investigation were locally sourced and satisfied the requirements of respective Polish Standards [10–11].

2.1. Characteristics of aggregates examined

Two limestones aggregates out of six various types of carbonate as well as gravel aggregates (Fig. 2), were selected for this examination.

Two commercial granularities of limestone aggregate were investigated separately, as 2–8 and 8–16 mm, to cover the desired 2–16 mm range. The key features of the selected limestone aggregates (type A, type B) are shown in Tables 1 and 2.

Table 1

Examined concrete matrix composition

Property	Aggregate type A – examined aggregate	Aggregate type B – examined aggregate
structure	sparite and micrite	sparite and micrite
texture	compact, structured	compact, unstructured
grain size	Ø 60-200 μm (sparite) and 1 μm (micrite)	Ø 50–100 μm (sparite) and 2 μm (micrite)

Table 2

Mineral composition of the examined limestone aggregates

Main minerals	Calcite	Dolomite	Quartz	Clay
Limestone aggregate – type A	98.9%	0.7%	0.1%	0.4%
Limestone aggregate – type B	95.2%	2.8%	0.4%	1.6%

2.2. Concrete proportions and specimen preparation

The impact of the defined exposure conditions on the durability of cement concrete was investigated for concrete matrix composition, as shown in Table 3.

Table 3

Examined concrete matrix composition

	Aggregate type A	Aggregate type B
cement – CEM I 42.5R NA	360 kg/m^3	360 kg/m^3
water	180 kg/m^3	180 kg/m^3
fine aggregate – Bukowno sand	620 kg/m^3	620 kg/m^3
coarse aggregate	1245 kg/m^3	1245 kg/m^3

The concrete matrix was used to form beams with a size 10 × 10 × 50 cm. After 28 days of storage in a wet environment at temperature $t = 20 \pm 2$ºC, the beams were cut into prisms with size approximately 4 × 4 × 16 cm (Fig. 3) and conditioned for two years in laboratory conditions prior to testing [6–8].

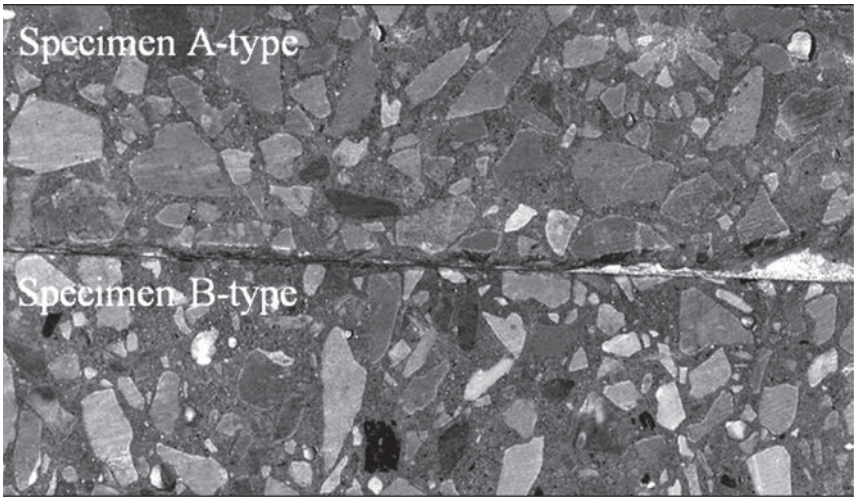

Fig. 3. Outer layer – the cut side – of the ordinary cement concrete prisms made with the use of limestone aggregate type A and B

2.3. Corrosive exposure

The environmental exposure applied to both types of concrete included storing in laboratory conditions – references sample and immersion to 5% Na_2SO_4 solution at a constant temperature of 20 ± 2ºC. The corrosive solution was changed every 28 days.

Concrete samples made with the use of various aggregates are tested in parallel.

2.4. Diagnostic features

2.4.1. Linear dimension changes cause by the corrosive exposure

The diagnostic feature adopted for the test was the change to the linear dimension (elongation) of the samples in the function of the presence of the Na^+ and SO_4^{2-} ions. During the length measurements, the samples were also weighed and observed for the presence of cracks and scratches. Any visible changes were snapped. The linear dimension changes were to be measured every 28 days. The study of the behaviour of both concrete types in the aggressive medium was carried out in parallel.

The obtained results are presented in 3.1. and 3.2.

2.4.2. Linear thermal expansion

The linear coefficient of thermal expansion (CTE) was determined on rectangular specimens with dimensions of approx. 48 × 48 mm and a total length of about L = 165 mm. The concrete samples were tested in a thermal chamber in a range of temperature conditions from chamber temperature (ca. 23°C) up to 60°C. The heating process was conducted for about 3 hours due to reaching the stabilised elongation value ΔL (Fig. 4). The displacement was measured with a WA-20 HBM Inductive Standard Displacement Transducer connected to a digital bridge QUANTUM MX840. An output voltage temperature sensor was also connected to the bridge. The WA-20 transducer generated the additional load F = 1,2 [N] on the examined concrete sample.

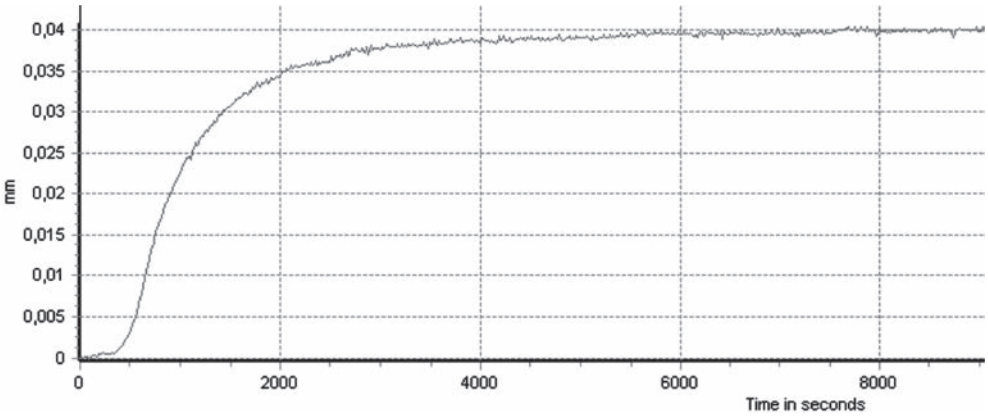

Fig. 4. An example diagram illustrating the elongation of the sample during the thermal examination as a function of exposure time

The linear coefficient of thermal expansion (CTE) was estimated by equation 1.

$$\alpha = \frac{\Delta l}{l_0 \Delta T} \tag{1}$$

where:
α – thermal expansion coefficient, 1/°C,
Δl – sample elongation, mm,
l_o – initial length, mm,
ΔT – change of temperature, °C.

The obtained results are presented in 3.3.

3. Results

3.1. Linear dimension changes cause by the corrosive exposure

The concrete prisms made of limestone aggregate type A and B were exposed in the conditions described in 2.4.1.

The dependence of the dimension changes of the samples as a function of exposure time and type of aggregate are shown on Fig. 5.

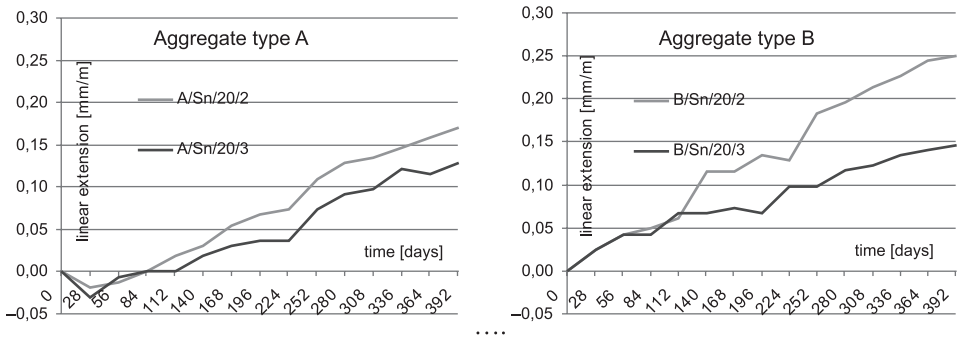

Fig. 5. The changes of concrete samples dimension as a function of aggregate type and exposure time

As expected, the linear extensions were strictly dependent on the type of aggregate examined at defined corrosion conditions. At the end point of this investigation, after 1 year of continuous exposure to a wet environment at t = 20ºC, the environment containing Na^+ and SO_4^{2-} ions was found to cause changes on a linear dimension. The most significant linear dimension changes were observed during the first six months – a large primary increase was continued by a sudden slope. In the case of concrete made with aggregate B, a slightly higher slope range was observed.

3.2. Cement concrete examination – visual inspections

Corrosion exposition to a medium containing sodium and sulphate(VI) ions can cause damage in concrete structure. The very first visible result of the sulphate(VI) ion attack is the presence of micro cracks and small scratches on the surface layer of the examined concrete sample. During the time of corrosive exposition, the micro cracks can enlarge and connect up to form a long continuous line.

Typical surface appearances of the prisms of both examined concretes after 1-year exposition to corrosive conditions are shown in Fig. 6 and 7. Visible cracks and micro cracks between particles and at their borders, marked with small yellow arrows on Fig. 6 and 7, are also shown on the surface layer of each sample.

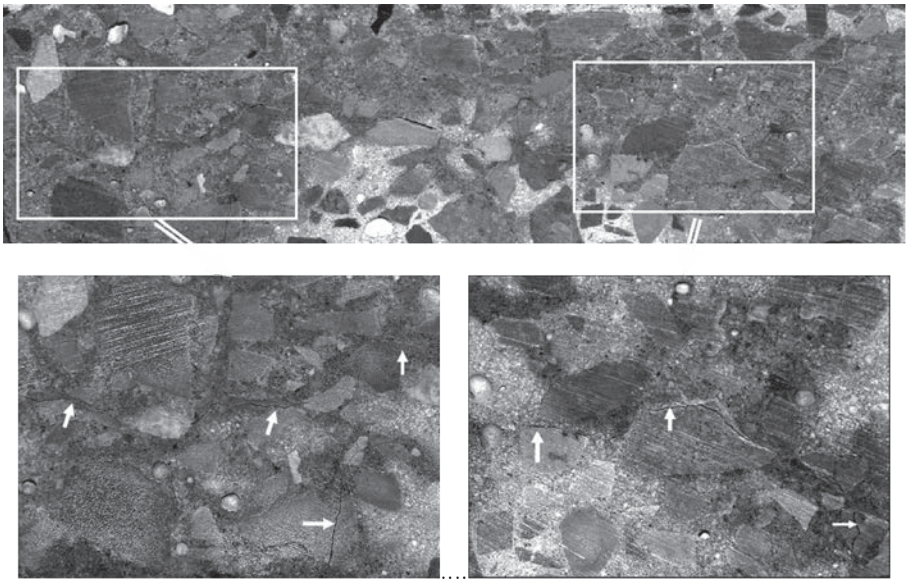

Fig. 6. The external surface of concrete type A prisms after 1-year exposition to sodium sulphate(VI) solution; magn. 1,5×

The macroscopic observation of the concrete sample surfaces exposed to the defined sodium sulphate(VI) solution revealed an increased presence of pores, cracks and scratches in the surface layer of each sample made of both types of limestone aggregates. In comparison, these observations were not made in reference samples.

In the case of both observed ordinary cement concretes with various types of limestone aggregate, the cracks and scratches could be observed as cohesive separately for concrete and aggregate as well as adhesive ones. The cohesive nature of aggregates destruction reveals information about their susceptibility to a corrosion environment containing Na^+ and SO_4^{2-} ions. The adhesive failure of concrete occurring at the border of cement mortar and all types of aggregates is typical for this sort of chemical load. All the changes of ITZ which were observed in the cases of concrete prisms of both limestone aggregates demand further observation. Accurate identification is possible after further testing of the samples under a scanning microscope. The results of this will be presented in future.

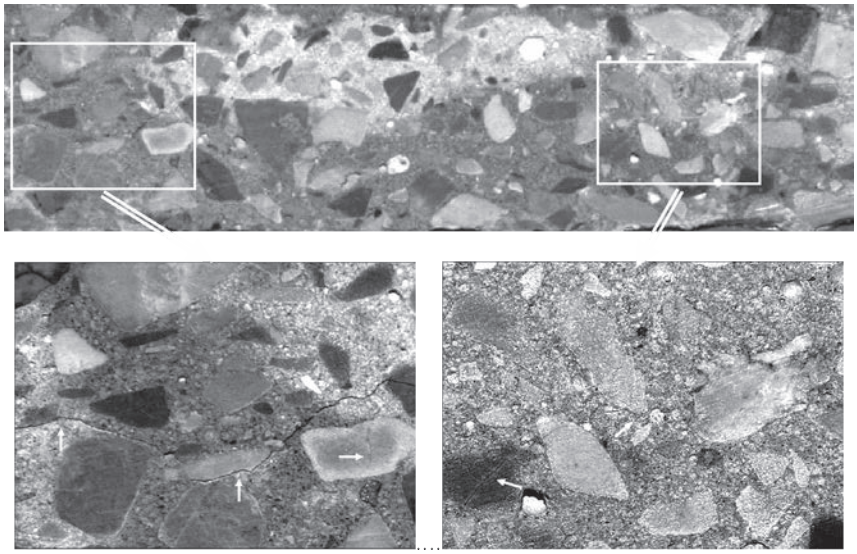

Fig. 7. The external surface of concrete type B prisms after 1-year exposition to sodium sulphate(VI) solution; magn. 1,5×

3.3. Linear thermal expansion

The concrete prisms made of limestone aggregate type A and B were examined in manner way described in 2.4.2.

The coefficients of thermal expansion obtained for the samples during the test and their characteristics are presented in Table 4.

Table 4

Values of coefficient of temperature expansion and specific gravity obtained for the examined concrete prisms

Specimen	CTE	Special gravity ρ [g/ccm]	Remarks
A/18.01.10	8.04 E-06	2.37	stored in laboratory conditions
A/Sn/20/2	6.85 E-06	2.40	exposed to chemical conditions
A/Sn/20/3	6.74 E-06	2.39	exposed to chemical conditions
B/19.01.10	8.25 E-06	2.41	stored in laboratory conditions
B/Sn/20/2	7.51 E-06	2.39	exposed to chemical conditions
B/Sn/20/3	7.15 E-06	2.38	exposed to chemical conditions

CTE results showed significant changes in their values for the chemically treated prisms exposed to the defined aggressive environment in comparison with the reference prisms. In the case of the A samples, the noticed loss of CTE value was approximately 15%. However, the loss of CTE values marked to the B samples showed differences from 9 to 14%.

Further observations are required to determine the model of behaviour and sustainability of concrete made with various types of aggregates exposed to the aggressive environment defined and variable temperature fields.

4. Conclusions

– Corrosive exposure to the sulphate medium caused changes in the surface layer of concrete prisms. Cracks and scratches on the surface of the tested samples were observed. The explanation of these phenomenon was presented in [1, 3, 4–8],
– Observed changes were strictly dependent on the aggregate's chemical composition,
– Studies have found changes in the values of CTE after the chemical examination,
– Further research is required to determine the nature of behaviour of concrete exposed to aggressive attack and various service temperature conditions.

Acknowledgements

These examinations were partially financially supported by grants L-1/234/DS/2011-2014.

References

[1] Neville A.M., *Właściwości betonu*, Polski Cement, Kraków 2000.
[2] Hassen S., Colina H., *Effect of a heating-cooling cycle on elastic strain and Young's modulus of high performance and ordinary concrete*, RILEM 2012, Materials and Structures, 45, 2012, 1861–1875.
[3] Poitevin P., *Limestone aggregate concrete, usefulness and durability*, Cement and Concrete Composites, 21, 1999, 89–97.
[4] Fiertak M., Dębska D., *Effect of the conditions of exposure to a corrosive environment on the deformation and strength of cement concrete contaminated with sulphates*. Kurdowski Symposium: Science of cement and concrete, Edited by W. Kurdowski, M. Gawlicki, Kraków 2001, 237–244.
[5] Owsiak Z., *Alkali-aggregate reaction in concrete containing high-alkali cement and granite aggregate*, Cement and Concrete Research, 34, 2004, 7–11.
[6] Dębska D., *Wpływ środowiska ciekłego na trwałość betonu cementowego z kruszywem dolomitowym*, Ochrona przed Korozją (Corrosion Protection), SIGMA-NOT, 56, 4, 2013, 134–143.
[7] Dębska D., *The impact of liquid environments containing Mg^{2+} and SO_4^{2-} ions on the durability of cement concrete with limestone aggregates*, Ochrona przed Korozją (Corrosion Protection), SIGMA-NOT, 57, 4, 2014, 124-128.
[8] Dębska D., *Wpływ siarczanu sodu i magnezu na trwałość betonów z kruszywem węglanowym*, Przegląd Budowlany, 5, 2014, 14-17.
[9] Grodecki M., Truty A., Urbański A., *Modelowanie numeryczne ścianek szczelnych*, Kwartalnik AGH Górnictwo i Geoinżynieria, r. 27, z. 3–4, 2003, 297–303.
[10] PN-EN 12620+A1:2010P, Kruszywa do betonu.
[11] PN-B-19707:2013-10P, Cement. Cement specjalny. Skład, wymagania i kryteria zgodności.

TECHNICAL TRANSACTIONS | **CZASOPISMO TECHNICZNE**
ENVIRONMENTAL ENGINEERING | ŚRODOWISKO
2-Ś/2015

TOMISŁAW GOŁĘBIOWSKI*

INTRODUCTION TO NUMERICAL MODELLING OF ELECTROMAGNETIC WAVE FIELD ON THE EXAMPLE OF GEORADAR DATA RECORDED IN RIVER DIKE

WPROWADZENIE DO MODELOWANIA NUMERYCZNEGO ELEKTROMAGNETYCZNEGO POLA FALOWEGO NA PRZYKŁADZIE BADAŃ GEORADAROWYCH PRZEPROWADZONYCH NA WALE PRZECIWPOWODZIOWYM

Abstract

Selected result of GPR surveys, which were carried out on the dike of the Vistula River, three days after the flood in 2010, was presented in the paper. Radargram was processed in a standard way, which allowed 2D visualization of main loose zones in the examined dike. Theoretical background of numerical modelling of electromagnetic wave field in the geological medium was presented in the paper. The results of numerical modelling were used for the evaluation of water and air saturation of loose zones during radargram interpretations.

Keywords: georadar, numerical modelling, river dike

Streszczenie

W artykule przedstawiono wybrany wynik z badań georadarowych wału wiślanego, które przeprowadzono trzy dni po powodzi w 2010 roku. Echogram poddano standardowemu przetwarzaniu, co pozwoliło na wizualizację 2D rozkładu głównych stref rozluźnień w badanym wale. W artykule zamieszczono podstawy teoretyczne modelowania numerycznego rozkładu pola elektromagnetycznego w ośrodku geologicznym. Na etapie interpretacji echogramu wykorzystano wyniki modelowania w celu określenia nasycenia rozluźnień wodą i powietrzem.

Słowa kluczowe: georadar, modelowanie numeryczne, wały przeciwpowodziowe

DOI: 10.4467/2353737XCT.15.225.4611

* Prof. DSc. PhD. Tomisław Gołębiowski, Department of Geotechnics, Faculty of Environmental Engineering, Cracow University of Technology

1. Introduction

Application of geophysical methods for the examination of technical conditions of river dikes is not a new matter. For years, for this purpose, selected methods were used, first of all: electrical methods [1– 4], georadar surveys [5–10], electromagnetic profiling [1–3], seismic surveys [1, 2, 11–13]. Unfortunately, despite long lasting tradition of using different geophysical methods for dike examination, the results of measurements are often difficult for unequivocal interpretation. It is caused by few facts, among others:

a) several looseness are small and their dimensions are on the boundary of the detection ability of geophysical methods,
b) loose zones, in the body of dike, are distributed randomly, therefore, it is difficult to prepare a proper interpretative model,
c) physical properties of looseness are depending on the amount of water, clay and air in the porous space, but the amount of these media is unknown during surveys.

The author focused, in the paper, on the analysis of abilities and limitations of the georadar method (GPR) for loose zones detection in the dike. Among different GPR measurement techniques, the most popular is short or zero offset reflection profiling, and therefore, such technique will be analysed in the paper.

GPR surveys were carried out on the Vistula river dike in Cracow (Fig. 1A), 3 days after the flood in 2010, when water declined to the basement of the dike (Fig. 1B). Georadar profile was designed in the middle of the top part of the dike, where no under- and over-ground interferences occurred in surrounding of the profile (Fig. 1C).

Geological information (Fig. 2A) obtained from the borehole WL-11 (Fig. 1C) depicted that the body of the dike was formed by sand and clayey sand, so attenuation of electromagnetic wave should not be very high (Table 1) and the GPR method should allow to examine the whole body of the dike up to the basement, i.e. to depth ca. 2.3 m (Fig. 2A).

It is assumed [14] that if the following criteria are met, i.e.:

– wetness $W_n > 19\%$,
– density $\rho < 1.70$ t/m^3,
– compaction factor $I_S < 0.92$,

the examined dike is in bad technical condition. The results of laboratory tests, carried out on the ground samples no. 1 and no. 2 (Fig. 2A), allow to assume that the whole dike in the investigation site is in a very bad technical condition. Also, the result of diving rod sounding (Fig. 2B) confirms a bad technical condition of the examined dike and undersoil to a depth of 4 m.

The aim of the GPR surveys was the two-dimensional (2D) visualization of loose zones distribution, detected formerly by borehole and geotechnical sounding.

GPR measurements were performed using the ProEx system (MALA Geoscience, Sweden) with 500 MHz shielded antenna with max. depth penetration of ca. 5 m and mean resolution of ca. 0.05 m. Traces were recorded every 0.025 m and for every one trace assumed 512 samples and sampling frequency was equal to 5000 MHz; stacking 32 times was defined during data acquisition for improvement of signal-to-noise ratio.

Radargram after standard processing in ReflexW program (SandmeierGEO, Germany) was presented in Fig. 3; the following processing procedures were used [15, 16]: t_0 correction, dewow function, DC correction, Butterworth filtering, 1D median filtering, gain function, background removal, stacking, 2D averaging filtering, Stolt migration. For better visualisation,

non-equal scales of vertical and horizontal axes were applied and amplitudes of reflections were normalised to the max. amplitude of the direct air wave. For the time-depth conversion, mean velocity $v = 0.085$ m/ns was assumed on the basis of diffraction hyperbolas analysis.

In radargram presented in Fig. 3, randomly distributed anomalies, i.e. high amplitude reflections (with red and black colours), are easily noticed. GPR anomalies may be correlated with the loose zones. The result of GPR surveys correlated well with information obtained from the borehole and geotechnical sounding and it may be assumed that the whole body of the examined dike is in bad technical condition. Analysing Fig. 3, it may be observed that more high amplitude reflections are located in the first (left) part of radargram, thus this part of the dike may be assumed as more intensively disintegrated.

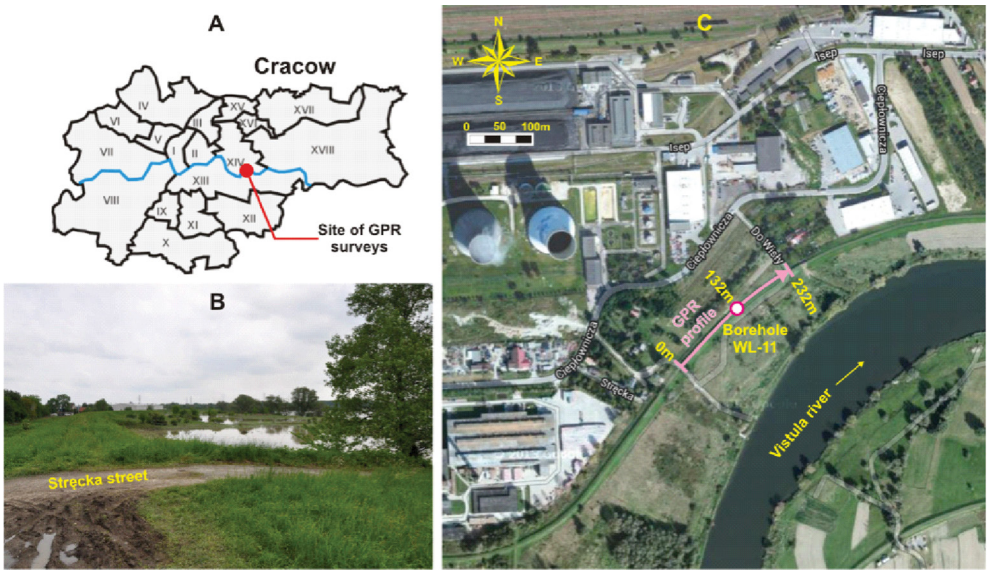

Fig. 1. A) Site of GPR surveys on the dike of the Vistula River in Cracow; B) Investigation site 3 days after the flood in 2010; C) Location of GPR profile and borehole on the top of the dike (base map: www.google.pl/maps)

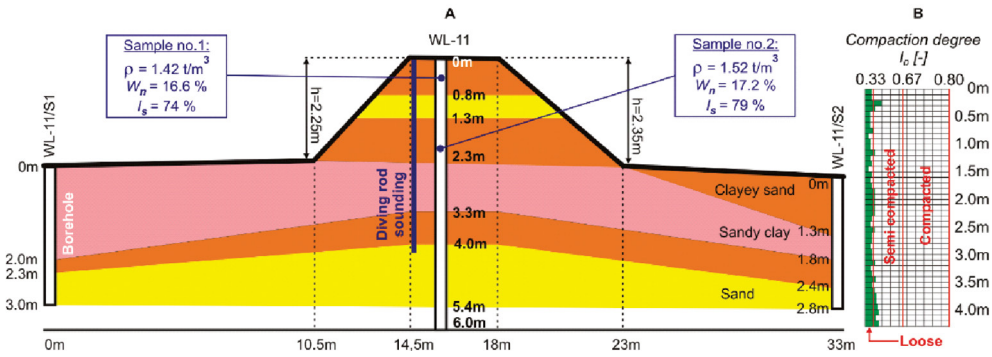

Fig. 2. A) Geological and laboratory data from borehole WL-11; B) Result of diving rod sounding

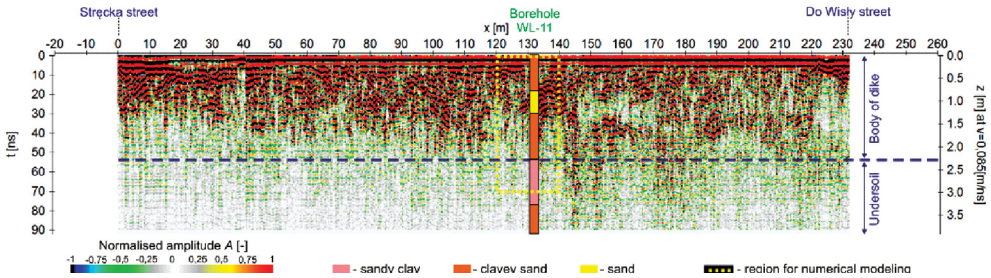

Fig. 3. Radargram after standard processing

Standard, i.e. visual, analysis of radargram allows only to draw conclusions presented in previous sentence, so only qualitative interpretation is possible. Application of numerical modelling for radargram interpretation allows to draw further conclusions, which will be presented in chapter 3.

2. Theoretical background of numerical modelling of electromagnetic wave for GPR method

The most popular technique of modelling of an electromagnetic wave field is the FDTD (*Finite Difference Time Domain*) technique [17], and this technique is commonly used for the GPR method [18–21]. Detailed information about the application of the FDTD technique for radargram interpretation may be found in above-mentioned publications and in the following part of the paper, only basic information will be presented.

In order to solve Maxwell equations (1)–(4) with the use of FDTD technique, the discretization of continuous geological model is needed.

$$\nabla \cdot \vec{E} = 0 \tag{1}$$

$$\nabla \cdot \vec{H} = 0 \tag{2}$$

$$\nabla \times \vec{E} = -\mu \cdot \frac{\partial \vec{H}}{\partial t} \tag{3}$$

$$\nabla \times \vec{H} = \sigma \cdot \vec{E} + \varepsilon \cdot \frac{\partial \vec{E}}{\partial t} \tag{4}$$

where:

∇ – nabla operator,
$\vec{E}$ [V/m] – electric component of electromagnetic field,
$\vec{H}$ [A/m] – magnetic component of electromagnetic field,
μ [H/m] – magnetic permittivity,

t [s] – time,
σ [S] – electrical conductivity,
ε [F/m] – electrical permittivity.

In discrete model, the components of electromagnetic wave field are defined only in the grid points (Fig. 4A) and numerical analysis is conducted with the assumption that electromagnetic wave is the TEM (Transverse Electromagnetic) wave (Fig. 4B).

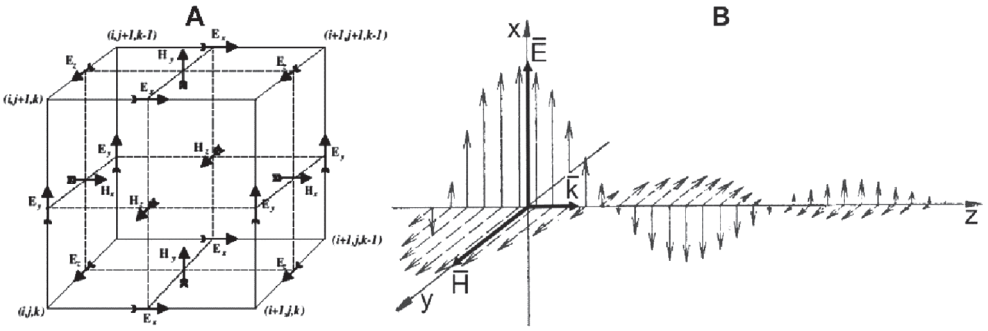

Fig. 4. A) A grid zone for solving of Maxwell equations with the use of FDTD technique (www.gprmax.com); B) Transverse Electromagnetic wave

The following notation may be introduced for the FDTD technique for 3D modelling:
– Δx, Δy, Δz – dimensions of grid zones in x, y and z directions,
– i, j, k – numbering of grid points in x, y and z directions,
– Δt – dimension of time step,
– n – number of time step.

Discrete form of Maxwell equations for the FDTD technique is as follow [22]:

$$E_x^{n+1}(i,j,k) \approx K_x(i,j,k)E_x^n(i,j,k) + P_x(i,j,k) \left[\frac{H_z^{n+1/2}(i,j+1,k) - H_z^{n+1/2}(i,j,k)}{\Delta y} - \frac{H_y^{n+1/2}(i,j,k+1) - H_y^{n+1/2}(i,j,k)}{\Delta z} \right] \quad (5)$$

$$E_y^{n+1}(i,j,k) \approx K_y(i,j,k)E_y^n(i,j,k) + P_y(i,j,k) \left[\frac{H_z^{n+1/2}(i,j,k+1) - H_x^{n+1/2}(i,j,k)}{\Delta z} - \frac{H_z^{n+1/2}(i+1,j,k) - H_z^{n+1/2}(i,j,k)}{\Delta x} \right] \quad (6)$$

$$E_z^{n+1}(i,j,k) \approx K_z(i,j,k)E_z^n(i,j,k) + P_z(i,j,k) \left[\frac{H_y^{n+1/2}(i+1,j,k) - H_y^{n+1/2}(i,j,k)}{\Delta x} - \frac{H_x^{n+1/2}(i,j+1,k) - H_x^{n+1/2}(i,j,k)}{\Delta y} \right] \quad (7)$$

$$H_x^{n+1/2}(i,j,k) \approx H_x^{n-1/2}(i,j,k) + \frac{\Delta t}{\mu_x(i,j,k)} \left[\frac{E_y^n(i,j,k+1) - E_y^n(i,j,k)}{\Delta z} - \frac{E_z^n(i,j+1,k) - E_z^n(i,j,k)}{\Delta y} \right] \tag{8}$$

$$H_y^{n+1/2}(i,j,k) \approx H_y^{n-1/2}(i,j,k) + \frac{\Delta t}{\mu_y(i,j,k)} \left[\frac{E_z^n(i+1,j,k) - E_z^n(i,j,k)}{\Delta x} - \frac{E_x^n(i,j,k+1) - E_x^n(i,j,k)}{\Delta z} \right] \tag{9}$$

$$H_z^{n+1/2}(i,j,k) \approx H_z^{n-1/2}(i,j,k) + \frac{\Delta t}{\mu_z(i,j,k)} \left[\frac{E_x^n(i,j+1,k) - E_x^n(i,j,k)}{\Delta y} - \frac{E_y^n(i+1,j,k) - E_y^n(i,j,k)}{\Delta x} \right] \tag{10}$$

where parameters K and P describe material properties of the analysed medium, i.e.:

$$K_{x,y,z}(i,j,k) = \frac{\varepsilon_{x,y,z}(i,j,k) - 0.5\Delta t \sigma_{x,y,z}(i,j,k)}{\varepsilon_{x,y,z}(i,j,k) + 0.5\Delta t \sigma_{x,y,z}(i,j,k)} \tag{11}$$

$$P_{x,y,z}(i,j,k) = \frac{\Delta t}{\varepsilon_{x,y,z}(i,j,k) + 0.5\Delta t \sigma_{x,y,z}(i,j,k)} \tag{12}$$

Usually, in algorithms for numerical modelling of GPR wave field material properties of analysed geological media are defined as follow:

- value of electrical conductivity σ [S] is defined in unit of [S/m],
- instead of electrical permittivity ε [F/m], value of relative dielectric constant ε_r [–] is defined, according the formula (13),
- instead of magnetic permittivity μ [H/m], value of relative magnetic permittivity μ_r [–] is defined, according the formula (14); for geological media, a constant value of μ_r, equals 1 (like for vacuum) is assumed for modelling.

$$\varepsilon_r = \frac{\varepsilon}{\varepsilon_0} \qquad \varepsilon_0 = 8.85 \cdot 10^{-12} \left[\mathrm{F/m}\right] \tag{13}$$

$$\mu_r = \frac{\mu}{\mu_0} \qquad \mu_0 = 4.5 \cdot 10^{-7} \left[\mathrm{H/m}\right] \tag{14}$$

where: ε_0 and μ_0 – adequately electrical and magnetic permittivity of vacuum.

For convergence and stability of numerical solution, two criteria (15), (16) have to be met, i.e. referred to max. dimension of grid zone Δ (i.e. Δx and Δy and Δz) and max. time step Δt.

$$\Delta \leq \frac{\lambda}{10} \tag{15}$$

$$\Delta t = \frac{1}{v \cdot \sqrt{\frac{1}{(\Delta x)^2} + \frac{1}{(\Delta y)^2} + \frac{1}{(\Delta z)^2}}} \tag{16}$$

where: λ [m] – wave length, v [m/s] – velocity of propagation of electromagnetic wave.

Velocity in equation (16) as well as attenuation of modelled medium α [dB/m] may be described by the following formulae:

$$v = \frac{c}{\sqrt{\left(\frac{\varepsilon\mu}{2}\right) \cdot \left(\left(1 + \frac{\sigma}{\omega\varepsilon}\right)^2 + 1\right)}} \tag{17}$$

$$\alpha = \omega \sqrt{\left(\frac{\varepsilon\mu}{2}\right) \cdot \left(\sqrt{1 + \left(\frac{\sigma}{\omega\varepsilon}\right)^2} - 1\right)} \tag{18}$$

where: c [m/s] – velocity of electromagnetic wave in vacuum ($3 \cdot 10^8$ m/s), ω [rad/s] – angular frequency.

On the upper boundary of the numerical model, a strip with material properties of air, i.e. $\varepsilon_r = 1$, $\mu_r = 1$, $\sigma = 0$ mS/m, is introduced. In the left, right and bottom boundaries of numerical model, the absorbing boundary condition is defined by increasing of attenuation (18) in the boundary area.

For excitation of propagation of the electromagnetic wave in the numerical model, a source, which simulates emission of wave from transmitter antenna, has to be defined. Proper definition of the source in modelling is a complicated problem, so only the main stages of the source construction will be described. At the first stage of source constriction, the type of source has to be defined, e.g. plane wave, point source, exploding reflector [16]. At the next stage, the orientation of transmitter and receiver antennae have to be defined [23, 24]. At the last stage, adequate source function (i.e. signal) for controlling of source has to be defined [16], e.g. Ricker, sinus, Kuepper signal or real signal adequately discretised from radargram.

In the paper, only the reflection technique is analysed, so only basic information about the reflection of the electromagnetic wave is presented in the following part of this chapter. The reflection of the electromagnetic wave is observed on the geological boundary or anthropogenic underground objects when difference of impedances Z (19) appears in the

geological medium. Two different situations (Fig. 5) may occur when the front of wave reaches the geological boundary.

$$Z = \sqrt{\frac{j\omega\mu}{\sigma + j\omega\varepsilon}} \tag{19}$$

where: j – imaginary unit.

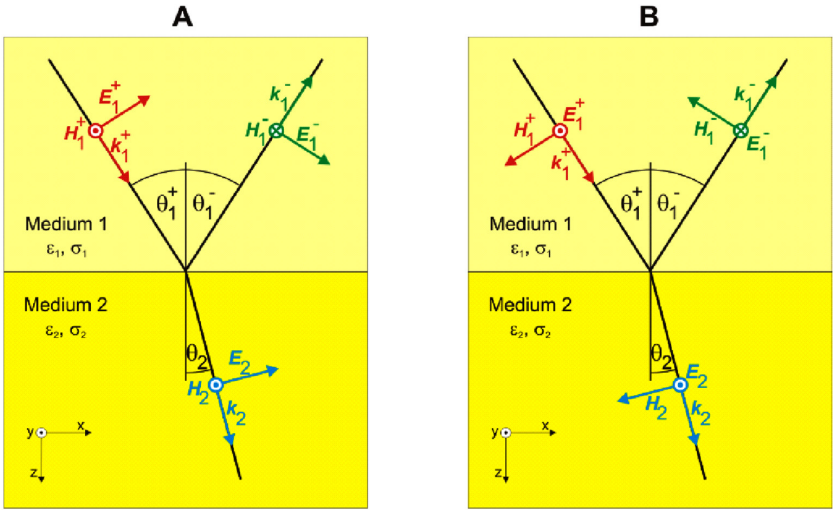

Fig. 5. Schemes for analysing of wave reflection for: A) perpendicular polarised wave (⊥), B) parallel polarised wave (||)

Reflection R and transmission T coefficients for both situations presented in Fig. 5 are as follow:

$$R_{\parallel} = \frac{Z_2 \cdot \cos\theta_2 - Z_1 \cdot \cos\theta_1}{Z_2 \cdot \cos\theta_2 + Z_1 \cdot \cos\theta_1} \tag{20}$$

$$R_{\perp} = \frac{Z_2 \cdot \cos\theta_1 - Z_1 \cdot \cos\theta_2}{Z_2 \cdot \cos\theta_1 + Z_1 \cdot \cos\theta_2} \tag{21}$$

$$T_{\parallel} = \frac{2Z_2 \cdot \cos\theta_1}{Z_1 \cdot \cos\theta_1 + Z_2 \cdot \cos\theta_2} \tag{22}$$

$$T_{\perp} = \frac{2Z_2 \cdot \cos\theta_1}{Z_2 \cdot \cos\theta_1 + Z_1 \cdot \cos\theta_2} \tag{23}$$

Scheme of reflection of electromagnetic wave, presented in Fig. 5, is valid only for simple situations, e.g. horizontal geological boundary or underground object with simple shape. In real conditions, geological structures are usually complicated, furthermore, heterogeneity and anisotropy often appear in the geological medium and objects with complicated shapes may occur in the geological medium. In the described real situations, a mathematical analysis of the process of propagation and the reflection of the electromagnetic wave is very difficult, and thus, the only solution is delivered by numerical modelling.

3. The results of modelling

When loose zones occur in a dike, two different situations have to be analysed, i.e.:

– presence of the so-called "dry looseness" i.e. looseness without direct hydraulic connectivity with the surface of a dike; in such a situation, loose zones are filled mainly with air; an example of such type of looseness are channels made by moles and voles;
– presence of the so-called "wet looseness"; in such a situation, presence of hydraulic connectivity between several looseness and surface of dike cause that different amount of air and/or water may appear in the looseness, depending of time of water supply from precipitation or from river (during the flood).

The second situation, described above, is more dangerous during the flood because the presence of hydraulic connectivity among several looseness causes movement of water inside of the dike, washing out of material and, in consequence, breaking of the dike. Therefore, the aim of numerical modelling was the answer to the question whether loose zones, in the investigated dike, were water saturated or not.

On the basis of geological information from borehole WL-11 (Fig. 2A), two-dimensional numerical models were constructed (Fig. 6); geotechnical data (Fig. 2B) delivered information that the body of the dike was equally disintegrated between top and basement of dike, which was presented in numerical models by equally distributed looseness (Fig. 6). Vertical dimensions of models (i.e. 2.3m) referred to the height of the examined dike (Fig. 2A); horizontal dimensions (i.e. 20 m) were adequate to the region around borehole WL-11 (Fig. 3 – yellow rectangle).

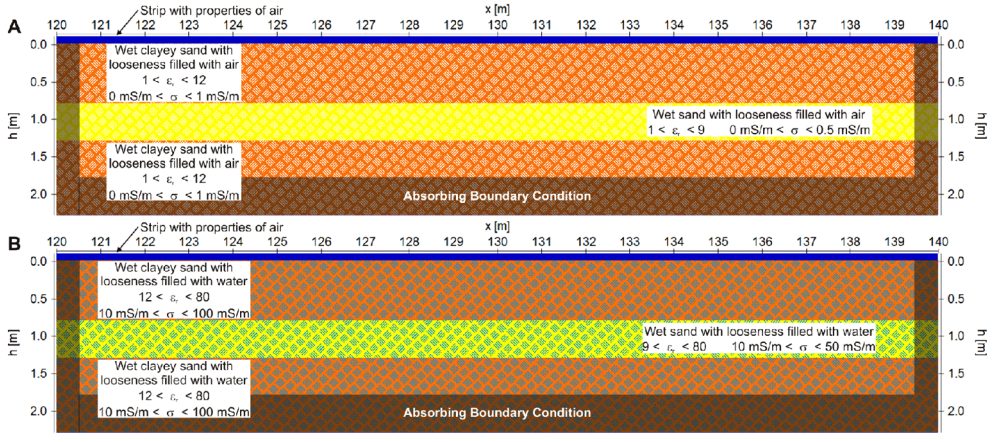

Fig. 6. Numerical models for analysis of looseness saturation with air (A) and water (B)

A strip, which simulates air, was inserted on the upper boundary of models; and on the other boundaries, absorbing boundary condition was defined (Fig. 6).

Models were discretised by a grid with dimensions $\Delta x = \Delta h = 0.01$ m and time step $\Delta t = 0.01$ ns was assumed according to the formulae (15, 16). Solving was carried out in time window $T = 90$ ns according to time window assumed during terrain surveys (Fig. 3).

The source of electromagnetic wave was defined as so-called "exploding reflector" and the source function, with central frequency 500 MHz, was assumed on the basis of discretisation of real signal taken from radargram. In source and registration points, Ey component of electromagnetic wave field was taken into account adequately to geometry of transmitter and receiver antennae used during terrain surveys.

The most difficult stage of models preparation was the proper construction of loose zones, which had random distribution in the dike (Fig. 7A). There is no possibility to describe the dimensions of several looseness and their distribution in space (Fig. 7A) in a deterministic way. It is also impossible to define the amount of water and/or air in porous spaces of the dike deterministically, so it is impossible to deliver equivalent material properties of mixture of sand (quartz), clay, water and air (Fig. 7B). In such situation, the only technique of construction of loose zones in numerical models seems to be an application of stochastical model. Detailed description of the application of stochastical models in interpretation of georadar data was presented in book [9], but in following part of this chapter, only basic information is presented.

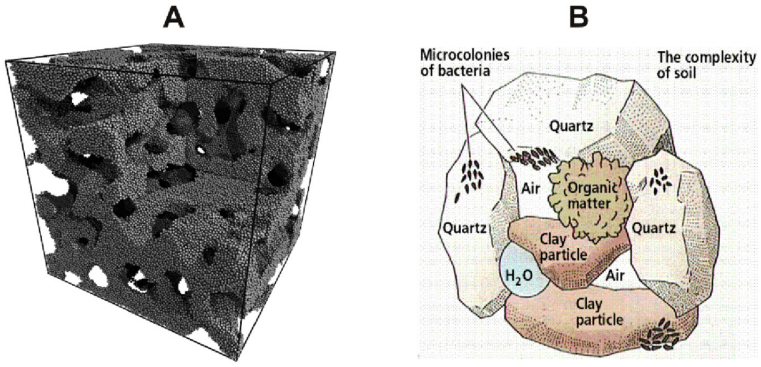

Fig. 7. A) Random distribution of loose zones in dike (www.utdallas.edu); B) Complexity of analysed medium (secretsofsoil.com)

A random generator was applied for construction of stochastical model. In the first step, „i" and „j" addresses of grid point were randomly chosen on the basis of self-similar distribution. In the second step, randomly chosen grid point assigned equivalent values of ε_r and σ (Table 1) using random generator with application of Gauss distribution, i.e.:

– for air-filled looseness (Fig. 6A), it was assumed that the values of ε_r changed randomly from 1 (value for air) to 12 (value for wet mixture of sand and clay) and σ changed randomly from 0 mS/m (air) to 10 mS/m (wet sand and clay),
– for water-filled looseness (Fig. 6B), it was assumed that the values of ε_r changed randomly from 12 (wet sand and clay) to 80 (value for water) and σ changed randomly from 10 mS/m (wet sand and clay) to 100 mS/m (looseness filled with water and clay minerals after the flood).

Value ε_r = 12, assumed for wet mixture of sand and clay, is adequate to the velocity v = 0.085 m/ns determined from radargram on the basis of diffraction hyperbola analysis. For all grid points, constant value of μ_r equals 1 was assumed. In the next step, second grid point was randomly chosen, and randomly chosen values of ε_r and σ were assigned to this grid point. This procedure was carried out as long as all grid points had assigned material properties.

The results of modelling, i.e. synthetic radargrams, for both analysed models shown in Fig. 8C,D; synthetic radargrams, were presented in the form of envelopes counted from Hilbert transform [16]. For comparison, measured radargram in form of amplitudes distribution (Fig. 8A) and in form of envelopes (Fig. 8B) were presented.

Table 1

Material properties of analysed media [25]

Medium	Relative dielectric constant ε_r [–]	Relative magnetic permittivity μ_r [-]	Electrical conductivity σ [mS/m]	Velocity of electromagnetic wave v [m/ns]	Attenuation α [dB/m]
Fresh water	80	1	0.5	0.03	0.1
Air	1	1	0	0.3	0
Sand (dry - water saturated)	3 – 30	1	0.01 – 1	0.17 – 0.05	0.01 – 0.3
Clay (dry - water saturated)	5 – 40	1	2 – 1000	0.13 – 0.05	1 – 300

During analysis of looseness filling (i.e. water and air), the parameters discussed below should be taken into account.

Velocity *v* of electromagnetic wave is higher in air-saturated looseness (v_{air} = 0.3 m/ns) than in water-saturated looseness (v_{water} = 0.03 m/ns) – Table 1; these facts might be used in an interpretation if a geological boundary would be recorded under the loose zone, e.g. a boundary between clayey sand and sand in analysed situation (Fig. 2A). Air-filling of looseness caused that reflections from this boundary appeared in radargram in lower times (due to higher velocity in air) than in region without looseness. When loose zones are filled with water, which characterises itself by low velocity, reflections from geological boundary appear in higher times in radargram. Unfortunately, no reflections from boundary between clayey sand and sand were recorded, so there was no possibility to analyses changes of velocity of electromagnetic wave in loose zones.

Reflection coefficient R in boundary between wet ground and water-filled looseness is lower (R = –0.4) than in air-filled looseness (R = 0.6); the mentioned fact is easily noticed in Fig. 8C,D were in Fig. 8C more high amplitude reflections were recorded than in Fig. 8D. Comparing result depicted in Fig. 8B (measured radargram) and Fig. 8C,D (synthetic radargrams), it might be assumed that distribution of reflections in Fig. 8B is similar to Fig. 8D; such observation allows drawing the conclusion that, in the analysed part of the dike, looseness were filled with water.

Polarisation of reflections origin from water-saturated looseness is opposite to polarisation of source signal; when looseness are filled with air, a polarisation of reflections is the same as in source signal. When well-separated looseness or voids occur in the investigated medium, polarisation becomes a very good indicator of looseness filling; in analysed situation (Fig. 8A) reflections are overlaid, so polarisation is not useful tool for analysis of looseness filling.

Loose zones, filled with different amount of water and clay (e.g. after the flood), have higher **attenuation** (Table 1) than air-saturated looseness; this fact causes that amplitudes of reflections are highly decreased is certain sub-region of analysed medium. The mentioned effect may be observed in Fig. 8B and Fig. 8D, which allow to draw the conclusion that looseness were filled with water in the analysed part of the dike. On the contrary, presence of air in looseness caused better propagation of wave, and thus, stronger reflections from deeper parts of the dike might be recorded (Fig. 8C).

Resolution of GPR method, which is a function of wave frequency and velocity, is higher in water-saturated medium (Fig. 8D) than in dry one (Fig. 8C). High resolution observed in radargram presented in Fig. 8B depicts that loose zones were water-saturated during the surveys; possibility of outlining of several sub-regions in loose zone is similar in Fig. 8B and Fig. 8D, which confirms interpretation presented in previous sentence.

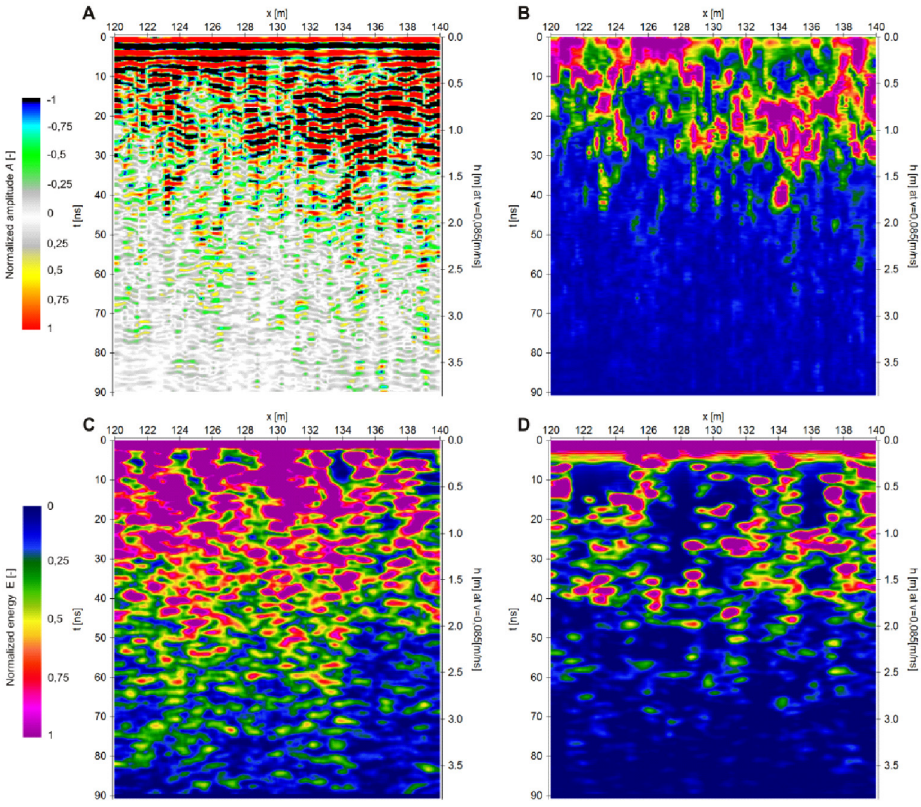

Fig. 8. Part of measured radargram around borehole WL-11 in form of amplitude distribution (A) and in form of envelopes (B); synthetic radargrams in form of envelopes with looseness filled with air (C) and water (D)

In the situation analysed in the paper, only three from five parameters might be taken into account. However, these parameters delivered information that loose zones were water-saturated, so a hydraulic connectivity was present in the examined dike.

Geological (Fig. 2A) and geotechnical (Fig. 2B) data delivered information that the whole body of the dike was highly disintegrated in point WL-11. Geophysical data (Fig. 3) showed that a large part of the dike around point WL-11 is disintegrated. The results of modelling depicted that there was a possibility of water migration within loose zones of the examined dike. All above-listed information show that the investigated part of the dike should be renovated immediately.

4. Conclusions

Contrary to geological or geotechnical surveys, geophysical methods deliver continuous information about loose zones distribution in the examined medium. These methods are faster, cheaper and non-invasive in comparison with drilling and sounding. Standard analysis of geophysical data allows only for qualitative interpretation, so in analysed situation, only outlining the loose zones in the dike was possible. Application of numerical modelling in interpretation allows, in certain situations, to carry out a detailed interpretation of measured data. In analysed situation, synthetic radargrams allow to draw the conclusion that looseness were water-saturated. In order to decrease ambiguity of interpretation, the results of geophysical measurements and numerical modelling have to be correlated with the results of geological or geotechnical surveys. This would allow to deliver information about amount of water in loose zones.

Acknowledgements

The works were conducted during realization of project no.: S-2/234/2014/DS and financed by Cracow University of Technology, Poland.

References

[1] Niederleithinger E., Weller A., Lewis R., Stotzner U., Fechner T., Lorenz B., Nießen J., *Evaluation of Geophysical Methods for River Embankment Investigation*, Report of project “Deistrukt”, Germany 2005.

[2] Inazaki T., Sakamoto T., *Geotechnical Characterization of Levee by Integrated Geophysical Surveying*, Proceedings of International Symposium on Dam Safety and Detection of Hidden Troubles of Dams and Dikes, Xi’an 2005.

[3] Asch T.H., Deszcz-Pan M., Burton B.L., Ball L.B., *Geophysical Characterization of the American River Levees using Electromagnetics, Capacitively Coupled Resistivity and DC Resistivity*, Open-File Report no. 2008–1109, U.S. Geological Survey, Reston, Virginia 2008.

[4] Golebiowski T., Tomecka-Suchon S., Farbisz J., *Using of Complex Geophysical Methods for Non-invasive Examination of the River Embankments*, Proceedings of European Symposium on "Problems of flood defense", Org. SITPF and NOT, Paris (in Polish) 2012.
[5] Prinzio M., Bittelli M., Castellarin A., Pisa P.R., *Application of GPR to the Monitoring of River Embankments*, Journal of Applied Geophysics, vol. 71, iss. 2–3, 2010.
[6] Marcak H., Golebiowski T., Tomecka-Suchon S., *Analysis of Possibility of Using of GPR Refraction Waves for Detection of Changes in River Embankments*, Quarterly AGH-UST Geology, vol. 31, iss. 3–4 (in Polish) 2005.
[7] Golebiowski T., *Changeable-offset GPR Profiling for Loose Zones Detection in Levees*, Proceedings of International Conference "Near Surface 2008", EAEG Org., Cracow 2008.
[8] Golebiowski T., *Velocity Analysis in the GPR Method for Loose Zones Detection in River Embankments*. Proceedings of International Conference "GPR 2010", Org. International Association of GPR, Lecce, Italy, 2010.
[9] Golebiowski T., *Application of the GPR Method for Detection and Monitoring of Objects with Stochastical Distribution in the Geological Medium*, Dissertation no. 251, AGH University of Science and Technology Press, Krakow (in Polish) 2012.
[10] Marcak H., Golebiowski T., *The Use of GPR Attributes to Map a Weak Zone in a River Dike*, Exploration Geophysics, 45(2), CSIRO Publishing, Collingwood 2014.
[11] Pilecki Z., *Recognising of Dike Undersoil Using of Seismic Method*. Monthly of WUG, 5 (117), Katowice (in Polish) 2004.
[12] Pilecki Z., Kłosiński J., *Evaluation of Technical Condition of Dike Using of Seismic Method,* Monthly of WUG, 6 (130), Katowice (in Polish) 2005.
[13] Chen Ch., Liu J., Xia J., Li Z., *Integrated Geophysical Techniques in Detecting Hidden Dangers in River Embankments*, Journal of Environmental and Engineering Geophysics, vol. 11, no. 2, 2006.
[14] Wilun Z., *Basis of Geotechnics*, KiL Ed., Warsaw (in Polish), 2000.
[15] Annan A.P., *Practical Processing of GPR Data*, Sensor and Software Inc., Canada 1999.
[16] ReflexW, *User Guide of ReflexW computer program*, SandmeierGeo firm, Karlsruhe 2014.
[17] Yee K.S., *Numerical Solution of Initial Boundary Value Problems Involving Maxwell's Equations in Isotropic Media*, IEEE Trans. Antenna. Propagation, no. 14, 1966.
[18] Golebiowski T., *Numerical Modeling of GPR Wave Field Using of FDTD Technique*, Geoinformatica Polonica, no. 8, Cracow (in Polish) 2006.
[19] Golebiowski T., *Application of Numerical Modelling of Georadar Wave Filed for Investigation of Hydrocarbon Contaminated Ground*, Ph.D. dissartation, AGH-UST, Cracow (in Polish) 2005.
[20] Golebiowski T., *Introduction to Interpretation of GPR Date Using of Numerical Modelling*, Polish Geological Review, vol. 52, no. 7, Warsaw (in Polish) 2004.
[21] Marcak H., Gołębiowski T., *Computer Simulation of Hydrocarbon Flow and Wave Field for Interpretation GPR Measurements in Contaminated Sites*, Proceedings of International Conference "SAGEEP 2005", EEGS Org., Atlanta 2005.
[22] Fornberg B., *Some Numerical Techniques for Maxwell's Equations in Different Types of Geometries*, University of Colorado, Department of Applied Mathematics, Boulder 2002.

[23] Marcak H., Golebiowski T., *Analysis of Detection Possibility of GPR Technique for Changeable Geometry of Antennae*. Proceedings of Conference on "Geophysics in Geology and Mining", vol. dedicated to prof. W.M.Zuberek, Faculty of Earth Sciences, Silesian University, Sosnowiec–Zawiercie (in Polish) 2010.

[24] Golebiowski T., Tomecka-Suchon T., *GPR Fractures Detection Using Changeable Antennae Orientation*, 5th International Conference and Exhibition, EAEG Org., St. Petersburg 2012.

[25] Annan A.P., *Ground Penetrating Radar*, Workshop Notes, Sensor and Software Inc., Canada 2001.

TECHNICAL TRANSACTIONS | CZASOPISMO TECHNICZNE
ENVIRONMENTAL ENGINEERING | ŚRODOWISKO
2-Ś/2015

MICHAŁ GRODECKI*

FAILURE MODES OF GABION RETAINING WALLS

MECHANIZMY ZNISZCZENIA MURU OPOROWEGO Z GABIONÓW

Abstract

The results of numerical simulations of the destruction of gabion retaining walls are presented. Special attention is paid to distinguishing possible destruction modes.

Keywords: gabion, retaining wall, FEM, stability.

Streszczenie

W artykule przedstawiono rezultaty symulacji numerycznych zachowania się muru oporowego z gabionów. Zwrócono uwagę na możliwe mechanizmy zniszczenia.

Słowa kluczowe: gabion, mur oporowy, MES, stateczność

DOI: 10.4467/2353737XCT.15.226.4612

* PhD. Michał Grodecki, Department of Geotechnics, Faculty of Environmental Engineering, Cracow University of Technology.

Symbols

ε_a – axial strain at steel mesh failure [–]
ϕ – internal friction angle [deg]
γ – soil bulk unit weight [kN/m^3]
c – cohesion [kPa]
E – Young modulus [kPa]
f_t – steel mesh tensile strength [kN/m]
M – steel mesh elastic modulus [kN/m]
SF – safety factor [–]

1. Introduction

The main subject of the study is the behaviour of the retaining wall made of gabions. A gabion is a cage, cylinder, or box made of steel wire mesh, filled with rock samples. In civil engineering, gabions are often used to form gravity retaining walls or gabion-faced reinforced soil retaining walls (when the steel mesh used for gabion cages is also used as a soil reinforcement). Despite their simplicity, the numerical modelling of gabion retaining wall-soil interaction is complicated. The main sources of complications are: nonlinear behaviour of the soil (both retained soil and gabion filling), and the interactions (friction) between steel mesh and soil and between gabions.

In engineering practice, stability calculations for retaining walls formed from gabions are usually performed using ultimate soil pressure theory, identical with the case of concrete retaining walls. The friction between the gabions and the retained soil (on the vertical surface of the wall) and the cohesion of the retained soil is usually neglected, which is on the safe side but could lead to uneconomical design. Usually only two possible destruction mode are taken into account – overturning and horizontal sliding.

When numerical analysis is used, gabions are usually modelled as an elastic continuum. The interface (contact) elements are used to describe the friction between the gabions and the retained soil or the friction between gabions (if the connections between gabions are not "perfect"). This approach fails to identify one of the possible destruction modes – shearing of the filling and tensional failure of the steel mesh. The retained soil is usually modelled with use of Coulomb-Mohr elasto – plastic model. Plane strain assumption is usually used (for example in [4]).

In some works a bit more sophisticated approach (which could be called homogenization approach) is used. Gabions are modelled using the Coulomb-Mohr elasto-plastic model. The friction angle of gabions is equal to the friction angle of the filling, and some additional cohesion is used. The value for additional cohesion is taken from membrane theory and can be verified in triaxial tests. According to [2] and [4] this additional cohesion can be calculated from:

$$c_r = \frac{\Delta\sigma_3}{2}\tan\left(45° + \frac{\varphi}{2}\right) \tag{1}$$

where:
c_r – additional cohesion

$$\Delta\sigma_3 = \frac{2M\varepsilon_c}{d}\cdot\frac{1}{\left(1-\varepsilon_a\right)}$$ – increment confining stress

$$\varepsilon_c = \frac{\left(1-\sqrt{1-\varepsilon_a}\right)}{1-\varepsilon_a}$$ – circumferential strain

M – membrane elastic modulus (kN/m)
ε_a – axial strain at steel mesh failure
d – characteristic dimension of the sample (lowest gabion dimension)

Mesh tensional strength does not appear explicitly in such this approach, but we can see that it is a function of axial strain at steel mesh failure and membrane elastic modulus:

$$f_t = \varepsilon_a M \tag{2}$$

In this homogenization approach, the elastic stiffness of the gabions should also be a function of filling and steel mesh stiffness. At this state of the research, the elastic stiffness of the filling (in fact Young modulus E) is used as an approximation of the gabion elastic stiffness – the influence of the steel mesh elastic stiffness is neglected.

Even in simple stability calculations the friction coefficient between gabions and subsoil should be identified. According to [3] it could can be performed using the following equation:

$$\alpha_{ds}\tan\varphi = \alpha_s\tan\delta + \left(1-a_s\right)\tan\varphi \tag{3}$$

where:
α_{ds} – friction coefficient between gabion and soil
δ – friction angle between steel and soil
a_s – ratio between steel area and gabion-subsoil connection area
φ – friction angle of the subsoil

If we choose to use the assumption typical in Polish design practice that there is no friction between soil and steel ($\delta = 0$) equation (3) can be simplified to:

$$\alpha_{ds} = 1 - a_s \tag{4}$$

This approach is on the safe side, because it leads to some underestimating of the friction forces between the gabions and the subsoil.

The problem of the friction between gabions is (as far as the author knows) has not yet been not solved to this day. In the absence of joints between gabions, the coefficient of friction between gabions could be tested in the laboratory (direct sliding test). If some steel joints are used to join gabions three different approaches could be used. The first assumes that the connection is "perfect" and that no interface element between gabions are necessary. This approach do not allow the failure of the wall caused by joints failure to be described. The second approach (more conservative) leads to using the Coulomb-Mohr law for the interface elements between gabions, where the friction angle would describe the friction between gabions, and cohesion would describe the strength of the joints. This approach allows failure of the wall due to joint failure to be described, but is not capable

of describing the resistance of the joints against opening of the gap between gabions. The third approach (closest to reality) leads to modelling the joints between gabions using truss elements perpendicular to the gabion surface. Friction in the interface elements is then responsible for describing the friction between gabions, and cohesion in interface elements describes the joint resistance against sliding and joints describe the resistance to opening the gap between gabions.

2. Numerical experiment

2.1. Simple retaining wall

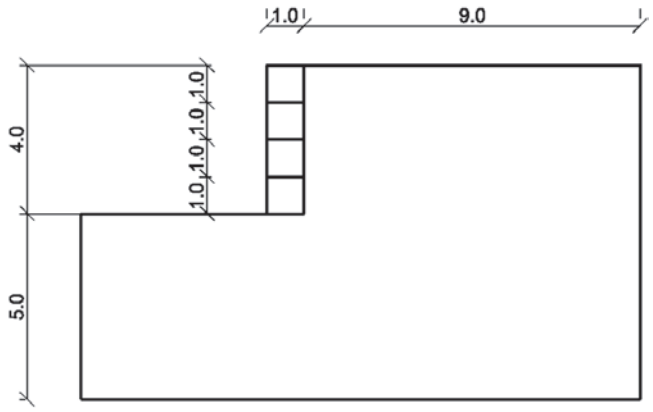

Fig. 1. Analysed object (dimensions in metres)

A stability analysis of a 4 m high model retaining wall was performed. A variety of retained soil and wall property combinations were used to obtain different destruction modes. All numerical simulations were performed in plane strain conditions, using the ZSoil Finite Element Method (FEM) software described in detail in [5] and [7]. The safety factor SF was estimated using the c-f reduction method described in [6]. The interface elements were used between soil and gabions. Filling and steel mesh properties were taken from [4]. The friction coefficient between gabion and subsoil and between gabions was calculated according to equation (3). No joints between the gabions were taken into account. The Coulomb-Mohr elasto-plastic model was used for retained soil and gabions. Additional cohesion for gabions was calculated as described in Chapter 1.

The stability loss modes obtained are presented below. The first shows overturning (typical of retaining soil with small cohesion and high friction angle), the second – horizontal sliding of the whole wall (typical of retained soils with high cohesion and low friction angle), the third – horizontal sliding of the part of the wall (top gabion) (could happen when there are no joints between gabions or there are joints without friction and a weak layer at the top of the structure appears), and the fourth – shearing of both retained soil and gabion (typical of weak gabion filling and weak steel mesh).

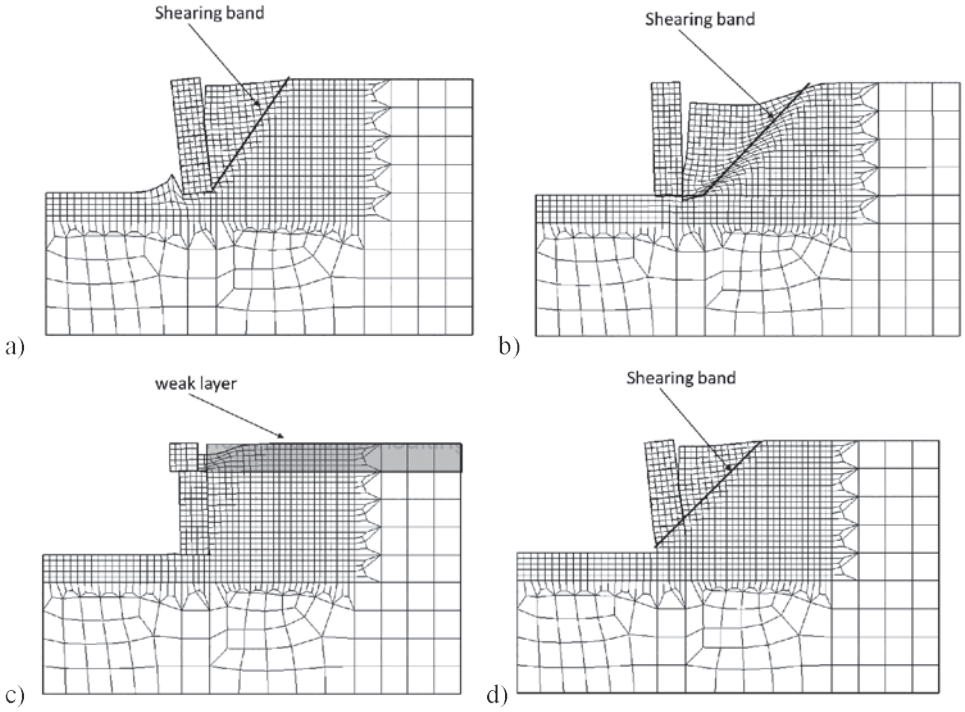

Fig. 2. Typical stability loss modes a) overturning, b) horizontal sliding of the whole wall, c) horizontal sliding of the part of the wall (top gabion), d) shearing of retained soil and gabion

For simplicity, this same value $E = 100$ MPa of the Young modulus for gabion and retained soil was used. The ratio between the tangent of the friction angle of interface and tangent of the friction angle of the soil or gabion was set to 0.95, cohesion of the interface was set to 0. Other parameters used in the simulations are listed below.

Table 1

Parameters used in the simple retaining wall stability analysis

	Retained soil		Gabions	
Stability loss mode	c [kPa]	ϕ [deg]	c [kPa]	ϕ [deg]
Overturning	5	35	23	43
Horizontal sliding of the whole wall	20	10	23	43
Horizontal sliding of the top gabion	5 (1 for weak layer)	45 (8 for weak layer)	23	43
Sheraring of the retained soil and gabion	5	35	20	43

2.2. Anti-flood embankment supported by gabions

Numerical simulation of 5 m high embankment behaviour (whose stability was analysed in [1]) was performed.

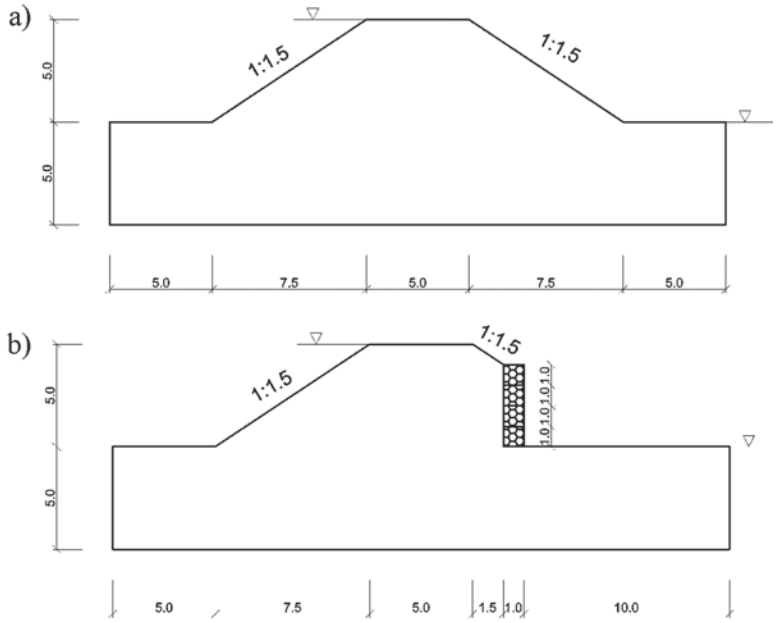

Fig. 3. Analysed embankment (after [1]) a) without gabions b) with 4 gabions

The safety factors obtained were compared with those obtained using the classic Fellenius or Bishop method presented in [1]. For simplicity Darcy`s coefficients for soil and gabions were assumed as equal (no drainage effect produced by gabions). Alternatively, for the highest wall (with 4 gabions) a ratio of 1:100 between Darcy's coefficients for soil and gabions were taken into account, which introduces a drainage effect produced by the gabions. Numerical simulations were performed in the steady state of the flow. The influence of the pore pressure on the mechanical behaviour of the embankment was introduced according to the effective stresses principle.

The results obtained show that safety factors for the embankment without gabions are comparable, regardless of calculation method. However, large differences in safety factors between the classic approach (using the cylindrical sliding surface assumption) and numerical analysis appear when the embankment is supported by gabions. This is because the assumption of a cylindrical sliding surface is not true for retaining structures. This assumption leads to unsafe results (overestimation of the safety factor) being obtained.

The drainage effect produced by the gabions leads to raising of the SF for the embankment from 1.23 to 1.31, which is a noticeable effect. This is due to a lowering of the water free surface in the vicinity of the gabions.

So for hydrotechnical structures the drainage effect of gabions is significant and should be taken into account in stability calculations.

Table 2

Results of the stability calculations for anti-flood embankment supported by gabions

Number of gabions	SF from Fellenius method (after [1])	SF from Bishop`s method (after [1])	SF from numerical simulations
0	1.564	1.605	1.56
2	1.634	1.689	1.53
3	1.543	1.609	1.37
4	1.459	1.522	1.23 (without drainage effect) – 1.31 (with drainage effect)

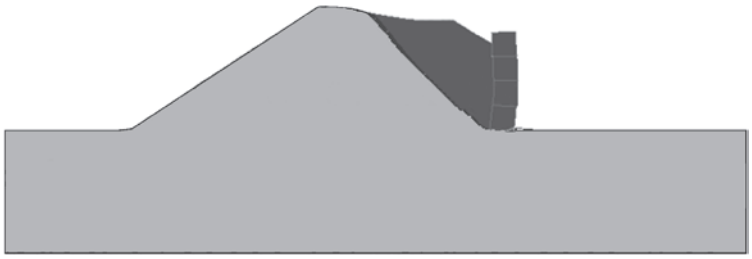

Fig. 4. Sliding surface for embankment with 4 gabions

3. Final remarks

The results of the numerical simulations described above show the complexity of the gabion retaining wall-soil interaction. Different destruction modes are obtained. Overturning is typical of retained soils with small cohesion but high friction angle, horizontal sliding of soils with high cohesion and small friction angle. Sliding between gabions is obtained where there are no joints between gabions (or joints are weak) and a weak layer of soil appears near the top of the structure. Destruction due to filling shear and steel mesh failure is obtained when weak material is used for filling and weak steel for mesh. The assumption of cylindrical sliding surfaces leads to unsafe results (overestimating of stability factor) being obtained and should not be used in engineering practice. For hydrotechnical structures, the drainage effect of gabions is significant and should be taken into account in stability calculations.

References

[1] Balawejder A., Kozłowski W., Surowiecki A., *Stateczność nasypu wzmocnionego ścianą gabionową w warunkach napływu wody*, Zeszyty Naukowe Politechniki Rzeszowskiej, Budownictwo i Inżynieria Środowiska, nr 3/2011/II.

[2] Bathurst, R.J., Rajagopal, K., *Large-scale triaxial compression testing of geocell reinforced granular soils*, Geotechnical Testing Journal vol. 16 no. 3, 1993, 296–303.
[3] Bergado D.T., Youwai S., Teerawattanasuk C., Visudmedanukul P., *The interaction mechanism and behavior of hexagonal wire mesh reinforced embankment with silty sand backfill on soft clay*, Computers and Geotechnics 30 (2003), 517–534.
[4] Jayasree P. K., *Performance of gabion faced reinforced earth retaining walls,* PhD Thesis, Cochin University of Science and Technology, 2008.
[5] Podleś K., Truty A., Urbański A., *Analiza zagadnień geotechnicznych w systemie Z_SOIL*, X Jubileuszowa Konferencja Naukowa "Metody Numeryczne do Projektowania i Analizy Konstrukcji Hydrotechnicznych", Korbielów 1998, 100–108.
[6] Truty A., Urbański A., Grodecki M., Podleś K., *Komputerowe modele zagadnień osuwiskowych oraz ich zabezpieczeń*, Zeszyty Naukowo-Techniczne Stowarzyszenia Inżynierów i Techników Komunikacji Rzeczpospolitej Polskiej w Krakowie nr 88 (zeszyt 144), 2009.
[7] *"Z_Soil.PC, Theoretical Manual",* ZACE Services Ltd., Lozanna 2014.

TECHNICAL TRANSACTIONS | CZASOPISMO TECHNICZNE
ENVIRONMENTAL ENGINEERING | ŚRODOWISKO
2-Ś/2015

MICHAŁ GRODECKI*

NUMERICAL SIMULATIONS OF THE HEAT FLOW IN A CONCRETE ROD

NUMERYCZNE SYMULACJE PRZEPŁYWU CIEPŁA W PRĘCIE BETONOWYM

Abstract

This paper discusses the results of numerical simulations of unsteady heat flow in a concrete rod. The temperature distributions obtained are compared with experimental results. The main goal of this paper is to find soil thermal parameters values for concrete which leads to obtaining the best correlation between the measured and calculated temperatures.

Keywords: concrete, heat flow, FEM, temperature

Streszczenie

W artykule przedstawiono rezultaty symulacji numerycznych nieustalonego przepływu ciepła w pręcie betonowym. Uzyskane rozkłady temperatur porównano z wynikami badań laboratoryjnych. Głównym celem pracy jest określenie parametrów cieplnych betonu prowadzących do uzyskania najlepszej korelacji pomiędzy pomierzonymi a obliczonymi wartościami temperatury.

Słowa kluczowe: beton, przepływ ciepła, MES, temperatura

DOI: 10.4467/2353737XCT.15.227.4613

* PhD. Michał Grodecki, Department of Geotechnics, Faculty of Environmental Engineering, Cracow University of Technology.

Symbols

α – thermal diffusivity [m^2/s]
λ – heat conductivity [W/(mK)]
c – heat capacity [J/m^3K]
$\mathbf{q}$ – heat flux [W/m^2]
t –- time [h], [min]
T – temperature [K]
W – internal heat source power [$J/(m^3 \cdot s)$]

1. Introduction

The main subject of the study is an unsteady heat flow in a concrete rod. I present: a mathematical model of the problem, a laboratory experiment, and numerical simulations of it. The temperature distribution obtained from numerical simulations is compared with the results of laboratory tests. The main goal is to find soil thermal parameter values for concrete which leads the best correlation between measured and calculated temperatures.

The problem of unsteady heat flow is described by Fourier's law:

$$\mathbf{q} = -\lambda\, \mathbf{grad} T \tag{1}$$

where:
$\mathbf{q}$ – heat flux,
T – temperature [K],
λ – heat conductivity [W/(mK)].

The following was obtained using the heat balance equation:

$$c\dot{T} - \lambda\Delta^2 T = W \tag{2}$$

where:
W – internal heat source power [$J/(m^3 \cdot s)$],
c – heat capacity [J/m^3K].

In the case of no internal heat source: $W = 0$. This leads to:

$$c\dot{T} - \lambda\Delta^2 T = 0 \tag{3}$$

$$c\dot{T} = \lambda\Delta^2 T \tag{4}$$

$$\frac{c}{\lambda}\dot{T} = \Delta^2 T \tag{5}$$

By introducing thermal diffusivity $\alpha = \dfrac{\lambda}{c}$, the following equation is obtained:

$$\frac{1}{\alpha}\dot{T} = \Delta^2 T \tag{6}$$

Equation (6) shows that this problem is governed by one material parameter, thermal diffusivity $\alpha = \lambda/c$ [m²/s].

According to [3] thermal effects have great importance for hydrotechnical concrete structures. Changes in the concrete temperature caused by annual variation in the water and air temperatures are the main source of deformation of such structures. It's worth mentioning that heat flow in gravity concrete dams is an example of an unsteady flow. As mentioned in [1], a thermal analysis must be performed to predict the cracking response of the concrete.

According to [1], the heat conductivity of the concrete is not a constant material property, it depends mainly on aggregate volume fraction and moisture condition.

So a proper estimation of the concrete's thermal parameters must be performed before any thermal and mechanical analysis of the concrete structure under thermal influence.

2. Numerical experiment

Numerical simulations of the heat flow in a concrete rod (50 cm long, 10 × 10 cm square in plane – Fig. 1) isolated with 10 cm Styrofoam were performed.

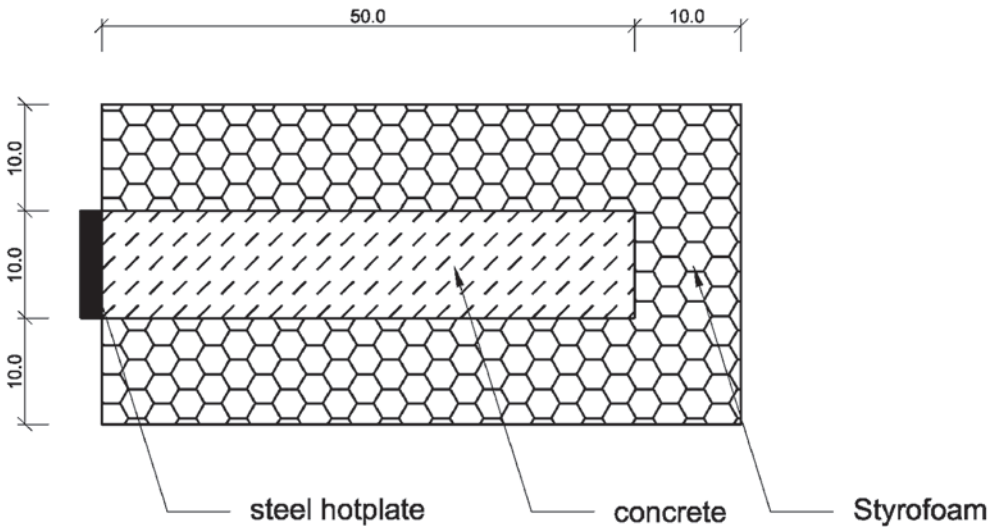

Fig. 1. Analysed concrete rod with Styrofoam heat isolation (dimensions in cm)

The experiment described in [6] was simulated. The initial (first estimate) values of material properties for the concrete are summarized in Table 1.

Table 1

Initial set of heat flow parameters for concrete based on sandstone aggregate

Source	λ [W/(m · K)]	c [kJ/(m^{3}K)]	α [m^2/h]
A.M. Neville „Właściwości betonu" (Eng: Properties of concrete)	2.9	2016–2808	$3.718 \cdot 10^{-3}$ $5.1798 \cdot 10^{-3}$
Standard PN-91/B-02020 – Ochrona cieplna budynków (Eng: Thermal protection of buildings)	1.8	2016	$3.214 \cdot 10^{-3}$

The experiment described in [6] shows that 10 cm thick thermal isolation consisting of Styrofoam leads to one-dimensional heat flow (no heat flow in the direction perpendicular to the axis of the rod). Such observation was verified during numerical simulations. In the 3D model, a Styrofoam isolation layer was introduced and a convection boundary condition on the outer surface of the isolation was used. In the 1D model, the Styrofoam layer was not introduced and "no heat flow" boundary condition on the outer surface of the concrete was used. In both models, the temperature boundary condition was used at the steel hotplate, describing the temperature change program used in the experiment described in [4].

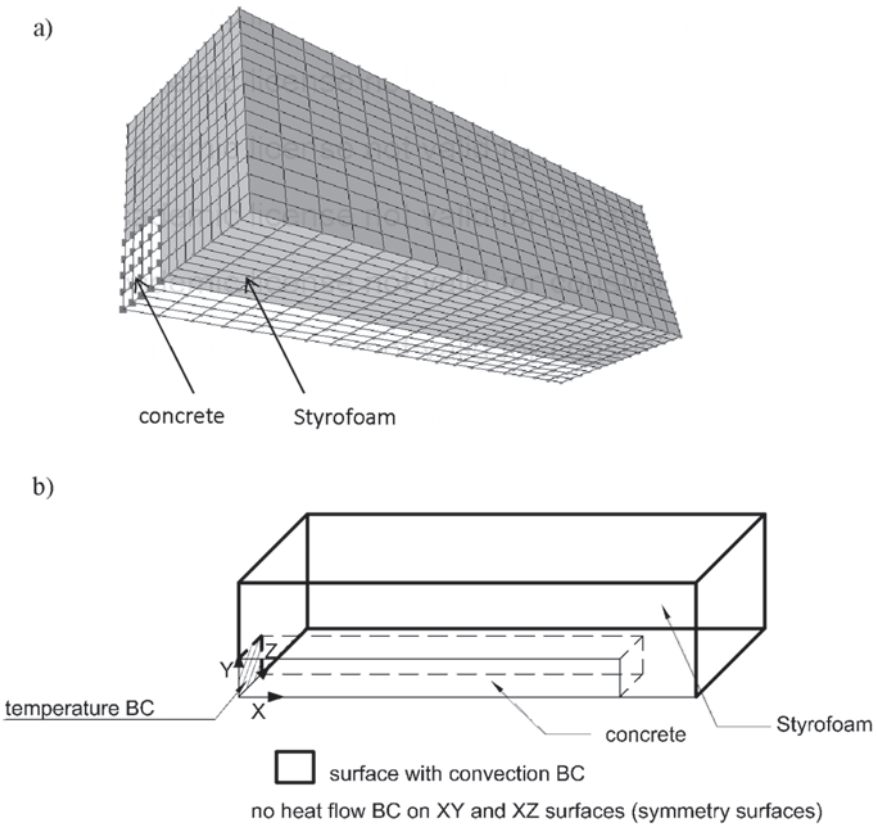

Fig. 2. 3D model a) overview b) boundary conditions

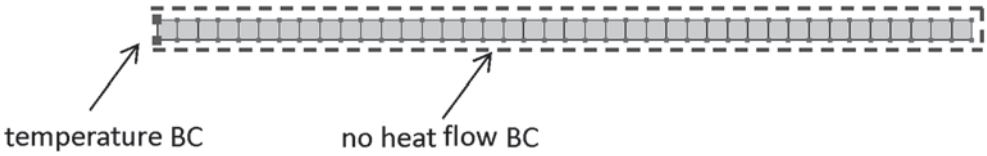

Fig. 3. Overview of the 1D model, with boundary conditions

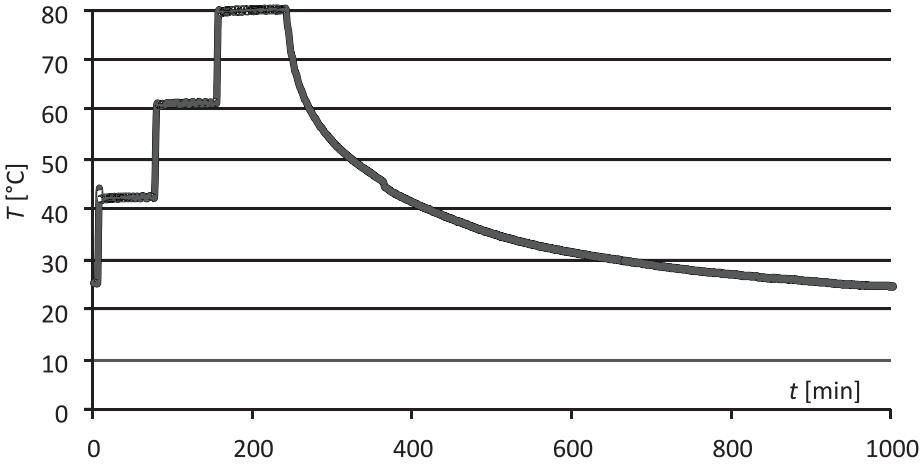

Fig. 4. Boundary condition at the steel hotplate – temperature changes in time

The results obtained show almost no difference between the 1D and 3D models for the obtained temperature field – the differences do not exceed 2°C. Hence, the 1D model is used in this paper from this point.

Then, the calculations for different values of thermal diffusivity α were performed to obtain a good correlation between numerical and experimental results (temperature field). The best correlation (minimum of sum of the squares of the temperature differences) was obtained for $\alpha = 2.441^{-3}$ m^2/h, which is a lower value than was suggested in [1] or [5]. The time-space temperature distribution obtained for $\alpha = 2.441^{-3}$ m^2/h are presented in Fig. 5–7. Comparison of the calculation results with measured temperatures shows a relatively good correlation in the heating phase, much worse in the cooling phase. The delay in the obtaining maximal temperature observed, especially for points located far from the cooling plate, shows that the observed heat flow is really transient. Maximum temperature drops down from 80°C at the hotplate to 31°C at a distance of 30 cm. As can easily be seen in Fig. 7 the location of the maximal temperature migrates from its location at the hotplate during the heating phase to a point located 20 cm from the hotplate in about 800 min.

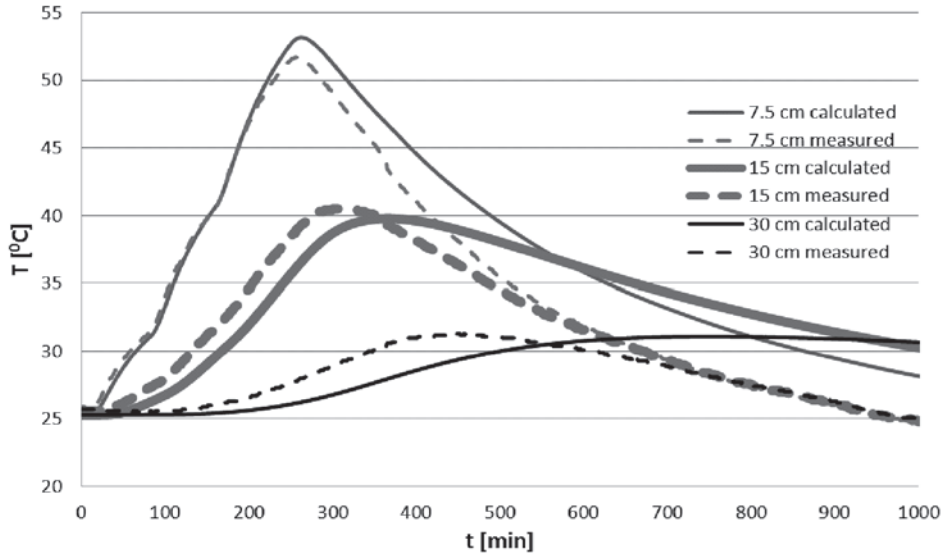

Fig. 5. Temperature changes in time at a different distance from the hotplate for $\alpha = 2.441^{-3}$ m^2/h

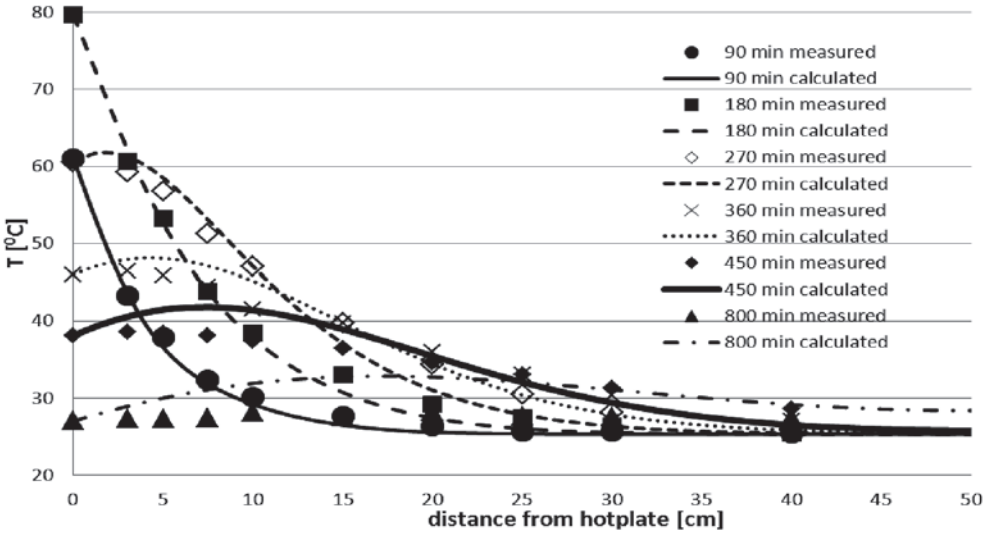

Fig. 6. Temperature distribution along the rod for different time instants for $\alpha = 2.441^{-3}$ m^2/h – calculated (lines) and measured (points)

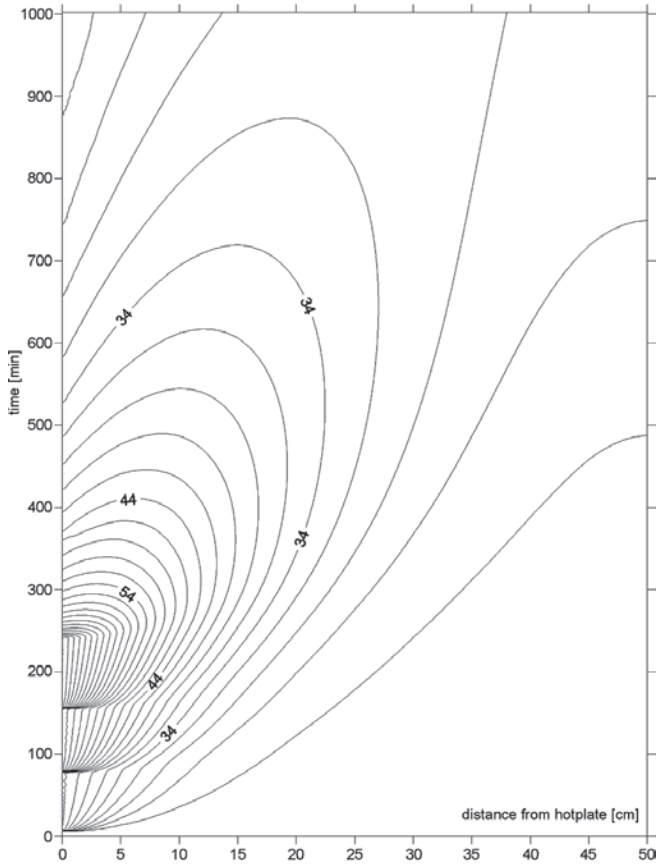

Fig. 7. Time – space temperature distribution – isolines of the calculated temperature [°C] for $\alpha = 2.441^{-3}$ m^2/h

3. Final remarks

The temperature distributions obtained from the numerical simulations show much better correlation with experimental values in the heating phase than in the cooling phase. In the cooling phase, the reaction of the numerical model is slower than it should be (compared to experimental results). This observation raises the question of whether heat conductivity has the same value when the concrete temperature rises and when it falls. No cracking during the cooling phase and no air humidity changes (which could have an influence on the heat flow) were observed in the real experiment. However, the maximum difference in obtained temperature does not exceed 6°C, which is quite acceptable. The maximum temperatures in different points of the rod are also properly estimated in the model.

References

[1] Kook-Han K., Sang-Eun J., Jin-Keun K., Sungchul Y., *An experimental study on thermal conductivity of concrete*, Cement and Concrete Research 33 (2003) 363–371.

[2] Neville A.B., *Właściwości betonu (Eng. Characteristics of concrete)*, Wyd. 4, Polski Cement Sp. z o.o., 2000.

[3] Urbański A., *Numerical modeling of thermal, filtration and mechanical phenomena in a selected section of a gravity dam*, Numerics in Geotechnics and Structures 2010, 93–108.

[4] Zając B., *Laboratory testing of transient heat flow in concrete*, in this issue of Technical Transactions.

[5] Polish standard PN-EN ISO 6946 Komponenty budowlane i elementy budynku Opór cieplny i współczynnik przenikania ciepła. Metoda obliczania, 1999 (Eng. Building components and elements of the building. Thermal resistance and heat transfer coefficient. The method of calculation)

[6] *"Z_Soil.PC, Theoretical Manual"*, ZACE Services Ltd., Lozanna 2014.

TECHNICAL TRANSACTIONS | CZASOPISMO TECHNICZNE
ENVIRONMENTAL ENGINEERING | ŚRODOWISKO
2-Ś/2015

GRZEGORZ KACPRZAK*

PROPOSITION OF DESIGNING METHOD FOR BARRETTES AS A NON-DIRECT FOUNDATION OF ENGINEERING CONSTRUCTION

PROPOZYCJA PODEJŚCIA PROJEKTOWEGO DLA POSADOWIENIA OBIEKTÓW INŻYNIERSKICH W SPOSÓB POŚREDNI NA FUNDAMENTACH SZCZELINOWYCH

Abstract

The paper presents barrettes, which are a useful method of designing non-direct foundations of engineering construction. The methodology is based on the distribution of forces acting on a foundation capping slab into each barrette, which depends on its stiffness. To determine the proper stiffness of an individual barrette comprising the foundation system, the transformational function of a pile with large diameter was used. Finally, the stiffness of each barrette as an element of foundation system was corrected in view of the group's impact.

Keywords: barrette, transformational function, settlement

Streszczenie

W artykule przedstawiono metodę projektowania fundamentów pośrednich obiektów inżynierskich, jakimi są barety. Metoda opiera się na rozdziale siły przyłożonej na płytę oczepową fundamentu na poszczególne barety, co zostało uzależnione od sztywności każdej barety. W celu oszacowania sztywności każdej barety będącej elementem fundamentu pośredniego, użyto funkcji transformacyjnych zdefiniowanych dla pali wielkośrednicowych skorygowanych ze względu na ich pracę w grupie.

Słowa kluczowe: bareta, funkcja transformacyjna, osiadanie

DOI: 10.4467/2353737XCT.15.228.4614

* PhD. Grzegorz Kacprzak, Institute of Roads and Bridges, Faculty of Civil Engineering, Warsaw University of Technology.

1. Fundamentals of barrette application

Section 7 of PN-EN 1997-1 [1], Eurocode 7 concerns the design of pile foundations. The provisions presented there apply to end-bearing piles, friction piles, tension piles and transversely loaded piles. They apply to piles installed by driving, jacking and screwing or boring, and piles installed with or without grouting. Reference is made in Eurocode 7 to other CEN standards that are relevant to the design of pile foundations (for example for the structural design of steel piles [3] – EN 1993-5: Eurocode 3, Part 5: Design of Steel Structures – Piling). Reference is also made to the execution standards for the carrying out of piling work like EN 1536:1999 [2] – Execution of special geotechnical work – Bored Piles.

Using this information, barrettes are used for the foundations of engineering construction like bridge supports in accordance with the European/Polish Standard PN-EN 1997-1 [1], Eurocode 7 and PN-EN 1536, Bored piles [2]. The latter Standard establishes general principles for the execution of bored piles as well as barrettes treated as bored piles which are formed in the ground by excavation and are structural members used to transfer actions and/or limit deformations. PN-EN 1536 applies to barrettes with the least dimension ≥ 0.4 m ($\geq$0.3 m for precast elements), a length to width ratio between its largest and its least dimensions ≤ 6 and a cross-sectional area ≤ 15 m^2 columns.

2. Design principles

PN-EN 1997-1 [1] states that the design of piles shall be based on one of the following approaches:

a) The results of static load tests, which have been demonstrated, by means of calculations or otherwise, to be consistent with other relevant experience,
b) Empirical or analytical calculation methods whose validity has been demonstrated by static load tests in comparable situations,
c) The results of dynamic load tests whose validity has been demonstrated by static load tests in comparable situations,
d) The observed performance of a comparable pile foundation, provided that this approach is supported by the results of site investigation and ground testing.

The most important limit states that the bearing resistance failure of the pile foundation (ultimate limit state, ULS) and excessive settlement (serviceability limit state, SLS) need to be considered in the design of piles.

The equilibrium equation to be satisfied in the ultimate limit state design of axially loaded piles in compression is:

$$F_{c,d} \leq R_{c,d} \tag{1}$$

where:

$F_{c,d}$ – the design axial compression load,
$R_{c,d}$ – the pile compressive design resistance.

Piles in a group should be checked for failure of the piles individually and acting as a block. The design resistance shall be taken as the lower value caused by these two mechanisms.

For the serviceability limit state designs the inequality to be checked is:

$$E_d \leq C_d \tag{2}$$

where:
E_d – the design value of the effect of the actions, the settlement of foundation,
C_d – the limiting value of the effect of an action, the limiting value of foundation movement.

Taking into account that the load settlement characteristics depend on the position of the pile in the pile group and one can distinct corner pile, boundary pile and inner pile, the general provisions of PN-EN 1997-1 [1] concerning verification for "compressive ground resistance" of pile groups were detailed in German Standard DIN 1054 [4], for ULS and SLS respectively:

$$F_{c,d}(\text{ULS}) \leq \sum R_{c,d,i}(\text{ULS}) \tag{3}$$

where:

$\sum R_{c,k,i}$ – the resistance of the pile group as the sum of all piles considering their individual resistance according to their position in the pile group

$$F_{c,k}(\text{SLS}) \leq \sum R_{c,k,i}(\text{SLS}) \tag{4}$$

where:
$F_{c,k}$ – the characteristic axial compression load,
$R_{c,k,i}$ – the characteristic pile resistance considering group effects

or

$$s_{e,k}(\text{SLS}) \text{ } '' \text{ } s_{a,k}(\text{SLS}) \tag{5}$$

where:
$S_{e,k}$ – the estimated average settlement of foundation,
$S_{a,k}$ – the acceptable settlement of foundation.

According to DIN 1054 [4], for determination of $\sum R_{c,k,i}$(SLS), $\sum R_{c,d,i}$(ULS) and the estimated value of average settlement $s_{e,k}$ of a pile group, an approximation procedure with nomograms for bored piles presented in Recommendations on piling [5] might be used. This method defines the group effect for individual piles taking into account their position in the pile group, soil conditions, pile group geometry and type of pile based on the load settlement characteristic of a single pile. In other words, the resistance of a single pile $R_{c,k,i}$ is modified by the pile group factors for resistance defined for a different level of settlement. Alike, the average settlement of the bored pile group due to the average load (in each step of the load) is estimated as the product of settlement of single pile and the pile group factors for settlement.

Alternatively to the procedures suggested by DIN 1054 [4], a very useful approximation for the settlement ratio developed by Randolph [6] can also be used. In this case, it is suggested for typical floating pile groups in which the centre-to-centre spacing is about 3 diameters, the pile group factor for settlement is approximately $n^{0,5}$ for clays and $n^{0,33}$ for

sands, where n is the number of piles in the group. The imperfection of this method compared to that proposed by DIN is the unification of the load settlement characteristic of each pile in the group (independently to pile position in the pile group). All the same, the settlement group factor can easily be defined, enabling fast estimation of load settlement relationships for a pile in the group. In order to illustrate this methodology, assume that the secant stiffness of the single pile (K_p) for hyperbolic pile load V_p – settlement s_p relationship is expressed as follows:

$$K_p = K_{pi}(1 - R_{fp}V_p / V_{pu}) \tag{6}$$

where

K_{pi} – initial axial stiffness of a single pile (based on the results of static load tests, the results of FEM analysis or the estimation by transformational function, see Chapter 3), kN/m,
V_p – pile load, kN,
V_{pu} – ultimate capacity of a single pile = characteristic maximal resistance of single pile (in the moment of q_b and $t_{\max}$ mobilization),
R_{fp} – hyperbolic factor for single pile, 0,80-0,85.

For a given load carried by pile V_p, the pile head settlement of pile group s_{pg} can be calculated using the modified initial axial stiffness of a single pile:

$$s_{pg} = V_p / \left\{ \left(K_{pi} / n^w \right) \times (1 - R_{fp}V_p / V_{pu}) \right\} \tag{7}$$

Finally, we can obtain the load V_p – settlement s_{pg} characteristic of a pile working in the pile group.

3. Load settlement characteristic of a single barrette

3.1. Transformational functions

According to the recommendations by Gwizdała [7], the load-settlement of a single bored barrette head can be determined with sufficient accuracy using the power function for the shaft and barrette tip resistance, respectively:

$$t = t_{\max} \left(\frac{z}{z_v} \right)^{\beta_1} \quad \text{for} \quad z \le z_v \tag{8}$$

where:

β_1 - 0.5 for cohesionless and 0.25 for cohesive soil,
$t_{\max}$ – the maximal unit shaft resistance of barrette, kPa,
z – the settlement of barrette head, m,
z_v – the barrette head settlement required to mobilize maximal resistance along the shaft, 0.01xD, m,
D – the barrette diameter, m.

$$q = q_b \left(\frac{z}{z_f} \right)^{\beta_2} \quad \text{for} \quad z \le z_f \tag{9}$$

where:
β_2 – 0.5 for cohesionless and 1/3 for cohesive soil,
q_b – the maximal unit barrette tip (base) resistance, kPa,
z – the settlement of barrette head, m,
z_f – the barrette head settlement required to mobilize resistance in the bottom of the barrette, 0,05xD, m,
D – the barrette diameter, m.

3.2. Barrette resistance based on CPT test results

Eurocode 7 describes three procedures for obtaining the characteristic compressive resistance $R_{c,k,i}$ of a single barrette:
a) directly from static barrette load tests,
b) by calculation from profiles of ground test results,
c) by calculation from ground parameters.

In the case of procedures a) and b) Eurocode 7 provides correlation factors to convert the measured barrette resistances or barrette resistances calculated from profiles of test results into characteristic resistances. In the case of procedure c), the characteristic barrette resistance is calculated from the ground parameter values. This procedure is the most common method in some countries, for example in Poland, Ireland and the UK. The compressive resistance of a single barrette is finally determined from the ground parameters as a sum of the characteristic base $R_{b,k}$ and shaft resistances $R_{s,k}$ depending on barrette head settlement using the following equations given in PN-EN 1997-1 [1]:

$$R_{s,k}(z) = \sum A_{s,j} \times t_j(z) \tag{10}$$

$$R_{b;k}(z) = A_b \times q(z) \tag{11}$$

where:
A_b – the nominal plan area of the base of the barrette,
$A_{s,j}$ – the nominal surface area of the barrette in soil layer j,
t_j – the unit barrette shaft resistance in soil layer j depending on barrette head settlement (8),
q – the unit barrette base resistance depending on barrette head settlement (9).

In order to determine the maximal unit shaft in soil layer j ($t_{max,j}$) or maximal barrette tip (base) resistance (q_b), the modified Bustamante and Gianeselli method presented by Gwizdała [7] can be used. This method is based on local Polish experience according to CPT test results.

4. Example of design – implementation of proposed designing method

The usefulness of this proposed design method was verified during the construction of a design for viaducts over the street Army Krajowej in the Market Rakowy and Sienny in Gdansk. The load-settlement behaviour of a single bored barrette head was measured in-situ by a load test and predicted using the sum of power function for shaft (Eq. 8) and barrette tip resistance (Eq. 9), (continuous line Fig. 1), as well as the hyperbolic function of Poulos (Eq.6), (dotted line Fig. 1.).

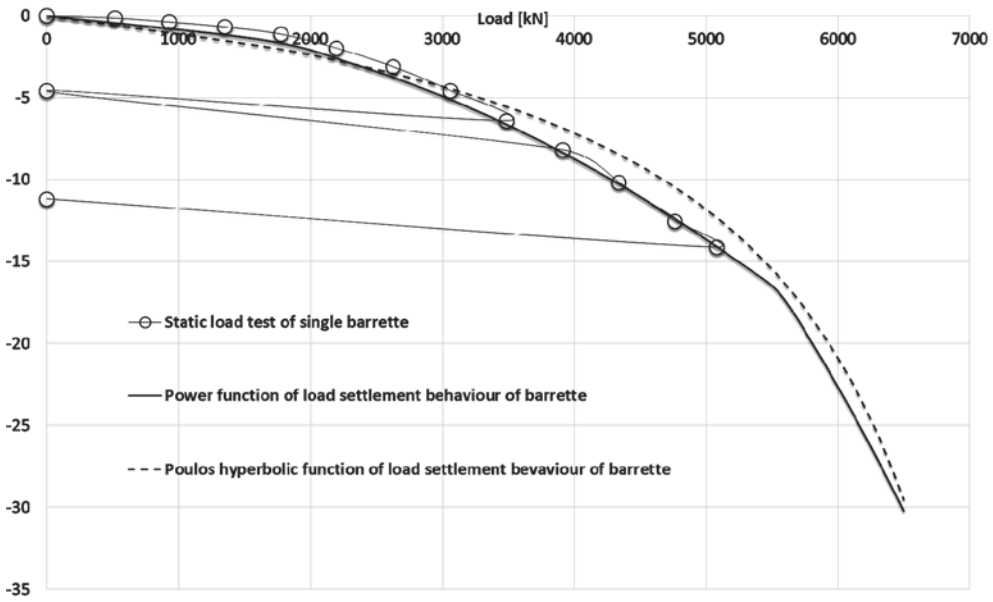

Fig. 1. Load-settlement relationship for single barrette

Finally, the load V_p – settlement s_{pg} characteristic of a barrette working in the barrette group was defined according to equation (7).

5. Summary

In order to determine the load settlement characteristic of a barrette working in a barrette group used as a common type of foundation for bridges, a useful design procedure was described. This methodology is based on transformational function as an alternative to a static load test. In order to represent the real behaviour of a barrette in a barrette group (its stiffness), the author suggests using a group factor according to provision of DIN 1054 or the approximation by Randolph.

References

[1] EN 1997-1:2004 Eurocode 7: Geotechnical design – Part 1: General Rules /PN-EN 1997-1:2008 Eurokod 7, Projektowanie geotechniczne Część 1: Zasady ogólne.
[2] EN 1536:1999 – Execution of special geotechnical work – Bored Piles.
[3] EN 1993-5: Eurocode 3, Part 5: Design of Steel Structures – Piling.
[4] German Standard DIN 1054:2010-12 Subsoil – Verification of the safety of earthworks and foundations – Supplementary rules to DIN EN 1997-1.
[5] Kempfert H.G., *Recommendations on piling (EA-Pfahle),* Deutsche Gesellschaft für Geotechnik e.V., Wiley Ernst and Sohn, 2013.
[6] Poulos, H.G., *Pile behaviour – theory and application*, Geotechnique 39, 1989, p. 365–415.
[7] Gwizdała K., *Fundamenty palowe. Technologie i obliczenia*, Wydawnictwo Naukowe PWN, rozdz. 5 i 6, Warszawa 2010.

TECHNICAL TRANSACTIONS | CZASOPISMO TECHNICZNE
ENVIRONMENTAL ENGINEERING | ŚRODOWISKO
2-Ś/2015

PIOTR KANTY, KRZYSZTOF STERNIK, SŁAWOMIR KWIECIEŃ*

NUMERICAL ANALYSIS OF CONSOLIDATION OF EMBANKMENT SUBSOIL REINFORCED WITH DYNAMIC REPLACEMENT STONE COLUMNS

ANALIZA KONSOLIDACJI PODŁOŻA WZMOCNIONEGO METODĄ WYMIANY DYNAMICZNEJ POD NASYPEM DROGOWYM

Abstract

The paper presents a comparative analysis of the consolidation of soil under a road embankment reinforced with stone columns. The results were obtained from the most common analytical and numerical methods applied in driven column dimensioning. The analytical approach exploits Terzaghi's one-dimensional theory and Barron's three-dimensional theory. The numerical calculations reflected the particular stages of the embankment construction in various two- and three-dimensional systems. The geotechnical parameters that were crucial for the research were determined on the basis of geoengineering documentation, laboratory and field studies. The paper begins with a short introduction presenting the dynamic replacement method.

Keywords: dynamic replacement, stone column, numerical analysis

Streszczenie

Przedmiotem artykułu jest analiza porównawcza wyników obliczeń konsolidacji podłoża wzmocnionego wbijanymi kolumnami kamiennymi, pod nasypem drogowym, otrzymanych na podstawie najczęściej stosowanych, przy wymiarowaniu kolumn wbijanych, podejść analitycznych i numerycznych. W podejściu analitycznym zastosowano jednowymiarową teorię Terzaghiego oraz trójwymiarową teorię Barrona. W obliczeniach numerycznych zamodelowano etapową budowę nasypu w różnych układach płaskich i przestrzennych. Parametry geotechniczne, niezbędne do obliczeń, ustalone zostały na podstawie dokumentacji geologiczno-inżynierskiej, badań laboratoryjnych i polowych. Całość rozważań poprzedzona została krótką informacją na temat wymiany dynamicznej.

Słowa kluczowe: wymiana dynamiczna, kolumny kamienne, analiza numeryczna

DOI: 10.4467/2353737XCT.15.229.4615

* MSc. Piotr Kanty, PhD. Krzysztof Sternik, PhD. Sławomir Kwiecień, Department of Geotechnics and Roads, Faculty of Civil Engineering, Silesian University of Technology.

Symbols

L – spacing of columns
D_{col} – diameter of a stone column
D_e – diameter of the unit cell
α – replacement ratio
x – general parameter
c' – effective cohesion
ϕ' – effective friction angle
E – resilient modulus
M – constrained (oedometric) modulus
ν – Poisson's ratio
ψ – dilatancy angle
e – void ratio
γ – unit weight
S – saturation ratio
S_r – residual saturation ratio
p_w – pore water pressure
k^*_{ij} – permeability tensor for unsaturated soil
k_{ij} – permeability tensor for saturated soil
k_r – scaling scalar function for the permeability tensor
k_v – permeability coefficient in vertical direction
k_h – permeability coefficient in horizontal plane
m_v – coefficient of compressibility

1. Introduction

When planning development of new roads passing through urban areas, it is most often impossible to bypass regions of soft foundation soil. Thus, it is necessary to strengthen the weak subsoil in order to limit the settlement of the road embankment, reduce the time of primary consolidation and to assure sufficiently high safety factor for the embankment's slopes. This can be achieved by installing stiff inclusions of granular material called stone columns. Stone columns in soft ground can be formed in two ways: by vibro replacement or dynamic replacement.

Vibro replacement (VR) columns are installed in the ground by means of a crane-suspended downhole vibrator. The vibrator is lowered, densifying and displacing the underlying stone (crushed stone, recycled concrete, gravel) and forming a column of 0.6–1.0 m in diameter (D_{col}). During installation the zone around a column is strongly affected by vibrations produced by working equipment (vibrator or rammer). The zone of the disturbed soil is called the smear zone.

In the dynamic replacement (DR) method, stone columns are formed in weak soil using the equipment that allows free drop of a heavy rammer from a pre-defined height. In the first phase, the rammer forms a crater (Fig. 1a) which is then refilled with coarse-grained material (Fig. 1b). Afterwards, the material is pressed into the soil forming the crater which is then

refilled once again and the whole process is repeated (Fig. 1b). The column is formed until the rammer cannot penetrate the soil anymore. This may mean that the column's base have reached a stiffer soil layer (Fig. 1c) or that the energy used during the process of column formation does not allow the soil to be penetrated any more (a so-called "floating column").

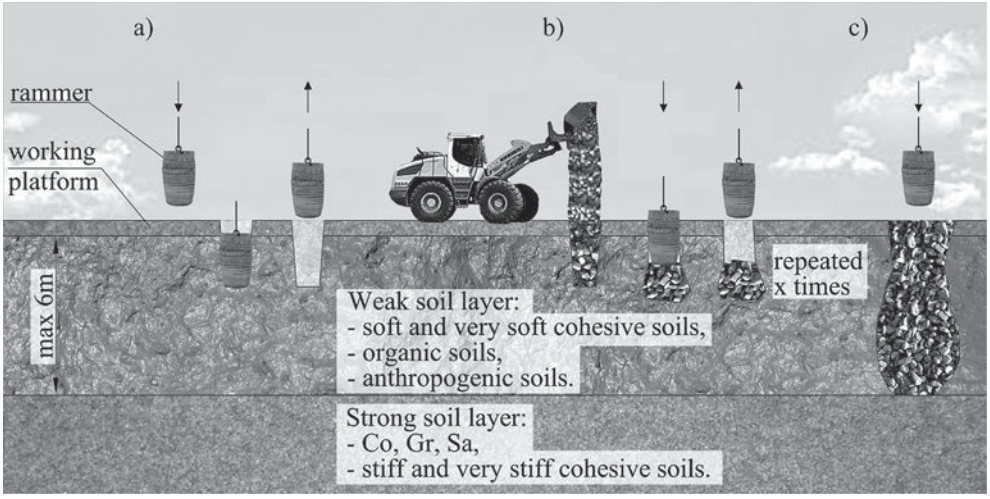

Fig. 1. Process of stone column formation

In Poland, the most common parameters applied in this technology are: rammer weight of 10–20 tonnes and drop height up to 25 m. The diameter of a column usually varies between 1.6–4.0 m [21]. In the case of a dynamic replacement column the impact of the falling rammer is so great that the whole volume of soft soil is remoulded and the smear zone cannot be distinguished. The number of rammer drops that need to be performed in order to form a column varies from 15 to 30. The ramming process results in the formation of columns of various shapes and diameters [22], which depend on soil susceptibility, applied energy and rammer shape. After the reinforcement process, the physical and mechanical parameters of the weak soil change [30].

Although analytical methods for designing vibro-column reinforcement exist [10, 24], there are no algorithms related to driven columns which would take into account the specific method of their construction [10, 11, 18]. While designing such columns, two factors are taken into consideration: the column's bearing capacity and settlement of the system consisting of the column and its surroundings [18]. Projects that take into account a drainage effect are very rare. The international literature describes this effect when it comes to vibro replacement columns [3, 4, 7], whereas for dynamic replacement columns it has not yet been examined. One of the few attempts to tackle this topic have been the model research described in [28] and [29]. The problem of the efficiency of DR column drainage in comparison to VR column has recently been discussed in [20].

The reduction of primary consolidation is achieved by two mechanisms: radial drainage towards columns which causes faster dissipation of pore water pressure and high column stiffness which reduces vertical load on soft soil and thereby the increase in pore water pressure. The acceleration of consolidation due to drainage was firstly recognized for vertical

drains disregarding their stiffness [1, 2, 13, 15, 17], whereas the effect of column stiffness was investigated among others in [1, 5, 12, 14, 32].

In this paper the problem of consolidation of soft foundation soil reinforced with stone columns under a road embankment has been investigated by means of numerical calculations. It is a continuation of work presented previously in [19, 23]. In engineering practice a geotechnical problem like this is most frequently solved analytically by making use of the unit cell concept or as a plane-strain numerical analysis. The first approach serves only to predict the settlement of reinforced soft soil ignoring the problem of stability of the embankment. The second approach requires conversion of parameters of reinforced subsoil from axisymmetry to plane-strain conditions.

Three-dimensional analysis is the background for comparisons with the results of simplified two-dimensional computations and an analytical solution.

2. Soil parameters

The computational analysis presented here is related to the embankment that is part of the S7 expressway in the city of Lubień. This embankment (Fig. 2) was 12 m high. The bottom and the top of the embankment were respectively 67 m and 31 m wide. The slopes were inclined at 1:1.5. The entire embankment was formed using the method of lime stabilized soil.

In the computations, the top of the embankment was loaded with a pressure of 25 kPa [9] which substitutes the weight of the road pavement and the load induced by traffic.

Prior to the research, drillings were performed in order to examine the initial geotechnical conditions under the embankment, which allowed it to be determined that the soil was formed of soft silty clay layers locally underlain by more dense gravel with stones and/or soft rock (Fig. 2). Table 1 presents the values of soil parameters.

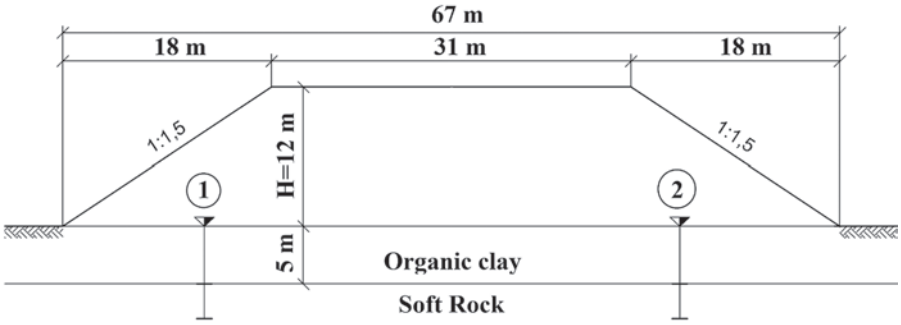

Fig. 2. Analysed embankment and foundation soil

Table 1

Soft soil parameters

Layer	ϕ [°]	ψ [°]	c [kPa]	ν [–]	E [MPa]	e_0 [–]	k [m/s]	γ [kN/m^3]
Organic clay	4.6	0	31	0.3	2.65	0.6	1.00E-09	14.18

After analysing the type, condition and thickness of the soft layer, the designer decided to strengthen the soil using the dynamic replacement method. According to the designs, the main part of the embankment was supposed to be strengthened by stone columns of about 2.2 m in diameter and 5 m in length, distributed in a 3 m × 3 m grid. Columns were formed of stone aggregate of fraction 0/400 mm. The equipment used for column formation is presented in Fig. 3a, whereas Fig. 3b shows the excavated column.

a) b)

Fig. 3. a) equipment used for soil reinforcement, b) excavated column

3. Numerical analysis of consolidation – basic models

3.1. Preliminary remarks

The analysis is divided into two parts. In the first part, the authors compare the approaches applied in the projects of soil strengthening with the dynamic replacement method executed in Poland. As some of them may raise doubts, all the methods were compared to the most reliable one, i.e. the three-dimensional model. The second part of the analysis aims to present some improvements to the presented models, as well as other methods described in the literature.

3.2. Assumptions for the calculations

The consolidation of the soil under a road embankment reinforced using the dynamic replacement method was calculated using both analytical and numerical (FEM) methods. At the first stage of the research, five models were analysed.

Model No. I is the analytical method presented by Barron [2] and Terzaghi [33] in which the stone column is considered only as a drain that accelerates the consolidation process. The calculations of settlements were performed using Priebe's method [27] and presented in a spreadsheet, taking into account the gradually increasing load, which corresponds to the increasing height of the embankment.

It was assumed that the total settlement occurs according to the average degree of vertical (U_v) and horizontal (U_R) consolidation. The U_v value is determined based on the following formula from Terzaghi's theory [33]:

$$U_V = 1 - \sum_{m=0}^{m=\infty} \frac{2}{M^2} \exp(-M^2 T_v) \tag{1}$$

where
M – the constrained modulus,
T_v – the time factor in vertical direction.

U_R value is determined following Barron's theory [2] according to the formula:

$$U_R = 1 - e^{\frac{-8T_R}{f(n)}} \tag{2}$$

where
T_R – the time factor in radial direction,
$f(n)$ = ln(n) – 0.75,
n – the ratio of unit cell radius ($R_e = D_e/2$) to drain radius ($R_{col} = D_{col}/2$).

Four other calculation methods applied the finite element method (FEM). The analyses were performed using Z_Soil ver. 11.15 program [36]. Two- and three-dimensional models were analysed during the research.

In the first of the numerical analyses (model No. II), a three-dimensional model (Fig. 4) was used to present the construction of the embankment on soil reinforced with stone columns. The process of constructing the embankment was represented by adding subsequent layers of finite elements and the load induced by road surface and traffic was replaced by a unit load of 25 kPa.

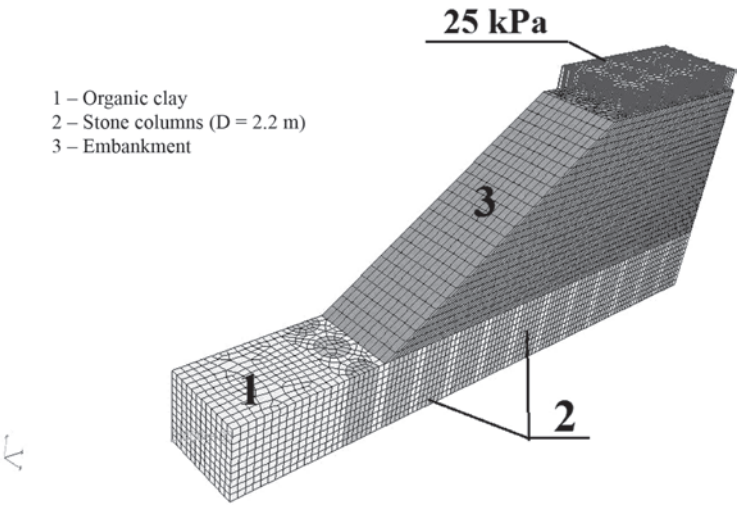

Fig. 4. Model No. II

Model No. III uses a unit cell (Fig. 5) determined on the basis of the method described in [10]. It simulates the work of a large system of repetitive cells placed under a vast construction, in which the columns are distributed in a square system with L spacing. The diameter of the unit cell was determined to be $D_e = 1{,}13 \times L$. The unit cell is modelled as an axisymmetric case.

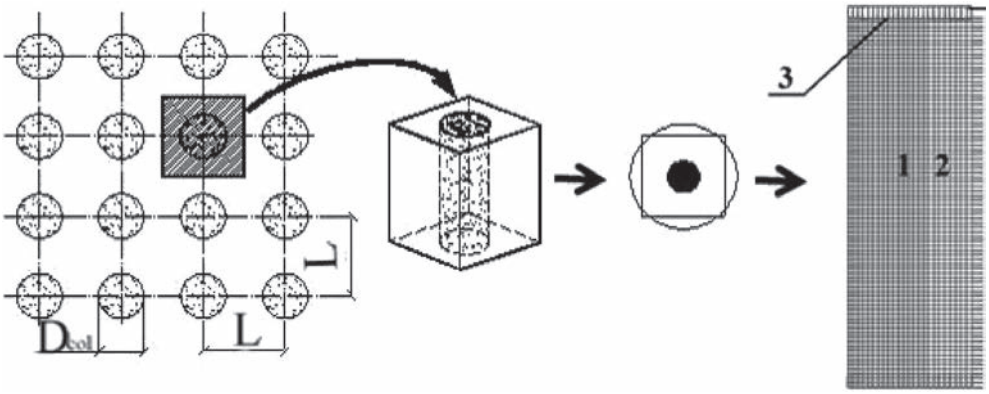

Fig. 5. Model No. III

Model No. IV presents the simulation of the construction of embankment in plane-strain, situated on homogenous soil which is characterized by averaged parameters (Fig. 6). The average value of each parameter was determined on the basis of the percentage of column material in the volume of the unit cell, i.e. using the replacement ratio α as weight coefficient. α is defined as the ratio of the surface of column's cross section to the surface of the unit cell:

$$\alpha = \frac{A_{col}}{A_e} = \left(\frac{D_{col}}{D_e} \right)^2 \tag{3}$$

Composite values of unit weight γ, cohesion c, friction angle ϕ, resilient modulus E and permeability coefficient k were determined by the formulae proposed by Dimaggio [8] and reported in [6]. Its general form with respect to any parameter x is given by the Eq. (4)

$$x = x_{col}\alpha + x_s\left(1-\alpha\right) \tag{4}$$

where:

x – average value,

x_{col}, x_s – represent a parameter for a column and soft soil respectively.

Model No. V is the simulation of the embankment in plane-strain conditions with columns represented by strip elements of width equal to the actual column's diameter (Fig. 7). Parameters for soft soil and stone column material remain unmodified in any way.

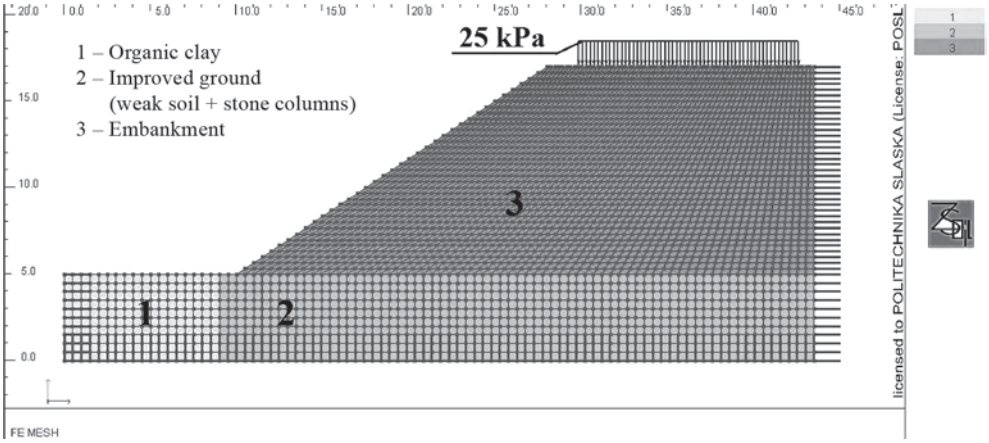

Fig. 6. Model No. IV

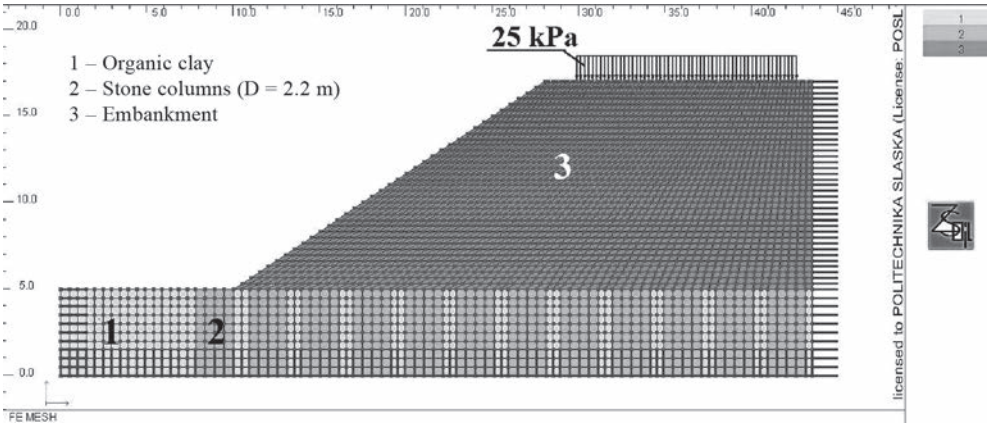

Fig. 7. Model No. V

The presented models IV and V are strongly simplified, however. In model No. IV, the average value of permeability coefficient was also determined based on equation (4), which may not be fully reliable.

Although all the other parameters for both weak soil and stone columns are of the same order, the difference between the permeability coefficient for both materials is huge.

In model No. V, the percentage content of the column increases significantly in the geometrical model, which leads to an increase in the replacement ratio. As a result, the settlements of the system may be underestimated.

3.3. Applied constitutive models and their parameters

All the data in the numerical analyses were described using the elastic-perfectly plastic model with Mohr-Coulomb surface modified by Menetrey and Willam [36]. For the

abovementioned model, five parameters need to be known: resilient modulus E, Poisson's ratio ν, friction angle ϕ, cohesion *c* and dilatancy angle ψ.

As previously mentioned, the embankment was formed with lime stabilized cohesive soil. The parameters of this model for the material forming the embankment were determined on the basis of the analyses in direct shear apparatus and oedometric tests [19]. Poisson's ratio was determined to ν = 0.3 and the dilatancy angle ψ = 0.

The parameters of the stone column and deposit materials used in each model were determined on the basis of back analysis, i.e. matching the results of laboratory and field tests to the results of the numerical analysis of the boundary value problem.

Triaxial compression allowed the values of friction angle ϕ and cohesion c to be determines and oedometric tests – the virgin and reloading constrained modulus. This research was presented in [18]. Poisson's ratio for weak soil was determined on the basis of the body of literature [35] and its dilatancy angle was equal to 0.

As the columns were formed from coarse-grained material of fraction up to 400 mm, it was impossible to analyse the material in laboratory tests. However, test loading of the completed column was performed using a plate located on the column's head, which induced a pressure of 0–1373 kPa. The results of the test loading were used to calibrate the numerical system "stone column – weak soil surrounding" [18]. The similarity of the "loading – settlement" curve obtained from the numerical models and as the result of test loading was considered to be the criterion of adequacy for the numerical model itself. Column parameters were heuristically determined on the basis of the numerical analyses. According to these, the coefficient of determination R^2 was found to be equal to 0.9982 [18]. In the analysis performed, the non-associated flow rule (ψ = 0) was used.

Values of the permeability coefficient for a column and soft soil were taken from the literature. Materials were assumed to be isotropic in terms of permeability. In analyses hydro-mechanical coupling (consolidation) is described by the Van Genuchten model [34], in which flow in a non-saturated medium depends essentially on two hydrodynamic characteristics: water retention and permeability. To determine the saturation ratio *S*, which is the function of pore water pressure p_w, the model makes use of two constants: the residual saturation ratio S_r and parameter β that describes the curvature of a water retention curve:

$$S = S\left(p_w\right) = \begin{cases} 1 & \text{if } p_w \le 0 \\ S_r + \dfrac{1 - S_r}{\left[1 + \left(\beta p_w / \gamma_w\right)^2\right]^{0.5}} & \text{if } p_w > 0 \end{cases} \tag{5}$$

The permeability tensor k^*_{ij} is obtained by scaling the k_{ij} tensor for a fully saturated medium by a scalar valued function k_r dependent on the saturation ratio *S*:

$$k^*_{ij} = k_r\left(S\right)k_{ij} \tag{6}$$

$$k_r(S) = \begin{cases} 1 & \text{if } S = 1 \\ \dfrac{\left(S - S_r\right)^3}{\left(1 - S_r\right)^3} & \text{if } S < 1 \end{cases} \tag{7}$$

Also the initial void ratio e_0 is required for complete specification of the model.
All parameters taken for analyses are presented in Tables 2 and 3.

Table 2

Mechanical parameters and soil weight

Model No.	Material No.	E [kPa]	ν [–]	γ [kN/m^3]	φ' [^{o}]	c' [kPa]
I	1	2 650	0.30	–	–	31
II, III, IV,V	1	2 650	0.30	14.18	4.6	31
I	2	76 000	0.20	16.53	42.0	–
II, III, V	2	76 000	0.20	16.53	43.5	5
IV	2	33 620	0.26	15.16	21.0	20
I, III	3	–	–	20.00	–	–
II, IV,V	3	45 000	0.30	20.00	35.0	45

Table 3

Hydraulic parameters

Model No.	Material No.	e_0 [–]	k_h [m/s]	k_v [m/s]	S_r [–]	α [–]
I	1	–	1.00E-09	1.00E-09	–	–
II, III, IV,V	1	0.60	1.00E-09	1.00E-09	0.20	0.5
I	2	0.84	–	–	–	–
II, III, V	2	0.84	1.00E-01	1.00E-01	0.00	10.0
IV	2	0.84	4.22E-02	4.22E-02	0.10	4.5
I, III	3	0.40	–	–	–	–
II, IV,V	3	0.40	1.00E-07	1.00E-07	0.20	1.0

3.4. Discussion of the results of the first stage analyses

All the results presented below were determined at a point located just under the foundation soil surface in the middle of the embankment. The point was decided to be representative of the comparison of the calculation results.

The results of the first stage analyses – depending on the applied model – show various values of soil settlements (Fig. 8) and consolidation time (Fig. 9, 10).

All the two-dimensional models underestimate the final settlements, in comparison to the three-dimensional model (model No. II). The differences are most significant for the plane-strain models, i.e. the one with the homogenized parameters (model No. IV) and the other with the stripes of columns of width equal to the column's actual diameter (model No. V). The settlements predicted on the basis of these models are over 60% smaller than those obtained from the 3D model. In the case of the unit cell (model No. III), as well as in the case of analytical calculations, the settlements are smaller by slightly over 20%.

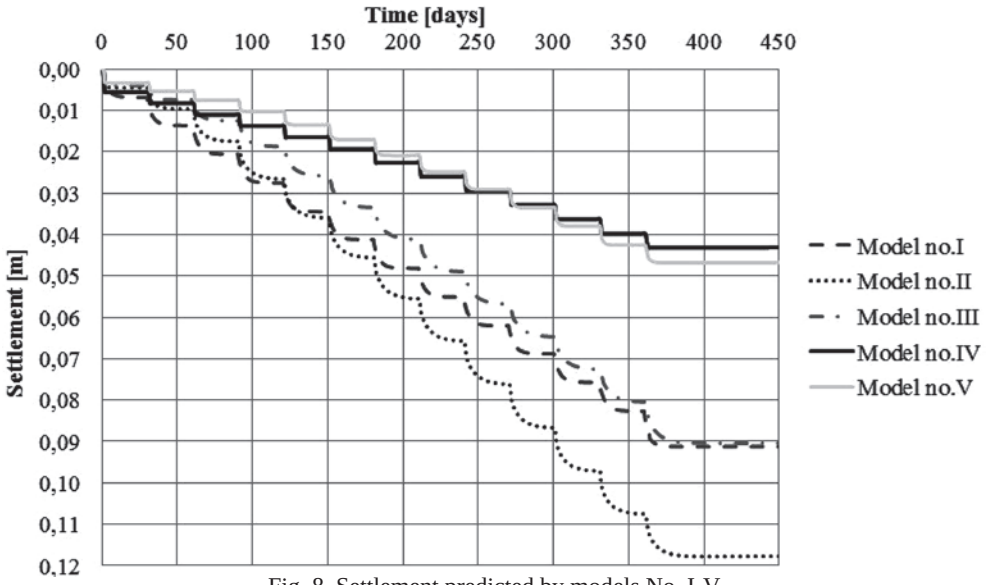

Fig. 8. Settlement predicted by models No. I-V

Figures 9 and 10 represent the diagrams of pore water pressure changes predicted in numerical models No. II–V.

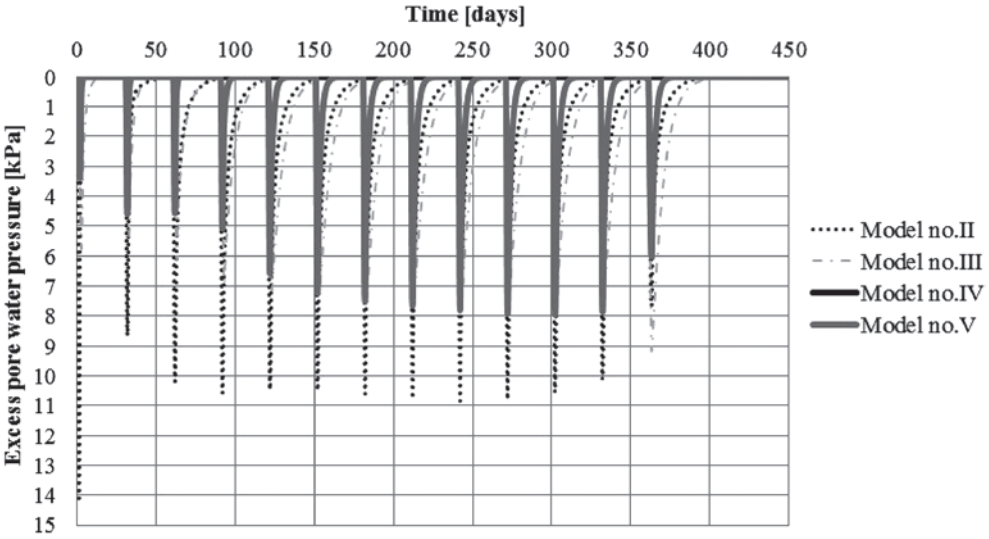

Fig. 9. Excess pore water pressure predicted by models II–V

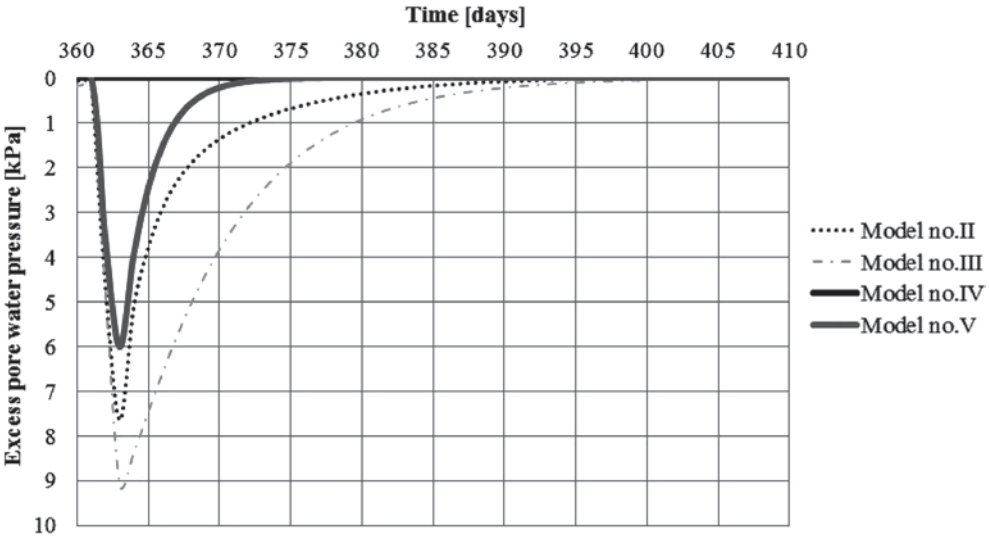

Fig. 10. Excess of pore water pressure in last steps of analyses predicted by models II-V

The excess pore water pressure and consolidation time of the reinforced soil are significantly underestimated by the plane-strain models (No. IV and V) compared with the predictions of the 3D model. When soft soil and columns are treated as a homogenized layer, the calculations show almost no increase in pore pressure resulting from the construction of the embankment. The pressure is immediately dissipated due to the high value of the permeability coefficient k. The consolidation time for model No. V is 60% shorter than the 3D model (model No. II). Only the estimations of the unit cell model (model No. III) indicate the time of water pressure dissipation longer by about 30%.

The conducted analysis revealed that the proposed methods IV and V, widely applied in engineering calculations, show significant discrepancies in the estimations of consolidation time of soil reinforced by stone columns. Therefore they should not be used for this purpose. For this reason, the analyses presented in the following part of this paper will try to propose modifications of the abovementioned models.

4. Computational analysis of the consolidation of reinforced soil under road embankment – other models

4.1. Assumptions for the calculations and parameters of the examined models

In the second, additional stage of the analysis, the authors propose some modifications to the 2D models (IV and V) and offer another model (No. VI).

In models IVa and IVb, as in model No. IV (Fig. 7) described previously, soft soil parameters were averaged. The difference between the models consists in the way the permeability coefficient and the friction angle were determined.

In models IVa and IVb, the averaged friction angle of soil was calculated in a different way than in model IV. The formula (4) was substituted with the following:

$$\tan\phi = \alpha \cdot \tan\phi_{col} + (1-\alpha) \cdot \tan\phi_s \tag{8}$$

The same approach was presented in e.g. [6] and [8].

Another essential modification introduced in both models was the method of calculating the average permeability coefficient in horizontal plane. The formula presented below was used in model IVa:

$$\frac{1}{k_h} = \frac{1}{k_{h\,col}}\alpha + \frac{1}{k_{h\,s}}(1-\alpha) \tag{9}$$

where:

$k_{h\,col}$, $k_{h\,s}$ – permeability coefficients in the horizontal plane for column and soft soil respectively.

Model IVb made use of the simplified formula presented in [26]. The value of k_h coefficient was calculated as follows:

$$k_h = K_{\text{composite}} \cdot k_s \cdot 10^4 \text{ [m/day]} \tag{10}$$

where $K_{\text{composite}}$ was drawn from the calibration graph presented in [25], prepared on the basis of the numerical calculations using the finite element method.

In both Va and Vb models, the diameters of the stone columns were the same as in V (Fig. 8); however, the parameters of columns and weak soil were changed. Column parameters were averaged due to their periodical structure, according to the approach presented by Dimaggio [6].

In model Va, the following formulae were used in order to calculate the permeability coefficient in horizontal and vertical plane [33] for column strip elements:

$$k_v = \frac{1}{L}\left[k_{col}D_{col} + k_s\left(L - D_{col}\right)\right] \tag{11}$$

$$k_h = \frac{L}{D_{col}/k_{col} + \left(L - D_{col}\right)/k_s} \tag{12}$$

Equations (11) and (12) were derived for water flow in parallel and perpendicular directions to layered subsoil by Terzaghi.

In model No. Vb the permeability of the soft soil was modified. Modification concerns only permeability coefficient in horizontal direction. Coefficient of permeability in vertical direction is assumed to be the same for axisymmetric and plane-strain conditions.

The calculations of the permeability coefficient in the horizontal plane were carried out on the basis of the method proposed in [15] and [32]. The method gives the possibility to

calculate the permeability coefficient in the horizontal plane in a plane-strain model ($k_{h,pl}$) on the basis of the values of this coefficient in an axisymmetric model ($k_{h,ax}$). The method is based on the assumption that the flow path length normal to the column perimeter corresponds to the flow path length in the plane-strain conditions and the radius of drainage zone R_e is taken equal to the equivalent plane-strain width B of the strip of columns:

$$\frac{k_{h,pl}}{k_{h,ax}} = \frac{F(N)_{pl}}{F(N)_{ax}} \left[\frac{m_{vs} m_{vc} (1-\alpha)}{m_{vc}(1-\alpha) + m_{vs}\alpha} \right]_{pl} \left[\frac{m_{vc}(1-\alpha) + m_{vs}\alpha}{m_{vs} m_{vc}(1-\alpha)} \right]_{ax} \frac{B^2}{R_e^2} \tag{13}$$

where:

α – replacement ratio,
R_e – radius of a unit cell,
B – plane-strain half width equivalent to R_e,
m_{vc} i m_{vs} – coefficients of compressibility for column and soft soil respectively,

$$F(N) = \left[N^2 / \left(N^2 - 1 \right) \right] \ln(N) - \left(3N^2 - 1 \right) / \left(4N^2 \right) \tag{14}$$

$N = D_e/D_{col}$ – for axisymmetric conditions,
$N = B/b_{col}$ – for plane-strain conditions,
b_{col} – half width of a column in plane-strain conditions.

It should be noted that assuming that the width of a stone column in plane-strain conditions is equal to the diameter in the axisymmetric case may result in excessive enlargement of the area replacement ratio. In model No. VI (Fig. 11), the diameter of a stone column was reduced so that in plane-strain conditions the replacement ratio was maintained. All the mechanical parameters remained unmodified in any way. The permeability coefficient for soft soil in the horizontal direction was calculated using the formula (13) as in model No. Vb.

The simplified assumption was made in the calculations: the parameters for soft soil under the embankment and next to it were the same. In real conditions, the values of the permeability coefficient for soil adjacent to the embankment is different from those for the soil among the columns (under the embankment).

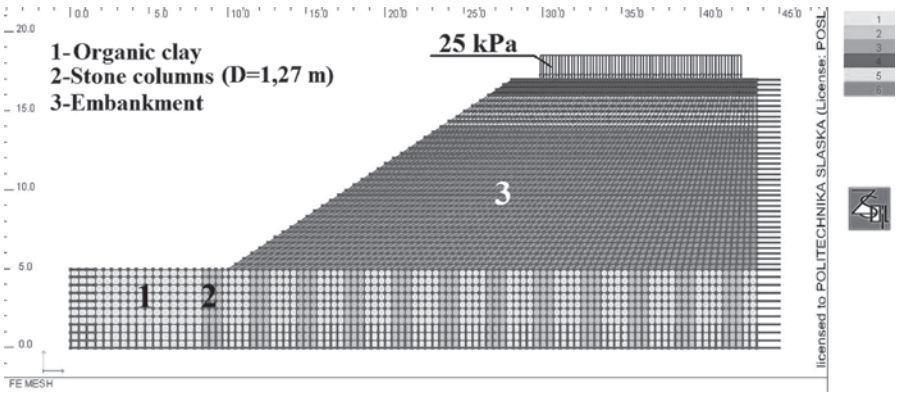

Fig. 11. Model No. VI

Tables 4 and 5 contain the mechanical and hydraulic parameters calculated according to the abovementioned assumptions.

Table 4

Mechanical parameters and soil weight

Model No.	Material No.	E [kPa]	ν [–]	γ [kN/m^3]	φ' [°]	c' [kPa]
IVa, Ivb, Va, VI	1	2 650	0.30	14.18	4.6	31
Iva, IVb	2	33 620	0.26	15.16	24.1	20
Va, Vb	2	56 440	0.23	15.90	35.2	12
VI	2	76 000	0.20	16.53	43.5	5
IVa, Ivb, Va, VI	3	45 000	0.30	20.00	35.0	45

Table 5

Hydraulic parameters

Model No.	Material No.	e_0 [–]	k_h [m/s]	k_v [m/s]	Sr [–]	α [–]
IVa, IVb, Va	1	0.84	1.00E-09	1.00E-09	0.20	0.5
Vb	1	0.84	1.17E–10	1.00E-09	0.20	0.5
VI	1	0.84	2.62E-09	1.00E-09	0.20	0.5
IVa	2	0.74	3.46E-09	4.22E-02	0.12	4.5
IVb	2	0.74	1.50E-06	4.22E-02	0.12	4.5
Va	2	0.66	3.75E–10	7.00E-04	0.05	7.5
Vb	2	0.66	1.00E-01	1.00E-01	0.05	7.5
VI	2	0.60	1.00E-01	1.00E-01	0.00	10.0
IVa, IVb, Va, VI	3	0.40	1.00E-07	1.00E-07	0.20	1.0

4.2. Results of computations and their discussion

Fig. 12 presents the values of the settlements predicted in 2D calculations and those obtained by models No. IV and V during the first and the second stage of the research. The total settlement obtained in the 3D model (No. II) is equal to 11.8 cm and for clarity is not presented in the diagram.

The comparison of the settlement values predicted by the model of homogenous subsoil with the averaged parameters of the column-weak soil system (model No. IV) shows that replacing the average value of the friction angle determined by formula (6) with the value calculated by formula (7) resulted in smaller settlement values. This shows that the predicted values obtained on the basis of models IVa and IVb differ greatly from those determined by the 3D model (No. II) due to the reduction of the friction angle value.

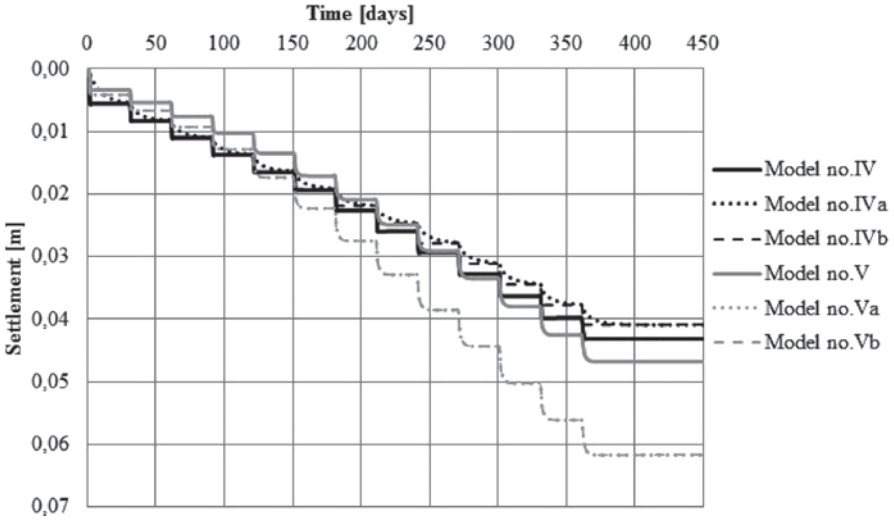

Fig. 12. Settlements predicted by the analysed 2D models

For models in which the width of the column is equal to the actual column diameter (Va and Vb), the modification of column parameters caused the results to be more similar to the results obtained from the 3D model (total settlement 11.8 cm). However, the settlement values obtained in the plane-strain models were underestimated. The graphs for models Va and Vb are almost identical.

Fig. 13 demonstrates the comparison of settlement values for the base 3D model and model No. VI, in which the real value of the replacement ratio was maintained by the proper choice of column width.

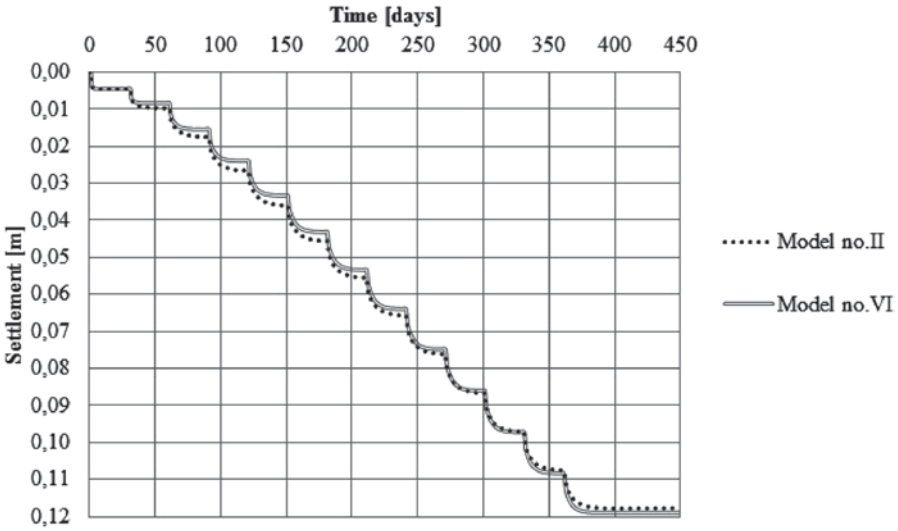

Fig. 13. Comparison of settlements predicted by models No. II and VI

The settlement values obtained from model No. VI are closest to the results from 3D model No. II. No modifications were introduced to the parameters of the column and soft soil in model No. VI but the strips representing columns were narrower. The total settlements and the load-settlement curves are almost identical.

Fig. 14–17 represent the excess pore water pressure calculated using the models examined in the second phase of the research and compare it to the values obtained from the base 3D model (No. II).

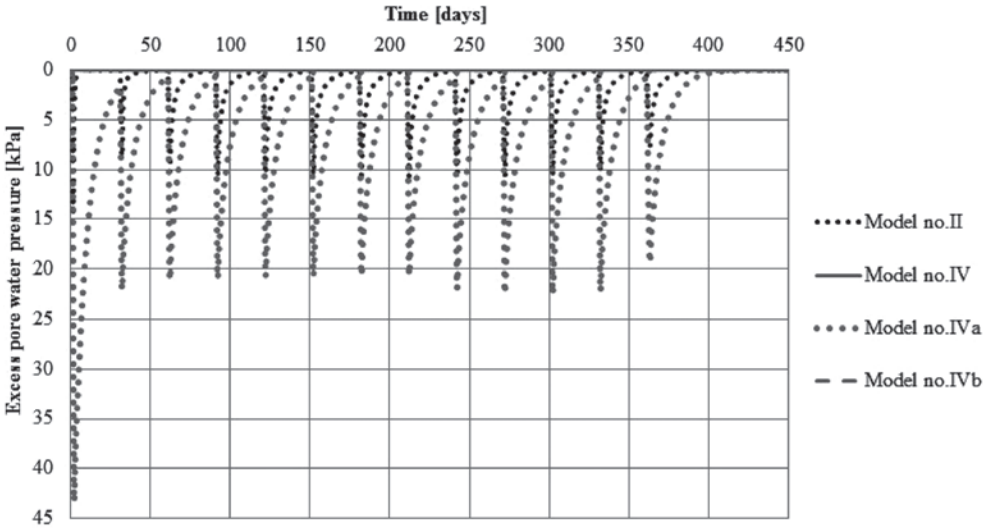

Fig. 14. Comparison of excess pore water pressure predicted by models No. II, IV, IVa, IVb

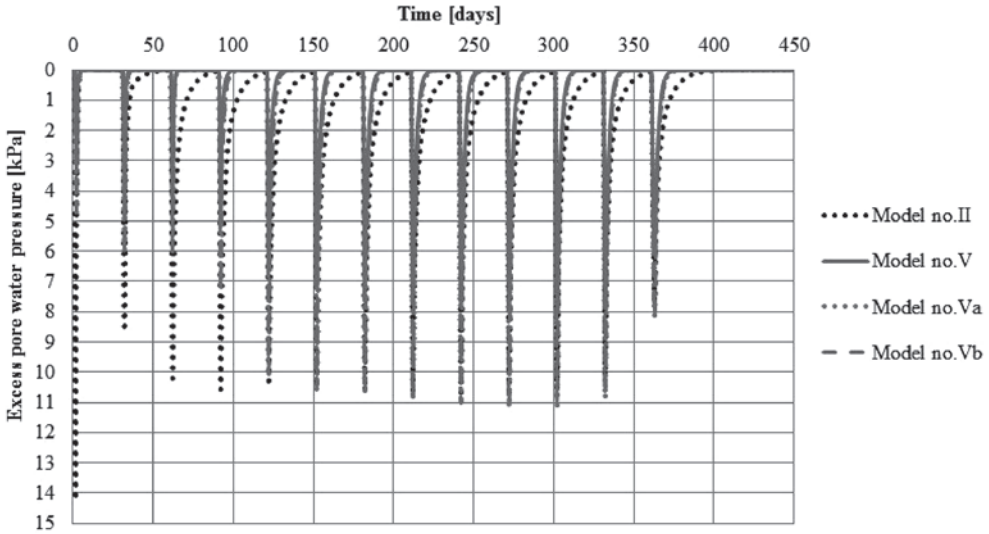

Fig. 15. Comparison of excess pore water pressure predicted by models No. II, V, Va, Vb

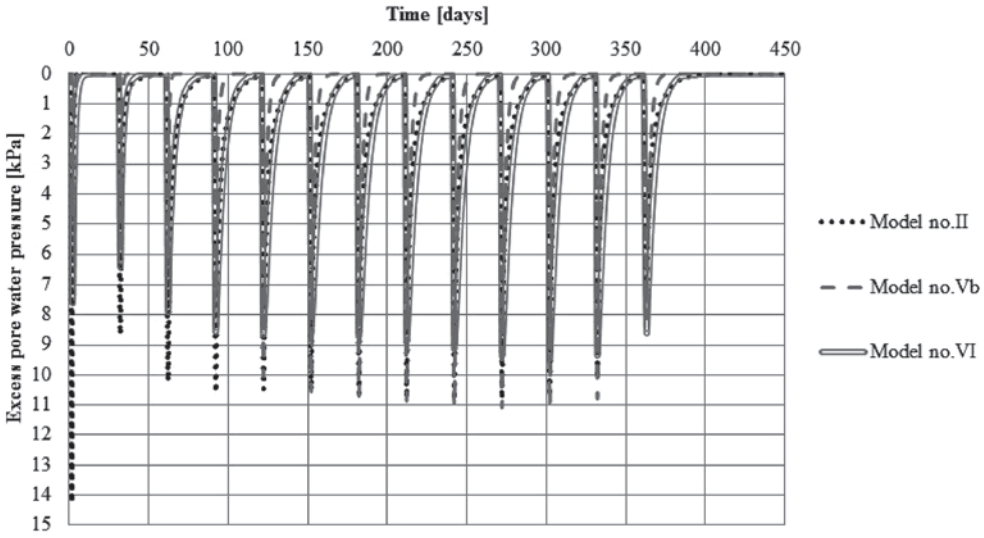

Fig. 16. Comparison of excess pore water pressure predicted by models No. II, Vb, VI

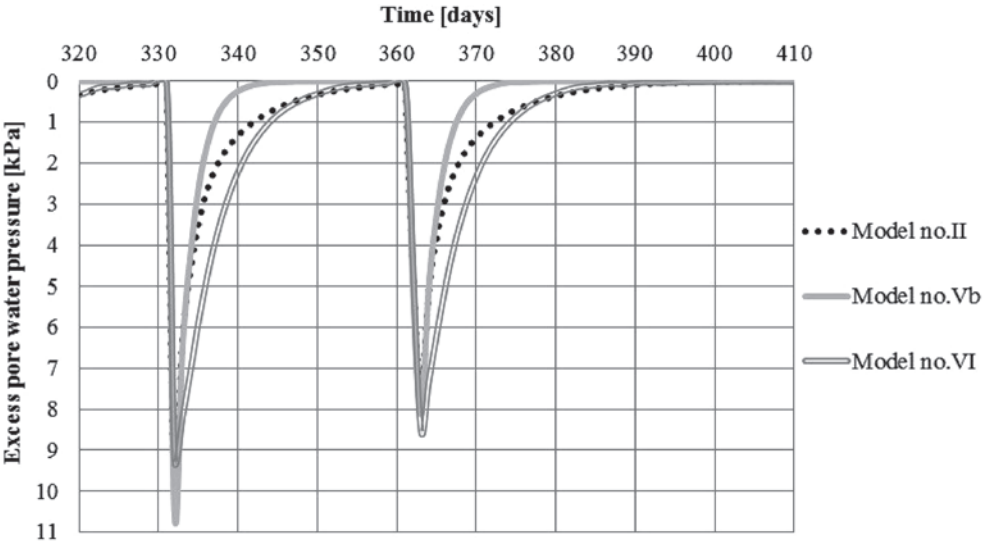

Fig. 17. Comparison of excess pore water pressure predicted by models No. II, Vb, VI in the last increment of loading

The discrepancy between results in the models with the averaged parameters and the 3D base model is the also largest for predictions of the consolidation time. Plane-strain models predict that the excess pore water pressure is dissipated almost immediately or on the contrary, the dissipation time is 60% longer (IVa) than for the 3D model. For 2D models with distinguished column strips characterized by averaged parameters and by the width the same as in case of the real column (Va and Vb), consolidation time is about 60% shorter.

The plane-strain models with the permeability coefficient in the horizontal plane converted from axisymmetric to plane-strain conditions by virtue of Eqn (13) [32] predict dissipation of pore water pressure in time in the way that is in the best agreement with the 3D consolidation results (Fig. 17). Although from the very close inspection of the diagram in Fig. 17 it follows that model No.VI overestimates the time of dissipation of excess pore water pressure by 60% with respect to the 3D model, it must be noted that the pore water pressure dissipation curve fits the best 3D results. At the end of the 3D consolidation model No. VI predicts only remaining 2% of the initial excess pore water pressure.

5. Summary

The paper has presented research on various attempts at calculating settlements and pore water pressure dissipation during construction of an embankment on soft soil reinforced with dynamic replacement stone columns. The authors sought a reliable plane-strain model which could be applied instead of a spatial analysis.

The results obtained by various simplified models were compared to the results obtained by the base 3D model marked as model No. II. The following computational attempts were checked.

Model No. I is an analytical method in which the stone column is considered only as a drain that accelerates the consolidation process. Priebe's analytical method for calculating settlement was used. Model No. III is an axisymmetric FEM model of a unit cell. Model No. IV is a plain-strain model where a zone of columns and soft soil under the embankment is homogenized. The average value of each parameter was determined using the replacement ratio α as weight coefficient. Model No. V is a plane-strain model with columns represented by strips of width equal to the actual column's diameter. Parameters for soft soil and stone column material remain unmodified in any way.

Models IVa and IVb are based on model IV but both employ the value of the friction angle for the homogenized zone calculated in a different way to that in model No. IV. Furthermore, these models assume anisotropic permeability of the homogenized zone. In model No. IVa the averaged coefficient of permeability in horizontal plane k_h was calculated by Eqn (9) whereas in model No. IVb the method for calculating k_h proposed in [25] was used.

In models Va and Vb, the diameters of stone columns were the same as in V but mechanical parameters for the columns were taken as average according to Dimaggio [6]. The permeability of column strip elements in model No. Va was modified according to Terzaghi's formulae to give coefficients of permeability in horizontal (k_h) and vertical (k_v) directions. In model No. Vb the permeability of the soft soil was modified according to the manner proposed in [15] and [32]. The coefficient of soil permeability in the horizontal direction in plane-strain conditions was calculated by matching the permeability in plane-strain and axisymmetric conditions. The coefficient of soil permeability in the vertical direction for soft soil remained unchanged.

In model No. VI the diameter of a stone column was reduced to obtain an equal replacement ratio in axisymmetric and plane-strain conditions. All mechanical parameters for soft soil and columns were not modified. Coefficients of permeability were assumed as in model No. Vb.

The computational analysis conducted showed that it is possible to obtain good agreement between results from a simplified plane-strain model and full 3D consolidation numerical analysis. This was achieved in model No. VI. The assumptions made in this model have been tested in the past but in combination with other geometrical and material configurations.

It has been found that to obtain satisfactory settlement the same replacement ratio must be preserved in the transition from spatial to plane-strain conditions. The permeability coefficient in the horizontal direction must be properly calculated since it has the essential influence on agreement between dissipation of pore water pressure in 3D and plane-strain conditions.

Although the mechanical parameters employed in the analysis were determined in laboratory and field tests for real soils the results obtained in the numerical calculations need to be verified by comparison with results of monitoring of the full scale embankment construction.

References

[1] Ambily A., Gandhi R., *Behavior of Stone Columns Based on Experimental and FEM Analysis*, Journal of Geotechnical and Geoenvironmental Engineering, 04, 2007, 405–415.

[2] Barron R., *Consolidation of fine-grained soils by drain wells*, Transactions ASCE, 113, 1948, 718–742.

[3] Castro J., Sagaseta C., *Consolidation around stone columns. Influence of column deformation*, International Journal for Numerical and Analytical Methods in Geomechanics, 33, 2009, 851–877.

[4] Castro J., Sagaseta C., *Deformation and consolidation around encased stone columns*, Geotextiles and Geomembranes, 29, 2011, 268–276.

[5] Castro J., Karstunen M., Sivasihamparam N., *Influence of stone column installation on settlement reduction*, Computers and Geotechnics, vol. 59, 2014, 87–97.

[6] Christoulas St., Giannaros Ch., Tsiambaos G., *Stabilization of embankment foundation by using stone columns*, Geotechnical and Geological Engineering, 15, 1997, 247–258.

[7] Dheeerendra Babu M.R., Nayak S., Shivashankar R., A *critical review of construction, analysis and behaviour of stone columns*, Geotech. Geol. Eng., 2013, 1–22.

[8] Dimaggio J.A., *Stone Columns: A Foundation Treatment*, Demonstration project No 46, FHWA, Washington DC, 1978, 1–69.

[9] Dz. U. 1999 nr 43 poz. 430. Rozporządzenie Ministra Transportu i Gospodarki Morskiej z dnia 2 marca 1999 r. w sprawie warunków technicznych, jakim powinny odpowiadać drogi publiczne i ich usytuowanie.

[10] Gryczmański M., *Metody analizy nośności i osiadania podłoża wzmocnionego kolumnami kamiennymi,* Inżynieria Morska i Geotechnika, vol. 5, 1993, 224–231.

[11] Hughes J. M. O., Withers N. J., *Reinforcing of soft cohesive soils with stone colum,*. Ground Engineering, vol. 7(3), 1974, 42–49.

[12] Han J., Ye, S., *Simplified method for consolidation rate of stone column reinforced foundations,* Journal of Geotechnical and Geoenvironmental Engineering ASCE, 127(7), 2001, 597–603.

[13] Hansbo S., *Consolidation of fine-grained soils by prefabricated drains*, Proc.10th Conf. Soil Mechanics and Foundations Engineering, vol. 3, Rotterdam, 1981, 677–682.

[14] Hassen G., de Buhan P., Abdelkrim M., *Finite element implementation of a homogenized constitutive law for stone column-reinforced foundation soils, with application to the design of structures*, Computers and Geotechnics, 37, 2010, 40–49.
[15] Indraratna B., Redana I., *Numerical modeling of vertical drains with smear and well resistance installed in soft Clay*, Canadian Geotechnical Journal, 37, 2000, 132–145.
[16] Indraratna B., Redana I., *Plane-strain modeling of smear effects associated with vertical drains*, Canadian Geotechnical Journal 123, 1997, 474–478.
[17] Indraratna B., Rujikiatkamjorn C., Wijeyakulasuriya V., Balasubramaniam A., *Soft clay foundation improvement with drainage and geo-inclusions, with special reference to the performace of enbankments and transportation system*, In Proc. of the Sri Lankan Geotech. Soc. First International Conference on Soil & Rock Engineering, Pinnaduwa H.S.W. Kulatilake Ed., Colombo, Sri Lanka, August 6–11, 2007. CD-ROM.
[18] Kwiecień S., *Analiza teoretyczna i doświadczalna wzmocnienia podłoża metodą wymiany dynamicznej*, Doctoral Thesis, Gliwice 2008.
[19] Kanty P., Kwiecień S., *Analiza porównawcza wyników obliczeń stateczności nasypu drogowego posadowionego na podłożu wzmocnionym metodą wbijanych kolumn kamiennych*, Technical Transactions, vol. 3-Ś/2012, 31–41.
[20] Kanty P., Sękowski J., *The influence of stone columns formation technique on the consolidation time of the surrounding soil*, 11th International Conference on New Trend in Static and Dynamic of Buildings, Bratysława, 3–4.10.2013.
[21] Kwiecień S., Sękowski J., *Kolumny kamienne formowane w technologii wymiany dynamicznej*, Monograph, WPŚ, Gliwice 2012.
[22] MenetreyPh., Willam K.J., A *triaxial failure criterion for concrete and its generalization*, ACI Journal, 92(3), 1995, 311–318.
[23] Machowski M., Kanty P., Kwiecień S., *Analiza porównawcza wyników osiadań podłoża wzmocnionego metodą wymiany dynamicznej pod nasypem drogowym*, Technical Transactions, vol. 3-Ś/2012, 67–78.
[24] McCabe B.A., McNeil J.A., Black J.A., *Ground improvement using the vibro-stone column technique,* Joint meeting of Engineers Ireland West Region and the Geotechnical Society of Ireland, NUI Galway, 15.03.2007, 1–12.
[25] Oo K., *Numerical study of floating stone columns. National University of Singapore*, Doctoral Thesis, 2013.
[26] Priebe H., *Abschatzung des Setzungsverhaltes eines durch Stopfveriichtung verbesserten Baugrundes*, Die Bautechnik, vol. 53(5),1976.
[27] Sękowski J., Cierpioł D., *Grunty spoiste stabilizowane wapnem. Zastosowanie do budowy wysokich nasypów autostradowych*, Autostrady Magazine, 5, 2010, 44–46.
[28] Sękowski J. Grzesik B., *Konsolidacja podłożą wzmocnionego wbijanymi kolumnami kamiennymi – badania laboratoryjne,* Roczniki Inżynierii Budowlanej, 8, 2008, 67–70.
[29] Sękowski J., Grzesik B., *Wpływ wbijanych kolumn kamiennych na wilgotność wzmocnionego podłoża,* Problemy geotechniczne i środowiskowe z uwzględnieniem podłoży ekspansywnych, Bydgoszcz 2009, 201–207.
[30] Sękowski J., Kwiecień S., Kanty P., *The influence of rammed stone column formation process on mechanical parameters of the surrounding weak soil,* XV Danube – European Conference on Geotechnical Engineering, Paper No. 226, Vienna, 09–11.09.2014, 353–358.

[31] Tan S., Oo K., *Stone column FEM modeling – 2D and 3D considerations illustrated by case history*, Int. Symp. On Tsunami Reconstruction with Geosynthetics, Bankok Thailand, 2005, 157–169.
[32] Tan S., Tjahyono S., Oo K., *Simplified Plane – Strain Modeling of Stone –Column Reinforced Ground*, Journal of Geotechnical and Geoenvironmental Engineering, 02, 2008.
[33] Terzaghi K., *Theoretical Soil Mechanics*, John Wiley & Sons, New York-London, 1943.
[34] Van Genuchten M. T. *A., Closed-form equation for predicting the hydraulic conductivity of unsaturated soils*, Soil Sci. Soc. Amer. J., 44, 1980, 892–898.
[35] Wiłun Z., *Zarys Geotechniki*. WKiŁ, ed. IV, Warsaw 2003.
[36] Zimmermann Th., Truty A., Urbański A., Podleś K., *Manual* Z_Soil 2010.

TECHNICAL TRANSACTIONS | CZASOPISMO TECHNICZNE
ENVIRONMENTAL ENGINEERING | ŚRODOWISKO
2-Ś/2015

BERNADETTA PASIERB*

NUMERICAL EVALUATION OF 2D ELECTRICAL RESISTIVITY TOMOGRAPHY FOR SUBSOIL INVESTIGATIONS

METODY NUMERYCZNE 2D TOMOGRAFII ELEKTROOPOROWEJ STOSOWANEJ W BADANIACH PODŁOŻA GRUNTOWEGO

Abstract

The use of numerical methods for the design and analysis of hydraulic engineering structures requires an accurate determination of the model of subsoil structure. The article presents one of the geophysical methods – electrical resistivity tomography (ERT), which allows for precise, spatially instant recognition of the substrate and the phenomena occurring within it. The methodology, the applied algorithm for numerical calculation, and data processing procedure are discussed. This article also introduces a method of inversion which relies on finding the actual model and presents examples of its application.

Keywords: Electrical Resistivity Tomography ERT, 2D inversion, investigations of subsoil

Streszczenie

Zastosowanie metod numerycznych do projektowania oraz analizy konstrukcji hydrotechnicznych wymaga określenia modelu budowy podłoża. W artykule zaprezentowano metodę tomografii elektrooporowej ERT stosowaną dzięki ciągłemu, przestrzennemu rozpoznaniu podłoża i zjawisk w nim zachodzących, m.in.: w geotechnice, hydrotechnice, a także w zagadnieniach obejmujących projektowanie konstrukcji inżynierskich. Przedstawiono metodologię, stosowane algorytmy do obliczeń numerycznych oraz procedury przetwarzania danych. Przybliżono metodę inwersji polegającą na znalezieniu modelu rzeczywistego ośrodka oraz zaprezentowano przykłady jej stosowania.

Słowa kluczowe: metoda tomografii elektrooporowej ERT, 2D inwersja, badania podłoża

DOI: 10.4467/2353737XCT.15.230.4616

* PhD. Bernadetta Pasierb, Institute of Geotechnics, Faculty of Environmental Engineering, Cracow University of Technology.

1. Introduction

Geophysical methods enable the identification of a surface zone vulnerable to changes caused by human activity and also by nature. They use the rules and the laws of physics, and the basis for their use is to differentiate the physical properties of the medium. These methods can be used comprehensively in solving diverse thematic issues: the recognition of geological and engineering subsurface, environmental monitoring, and detection of anthropogenic objects. From the whole range of engineering geophysics methods, taking into account the accuracy and the ability to use a variety of field conditions, the electrical resistivity tomography method (ERT) is the most versatile as well as the method of ground penetrating radar (GPR) and multichannel analysis of surface waves (MASW). These methods are primarily used to solve geotechnical issues. The article presents the method of electrical resistivity tomography and shows some examples of research with its use.

2. Research methodology

The basis for the application of geophysical methods are the differences in the physical properties of the medium (e.g. electrical resistance, magnetic permeability, density, dielectric constant, etc.), and the dependence of the properties on the medium structure.

The method of electrical resistivity tomography (ERT) belongs to a group of geophysical methods which offers non-invasive investigation of subsoil. Assumption methods were developed in the early twentieth century by the Schlumberger brothers. The ERT method is based on the study of changes in the electric field generated by a system of electrodes which are DC powered. The apparent resistivity of rocks, representing the result of the entire heterogeneous, complex anisotropic layers, is determined in accordance with Ohm's law (1) by measuring the intensity and the voltage between the measuring (potential) electrodes [1].

$$\rho_a = k \frac{\Delta V}{I} \tag{1}$$

where:

ρ_a – apparent resistivity [Ωm],
ΔV – measured voltage [mV],
I – current emitted into the subsoil [mA],
k – geometrical factor depending on the individual distance between the electrodes.

Various types of electrode combinations can be used, such as Wenner, Schlumberger, or Dipole-Dipole arrays, differing among others, in: (i) degrees of profile coverage, (ii) penetration depth and (iii) sensitivity to vertical and horizontal changes in resistance. Each type of electrode configuration has its advantages and limitations.

Geophysical measurements using resistivity methods can be performed by traditional Vertical Electrical Sounding (VES) and Electrical Profiling (EP) techniques. Vertical electrical sounding enables tracing of changes in electrical resistivity with the increasing depth of penetration on middle-point of the measuring system, as a result of increasing the

spacing of current electrodes (Fig. 1). Electrical profiling consists of a predetermined series of measurements taken along a line measuring system with a specific profile sampling step, with a constant distance between the electrodes. The information received from the electrical sounding and profiling are one-dimensional, which means that the electrical resistivity changes are determined either vertically (in the case of sounding probes) or horizontally (for resistivity profiling) [2, 3]. The penetration-range of these methods is determined as approximately one third the spacing of current electrodes.

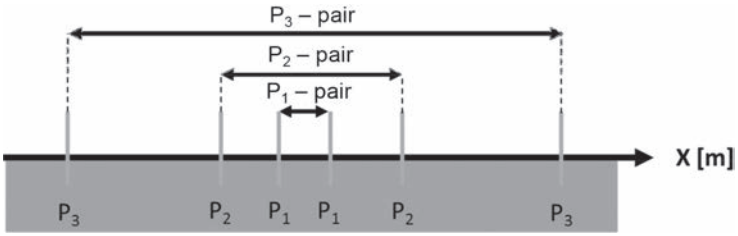

Fig. 1. Vertical Electrical Sounding [after: 4, revised]

The ERT method is a combination of both of these measurement techniques. Measurements are performed along the profile, following a sequence, which is run by a switching unit and controlled by a computer (usually integrated within a resistivity measurement apparatus) – based on the automatic selection of electrodes within the defined system, i.e. electrode array (e.g. Schlumberger array). The electrodes are selected from all those connected to the cable until all the programmed combinations are completed (Fig. 2). The number of recordable measurements can be as many as several thousand. The maximum distance between the measuring system depends on the length of the profile and translates into the depth range of the research, which is $^{1}/_{3} - {}^{1}/_{6}$ the distance between the extreme electrodes [5].

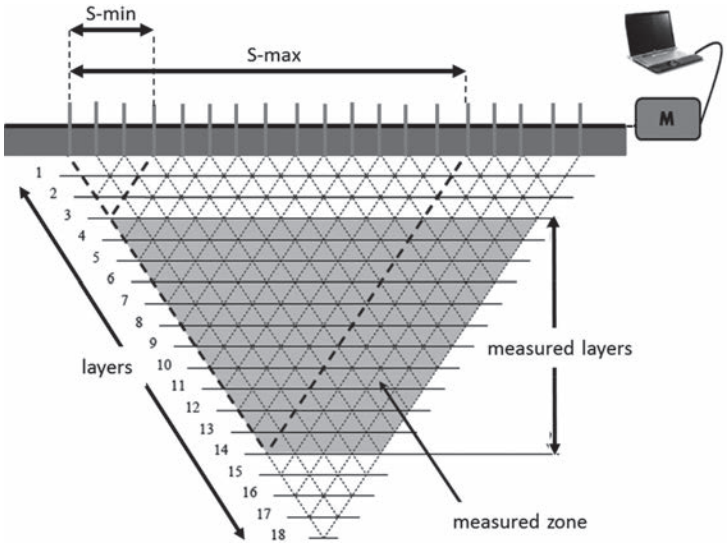

Fig. 2. Representation of the measure zone [after: 4, revised]

The measurement results are presented in the form of cross-sections showing the distribution of apparent resistivity on 2D imaging in an x-z plane: x – along the profile and z – depth. The distribution of resistivity describes by the medium bound by the surface above and by the depth of penetration bottom. The trapezoidal cross-sectional shape is the result of decreasing number of measurements with increasing distance between current electrodes.

3. Data processing and inversion introduction

The procedure for data processing and interpretation are performed using the inversion method. The main objective of the inversion is to find the actual model whose parameters are suitable for the measurement data. The first stage solves a *direct problem* that allows determination of the theoretical parameters for the assumed model of the medium. In the case of electrical sounding, a 1D model is established, which is a flat-parallel layers system, where the change of the resistivity is established in only one vertical direction (Fig. 6a). The ERT method assumes a 2D model of the medium, which allows for variability of parameters in both directions vertical and horizontal (Fig. 6b). When creating the model, external conditions are introduced, known as a *priori* information. The two-dimensional model uses discretization of the subsurface into a number of blocks using a rectangular mesh with 2 or 4 nodes per node spacing – distance between adjacent electrodes [5]. The 2D model takes into account the variability of the parameters in the vertical plane cross-section, while along the perpendicular direction the parameters are fixed, within each of the blocks. The two-dimensional model allows the imaging of more complex structures and phenomena of limited spatial extent, which are impossible with the described traditional methods using flat-parallel models.

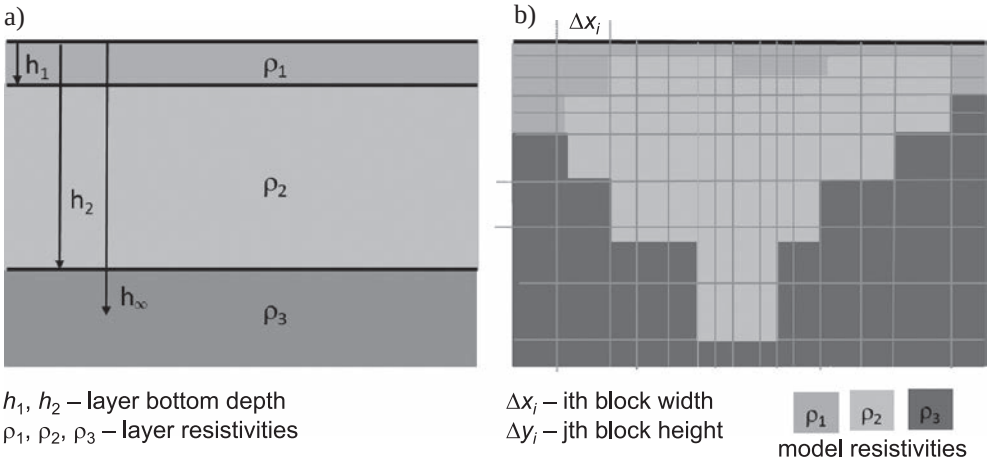

Fig. 3. a) The model of layers based on 1D measurement used by VES method; b) The 2D block model of the subsurface used by ERT method [after: 3, revised]

The solution of a *direct problem* 2D, for such assumed medium geometry relies on solving the equation of the distribution of electrical conductivity as a function of the length profile – x and the depth – z, which is described be the Poisson equation [6–8]:

$$\frac{\partial}{\partial x}\left(\sigma\frac{\partial V}{\partial x}\right)+\frac{\partial}{\partial z}\left(\sigma\frac{\partial V}{\partial z}\right)-k_l^2\sigma V=-\frac{I}{2}\delta(x)\delta(z) \tag{2}$$

where:
σ – electrical conductivity [S/m],
V – electrical potential [V],
I – current [A],
k_l – wave number,
δ – Dirac delta.

The differential equation (2) is solved using numerical methods: the finite difference method or the finite element method. The finite difference method is faster and easier, but it offers results in low accuracy solutions. There are problems associated with matching mesh to the surface, as well as difficulties with the boundary conditions. Finite difference method does not give as good results for a large denivelation area [5]. In such cases, if the data set contains topography, the default choice is the finite element method. Additionally, topographical reduction is introduced, which takes into account the morphology of the surface.

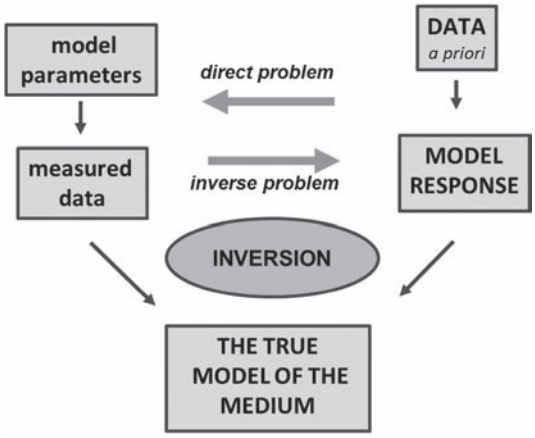

Fig. 4. Schematic diagram of a *direct* and *inverse problem*

The determined elements of the model are then used to calculate the *inversion*. The objective of the inverse problem is the iterative minimization of error fit of parameters using a theoretical model with measurement parameters (optimization of processing parameters to minimize the error). A schematic diagram of the *direct* and *inverse problems* is shown in Fig. 4. To eliminate the ambiguity of the solution of the inverse problem, it is necessary to impose boundary conditions that control the changes of the model – because there are many possible models of resistivity medium having the same solution. One of them is the smoothness condition – using the method of *smoothness inversion* in the 2D inversion, and

creating a model of gentle, gradual changes in parameter values. The smoothness inversion method is based on the modified Gauss-Newton and Marquardt-Levenberg algorithms used to solve the inverse problem. The Gauss-Newton method (linear least-squares method) is to minimize the sum of squared differences between the theoretical values, resulting from the model and the observed values. It is the simplest solution of the 1D inversion giving satisfactory results for structures with little sophistication, in the absence of disturbing bodies. Adding the *Lagrange multiplier* λ_L, (also called the *damping factor* or *factor Marquardt*), which attenuates the magnitude (size) changes in the model parameters related to noise and interference measurements, the Gauss-Newton algorithm converts to the Levenberg-Marquardt algorithm. Whereas, if introducing the smoothing matrix *C* (so-called flatness filter) to the Levenberg-Marquardt algorithm, it leads to a smoothing of the assumed model and impose a smoothness condition directly on the model parameters. The resulting algorithm used for the smoothness inversion method has the form [5, 9, 10]:

$$\Delta q = \left(J_i^T J_i + \lambda_L C \right)^{-1} J_i^T g_i - \lambda_L C r \tag{3}$$

where:

Δq – model perturbation vector (vector correction),
J – Jacobian matrix of partial derivatives,
J^T – transposed Jacobian matrix,
$J^T J$ – matrix mathematical model,
i – index indicates the i-th iteration,
λ_L – Lagrange multiplier – damping factor,
C – smoothing matrix – flatness filter,
$g = (g_1, g_2, g_3, \ldots\ldots, g_N)^T$ – discrepancy vector representative of the differences between the measured and calculated apparent resistivity values,
r – vector containing the logarithm of the model resistivity values.

One advantage of this method is that the damping factor and flatness filters can be adjusted to suit different types of data. The objective of minimizing the difference between the parameters of the theoretical model and the measured data uses the *conventional Gauss-Newton method*, when the Jacobian matrix of partial derivatives *J* is recalculated after every iteration. It is much slower than the *quasi-Newton method*, but in areas with large resistivity contrasts of greater than 10:1, it gives better results. If there are too many data sets and less memory capability – a low power computer – it is desirable to shorten the inversion process e.g., by using a quasi-Newton method. In this option the Jacobian *J* is calculated only for the first iteration and then approximated. This technique can be more than 10 times faster than the conventional least-square method. A third option is to use the *combined method*, where the matrix *J* is recalculated for the first two or three iterations, after which the quasi-Newton method is used [5, 9]. In many cases, this provides the best compromise. After each iterating process, the damping factor is reduced and optimized so as to reduce the number of iterations. It requires converging by finding the optimum damping factor that gives the least RMS error [11]. To sharpen the boundary between structures, select abrupt changes in values to apply the *robust inversion*. The robust inversion algorithm is described by the formula [8, 12]:

$$\Delta q = \left(J_i^T R_d J_i + \lambda_{Li} W^T R_q W \right)^{-1} J_i^T R_d g_i - \lambda_{Li} W^T R_q W q_{i-1} \tag{4}$$

where:
Δq – model perturbation vector (vector correction)
W – weighting matrix of the inverse of the measurement errors on the diagonal
R_d – diagonal matrix with odds ratios coordinate vectors g and d on the diagonal
R_q – diagonal matrix with odds ratios coordinate vectors g and q on the diagonal
R_d = diag $\{g_1/d_1, g_2/d_2, \ldots\ldots\ldots g_N/d_N\}$, R_q = diag $\{g_1/q_1, g_2/q_2, \ldots\ldots\ldots g_N/q_N\}$

The robust constraint is less sensitive to very noisy data points, but might give a higher apparent resistivity RMS error [5]. Assuming the *robust inversion* options, the inversion process tends to create models of areas consisting of a fixed resistivity value. The block structures formed then show the geological structure with clearly sharp boundaries. The 2D inversion process ends when successive iterations no longer cause significant changes to the final model, or the RMS errors achieved is satisfactory. The inversion method is used in two- or three-dimensional resistivity inversion, and it is used in the program interpretation Res2dinv or Res3dinv.

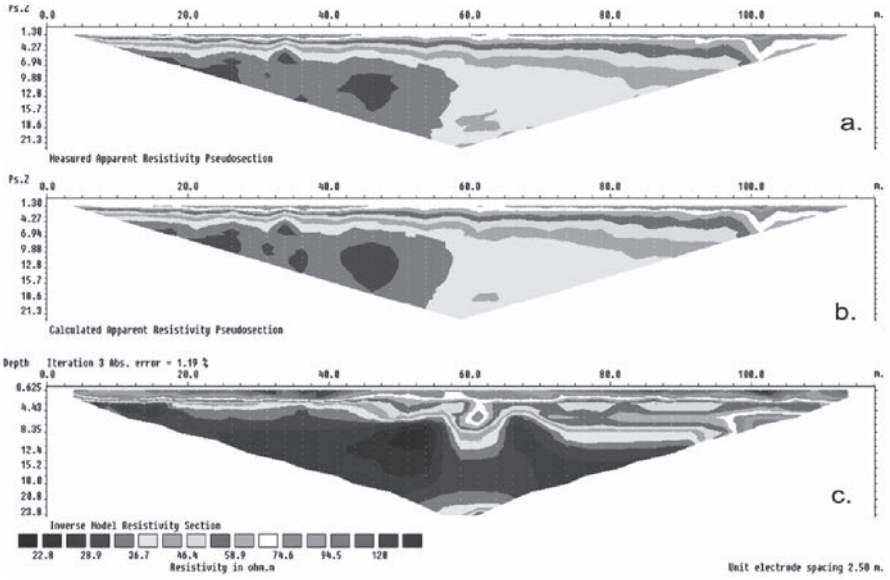

Fig. 5. Screenshot of the program Res2Dinv showing ERT inversion method: a – cross-section of apparent resistivity measured, b – cross-section of apparent resistivity calculated on the basis of the model, c – actual model of resistivity obtained by the inversion

The resulting two-dimensional distribution of the electrical resistivity of the subsoils is as close as possible to the actual distribution of resistivity along the test profile. Further interpretation is based on the description obtained from the inverse geoelectrical model and referencing it to the subsurface conditions – the geological structure. Fig. 5 shows the steps of creating an actual model of resistivity, starting from measured apparent resistivity pseudosection, through the calculated apparent resistivity pseudosection to the inverse model resistivity section. We can compare the observed apparent resistivity pseudosection with an inversion model.

4. The possibilities of applications

The ERT method is one of the most popular geophysical methods. It is used in geological mapping (i) to identify geological structure, (ii) to determine depth and thickness of the layers. In hydrogeological studies, ERT measurements are recommended for the detection of aquifers and spread-range of mineralized water in the subsurface. Within geotechnical and hydrotechnical engineering studies, ERT serves to determine the state of earth structures, especially locations of zones of loosening and relaxation, determination of weakness of the subsoil and the locations of sinkholes and voids. In environmental studies the ERT method is very effective in the location of pollution sources and mapping the aureole around potential sources of contamination resulting from landfill, waste water treatment, fuel tanks, and soil contamination by heavy metals. The ERT method can be led by monitoring pollution migration changes. It also plays a significant role in the detection of underground anthropogenic objects and planning of archaeological research by the location and identification of underground architectural remains [13].

5. Examples of application of the ERT method

The ERT method was used as a method enabling identification of the geological structure of the subsoil. It has been also used to detect underground anthropogenic objects and geotechnical structures. The ARES equipment from GF Instruments manufacturer was applied. The procedure and interpretation of the data was performed using Geotomo RES2DINV Software [5].

5.1. Application of ERT in geological structure research and anthropogenic objects identification

The ERT method recognized a landslide zone structure on the railway line Krakow–Warsaw, in Sadowie village, which runs in an artificial dig [14]. Landslide movements of the adjacent slopes have been recorded there for many years (1934–2011). After heavy rainfall in 2010–2011, the reactivation of landslide movement and soil displacement occurred, causing the track to be pushed out almost 1 m at a height. The landslide niche has moved beyond the edge of the slope, destroying the road running nearby and came to the borders of the residential area. Three parallel profiles with a length of 150–180 m were taken along the landslide. A Schlumberger array was used for the electrode spacing of 5 m. In the realized 2D inversion process, the robust model inversion constraint was used for the results of measurements carried out on the slopes. As a result of research and available data, it was found that the Quaternary sediments consist of loess (silty clay, silt) layers of thickness – of 3–4 m. Below them, there are Miocene clays with a thickness of about 30 m. Marls form the oldest bedrock in the area. The dominant feature of both Quaternary and Miocene clays in their part of the top section is their high humidity. Increased infiltration of rainwater (surface) through a layer of silt and silty loam to the series causes high saturation with water. Major changes of saturation between subsurface zones and the top of clays cause significant response of the physical properties of the grounds, which marks a significant decrease in resistivity,

clearly visible in the cross-sections. That is why the localized boundary between Quaternary formations and Miocene clays should be treated not as a potential slip surface for periodically occurring mass movements, but only as the zone of soil displacements, even a few metres thick. Near the railway embankment, a zone of strong saturation, which has a low resistivity, was also interpreted. Replaced in this part of the soils marks already high values of resistivity. Occurrences of carbonate rocks are visible in the subsurface zone with much higher values, sometimes up to resistivity of 400 Ωm. They can significantly affect the direction of water run and infiltration. Permanent ground vibrations, caused by passing trains, are also conducive to the formation of the landslide. The results also showed construction elements such as piles in the subsurface, which are designed to protect and strengthen the slope.

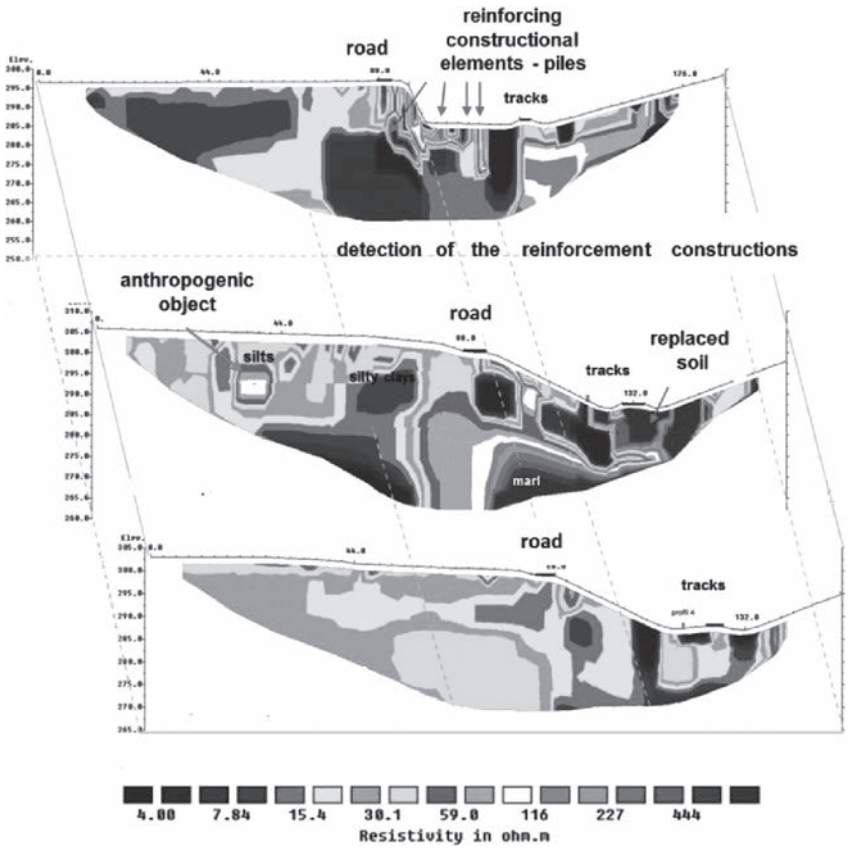

Fig. 6. ERT cross-section in Sadowie landslide area

5.2. The ERT in non-invasive river dike judgement

In the frame of protection against floods the river embankments' quality and stability were monitored, using the electrical resistivity tomography method. The reconnaissance studies were carried out in the area of Nowa Huta in order to evaluate the state of a fragment

of the flood embankment of the Vistula River [15]. The aim of the study was to indicate: (i) loosened and weakened areas in the body of the river dike, and (ii) location of the place where penetration of water occurs. The ERT profile was 117.5 m in length and was performed along the crown of an embankment through the geotechnical hole, which allowed the correlation of geophysical results with the hole-data. Measurements were performed with the dipole-dipole array, with electrode spacing of 2.5 m. The default and *robust inversion* options were used. The ERT cross-section obtained for *robust inversion* was more clearly and sharper than for default inversion. The flood embankment was about 4 metres high and was made of a mixture of uncontrolled soils. Silt, silty sands, sand and loamy sands as well as clays, sandy clays and compact clays, basement fine sands and medium sand were found. The water table level is about 1.4 m below the surface.

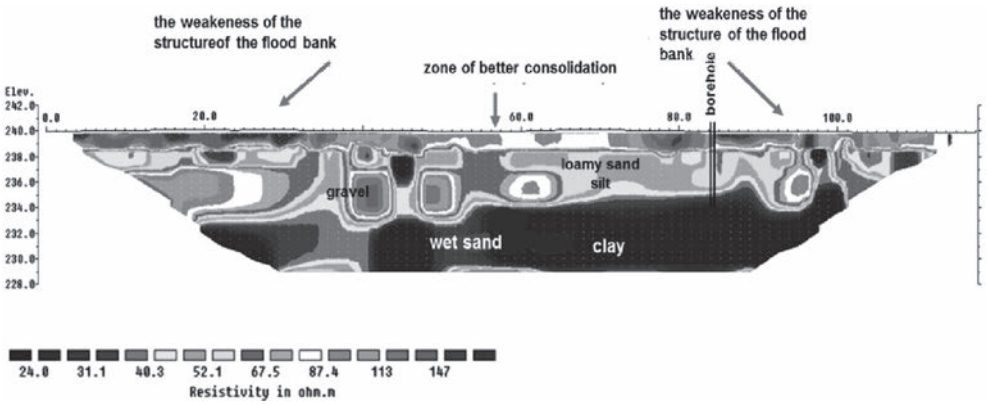

Fig. 7. Resistivity section along the crown of the flood embankment

Analysing the results of the cross-section (Fig. 7) we can distinguish three main anomalous zones: first at depth of about 1.5 m – zone with high resistivity 100–150 Ωm, which is strongly weathered and composed of loosened silty sands. Soils with better consolidation and reduced resistivity values (about 80–90 Ωm) occur in this zone between 45–75 m at the crown of flood embankment. In the second zone at the depth of 1.5 – 5m, there are soils with variable resistivity values, between 50–150 Ωm. One can isolate areas of more or less consolidation indicating the inhomogeneous structure of river dike. The low resistivity zone of 5 m depth, represents a third zone – a zone of flood embankment base – where the soils represents typical river terrace deposits: clay and silt, and watered sand with other blended gravel. At high water level, the zone of elevated resistivity values can cause water leakage and infiltration.

6. Conclusions

Geophysical surveys play an increasing role in the geotechnical recognition of subsoils. A meaningful advantage is their non-destructive and non-invasive character and obtaining continuous information from the medium. Electrical resistivity investigations have a wide

range of applications, and they are used to recognize geological structure and to identify occurring engineering geological phenomena. They also serve to determine the aquifers and range of their extent. In environmental studies they are used for ground water protection, especially to determine the sources of contamination and their migration. They are also used to detect underground anthropogenic objects. From the point of view of the geotechnics, they may be useful for monitoring of the processes taking place in the subsoils: landslide risk assessment, mapping of slope deformations, slope stability monitoring, and river dike quality and stability investigation. They are applied to define and indicate vulnerable zones susceptible to weakness, damage and suffosion. As shown by the provided examples, they are also used to predict or determine places in order to implement geotechnical control.

The technical or methodological development in recent years – measuring equipment and the use of more advanced measurement techniques – has resulted in the use of more sophisticated algorithms and improved data processing procedures (e.g. *smoothness inversion*, *robust inversion*) using numerical methods. These make it possible to create more accurate models taking into account the medium's shape and dimensions and its spatial distribution. As shown in the article we are able to present research results in the form of 2D images by applying the electrical resistivity tomography method. The method is also much more precise than the traditional soundings and profiling techniques. An additional advantage is the speed of the obtained results. The use of the procedure interpretation enables the results to be obtained practically already on site. The wide range of applications, flexibility and efficiency bring additional benefits. The low costs of investigations relative to other methods undoubtedly increase its advantages.

References

[1] Kozera A., *Geofizyka Poszukiwawcza*, Wydawnictwo Geologiczne, Warszawa 1987.

[2] Pasierb B., *Techniki pomiarowe metody elektrooporowej*, Czasopismo Techniczne, z. 2-Ś/2012.

[3] Rudzki M., Krawiec A., *Ocena zanieczyszczenia wód podziemnych z wykorzystaniem metody tomografii elektrooporowej*, Współczesne problemy hydrogeologii, tom XIII cz. 2, Wydanie AGH, Kraków 2007.

[4] GF Instruments, s.r.o. *Geophysical Equipment and Service – ARES – Short guide for resistivity imaging, User manual* v 5.46, Copyright 2010.

[5] Loke M. H., *Tutorial: 2-D and 3-D electrical imaging surveys*, Copyright 2004.

[6] Oldenburg i Li., *Inversion of induced polarization data*, Geophysics 59 (9), 1994, 1327–1341.

[7] Binley A., Kemna A., *DC resistivity and induced polarization methods*, Hydrogeophysics, vol. 50, 2005, 129–156.

[8] Żogała B., *Metody geoelektryczne w badaniach gruntów skażonych substancjami ropopochodnymi*, Wydawnictwo Uniwersytetu Śląskiego, Katowice 2013.

[9] Loke M.H., Dahlin T., A *comparison of the Gauss-Newton and quasi-Newton methods in resistivity imaging inversion*, Journal of Applied Geophysics 49, 2002, 149–162.

[10] Marquardt D.W., *Generalized inverse, ridge regression, biased linear estimation and nonlinear regression*, Technometrics 12, 1970, 591-613.

[11] Aizebeokhai A.P., Olayinka A. I., Singh V. S., *Application of 2D and 3D geoelectrical resistivity imaging for engineering site investigation in a crystalline basement terrain, southwestern Nigeria*, Environ Earth Sci, 2010, DOI 10.1007/s12665-010-0464-z.

[12] Farquharson C.G., Oldenburg D.W., *Non-linear inversion using general measures of data misfit and model structure*, Geophysical Journal International 134,1998, 213–227.

[13] Pasierb B., *Metoda tomografii elektrooporowej w rozpoznaniu geologicznym podłoża i obiektów antropogenicznych*, Czasopismo Techniczne, z. 2-Ś/2012.

[14] Pasierb B., Chrzanowska etc., *Zastosowanie metody obrazowania elektrooporowego w rozpoznaniu osuwiska skarpy przekopu na linii kolejowej Kraków-Warszawa w miejscowości Sadowie"* w ramach *„Usuwanie skutków powodzi z 2010 na trasie lini kolejowej nr 8 Warszawa Zachodnia–Kraków Główny w zakresie wykonania zabezpieczenia skarpy przekroju w km: 299, 650-299, 800 na odcinku Niedźwiedź–Zastów*, prace PK nr umowy Ś-2/466/11, Kraków 2011.

[15] Pasierb B., etc., *Techniczna analiza przydatności nieinwazyjnej metody kontroli wałów przeciwpowodziowych pn. „Nieinwazyjna metoda badań obwałowań*, opracowanie pod kierunkiem Łój M., Prace AGH, nr 1/2013.

TECHNICAL TRANSACTIONS | CZASOPISMO TECHNICZNE
ENVIRONMENTAL ENGINEERING | ŚRODOWISKO
2-Ś/2015

PAWEŁ POPIELSKI*, JANINA ZACZEK-PEPLINSKA**, EWA BARTNIK***,
ADAM KASPRZAK**, BŁAŻEJ SMOLIŃSKI**

CONTEMPORARY TECHNIQUES OF DATA ACQUISITION FOR PREPARATION OF NUMERICAL MODELS OF HYDROTECHNICAL STRUCTURES

NOWOCZESNE TECHNOLOGIE POZYSKIWANIA DANYCH DO PRZYGOTOWANIA MODELI NUMERYCZNYCH BETONOWYCH OBIEKTÓW HYDROTECHNICZNYCH

Abstract

This paper presents an analysis of possible uses of contemporary data acquiring methods for elaborating hydrotechnical object numerical models. The subject is considered in two aspects – preparation of a geometrical model based on the results of a geodetic survey of the structure as well as subsoil parameters, and data acquisition for building material characteristics. The results presented for non-invasive measurements of hydrotechnical concrete parameters and geometry of the modelled object are based on the example of Rożnów Dam. The research uses data obtained by terrestrial laser scan and sclerometer tests (taken with a Schmidt hammer).

Keywords: numerical modelling, geodetic survey, laser scanning, sclerometer measurements

Streszczenie

W artykule przedstawiono analizę możliwości wykorzystania współczesnych metod pozyskiwania danych do przygotowania modeli numerycznych obiektów hydrotechnicznych. Zagadnienie rozpatrzono w dwóch aspektach – przygotowanie modelu geometrycznego na podstawie wyników inwentaryzacji geodezyjnej konstrukcji oraz pozyskanie danych o parametrach podłoża i właściwościach materiałów budowlanych. Zaprezentowano wyniki nieinwazyjnych pomiarów parametrów betonów hydrotechnicznych i geometrii modelowanego obiektu na przykładzie zapory Rożnów. Wykorzystano m.in. dane pozyskane za pomocą naziemnego skaningu laserowego oraz dane z pomiarów sklerometrycznych (młotek Schmidta).

Słowa kluczowe: modelowanie numeryczne, pomiary geodezyjne, skaning laserowy, pomiary sklerometryczne

DOI: 10.4467/2353737XCT.15.231.4617

* DSc. PhD. Paweł Popielski, Department Hydro-Enginering and Hydraulics, Faculty of Environmental Engineering, Warsaw University of Technology.

** PhD. Janina Zaczek-Peplinska, Chair of Geodesy Engineering and Control-Measuring Systems, Faculty of Geodesy and Cartography, Warsaw University of Technology.

*** Eng. Ewa Bartnik, MSc. Eng. Adam Kasprzak, Eng. Błażej Smoliński, Faculty of Environmental Engineering, Warsaw University of Technology.

1. Introduction

Hydrotechnical objects such as concrete dams are considered to be one of the largest man-made structures. Due to their massive, complicated shapes, long exploitation periods and static and dynamic loads, they are equipped with a number of control and measurement devices. Their condition must be frequently checked and assessed, as in reality failure is often followed by catastrophe and flood downstream. The Problem of dam monitoring relates to the constant observation of dislocations and filtration occurring within the object.

Any phenomenon occurring as a result of hydrotechnical object operation can be researched empirically by observations and sample gathering as well as by using verified numerical models based on researched object surveys. The method adopted for calculations should model, to the necessary extent, the actual processes influencing the final results in a significant way. It should also allow for the use of current knowledge as far as the processes of change in material parameters are concerned. The possibility of modelling various object realisation variants taking into consideration the key determinants for the course of the process factors analysed (generating initial tensions, modelling of phased structure erection, ground water level changes and consequent load changes) is essential [4].

Numerical models allow for the estimation of forces and dislocations within a substructure and within a constructed or operating object. Depending on the object's geometry, variability in natural conditions and expected accuracy numerical simulation can be realized using a 2D or 3D model. An analysis of the interaction between the structure and the substructure should make up a process accompanying the whole investment cycle and further exploitation of the object.

In order to produce a numerical model, current values of material parameters and verified object geometry are essential. While establishing the values of parameters, new bore samples can be obtained, but the cost is high and the process contributes to gradual degradation of the object. An alternative to these problematic methods is offered by non-destructive examination methods such as sclerometry and ultrasound surveys, verified by limited destructive probing tests. The accuracy of results depends on the calculation parameters adopted for the analysis. The correct definition of these parameter values is fundamental for correct numerical modelling.

2. Research subject

The hydrotechnical object which serves as an example for this research is the gravity dam in Rożnów, constructed on 80+000 km of the Dunajec River in Rożnów village, Gródek n/Dunajcem commune, Nowy Sącz County, Lesser Poland province. According to [8], the Rożnów Dam is an object of 1st class importance.

This dam (Fig. 1) is one of the oldest objects of its type in Poland. It was erected between 1935–1941 and remains operational. The reason behind the object's construction was the need to prevent frequent floods occurring in the surrounding areas. The dam is 49 m high and 550 m long, with a 9 m wide crest. The object was fitted with 7 overspill sections with segment locks and 5 bottom outlets located in the western part of the dam. There is a power plant complex located in the middle of the dam, with 4 Kaplan turbines installed. The combined power output of the generators is 56 MW at 29 m head.

Fig. 1. Rożnów Dam [source: author's own]

3. Establishing object geometry using laser scanning

Terrestrial laser scanning is a relatively new measuring technique situated on the border between classical geodesic surveys, photogrammetry, and computer science.

The scanner operates by emitting a laser beam towards all the objects within the field of view. The scanner uses a mechanism dispersing a laser beam in two directions (vertical and horizontal). The reflected beam returns to the scanner, providing information on the location of the scanned points. The following data is obtained as a result of scanning:

– points collection (cloud) with defined XYZ coordinates,
– intensity of beam reflection from scanned surfaces (additional information),

Scanners can be divided depending on the type of electromagnetic wave emitted. There are two types of instruments: pulse based and phase based scanners. The terrestrial laser scanning survey was conducted by the Geodesy and Cartography Students Society "Geoida" of the Warsaw University of Technology. The surveys conducted [6] [7] were performed using a Riegl VZ-400 laser scanner which is a pulse based scanner using an infrared laser beam. The scanner mechanism is based on a rapidly rotating multi-faced mirror, emitting parallel beams. The frequency of pulses, which is up to 200 kHz, allows 100 scans per second to be taken. The range of the laser is up to 600 m and the accuracy of single point measurement, as per manufacturer's specification, is 3mm. The field of view is 360˚ in the horizontal plane and 100˚ in the vertical plane. As a result of the scanning conducted point clouds were acquired, which were the subject of further processing including: registration, geo-referencing and "combining" in Ascan software made by the Polish manufacturer AstraGIS [7]. The results obtained are presented in Fig. 2.

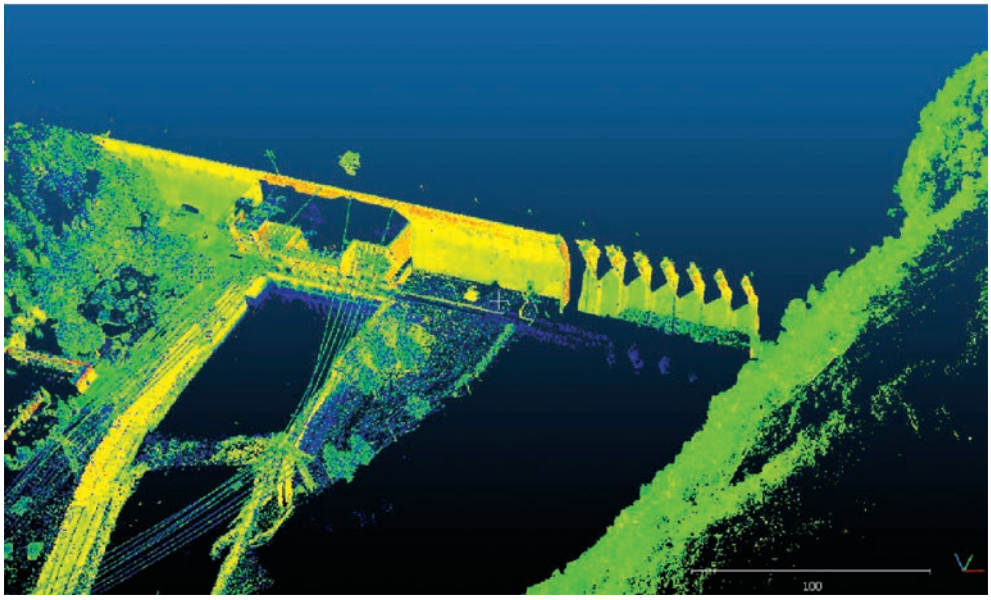

Fig. 2. Scan of Rożnów Dam – point cloud coloured accordingly to the registered intensity values

4. Establishing concrete parameters

4.1. Ultrasound method

Ultrasounds are mechanical oscillations of medium (pressure waves) of frequency at least 20 000 Hz. This frequency is greater than the upper limit of the human hearing range. For concrete constructions, testing waves of frequency between 30 000 Hz and 500 000 Hz are commonly used. Frequency affects the accuracy of measurements. The range of frequencies used for testing allow for higher resolution of the method, but also shortens the effective testing range. A specialist ultrasonic concrete tester is used for testing. The device measures

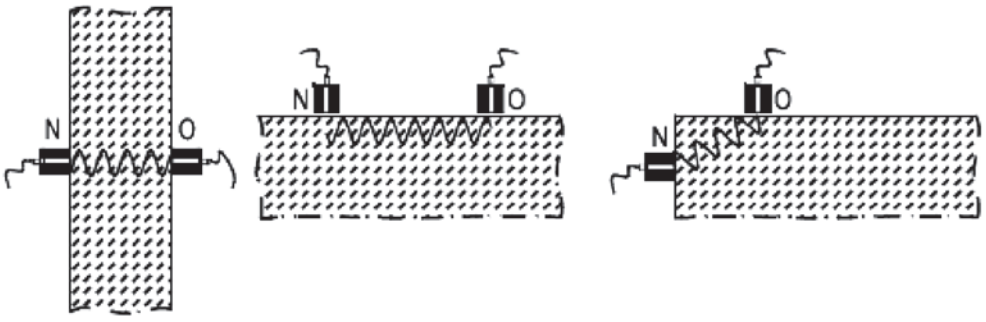

Fig. 3. Head arrangement a) across, b) parallel; c) diagonal N – transmitter head O – receiver head

the time of waves travelling through the medium. In all solid materials longitudinal and transverse waves occur. On the edge of different materials and along the defects waves are partially deflected whereas on the edge of solid material and atmosphere, waves deflect completely. The speed of ultrasound wave propagation in concrete is measured by placing two heads (transmitter and receiver) on the surface of the surveyed object and measuring the time it takes the waves to travel between those devices. The heads can be arranged in different configurations. (Fig 3). It should be noticed that the diagonal setup can cause measurement errors, resulting from angular wave deflection and its impairment.

For concrete testing, the following methods are commonly used:

- echo – relies on deflection of the wave from the object surface; the method requires access to the object from one side,
- direct transmission – relies on the weakening of the wave beam by faults; the method requires access from both sides and is used when flaws (cracks) are located relatively shallowly,
- TOFD (time of flight diffraction) – this method is based on the phenomenon of diffraction during wave propagation and dispersion on flaws perpendicular to the direction of the wave. This method is most often used for examining the quality of welds. Aside from cracks, it shows also flaws in medium continuity.

Based on the measured speed of ultrasound waves, concrete compressive strength R can be defined using ultrasound methods. Calculations are conducted following current standards and guidance [13].

4.2. Seismic methods

For assessing the technical condition of hydrotechnical objects geophysical and seismic methods can also be useful. These methods are based on the emission of different types of waves into the tested medium and measuring the parameters of their propagation. Such methods are automated and computerized. This allows the equipment to be adjusted to the specific research conditions. By controlling wave frequencies, different testing depths can be achieved. Depending on the research method, waves can be generated in a different way. Usually this is done mechanically, using hammers of different weights. The emitted wave, depending of the medium properties, propagates with different speed, deflects, or reflects. Using special electronic sensors and computing devices, registration of disturbances can be performed.

Observation of changes in wave propagation allows areas with anomalies to be localised. In the case of large concrete structures such as water dams these anomalies are: fractures, cracks, stratifications, and areas of higher filtration. It should be stressed that most of the phenomena often occur "in depth", thus making them invisible, and therefore difficult to discover. All the phenomena listed above directly affect the technical condition of hydrotechnical objects. The earlier and more precise the discovery of such occurrence and anomaly, the higher the chances of preventing potential catastrophe. It is worth emphasizing that seismic methods are often the only solution to screening and assessing the object thoroughly. Traditional methods provide data of punctual or superficial character, so results obtained this way are laden with a wide degree of inaccuracy.

An unquestionable advantage of the seismic method is its non-invasive character, which does not require physical interference with the structure. Such examinations are conducted in

a short period of time, usually in an uncomplicated manner. Information about the medium to be tested are obtained relatively quickly, allowing for preliminary assessment of the results while tests are being conducted, or shortly after finishing them.

Research conducted using these methods is usually inexpensive and more effective compared to traditional probing (e.g. drilling), which, on the other hand, is necessary for the calibration of geophysical tests. Thanks to digital registration of data, results can be integrated with numerical models and subsequently detailed analysis based on precise material parameters can be conducted. "Seismic methods are definitely relatively contemporary research methods." All the advantages and efficiency of seismic methods mean that they are used more frequently in new fields of research.

4.3. Scleromertic method

For the purpose of this paper, sclerometer tests of the Rożnow dam's concrete surface layer on the downstream face were conducted using a Schmidt sclerometer, commonly called a Schmidt hammer (Fig. 4.). Tests were conducted by the Scientific Circle of Civil Engineering Students.

The Schmidt sclerometer was developed in 1950 by Ernst O. Schmidt and has undergone further modifications and new applications.

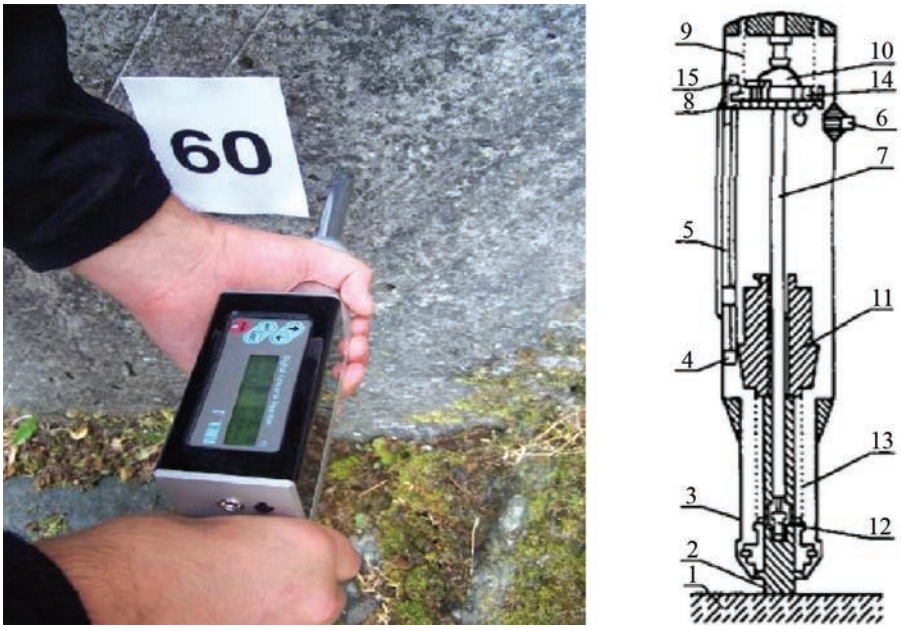

1 – examined concrete, 2 – impact plunger, 3 – housing, 4 – indicator, 5 – scale, 6 – spring release button, 7 – hammer guide bar, 8 – disk, 9 – compression spring, 10 – trigger regulation, 11 – hammer mass, 12 – guide, 13 – impact spring

Fig. 4. Schmidt hammer construction scheme [12]

The measurement is conducted based on the assumption of direct relations between strength of concrete and its hardiness. It is defined by the distance the rod rebounds after putting it against the wall with a defined force triggered by a system of springs (Fig. 5). Assessment of concrete strength is possible thanks to the rebound value obtained after each measurement, and regression curves are prepared for a specific type of concrete. Based on these readings, the compressive strength of the concrete can be determined. Generalising, for concretes of the same type and parameters, the higher the rebound value the greater the compression strength of the material. For the purposes of this survey, a Controls Digital Concrete Hammer type N with a digital meter and data register Schmidt hammer has been used. Its characteristics are standard impact energy at 2.207 Nm and it is designed for analysing objects and elements above 100mm thick and strong in structure.

65 test areas were designated on the downstream face of the non-overflow sections of the object on different levels, along the joint of the wall, in the middle of section and next to the observed cracks (Fig. 5).

The results of conducted measurements obtained for selected points are presented in Table 1. For result elaboration, a statistical method was applied. For each of the test series, the average rebound was defined, as well as standard deviation. Data was verified based on the conditions defined in [11]. Based on this analysis, the results obtained can be recognized as correct. In order to determine concrete strength, the method of hypothetical regression curve matching for adequate content, construction technology and age of concrete was adopted. To determine strength [8] was used. According to the above guidance, it is advised to assume a relation between concrete strength and rebound value in the form:

$$R = aL^2 + bL + C \text{ [MPa]} \tag{1}$$

where:

R – compressive strength of concrete [MPa],
L – rebound value [-],
$a, b, c,$ – regression curve empiric values [–].

Missing factor values and corrective factors should be assigned based on a strength analysis of actual samples collected on the object. Taking into consideration the absence of such samples, the following relation has been used:

$$R = 0.0356L^2\text{-}0.795L + 6.4 \text{ [MPa]} \tag{2}$$

According to [12], the above formula is true for concretes (of analogous origin to the Rożnów dam concretes) where:

– Concrete/water ratio: 1–3,
– Cement content: 250 kg/m^3 and 350 kg/m^3,
– Aggregate: river gravel,
– Compaction: mechanical,
– Curing: natural.

The results of the calculations obtained during research average rebound values with respect to the above formula, and values of concrete compressive strength for control points were derived. The results are presented in Table 2.

Results of sclerometer tests. Obtained rebound values

Measurement point number	Rebound value L [–]																Average Rebound value L [–]
	1	2	3	4	5	6	7	8	9	10	11	12	13	14	15	16	
1	31.7	31.9	32.3	32.6	33.1	33.3	33.3	34.8	34.9	35.0	35.7	35.8	36.0	36.1	37.2	37.3	34.41
2	26.0	28.0	28.6	29.1	30.4	30.6	31.4	32.2	33.1	33.2	33.9	34.1	34.6	34.7	34.7	35.3	32.16
3	23.6	23.7	24.0	25.3	27.6	28.4	29.0	29.0	29.1	30.3	31.7	32.4	32.9	32.9	33.2	33.5	29.38
4	20.1	21.4	22.1	22.5	22.8	24.1	24.9	25.0	25.2	25.6	27.7	28.6	29.0	29.6	30.8	31.3	25.59
5	20.6	20.6	20.6	21.4	21.9	23.3	23.6	24.3	25.9	26.3	26.5	26.6	27.4	28.0	33.2	39.0	26.28
6	20.9	24.2	24.4	24.6	25.1	26.1	26.4	26.6	26.9	27.0	28.8	29.8	30.4	30.5	32.3	33.4	27.22
7	28.7	28.8	30.1	30.7	31.0	32.1	32.5	32.7	32.9	33.2	34.3	34.4	34.5	34.8	35.8	36.0	32.77
8	24.7	25.9	27.8	28.9	29.6	30.5	31.7	31.9	31.9	32.2	32.7	33.5	36.5	36.6	37.5	38.6	31.98
9	24.2	24.3	26.7	27.1	27.4	28.1	28.1	28.2	28.5	28.7	28.8	30.6	30.9	30.9	32.5	36.3	28.67

Table 2

Concrete compressive strength R

Control point number	Average rebound value L [–]	Concrete compressive strength R [MPa]
1	34.41	21.20
2	32.16	17.65
3	29.38	13.77
4	25.59	9.37
5	26.28	10.09
6	27.22	11.14
7	32.77	18.58
8	31.98	17.38
9	28.67	12.87

Fig. 5. Taking tests and control points

The results obtained were related to average strength values acquired from barrel samples, researched during the construction of the Rożnów dam, which were determined at 350 kg/cm^2 [2]. The results acquired during the calculations are significantly lower, and certainly do not reflect the actual technical condition of the surveyed structure. Decreases in strength reaching even 50% are very unlikely. The results were in accordance with initial anticipations. The occurrence of the lowest concrete strength values for control points were located close to scratches and cracks.

Errors and inaccuracies might arise as a result of the regression curve selection based on the literature, caused by the inability to acquire and test actual samples. It should also be kept in mind that the range of tests conducted was rather short and develop from the characteristics of the method used. Only the surface layers of the structure were examined. During 70 years of service period, the surface has been exposed to adverse factors including changes in working conditions, humidity changes, and freezing.

For these reasons, the results cannot be regarded as wholly reliable without verification using other research methods.

It should be emphasized that the Rożnów dam is continuously operating and undergoes frequent inspections regarding technical condition and further service. Research involving the Schmidt hammer tests does not require complex methodology, and results can be obtained quickly. Data elaboration causes no difficulty and interpretation of the results is relatively easy. All these aspects support this method.

Without doubt, a major disadvantage of the sclerometer method is its range – limited only to the surface layers of concrete. It is accepted that the Schmidt hammer provides reliable information on concrete strength up to 20 cm depth (40 cm access from both sides). There is a considerate insufficiency of this method related to the inability to research the material characteristics of layers of concrete located more deeply. In that respect, this method can serve as demonstrative and cannot be regarded as wholly conclusive with reference to the structure as a whole, especially for hydrotechnical objects and water dams.

In order to acquire more accurate information and results, it is necessary to obtain samples using traditional boring methods and conduct destructive testing in order to determine the regression curve values. Seismic screening of at least some sections of the structure would also be very helpful in the course of correct assessment of its technical condition. This would allow results to be compared against other methods.

5. Numerical modelling

The numerical model was prepared for a typical section of the dam, number 18. It is the deepest founded non-overflow section of the object. The engineering software Z-Soil was used for the calculations. The software applies the finite elements method for calculations and can be used to solve geo- and hydrotechnical problems. Section geometry was established based on archival Polish and German plans. Due to the lack of geological documentation, the stratigraphic arrangement of geological layers was adopted based on studies published in the 1930's and scientific articles regarding dam foundations [1] (Fig. 6). Modelling the anti-filtration sealing layers was challenging, as they have been implemented in the form of injections, as there were also no reliable surveys documenting faults in the rock formations. It was decided to represent consolidation grouting as two "slurry walls".

The geometry of the object was modelled in AutoCAD software as a 2D section. After importing a two dimensional model into Z-Soil, it was developed into a 3D model. Material parameters were adopted from dam archives sources, the literature, and material tests conducted on site.

In the next step, boundary values were applied (Fig. 7). High and low water levels were taken into consideration in the form of surface loads. Water levels were determined based on

literature data. [8, 9]. On the lower model plane, unmovable supports were located whereas towards the sides, supports allowing only for vertical movements were located.

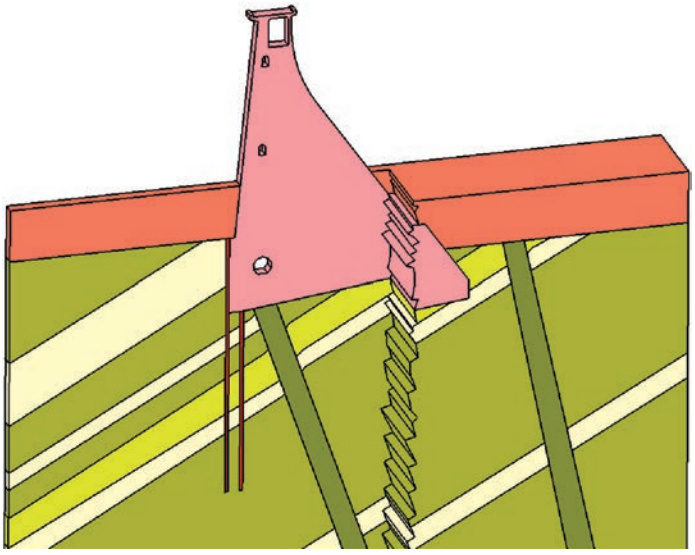

Fig. 6. Layout of subsoil layers

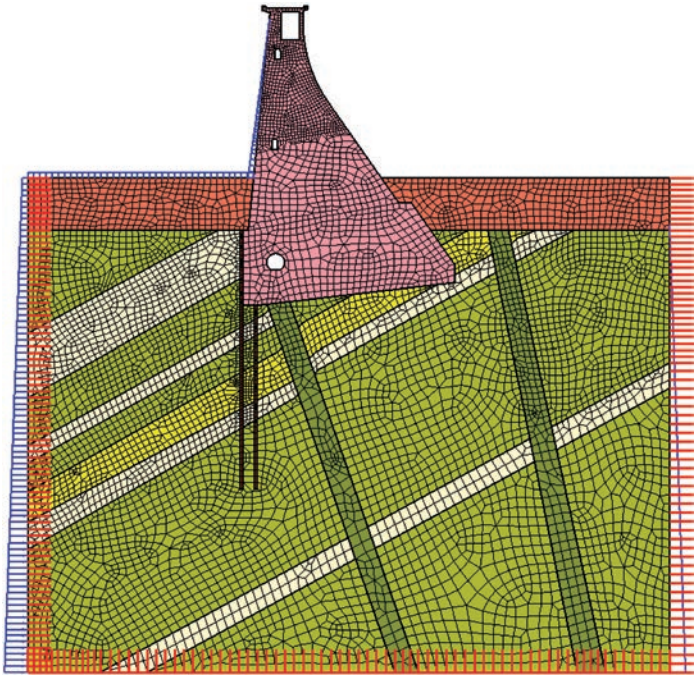

Fig. 7. Boundary conditions

During numerical analysis, calculations for "empty reservoir" and water damming structure were conducted. Fig. 8 shows the displacements in the form of a deformed mesh for the case when water is dammed by the object. The values for maximal displacement and the directions in which they occur are shown in the window on the right. The highest displacements, of .035 mm, were observed along the Y axis. Deformations are scaled-up because they should indicate the direction of the determined displacements. If the scale of the displacement was the same as the model scale, they would not be noticeable.

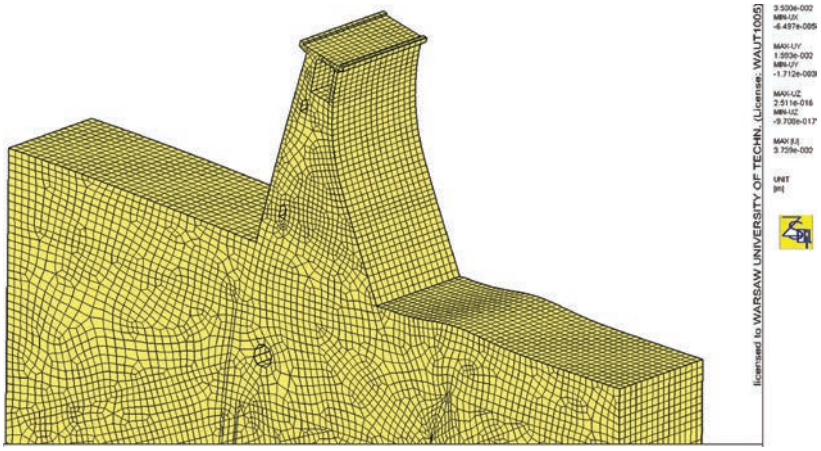

Fig. 8. Finite elements mesh displacement for damming structure

Displacements were visualized also as an isolinear map. Fig. 9 shows the absolute values of displacement for the dam damming up water.

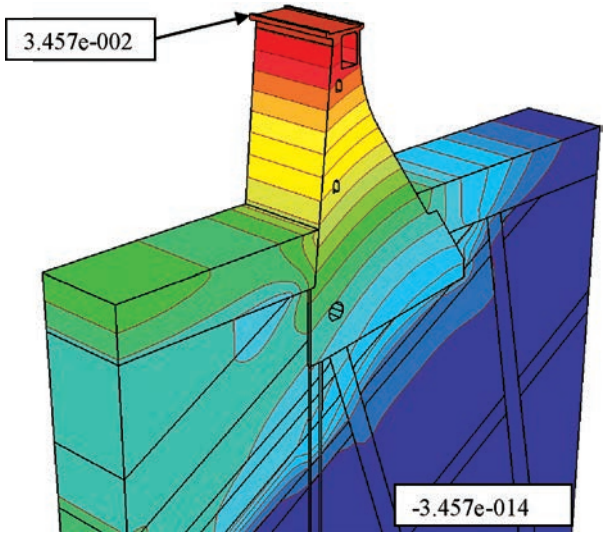

Fig. 9. Absolute displacements

The software used for model handling allows the methods of presenting the results to be combined. Fig. 10. shows an isolinear map that is a combination of the displacement diagram and the determined 2D model sections deformations. The projection of displacements within a given section can be applied in order to show displacements in a legible way in comparison with two adjacent dam sections with different foundation conditions.

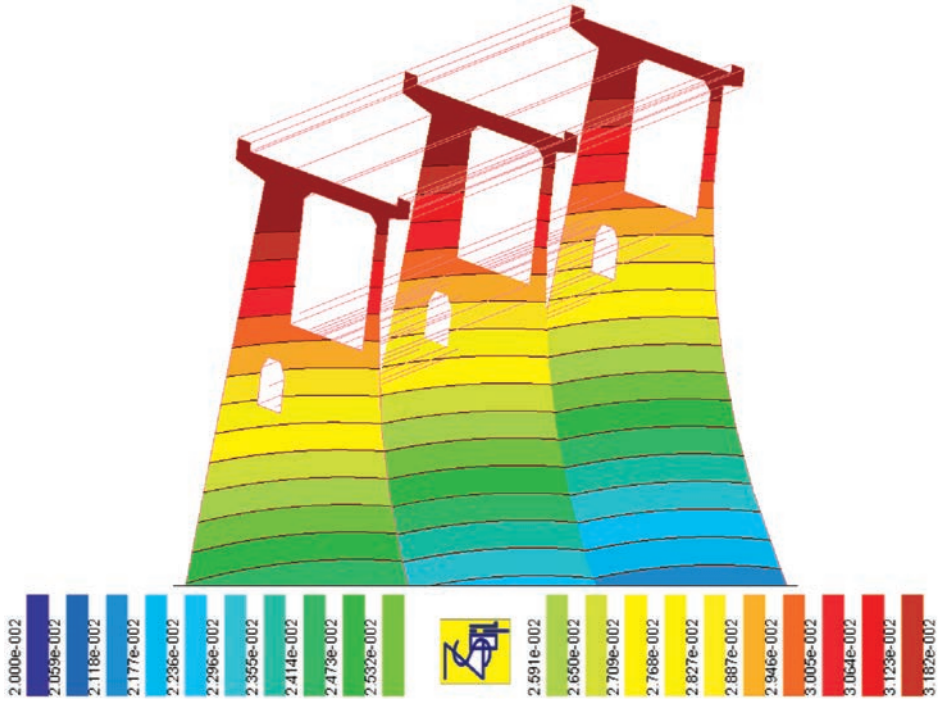

Fig. 10. Combination of graphs presenting displacement and model deformations of determined flat cross sections cut at 7.5 meters. Non-uniform scale.

5.1. Comparison of geometrical data with laser scanning results

In order to verify geometrical model accuracy, the results of the survey utilizing laser scanning method were compared with the entered archival data [3]. The data were compared in the form of vertical cross-sections of surveyed (generated in ASCAN application) and modelled sections. The comparison was executed in AutoCAD (Fig. 11). Diagrams include sections acquired based on data acquired from different sources. The common element for all cross-sections was the lowest point located at the bottom of the downstream face of the dam (E). At the base of the downstream face differences between the cross-sections are slight. Closer to the crest of the dam (further away from the base station of survey) the differences were increasing. They are visible around point D and equal 2.5 cm. The highest disparity reaching 6.2 cm was recorded at the crest of the dam around area A. This might result from the inaccuracy of the scanning method or local concrete dwindling.

In the case of massive, large scale objects such differences are insignificant in the scale of the whole structure, and their influence on the calculation results are insignificant [3]. A comparable error is made by simplifying the geometry during model elaboration using archival data.

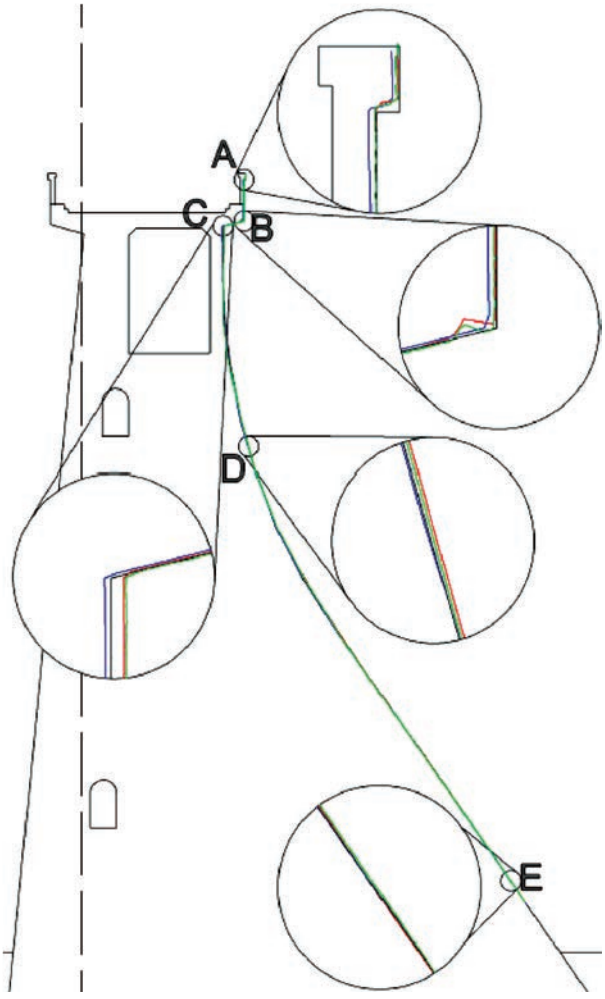

Fig. 11. Comparison of 18 section geometry with laser scanning

The methods allowing data to be obtained for preparing the numerical model were chosen based on the analysis conducted. Fig. 12 shows the relationships between data sources and specific model elements which could be generated using this information:

1. Data likely to be obtained from design and construction documentation, such as the geometry of particular object elements, foundation levels, internal galleries and other internal installation localizations, structure sub-base modifications realized during construction. Other material parameter data which can be obtained result from field and laboratory research.

2. Data likely to be obtained using geological and hydrogeological reconnaissance and using geophysical tests of subsoil.
3. Structure shape that can be acquired using geodesic surveys and laser scanning (e.g. geometry of downstream face and inspection galleries) and indications of control measurement devices (e.g. dislocations of selected points).
4. Data that can be obtained from the Building Log and from reservoir water level studies (e.g. barymetric measurements), indications of control-measuring devices (e.g. reservoir water levels).

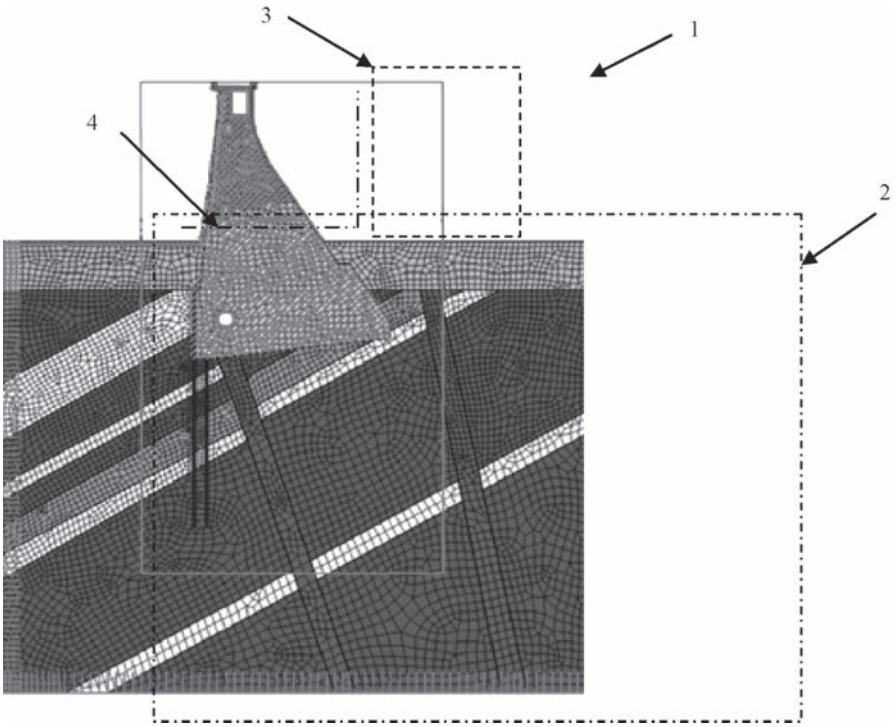

Fig. 12. Combination of data sources for generating specific elements of the numerical model

6. Conclusions

– Acquiring data for the preparation of water dam numerical models is an interdisciplinary problem and requires cooperation from many specialists.
– Information and data from different realms such as object geometry, sub base, material parameters, geology, hydrogeology and object operation conditions are necessary.
– Geometry can be established based on archival information as well as geodesic surveys.
– The laser scanning method can be very useful as a source of data for objects lacking complete technical project documentation as well as for assessing geometry changes, for example documentation of the development of scratches and cracks, etc.

Bibliography

[1] Balcerski W., *Problemy statyczne fundowania zakładu wodno-elektrycznego w Rożnowie*, Gospodarka Wodna, Warszawa 1938.

[2] Jarząbek S., *Laboratorium betonowe w Rożnowie*, Życie Techniczne, Nr 9, 1937.

[3] Kollis W., *Studja dla projektu zbiornika wodnego w Rożnowie na Dunajcu*, Warszawa 1935.

[4] Popielski P., Zaczek-Peplinska J., *Wykorzystanie modeli numerycznych w eksploatacji budowli pietrzących*, Materiały XII Międzynarodowej Konferencji Technicznej Kontroli Zapór, Stare Jabłonki 2007, 241–255.

[5] Zaczek-Peplinska J., Popielski P., *Wykorzystanie naziemnego skaningu laserowego do weryfikacji geometrii numerycznych modeli obiektów hydrotechnicznych na przykładzie sekcji zapory betonowej Besko,* Czasopismo Techniczne 1-Ś/2013, Wydawnictwo Politechniki Krakowskiej, Kraków 2013.

[6] Grant Rektorski PW, *Analiza możliwości wykorzystania geofizycznych metod sejsmiki powierzchniowej do oceny stanu technicznego wałów przeciwpowodziowych*, Koło Naukowe Inżynierii Wodnej Politechniki Warszawskiej, Warszawa 2013.

[7] Grant Rektorski PW, *Opracowanie modelu numerycznego zachowania się zapory betonowej i jego weryfikacja na podstawie geodezyjnych pomiarów okresowych z uwzględnieniem okresu wezbrań sezonowych,* Stowarzyszenie Studentów Wydziału Geodezji i Kartografii Politechniki Warszawskiej "Geoida", Warszawa 2013.

[8] OTKZ IMGW, *Ocena stanu technicznego i bezpieczeństwa zapór w Rożnowie i Czchowie – zapora Rożnów*, marzec 2012.

[9] OTKZ IMGW, *Zapora w Rożnowie – Wyznaczenie przemieszczeń*, marzec 2012.

[10] Rozporządzenie Ministra Środowiska z dnia 20 kwietnia 2007 r. w sprawie warunków technicznych, jakim powinny odpowiadać budowle hydrotechniczne i ich usytuowanie (Dz.U.2007.86.579).

[11] Norma PN-EN-12504-2:2002, Badania betonu w konstrukcjach. Część 2. Badania nieniszczące. Oznaczenie liczby odbicia.

[12] Instrukcja ITB 210/1977, *Instrukcja stosowania młotków Schmidta do nieniszczącej kontroli jakości betonu.*

[13] Instrukcja ITB 209/1977, *Instrukcja stosowania metody ultradźwiękowej do nieniszczącej kontroli jakości betonu.*

[14] Drobiek Ł., Jasiński R., Piekarczyk A., *Metody lokalizacji wad konstrukcji betonowych – metoda ultradźwiękowa,* Przegląd Budowlany, 9, 2007.

TECHNICAL TRANSACTIONS | CZASOPISMO TECHNICZNE
ENVIRONMENTAL ENGINEERING | ŚRODOWISKO
2-Ś/2015

KRZYSZTOF RADZICKI*

THE CONCEPT OF QUASI-3D MONITORING OF SEEPAGE AND EROSION PROCESSES AND DEFORMATIONS IN DAMS AND DIKES, CONSIDERING IN PARTICULAR LINEAR MEASUREMENT SENSORS

KONCEPCJA MONITORINGU QUASI-3D PROCESÓW FILTRACYJNO-EROZYJNYCH W ZAPORACH I WAŁACH, ZE SZCZEGÓLNYM UWZGLĘDNIENIEM CZUJNIKÓW LINIOWYCH

Abstract

The primary purpose of this article is to present the concept of quasi-spatial monitoring of seepage and erosion processes and phenomena in the area of georisk, using invasive instrumental measurement methods, including, in particular, linear or quasi-linear measurement sensors. Along with the risk of water overflow over the crest of earth damming hydraulic structures, these processes and phenomena pose the main threats for their safety and are the main causes of their repairs. The proposed solutions seem to be valuable ones and have a high application potential. Taking into account the development of measurement methods and the field of the automatic control of the condition of a structure, they will probably be used increasingly frequently in the damming hydro-engineering constructions.

Keywords: dam and dike monitoring, condition assessment, automatic monitoring system, linear sensor, thermal monitoring, seepage, erosion, deformation

Streszczenie

W artykule skupiono się na przedstawieniu koncepcji quasi-przestrzennego monitoringu procesów filtracyjno-erozyjnych oraz zjawisk z obszaru georyzyka z zastosowaniem instrumentalnych, inwazyjnych metod pomiarowych ze szczególnym uwzględnieniem liniowych lub quasi-liniowych czujników pomiarowych. Te procesy i zjawiska, wraz z zagrożeniem przelania się wody przez koronę ziemnych obiektów piętrzących stanowią główne zagrożenia dla ich bezpieczeństwa oraz stanowią podstawowe przyczyny ich remontów. Zaproponowane rozwiązania wydają się cenne i mają duży potencjał aplikacyjny. Biorąc po uwagę rozwój metod pomiarowych oraz dziedziny automatycznej kontroli stanu konstrukcji prawdopodobnie będą stosowane coraz częściej w budownictwie hydrotechnicznym.

Słowa kluczowe: monitoring zapór i wałów, ocena stanu, automatyczny system kontroli technicznej, czujnik liniowy, termomonitoring, filtracja, erozja, przemieszczenie

DOI: 10.4467/2353737XCT.15.232.4618

* PhD. Krzysztof Radzicki, Institute of Water Engineering and Water Management, Faculty of Environmental Engineering, Cracow University of Technology.

1. Introduction

Surveillance and monitoring systems of earth damming hydraulic structures play an important role in the monitoring and assessment of the condition of these structures.

A properly designed network of measurement sensors and, in particular, a system for automatic monitoring of the condition of an earth damming hydraulic structure and a correct analysis of the measurements carried out using them minimise the risk of their failure/collapse, especially when the early detection of destructive and unfavourable processes ensures that appropriately early preventive measures can be taken. The minimisation of the risk of a failure of a damming hydraulic structure limits the risk of potentially very serious flood related losses caused by the impact of a flood wave arising as a result of a breach of this structure. Moreover, an effective measurement system enabling the early detection and assessment of the growth rate and range of the destructive process makes it possible to minimise the costs of possible repairs. The accurate identification of the condition of a structure and its prediction for the future enable the optimisation of the repair policy. This is particularly important for the entities which manage the systems of damming hydraulic structures and operating and repair policy.

Particularly in the last decade, the abovementioned arguments and needs brought about the development of new innovative instrumental measurement methods, the implementation of measurement methods developed in other fields in hydro-engineering construction and the intensive development of the already existing methods. Given their application prospects and effects, particularly interesting devices include linear or quasi-linear sensors enabling, respectively, the linear or quasi-linear measurements of specific values along the section measured. The abovementioned trend in the development of measurement methods is, more broadly, part of the field of SHM (Structural Health Monitoring) which is developing intensively in the construction sector.

At present, measurement sensors are applied in particular for monitoring water dams, but, increasingly, they are also used to monitor flood protection dikes.

The primary purpose of this article is to present the concept of quasi-spatial monitoring of seepage and erosion processes and phenomena in the area of georisk, using invasive instrumental measurement methods, including, in particular, linear or quasi-linear measurement sensors. Along with the risk of water overflow over the crest of earth damming hydraulic structures, these processes and phenomena pose the main threats for their safety and are the main causes of their repairs.

2. The concept of the quasi-3D monitoring of risks in the area of georisk and seepage and erosion processes using instrumental methods

A potential ideal measurement method in the field of the monitoring of the condition of a structure should enable in particular: the early detection of a threat at any place in the structure and the exact identification of its location and range, as well as enable the determination of the growth date of a possible destructive process. In consequence, it should be characterised, inter alia, by a high resolution of measurements, along with a simultaneous measurement of the values of the measured parameters in a continuous manner in space and

the possibility of implementing this method in automatic systems of measurements for their periodical or incidental condition assessment or/and real time monitoring of the conditions of a structure on a 24/7 basis. Other expected features would also include low cost and easy application. Certainly, these features would also be desirable for the methods applied in hydro-engineering construction [7, 9].

At the present level of the development of measurement methods, there is no such ideal method which would demonstrate, at the same time, all the features listed above. In consequence, it is necessary to use a set of measurement solutions, in accordance with a suitable methodology which, depending on the needs, makes it possible to achieve to the optimum extent the most important expected results. Each time, these solutions are adapted to the individual case of a structure. It should be noted that the abovementioned methodology also develops along with the advancement of measurement methods and the growth of knowledge in a given area.

In the monitoring of hydraulic structures, particularly given the frequently large dimensions of these structures, in terms of both their cross-section and especially their length, a very important feature of the monitoring method is the possibility of making spatial measurements, in particular in a continuous manner along the length of the structure. Such a possibility is offered by non-invasive geophysical methods, including the method of electrical resistivity or seismic tomography. These methods are important tools for examining damming hydraulic structures; however, they have a number of limitations [4, 3, 9]. It can be expected that, despite their intensive development, non-invasive geophysical methods are not likely to achieve the spatial resolution and accuracy of invasive measurements by instrumental methods. It is hardly likely that relatively small, local changes in the ground medium, particularly those related to the initial phase of the development of destructive processes, can be identified using non-invasive geophysical methods. In turn, early information on such changes – the growth rate of which in the case of damming hydraulic structures under the pressure of dammed-up water can be very high – is important for the assessment of their condition and the prevention of possible threats [4, 9]. On the other hand, invasive instrumental methods do not enable a full extent of spatial measurements. When, in turn, invasive instrumental methods are considered, they do not enable the full implementation of spatial measurements. However, the use, firstly, of the appropriate measurement tools and, secondly, of the appropriate methodology for their application make it together possible to achieve the effect of quasi-spatial (quasi-3D) measurements.

At present, it is interesting to note two groups of instrumental methods which make it possible to achieve the effect of quasi-3D measurements and offer a significant application potential in the range of hydro-engineering construction. The first one is the thermal method for the detection of seepage and erosion processes, while the other is a set of measurement tools enabling the monitoring of deformations of the medium investigated. In both, the key element is a linear measurement sensor enabling continuous or quasi-continuous linear measurements in space. Depending on the needs, it is installed in the main body and/or the foundation along the length of the hydraulic structure. Such a solution enables the detection of places and cross-sections where an adverse phenomenon or process is occurring along the length of the structure.

Obviously, the more linear sensors are placed in the cross-section of the hydraulic structure, the fuller the effect of the quasi-spatial monitoring achieved. However, on the other hand, as the number of sensors grows the costs of the monitoring system increase and also the construction

work becomes more complicated, in the case of a newly built or repaired hydraulic structure. Therefore, the essence of more effective systems for quasi-3D measurements is the design of the optimum number and locations of linear sensors which would make it possible to acquire information on the key zones of the hydraulic structure along its length.

The linear measurement along the length of the structure is supplemented with appropriately situated single sensors or also with the abovementioned linear sensors in selected cross-sections of the hydraulic structure in order to ensure fuller, quasi-spatial monitoring of the destructive process. Sensors in the measurement cross-sections of the hydraulic structure can be planned and installed beforehand at the places of the expected potential largest adverse changes and the highest risk, including georisk, e.g. the largest computational consolidation deformations. Where necessary, they can also be added to the necessary extent in a cross-section where an adverse phenomenon has occurred, after the cross-section at risk has been identified by the linear monitoring system installed along the length of the hydraulic structure. Both of the abovementioned methods are described in greater detail in the subsequent sections of the article.

3. The method for the thermal monitoring of seepage and erosion processes in the concept of quasi-3D monitoring

Internal erosion is one of the basic threats for dams and dikes. Appropriate monitoring of this process is of key importance for ensuring the safety of these structures and minimising the costs of their possible repairs. Among the existing methods for monitoring seepage and erosion processes, the thermal monitoring method has become particularly valuable and increasingly popular in recent years [5, 6].

Thermal methods for analysis of water flow in the ground are based on the relations between heat and fluid transport processes, which are coupled processes. A change in the moisture content of the ground, in particular, the emergence of water seepage and changes in its velocity, significantly disturb the heat distribution in the body of the structure and the underlying ground. Since the erosion process affects the seepage vector field, it also directly influences the temperature field of the ground medium.

Each of the erosion process types causes a characteristic disturbance in the hydro-thermal field [11, 12]. In consequence, the thermal monitoring method allows for the detection and analysis of both seepage and erosion processes.

As an example, Figure 1 shows a numerical analysis of the impact of the different suffusion process development stages on the thermal field of a dam cross-section at the same time instant of the same structure under the same thermal and hydraulic loadings. It can be clearly seen that the heat flow from the reservoir into the structure body grows in the area of the highest hydraulic gradients as the erosion process develops.

The method for the thermal monitoring of seepage and erosion processes and examples of its applications have been described in many articles, including e.g. [2, 8, 10].

One of the reasons for the success of the thermal monitoring method is the application of linear temperature measurements. The capacity to carry out continuous measurements all along the structure brought about a quality change in the monitoring of seepage and erosion processes compared with the point monitoring carried out only at selected places in the structure.

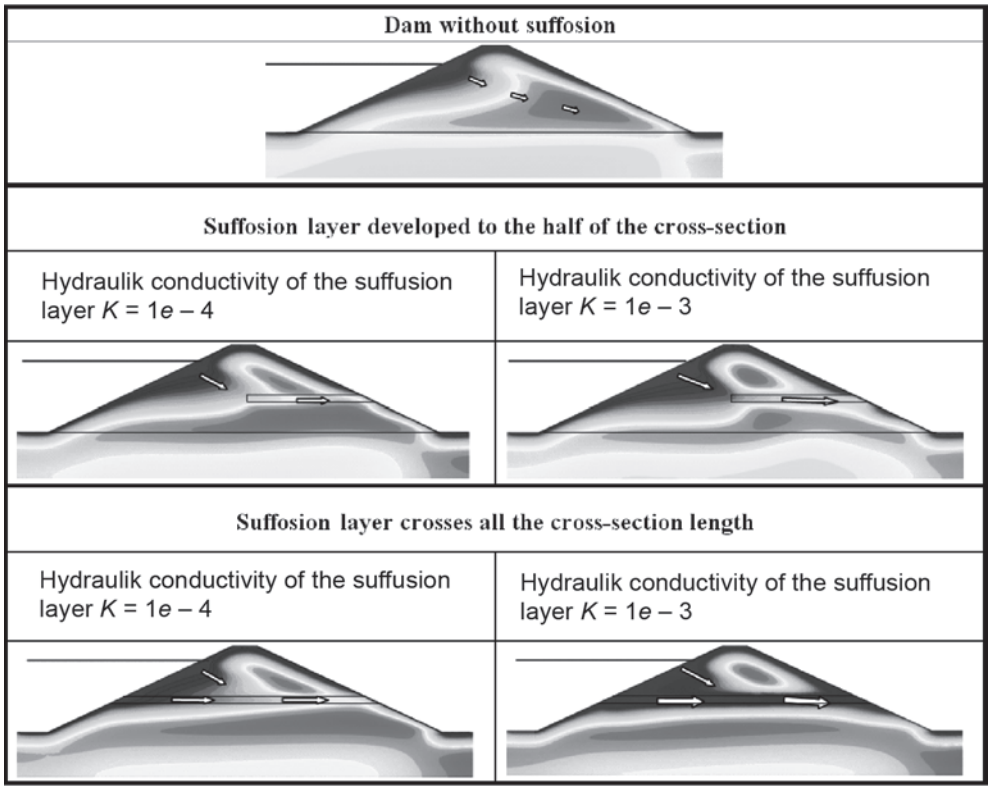

Fig. 1. Temperature fields of a dam cross-section registered at the same time instant for different lengths of the suffusion layer and for different values of suffusion layer hydraulic conductivity [12]

One of the linear technologies applied in thermal monitoring entails temperature measurements using a fibre optic using the spectral analysis of backscattering and its comparison with the spectrum of the light fed into the fibre by a laser [14]. At present, the system used to monitor hydraulic structures makes it possible to measure the temperature of a fibre optic with a spatial resolution of one metre and enables temperature measurements with a resolution of at least 0.1°C over a section of one cable up to tens of kilometres in length. The fibre optics applied to measure temperatures on hydraulic structures have watertight, armoured jackets. This ensures their easy installation on the construction sites, tightness, very high strength and durability of at least several dozen years.

Technologies alterative to fibre optics are two solutions which will be called the "multi sensor cable" technology and "multi hammered points sensor" [13].

The "multi sensor cable" is a cable inside which single temperature sensors and communication and supply cables have been placed and integrated. In such a cable, single temperature sensors are distributed along its length at constant or individually set intervals.

The main advantage of this solution for short measurement sections of up to several hundred metres is its cost which is even several times lower than that of a fibre optic-based thermal monitoring system. An example of such a "multi sensor cable" is MCableS® from

Neostrain [13]. In addition to its installation along a structure, the "multi sensor cable" technology is also applied in water temperature measurements in piezometers. Given its small diameter, a "multi sensor cable" does not prevent manual periodic measurements in a piezometer, which are more often than not required for dams in order to verify automatic pressure measurements.

The "multi hammered points sensor" is mounted without excavation by inserting successive sensors in a series, one after another. The sensors are characterised by a small diameter and their mounting does not leave a large hole. Still, after a sensor has been installed, the hole is secured, inter alia, by filling it with bentonite. It is easy and cheap to "replace" a damaged sensor in the measurement system. Near a damaged sensor, a new sensor is inserted and incorporated into the system. Coupled with the no-excavation installation, application of multi hammered points sensor can reduce the cost of the thermal monitoring system and its installation even by a factor of a dozen or so compared with the fibre optic-based temperature measurement system and enable its installation in situations where for different reasons it is impossible or difficult to carry out earthworks. An example of a "multi hammered points sensor" is MPointS® [13].

In both these measurement solutions the distance between sensors must be so selected as to ensure "quasi" continuous measurements which match fibre optic sensors as regards their spatial resolution.

The above-mentioned technologies make it possible to install a system for carrying out both the quasi-continuous thermal monitoring all along the damming structure, particularly in its downstream toe, and vertical measurement profiles – both with any density of temperature sensors in space.

The combination of continuous temperature measurements along a retaining hydraulic structure and vertical measurements of temperature profiles carried out in selected cross-sections of the structure enables a more detailed quasi 3D analysis of destruction processes in the cross-section of interest here. After a destruction process has been detected to develop along the hydraulic structure using the linear measurement method, additional vertical

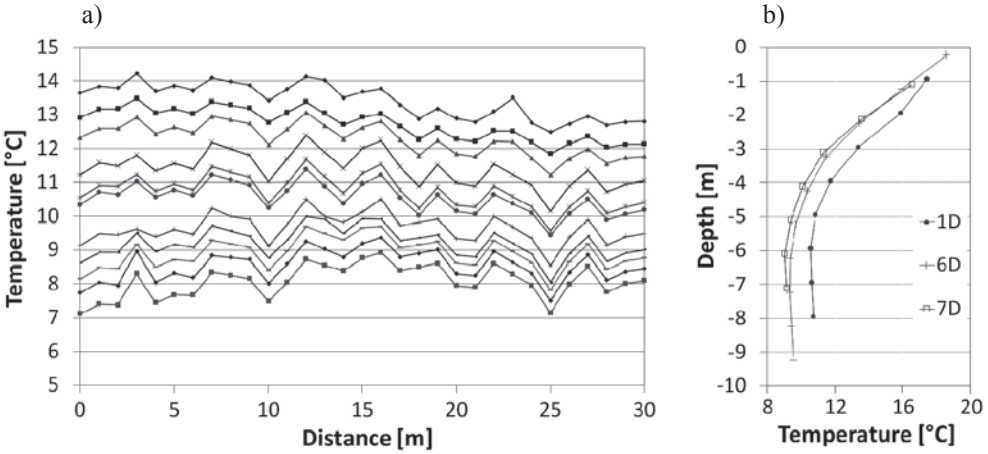

Fig. 2. An example of temperature measurements carried out on the Kozłowa Góra Dam: a) in a section of a linear sensor installed along the dam in its downstream toe, b) in a vertical measurement profile

temperature measurements can be carried out in this cross-section. Depending on the needs, the abovementioned method for water temperature measurements in a piezometer can be applied for this purpose; however, particularly in the case of hydraulic structures which periodically dam up water, such as e.g. flood control dikes, sensors which are driven or drilled directly into the ground can be used.

The system for quasi-3D thermal monitoring considered here was designed and installed on the Kozłowa Góra Dam, where MPointS® was run along the dam, while in its cross-sections, in piezometers, a MCableS® was installed to carry out the measurements of vertical temperature profiles. Fig. 2 shows an example of a temperature measurement implemented using this system.

4. Deformation measurements by the instrumental method in the concept of quasi-3D monitoring

Deformation measurements are an important element in the monitoring of destructive phenomena and processes unfolding in the foundation and/or the main body of a damming hydraulic structure. A significant risk of deformations of hydraulic structures can result, inter alia, from the large dimensions of a hydraulic structure, i.e. the substantial loads generated by water damming in a reservoir, and seepage processes. Moreover, in general, civil structures, including hydraulic structures, are increasingly often localised in areas of enhanced georisk. Such areas are those where adverse geological phenomena occur (e.g. karstic phenomena and formations, landslides, suffusion, floating earth, glacitectonic effects) and areas degraded by man (in particular, the areas where mines and steelworks used to operate).

In the case where investment projects are carried out on weak soils, an appropriately selected monitoring system will provide investors with information about possible non-uniform subsidence, soil push-out from under a structure, tilting and displacements of a structure, the degree of consolidation of the underlying ground etc. In effect, this valuable information provides the basis for the adoption of the optimum decisions in the course of an investment process, the correct management of work, and, after its completion, the monitoring and acquisition of accurate assessments of the condition of the hydraulic structure.

In accordance with the concept of the quasi-spatial deformation monitoring as proposed in Section 2, its basic element is a linear or quasi-linear displacement sensor. Such a sensor could be a fibre optic sensor, which operates in the same way as the previously described temperature sensor, i.e. on the basis of the analysis of the spectrum of light dispersed in the fibre optic [1]. However, at present, these sensors have a number of limitations: they only enable a qualitative measurement of deformations; have low tensile strength (sensors with a glass core) and have a relatively very expensive measuring head. Another interesting measurement solution enabling quasi-linear measurements of vertical displacements in a pre-determined measurement profile up to several hundred metres long, with an accuracy of up to single millimetres is a hydroprofile meter. In this device, the measurement sensor is a hose through which a liquid is pushed. The level of the liquid is measured at pre-determined points relative to the reference level, determining the position of the hose at these points. An adequately dense measurement of the position points of the measuring hose makes it possible to achieve quasi-continuous measurements.

Hydroprofile meters are ever more widely used for monitoring embankments and foundations in civil engineering, particularly for monitoring road embankments. However, they have not been often used for hydraulic structures.

In the quasi-3D deformation monitoring system, linear monitoring using a hydroprofile meter can be complemented with classical point deformation sensors, selected on a case by case basis for a given issue and enabling its broader assessment in terms of both the parameters measured and their spatial distribution. These sensors can include inclinometers, extensometers, hydro-levelling instruments and others.

5. An example of the quasi-3D system for the monitoring of seepage and erosion processes and deformations in an earth dam

Both of the measurement methods for the quasi-3D monitoring of the seepage and erosion processes and deformations described in the previous sections were proposed as elements of the monitoring of one of the earth dams which are now at the design stage in Eastern Europe. A schematic diagram of the proposed monitoring solution is shown in Fig. 4. This dam, of a planned height of a dozen or so metres, will have a waterproof element (represented by a yellow colour in Fig. 3) on the waterside, which will be linked to the cut-off wall planned in the ground underlying the waterside toe of the hydraulic structure.

The concept of the quasi-3D system for the monitoring of this dam is, firstly, based on linear systems for the thermal monitoring of seepage and erosion processes and displacements, continuous along the length of the dam. Another important element of this concept are vertical temperature and displacement measurement profiles placed in selected measurement cross-sections of the hydraulic structure. These cross-sections are situated along the entire length of the dam, in particular in the zones of the highest potential risk, including those of the highest georisk caused by the existence of weaker soils in the ground underlying the zones.

In the scope of the thermal monitoring system, the design includes the installation in the main body of the dam of linear fibre optic temperature sensors placed along the entire length of the dam in two zones. The first zone is the space of the main body situated directly close to the waterproof element of the dam, on its upstream side. The other zone is the downstream toe of the dam. Minimising the costs of the thermal monitoring system, such a localisation of linear fibre optic temperature sensors enables the linear monitoring of both the zone of potential penetration of the leak into the hydraulic structure and its very early detection, and also makes it possible to control the zone of the potential accumulation of the leak on the downstream side.

In addition, in planned measurement cross-sections, it was proposed that vertical thermometric profiles should be placed in piezometers. They complement the quasi-3D system for the monitoring of the dam with the possibility of its hydrothermal analysis also in its transverse planes with respect to the system of linear sensors.

The temperature measurements in the main body of the dam would also be complemented with a system of the measurements of external thermal loads acting on the dam, including appropriately designed systems for measuring the temperatures of the air and the water in the reservoir.

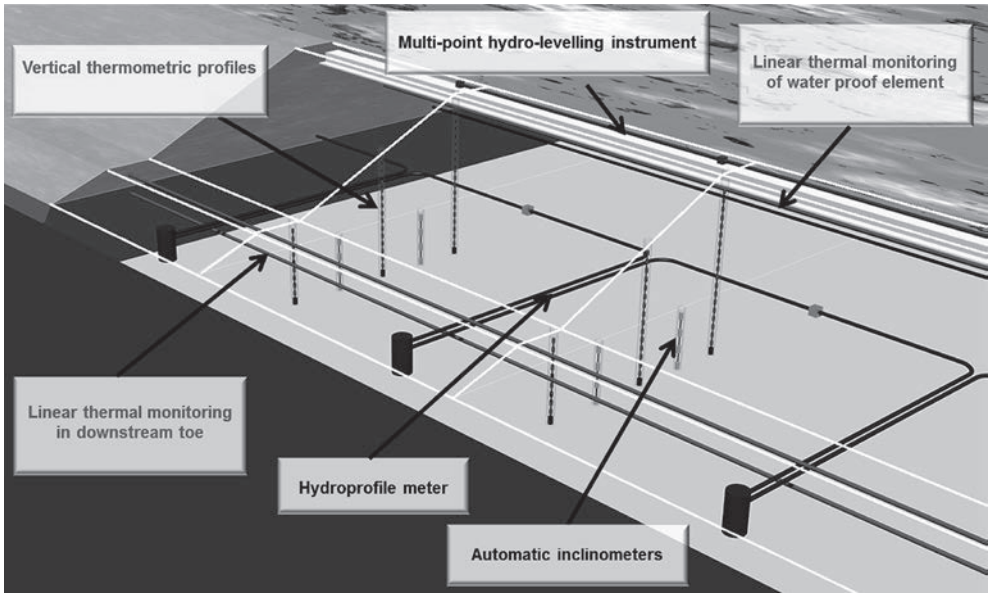

Fig. 3. Elements of the setup of quasi-spatial systems for the thermal monitoring of seepage and erosion processes and deformation monitoring

In the scope of the quasi-3D system for measuring deformations of the dam, hydroprofile meters were chosen for the linear monitoring of vertical displacements along the length of the dam. The measuring hoses of the hydroprofile meters are placed in the zone of contact between the main body of the dam and the underlying ground in order to directly measure the impact of displacements of the ground underlying the dam on its main body. The measurement section of each of the hydroprofile meter begins with a measurement and access well (blue cylinders in Fig. 3), situated in the downstream toe of the dam. From the well, the measuring hose enters the main body of the dam. The hose runs along the axis of the dam, turns and runs along the axis, finally to return to the successive well which is, at the same time, the initial well for another hydroprofile meter. This arrangement ensures the continuity of measurements along the axis of the dam and, in addition, continuous horizontal profiles of vertical displacements between the axis of the dam and the measurement and access wells.

The linear system for measurements of horizontal deformations along the dam is complemented by the vertical profiles of automatic inclinometers situated in the planned measurement cross-sections of the dam. Moreover, the sensors of automatic multi-point hydro-levelling instruments are placed on the crest of the dam, enabling high-precision measurements of the vertical displacements of this element of the dam.

The system for the monitoring of the dam is complemented with other sensors, including benchmarks, pressure sensors in piezometers, instruments for measuring drainage discharges etc.

6. Final remarks

The development of measurement methods and the development of the methodology for their measurements and analysis, including the development of automatic systems for controlling the condition of built structures, make it possible to use more efficient and effective measurement solutions. This also applies to hydro-engineering construction, in particular damming hydraulic structures, such as dams and flood protection dikes. For these structures, the minimisation of the risk of failure and/or repairs is a very important issue.

The linear sensors for the thermal monitoring of seepage and erosion processes and displacements presented in the article seem to have a very high potential for the application in the monitoring of damming structures for which the monitoring of these parameters is particularly important in the assessment of their safety and condition.

The article presents in particular the concept of quasi-spatial monitoring of seepage and erosion processes and displacements. This is a solution the application of which uses especially the advantages of linear sensors and is based on their appropriate use in the system for monitoring a hydraulic structure.

The proposed solutions seem to be valuable ones and have a high application potential. Taking into account the development of measurement methods and the field of the automatic control of the condition of a structure, they will probably be used increasingly frequently in hydro-engineering construction.

References

[1] Artieres O., Beck Y.-L., Fry J.-J., Guidoux C., Pinettes P., *Monitoring of earthdams leaks and stability with fibre optics monitoring solution for canal dykes*, Proc. of 8th ICOLD European Club Dam Symposium, Innsbruck, Austria, September 22–23, 2010, 423–437.

[2] Beck Y.L., Cunat P., Guidoux C., Artieres O., Mars J., Fry J.J., *Thermal monitoring of embankment dams by fiber optics*, Proc. of 8th ICOLD European Club Dam Symposium, Innsbruck, Austria, September 22–23, 2010, 461–465.

[3] Fauchard C., Meriaux P., *Geophysical and geotechnical methods for diagnosing flood protection dikes. Guide for implementation and interpretation*, Cemagref-Edition, Paris 2007, 124.

[4] FloodPRoBe, Rapid and cost-effective dike condition assessment methods: geophysics and remote sensing, Report Number: WP3-01-12-20, 2013, 136.

[5] Fry J.J., *How to Prevent Embankments from Internal Erosion Failure?*, Proc. of International symposium on dams for a changing world, 5 june, Kyoto 2012, 6.

[6] ICOLD, *Internal erosion of existing dams, levees and dikes, and their foundations*, Bulletin no. 164, Volume 1, Internal erosion processes and engineering assessment, 2013.

[7] Radzicki K., *Badania filtracji w ziemnych budowlach piętrzących metodami termodetekcji*, Gospodarka Wodna No. 5, 2005, 372–376.

[8] Radzicki K., *Analyse retard des mesures de températures dans les digues avec application à la détection de fuites (Zastosowanie analizy odpowiedzi opóźnionej*

w pomiarach temperatury ziemnych obiektów hydrotechnicznych do identyfikacji przecieków), Ph.D thesis, AgroParisTech, Paris 2009, 198.

[9] Radzicki K., K. Bonelli S., *Thermical seepage monitoring in the earth dams with Impulse Response Function Analysis model*, 8h ICOLD European Club Symposium, 22–25 september, Innsbruck 2010, 649–654.

[10] Radzicki K., Bonelli S., A *possibility to identify piping erosion in earth hydraulic works using thermal monitoring*, Proc. of 8h ICOLD European Club Symposium, 22–25 September, Austria 2010, 618–623.

[11] Radzicki K., Bonelli S., *Monitoring of the suffusion process development using thermal analysis performed with IRFTA model*, Proc. of 6th ICSE, 2012, 593–600.

[12] Radzicki K., *The important issues of levees monitoring with special attention to thermal-monitoring method application*, Proc. of South Baltic Conference on New Technologies and Recent Developments in Flood Protection, 5–6 June, Gdańsk 2014, 11.

[13] Radzicki K., Siudy A., Stoliński M., *An innovative 3d system for thermal monitoring of seepage and erosion processes and an example of its use for upgrading the monitoring system at the Kozłowa Góra dam in Poland*, Q.99-R.7, 25th Congress on Large Dam, 2015, 85–101.

[14] Vogel L. B., Cassens C., Graupner A., Trostel A., *Leakage detection systems by using distributed fiber optical temperature measurements*, Proc. Of SPIE Smart Structures and Materials 2001, vol. 4328, 2001, 23–34.

TECHNICAL TRANSACTIONS | CZASOPISMO TECHNICZNE
ENVIRONMENTAL ENGINEERING | ŚRODOWISKO
2-Ś/2015

BERNARD TWARÓG*

DETERMINATION OF CHARACTERISTIC FLOW VALUES DOWNSTREAM OF THE RACIBÓRZ RESERVOIR USING MONTE CARLO METHODS BASED ON COPULA FUNCTIONS

OKREŚLENIE WARTOŚCI PRZEPŁYWÓW CHARAKTERYSTYCZNYCH PONIŻEJ ZBIORNIKA RACIBÓRZ Z ZASTOSOWANIEM METOD MONTE CARLO OPARTYCH NA FUNKCJACH COPULA

Abstract

This case study of the Racibórz reservoir discusses the application of a determination method of characteristic flow values below retention reservoirs. The study describes the selected theoretical foundations, the individual steps of the *Monte Carlo* (MC) method used to generate hypothetical flood wave hydrographs, and the results of simulations leading to the determination of characteristic flow values below retention reservoirs. The method is based on probability density functions for a multidimensional random variable obtained using copula link functions. The results of the analyses are represented in tables and graphs. The results of the simulation analysis are presented for comparison purposes, assuming a constant and a variable time for the hypothetical base flood elevation.

Keywords: copula functions, multivariate distributions of a random variable, flood wave characteristics, Monte Carlo method, random number generator, flows with a defined probability of exceedance, retention reservoirs

Streszczenie

W artykule zapresentowano aplikację określania wartości przepływów charakterystycznych poniżej zbiorników retencyjnych na przykładzie zbiornika Racibórz. Przedstawiono wybrane podstawy teoretyczne, poszczególne kroki metodyki, zastosowanie metody Monte Carlo (MC) do tworzenia hipotetycznych hydrogramów fal powodziowych oraz wyniki obliczeń symulacyjnych prowadzące do określenia wartości charakterystycznych przepływów poniżej zbiorników. U podstaw tej metody są funkcje gęstości prawdopodobieństwa wielowymiarowej zmiennej losowej budowanej z wykorzystaniem spinających funkcji copula. Wyniki analiz w artykule zostały przedstawione w postaci tabelarycznej i graficznej. Dla porównania przedstawione są wyniki analizy symulacyjnej przy założeniu stałego i zmiennego czasu podstawy hipotetycznej fali powodziowej.

Słowa kluczowe: funkcje copula, rozkłady wielowymiarowej zmiennej losowej, parametry fali powodziowej, metoda Monte Carlo, generowanie liczb losowych, przepływy o określonym prawdopodobieństwie przewyższenia, zbiorniki retencyjne

DOI: 10.4467/2353737XCT.15.233.4619

* PhD. Bernard Twaróg, Institute of Hydraulic Engineering and Water Management, Faculty of Environmental Engineering, Cracow University of Technology.

1. Introduction

Monte Carlo methods are useful in determining characteristic flow values downstream of retention reservoirs due to their capability of generating (multidimensional) populations of elements with statistical characteristics consistent with experience. The experiment (generating characteristics of hypothetical flood waves) is unrelated to time, but the process of generation of those characteristics is based on marginal distribution values determined for extreme annual flood wave parameters. Consequently, it may be assumed that a population obtained using a Monte Carlo method corresponds to the population of extreme annual flood waves. This assumption also supports the statement that the proposed method of determining characteristic flows is reliable.

The events in 2010 emphasised deficiencies in the impounding structure controls. The control procedures applied in more than 80% of impounding structures during the flood of May 2010 failed to meet the conditions defined in the basic document binding on a reservoir manager – the Instructions for Water Management in the Reservoir. This study represents another step towards applying a stochastic approach to generating hypothetical hydrographs of flood waves and assessing characteristic flow values downstream of reservoirs.

The main stimulus underlying this study was the need to obtain clear and precise information about the flood control effectiveness of the Buków-Racibórz embankment and polder system. The varying level of detail in available information and substantial differences in the published values of reduction capacities cast doubt on the reliability of data used as a design basis for engineering structures located downstream of the polders in the Oder river valley that are governed by the Regulations contained in Journals of Laws Dz.U. No. 86, item 579, Dz.U. of 2015, item 329, Dz.U. No. 63, item 735, Dz.U. of 2013 item 104. The described status leads to erroneous decisions in the planning process of flood control measures and in designs of engineering structures such as roads, railways, bridges, wrong dimensions and locations of floodplains that have a significant effect on zoning and spatial planning, and on the amounts of premiums paid by insurance takers. The effects of the described status include external costs. If the reduction values assumed in economic analyses are too low, they may result in external benefits: the conditions are safer than estimated and excessively high bridges, embankments, large culverts, large dry detention basins are designed that are more expensive than necessary, insurance takers pay excessively high premiums, etc. On the other hand, if the reduction values assumed are too high, external costs appear, i.e. a portion of unreasonable costs of project implementation is paid by society, already overburdened with taxes (and in particular by potential flood victims), the conditions are less safe than assumed, and threats and losses are higher in the case of flood. Both cases may lead to the conclusion that a planned capital expenditure project does not meet social needs for flood protection level and thus entails an undesirable deadweight flood loss in the economic balance sheet.

The problem analysed consists in determination of maximum annual flow values with a defined probability of exceedance. A statistical analysis is impracticable in numerous cases due to insufficient data sets. This is particularly true for river valley stretches situated downstream of dam cross-sections of retention reservoirs. The difficulties described often cannot be overcome downstream of retention reservoirs. The problem is particularly grave because statistical values play a key role in the assessment of existing conditions and

development of guidelines for engineering and hydraulic structure design. Moreover, if an assessment of such statistics downstream of reservoirs is impossible, experts are forced to take unreasonable steps, assuming no reduction of maximum flows while such reduction takes place. This approach has an obvious effect on the capital expenditure of projects implemented, increasing their costs and reducing their economic efficiency.

A known probability distribution is necessary to apply MC methods, so that the reservations described above also apply to parameter estimation of a multivariate distribution. In addition, known applications of multivariate normal distribution did not ensure consistency of experimental materials with the results of MC methods – marginal theoretical distribution functions with empirical ones. This inconvenience, or rather material deficiency, is remedied by the use of the copula function in generating a probability density function for a multidimensional random variable.

2. A brief history of the Racibórz reservoir

Following the disastrous flood of 1880, the idea was put forward to construct a retention reservoir in the Oder river valley upstream of Racibórz. The first concept of a suburban dam on the Oder River to be constructed as part of the planned Oder–Danube canal was developed as early as 1833. The capacity of the reservoir was estimated in 1905–1906 at 640 million m^3. Modifications introduced in the following years, principally due to plans to transform the canal into a large transport route connecting the Oder with the Danube Rivers resulted in a reduced total reservoir capacity of 390 million m^3. A navigable canal was planned, bypassing the reservoir along its eastern side. Due to the partition of the reservoir among Poland, Czechoslovakia and Germany after World War I, the idea of canal construction was shelved. In order to protect Racibórz against floods, the German authorities commenced in 1934 the construction of the Neue Oder canal (known as Ulga at present), planning to excavate about 4 million m^3 of earth. The work was completed in 1942. The canal was capable of transporting 2,000 m^3/s of water along its paved bed. Following the flood of July 1997, it was revealed that about 1 million m^3 of mud had deposited in the canal. The canal was cleaned after that disaster. When the first Polish concept of making the Oder navigable was proposed in 1954, the total planned capacity amounted to 695 million m^3. Czechoslovakia used its absolute veto against the construction of such a large reservoir and objected to all subsequent designs proposed.

A concept developed in 1957 assumed that water from the Oder would be supplied to the Warta drainage area and to the Upper Silesia conurbation using a reservoir with a total capacity of 326.4 million m^3. Four new versions of the reservoirs were developed in 1962. The first version provided for a capacity of 247 million m^3, the second – 290, the third – 302, and the fourth – 507 million m^3. The shape of the reservoir in its plan view was the same in the first three versions, the fourth version was completely different from previous ones.

All versions were submitted to the Czechoslovakian government that approved the first concept by way of a special resolution adopted in 1961. However, in time the solution turned out to be economically inefficient for Poland, the plans were abandoned, and the negotiations with Czechoslovakia discontinued. In 1975, the Czechs submitted a proposal to make the river navigable between Koźle and Ostrava, with prospective construction of an

Oder–Danube canal. The need emerged again to develop a comprehensive solution to water management problems. A compromise was proposed by *"Hydroprojekt"* of Wrocław – the construction of the reservoir was to be combined with aggregate mining from its prospective basin. Following the flood of July 1997, the flood control function of the planned reservoir rose in importance.

3. The Racibórz reservoir – structure parameters

The flood control reservoir Racibórz Dolny on the Oder River in the Śląskie province (a polder) is planned as a component of the flood control system in the Oder valley. It is designed as a polder collecting water only in periods of flood wave passage, and with no water management functions outside flood periods.

The basic parameters of the reservoir are as follows:

– dam crest elevation: 197.50 m above sea level,
– maximum impoundment level: 195.20 m above sea level,
– water volume at maximum impoundment: 185.0 Mm^3,
– maximum water surface area: 26.3 km^2,
– total length of earthen dams: 21.8 km,
– maximum height of earthen dams: 11.1 m.

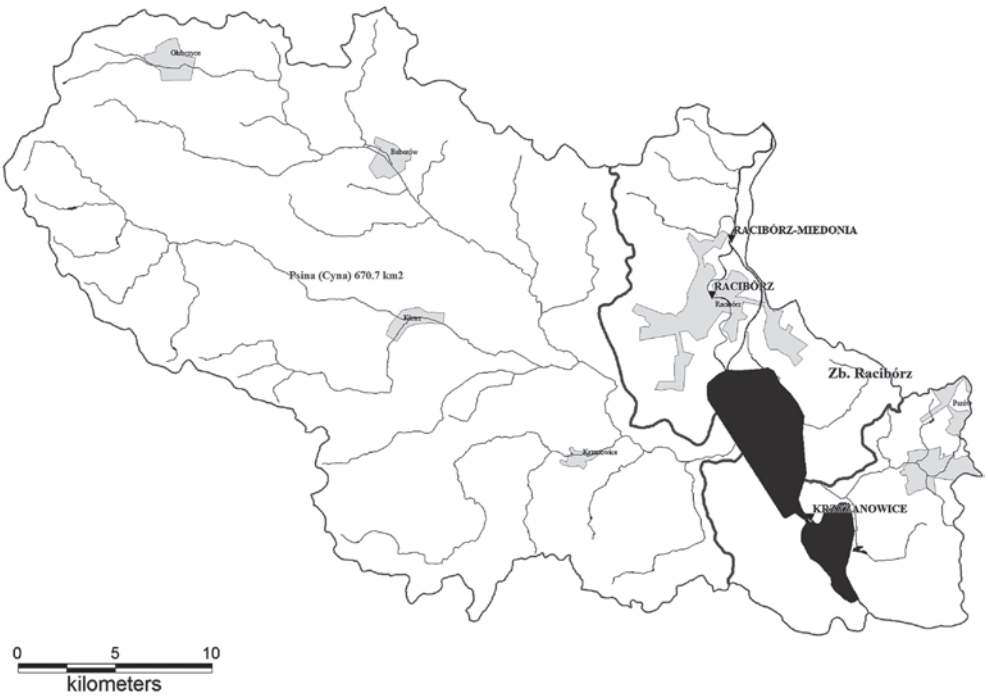

Fig. 1. Location of the Racibórz reservoir with indicated drainage area of the Psina River

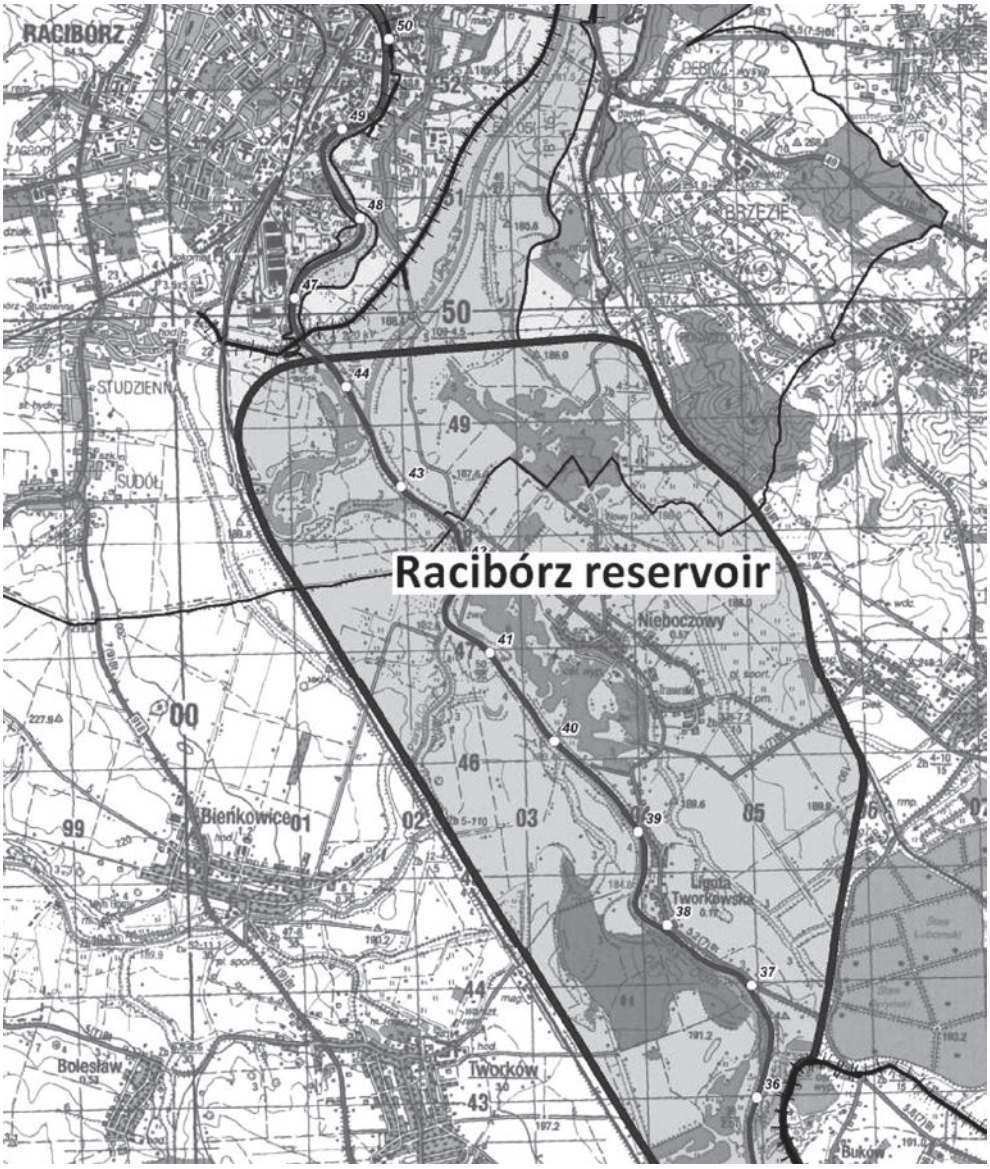

Fig. 2. The Racibórz reservoir [16]

4. Hydrological model used in the analysis

Table 1

Parameters of water-level gauges near the cross-section of the Racibórz–Buków polders

River	Name of water-level gauge	km of river course	Drainage area [km^2]
Oder	Krzyżanowice	712.85	5875.14
Oder	Racibórz-Miedonia	693.63	6728.90

The method used to define a random sample was described in other studies published by the author [1–4]. This study is focused on application of the proposed approach to using MC methods with certain modifications in order to generate hypothetical hydrographs of flood waves. Statistics of flood waves have been estimated on the basis of characteristics obtained at the water-level gauge cross-section in Racibórz–Miedonia, confirmed as reliable for an assessment of the Racibórz reservoir. It is the nearest water-level gauge downstream of the dam cross-section providing a sufficient set of hydrological materials collected (hydrographs of extreme flood waves).

Table 2

Sample characteristics of extreme waves used in analyses of flood control efficiency of polders [10]

Probability of exceedance	Peak value [m3/s]	Volume [Mm3]
0.100	1078	314.7
0.030	1781	519.9
0.020	2031	593.0
0.010	2364	690.1
0.005	2885	842.2
0.003	3199	934.0
0.002	3504	1,022.9

A log-normal distribution is used to describe both the peak wave form and the wave volume. The adopted parameters for the probability density function for maximum annual flows are those for the Racibórz-Miedonia water-level gauge, based on a study for the ISOK project [14]. The values of distribution parameters describing the second random variable, i.e. wave volume, are taken from analyses of the Buków polder performed for the Regional Water Management Board in Gliwice [9, 10].

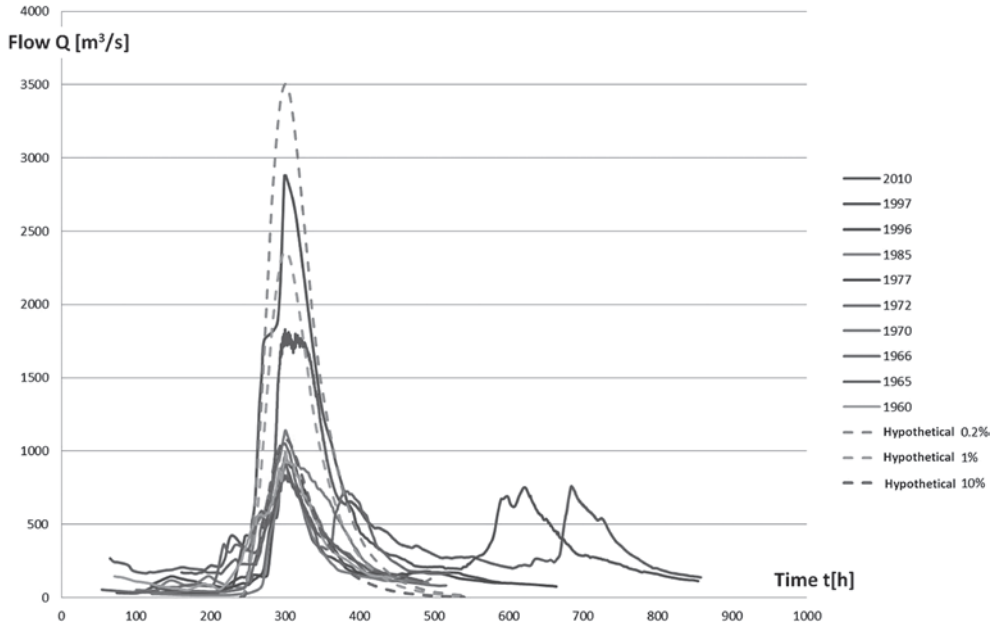

Fig. 3. Sample largest flood waves, the Krzyżanowice water-level gauge [10]

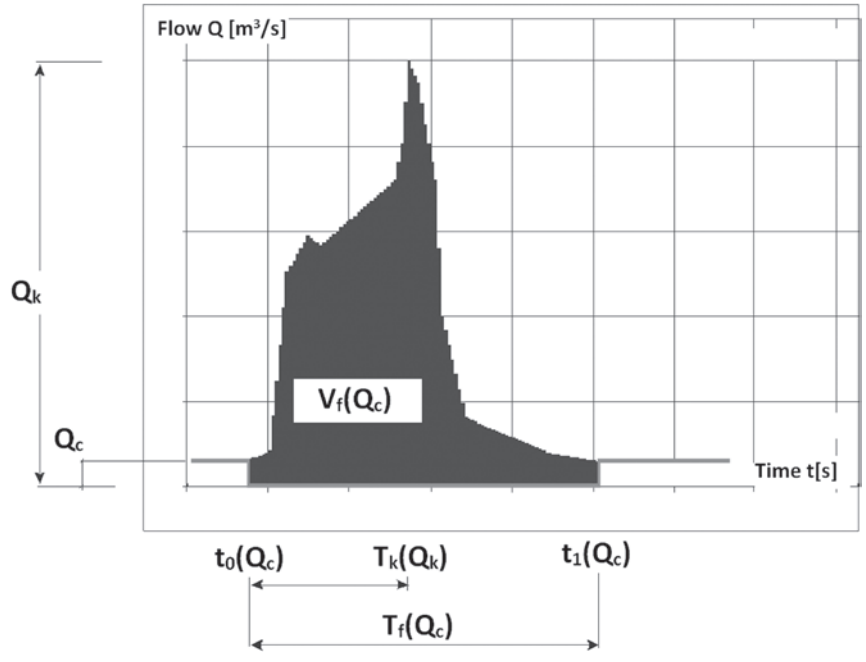

Fig. 4. Method used to assess flood wave characteristics

5. Assumptions underlying hypothetical inflow hydrographs

The use of non-deterministic formulas to generate flood wave hydrographs requires application of equations linking their parameters. The basic equation describes the volume of a flood wave. A variation problem may be defined to find a hydrograph function based on equations describing the hydrograph form [1–4], but such an equation will not always have a solution:

$$V_f - \int_{t_0}^{T_f} [Q(t, \Psi)]dt = 0 \tag{1}$$

where:
$\Psi(T_k, Q_k, T_f)$ – decision variable vector,
t [s] – time
V_f [m^3] – flood wave volume,
T_f [s] – flood wave duration,
T_k [s] – time of appearance of peak wave,
$Q(t)$ [m^3/s] – wave hydrograph,
Q_k [m^3/s] – flood wave peak.

The above section contains a brief discussion of the theoretical assumptions adopted in generating hypothetical flood wave hydrographs. A set of points in a two-dimensional space containing peak and volume values is generated using a Monte Carlo method [3, 4]. The following equations are then solved for all points in the generated set, depending on parameters *a*, *b* and thus forms of hypothetical flood wave hydrographs are obtained.

The analysis discussed includes formulas for two types of hypothetical flood wave populations. A population with a constant time of base flood elevation and a population with a variable time of base flood elevation were developed.

The relation between the flood wave volume and wave duration time is obtained using correlation analyses. The moment of appearance of the peak value equals to 25% of the wave duration time.

5.1. The case with a variable time of base flood elevation

For any:
$T_k \in (0, T_f)$, let us assume that:

$$Q(t) = \begin{cases} \dfrac{Q_k}{T_k^{1/a}} t^{1/a}, t \in [0, T_k] \\ \dfrac{Q_k}{(T_f - t)^{1/b}} (T_f - t)^{1/b}, t \in [T_k, T_f) \end{cases} \tag{2}$$

$$T_f = 0.5014 V_f$$
$$T_k = 0.25 T_f$$

where:

V_f [Mm^3] – flood wave volume,
T_f [h] – flood wave duration,
T_k [h] – time of appearance of peak wave,
$Q(t)$ [m^3/s] – wave hydrograph,
Q_k [m^3/s] – flood wave peak,
a, b – optimized parameters of a function describing the inflow hydrograph satisfying the equation of flood wave volume (coordinates of the decision variable vector).

5.2. The case with a constant time of base flood elevation

For any:
$T_k \in (0, T_f)$, let us assume that:

$$Q(t) = \begin{cases} \dfrac{Q_k}{T_k^{1/a}} t^{1/a}, t \in [0, T_k] \\ \dfrac{Q_k}{(T_f - t)^{1/b}} (T_f - t)^{1/b}, t \in [T_k, T_f) \end{cases} \tag{3}$$

$$T_f = 322$$
$$T_k = 0.25 T_f$$

Regardless of the population type, the basic equation to be satisfied by the equation of a hypothetical flood wave for the conditions indicated above is given below:

$$V = \frac{Q_k}{T_k^{1/a}} \int_0^{T_k} t^{1/a} dt + \frac{Q_k}{(T_f - T_k)^{1/b}} \int_{T_k}^{T_f} (T_f - t)^{1/b} dt \tag{4}$$

6. Application of a Monte Carlo method with the use of the copula function

Copula functions are used as a statistical tool in multi-dimensional modelling of random variable distributions. They link marginal unidimensional probability distributions for a single random variable into a complete multivariate distribution of a multidimensional random variable. Below the reader will find an example of generating a multivariate random variable distribution based on a function from the Archimedean copula family, known as the Gumbel-Hougaard copula. The form of this function is often used in generating extreme distributions describing characteristics of hypothetical flood waves [3].

$$F(u_1,u_2,...,u_m)=\exp\left(-\left[\sum_{k=1}^{m}(-\ln u_k)^{\theta}\right]^{\frac{1}{\theta}}\right) \tag{5}$$

where:
F – cumulative distribution function,

$u_1=F_1(x_1),u_2=F_2(x_2),...,u_m=F_m(x_m)$ – represent any marginal distribution function,
Θ – an optimum parameter for the selected copula function,
m – dimension of a multidimensional random variable.

7. Two-dimensional distribution of flood wave characteristics

A two-dimensional random variable distribution based on a function from the Archimedean copula family, known as the Gumbel-Hougaard copula, was used to generate flood wave characteristics.

$$F(u_1,u_2)=\exp\left(-\left[\sum_{k=1}^{2}(-\ln u_k)^{\theta}\right]^{\frac{1}{\theta}}\right) \tag{6}$$

where:
F – cumulative distribution function,

$u_1=F_1(x_1)$, $u_2=F_2(x_2)$ – are marginal distribution functions,

Θ – an optimum parameter for the selected copula function,

$u_k=\int_0^{x_k}\frac{1}{\zeta_k\sigma_{x_k}\sqrt{2\pi}}e^{\frac{-(\ln(\zeta_k)-\mu_{x_k})^2}{2\sigma_{x_k}^2}}d\zeta_k$ – marginal distribution function of random variable k,

σ_{x_k}, μ_{x_k} – parameters of marginal distribution of random variable k.

Table 3

Values of adopted statistical parameters

Parameters of estimated marginal distributions	Random variable	μ	σ
Log-normal marginal distribution	Q_k/ wave peak	**5.6819**	**0.8943**
Log-normal marginal distribution	V_f/ wave volume	**5.5349**	**0.5422**
Gumbel-Hougaard copula			
Theta	53.3039		

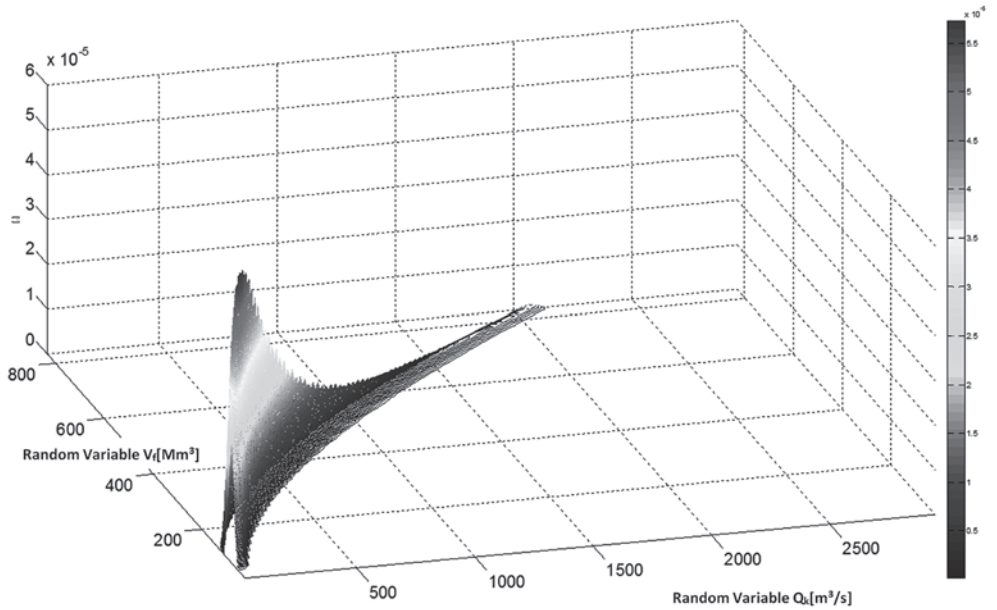

Fig. 5. Probability density function of the two-dimensional random variable (Q_k [m^3/s], V_f [Mm^3])

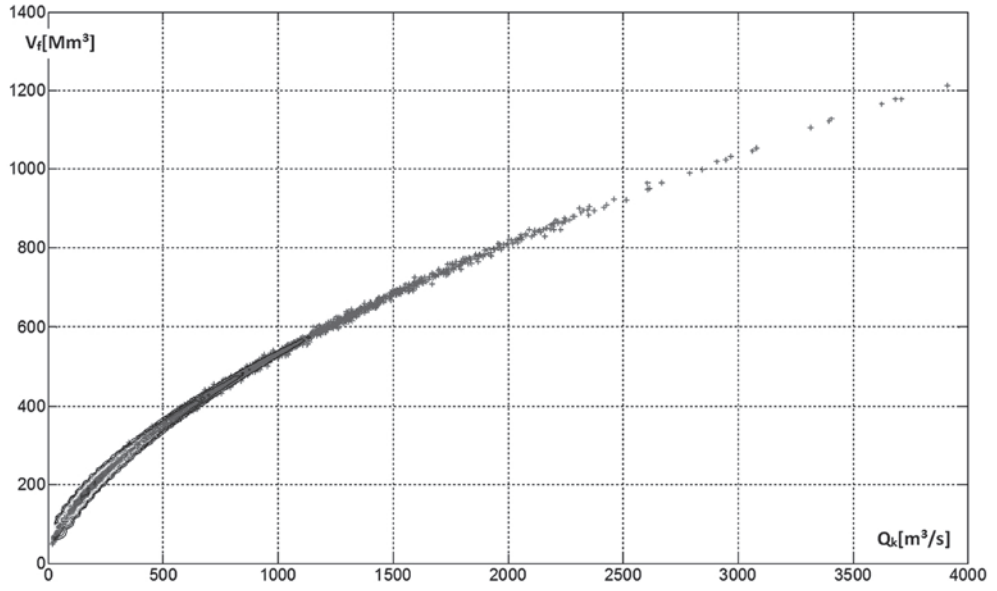

Fig. 6. The characteristics of flood waves generated using a Monte Carlo method and a two-dimensional random variable distribution (Q_k [m^3/s], V_f [Mm^3]), 10 000 points

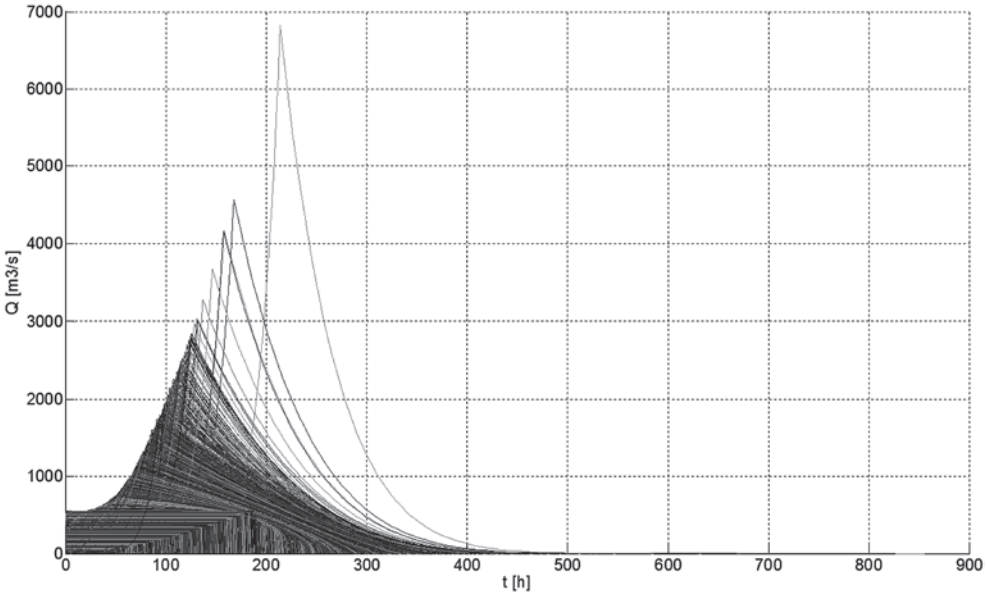

Fig. 7. Obtained hydrographs of flood waves based on the generated parameters, 10 000 waves

8. Control algorithms of the Racibórz reservoir adopted in the analysis

This study is based on the three most popular reservoir control algorithms. These are known as fixed outflow, semi-fixed outflow and step outflow control methods. The basic assumptions for the algorithms and rules for determining outflow from the reservoir are discussed below.

8.1. Fixed outflow control

One of the methods used to manage water volumes in reservoirs is management with a fixed outflow or discharge. This method ignores forecast inflows to the reservoir. If the fixed outflow method is used, control decisions are made depending on current circumstances.

The adopted flood control capacity equals 185 [Mm^3], and the value of allowable (safe) flow is $Q_{all} = 470$ [m^3/s].

8.2. Semi-fixed outflow control

In the semi-fixed outflow control regime, the values of outflow U are determined as a function of inflow $U = f(Q)$ or the retention volume V at the beginning of the analysed period $U = f(V)$, or of both those factors simultaneously $U = f(Q, V)$. Both U and V are thus

random variables. The functions must be defined so as to obtain desired changes in time of both outflow from the reservoir and storage volume.

An example of semi-fixed outflow control is provided by the rule of determining outflows in proportion to excessive inflows compared to an assumed balanced (e.g. safe) flow downstream of the reservoir. If the inflow value exceeds the flow Q_{WYR} downstream of the reservoir, the outflow volume is determined by the equation:

$$U = Q_{WYR} + K \cdot (Q - Q_{WYR}) \tag{7}$$

however, assuming that until Q_{WYR} is reached, the outflow and inflow volumes are equal, and consequently the retention volume is constant in the initial flood stage. After wave passage, i.e. when the inflow value is less than Q_{WYR}, the flood retention volume is discharged with an outflow equal to Q_{WYR}.

The flood control capacity adopted in the analysis equals 185 Mm^3, the value of allowable (safe) flow is Q_{all} = 470 m^3/s, and the proportionality constant K = 0.5.

Step outflow control

As the volume of water that may be discharged from the reservoir rises, the controlled outflow volume is increased stepwise.

$$U(t) = f(Q(t), V_{akt}(t), Q_{1WYR}, Q_{2WYR}, Q_{3WYR}, ...) \tag{8}$$

where:

$U(t)$ [m^3/s] – controlled discharge,
$Q(t)$ [m^3/s] – inflow to the reservoir,
$V_{akt}(t)$ – water retention in the reservoir,
Q_{1WYR}, $Q_{2\,WYR}$, $Q_{3\,WYR}$ [m^3/s] – characteristic outflow values.

The adopted flood control capacity equals 185 Mm^3, and the adopted values of flows equal: 470 m^3/s, 800 m^3/s, 1070 m^3/s and 1600 m^3/s.

9. Results of analyses

An analysis of the control rules applied in reservoir management under flood conditions requires that certain reservoir parameters be adopted, namely a total capacity and a flood control capacity. The control rule used is another indispensable component. One value of the Racibórz reservoir capacity and three control rules applied under flood conditions are assumed in the calculations discussed. The adopted value of safe outflow downstream of the reservoir, as proposed in the study [8, 9], equals to 470 m^3/s.

A set of parameters for 10 000 hypothetical hydrographs was obtained from a set of 10 000 points in a two-dimensional space, using a Monte Carlo method and assuming log-normal marginal distributions. Equations for 10 000 cases were subsequently solved to obtain 10 000 hydrographs of hypothetical flood waves. A simulation of the Racibórz reservoir operation was then conducted for the entire set. Outflow hydrographs were obtained from

the simulation. Peak values of those hydrographs were used to assess the values of outflows downstream of the reservoir with a certain probability of exceedance.

The figures below illustrate selected simulation results in the form of outflow hydrographs, histograms of maximum outflow values and graphic comparisons of cumulative distribution functions of empirical maximum inflows to the reservoir and maximum outflows from the reservoir.

Analyses of the control rules were performed for two populations, each consisting of 10 000 hypothetical flood waves. The first population was solved for a variable duration time of the hypothetical flood wave. The second population was developed for a constant duration time of the hypothetical flood wave.

9.1. An analysis of Racibórz polder control for a population of hypothetical flood waves characterised by a variable time of base flood elevation

9.1.1. The case of fixed outflow control rule

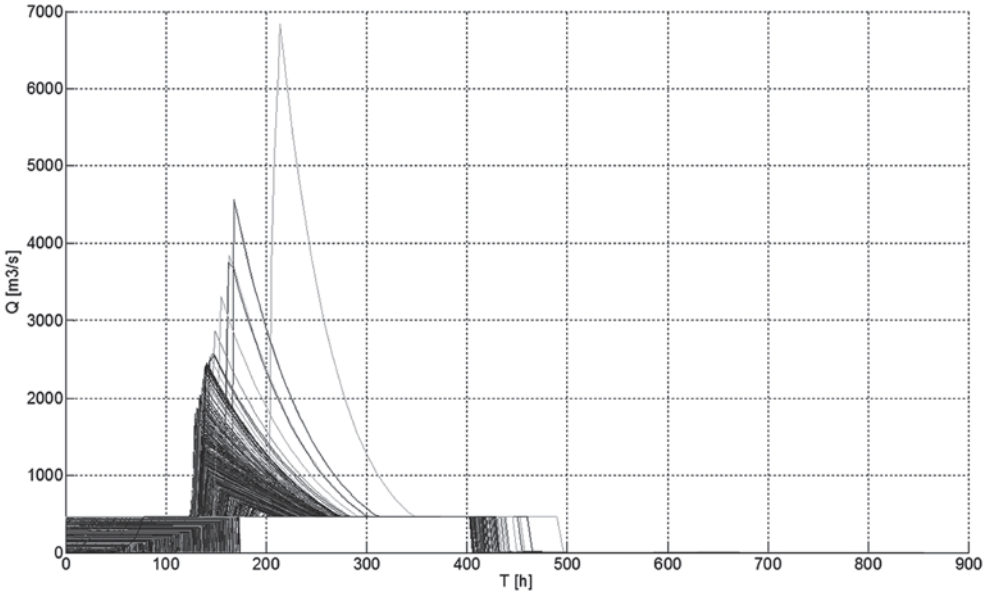

Fig. 8. Hydrographs of outflows from the Racibórz reservoir, 10 000 waves, a variable time of base flood elevation

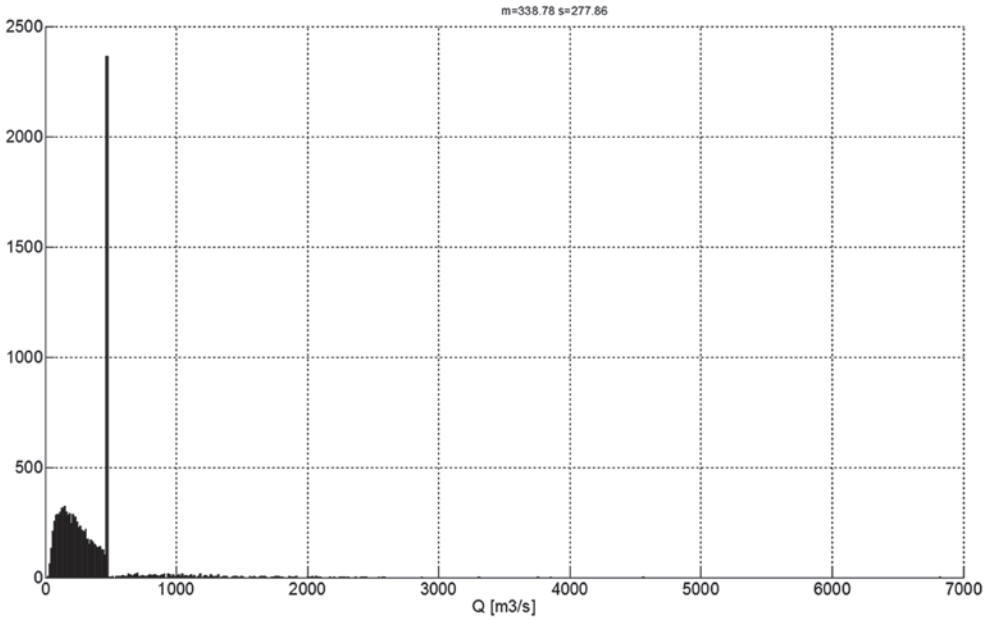

Fig. 9. A histogram of maximum outflow values, 10 000 waves, a variable time of base flood elevation

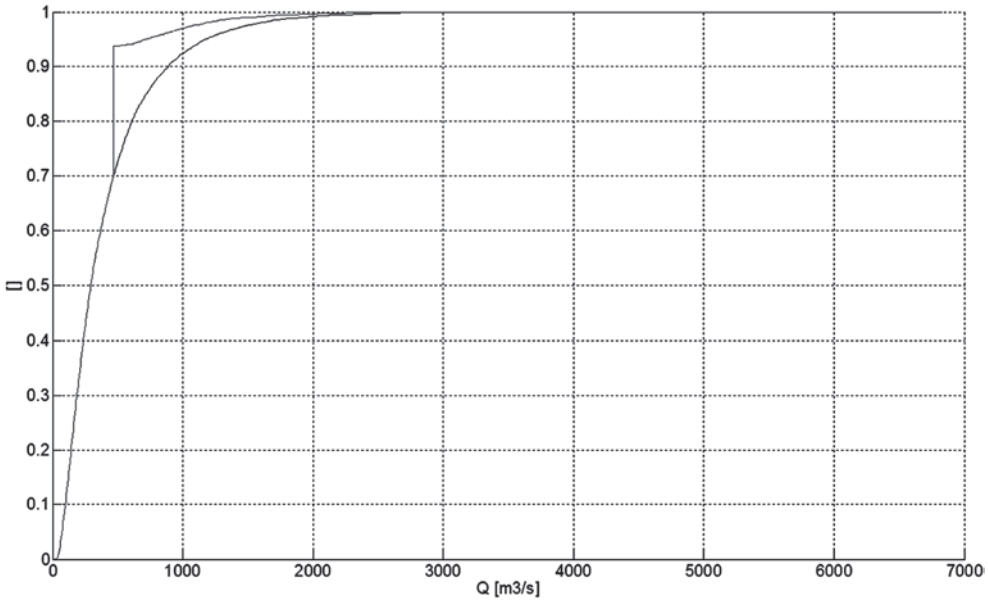

Fig. 10. Empirical cumulative distribution functions of maximum inflow values (blue) and maximum discharged outflows (red) in the reservoir, 10 000 waves, a variable time of base flood elevation

9.1.2. The case of semi-fixed outflow control rule

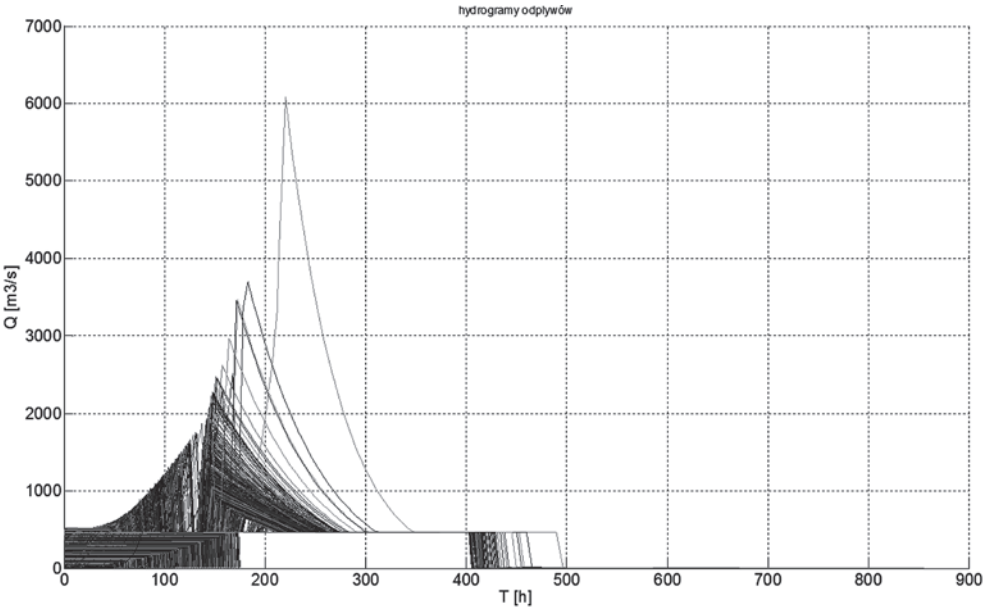

Fig. 11. Hydrographs of wave outflows from the Racibórz reservoir, 10 000 waves, a variable time of base flood elevation

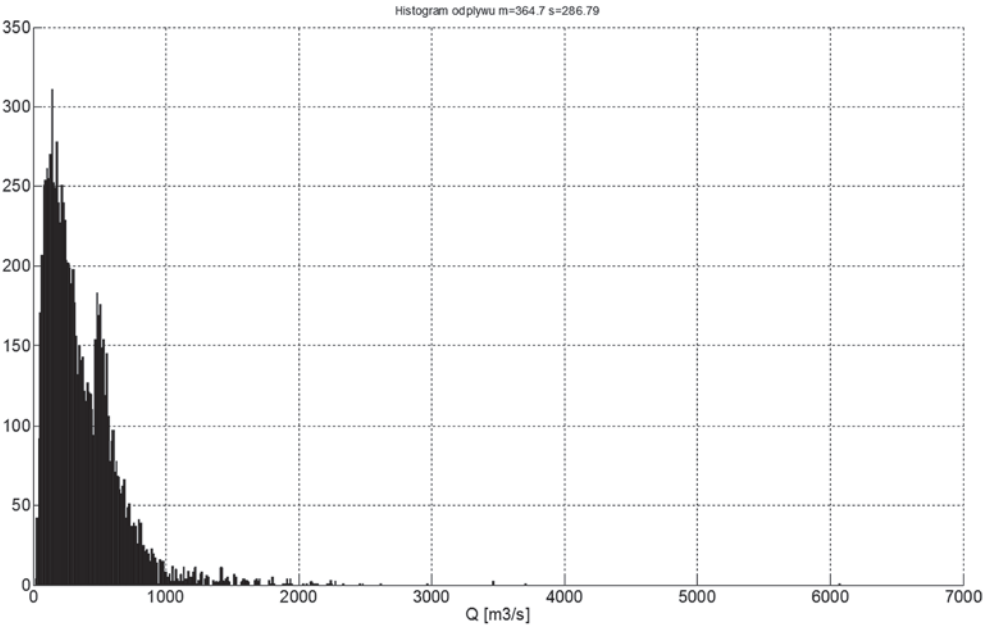

Fig. 12. A histogram of maximum outflow values, 10 000 waves, a variable time of base flood elevation

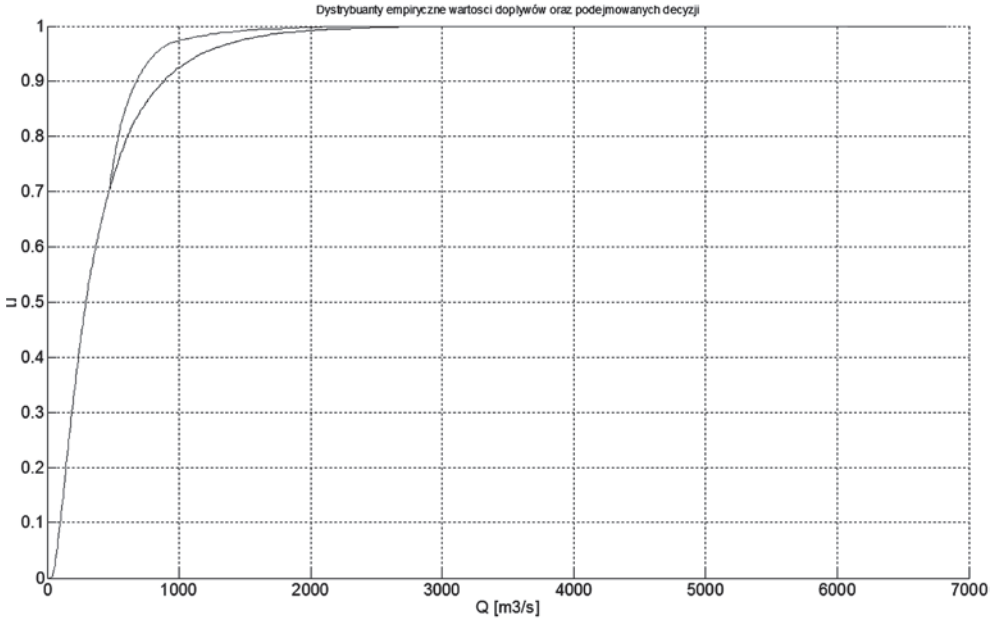

Fig. 13. Empirical cumulative distribution functions of maximum inflow values (blue) and maximum discharged outflows (red) in the reservoir, 10 000 waves, a variable time of base flood elevation

9.1.3. The case of step outflow control rule

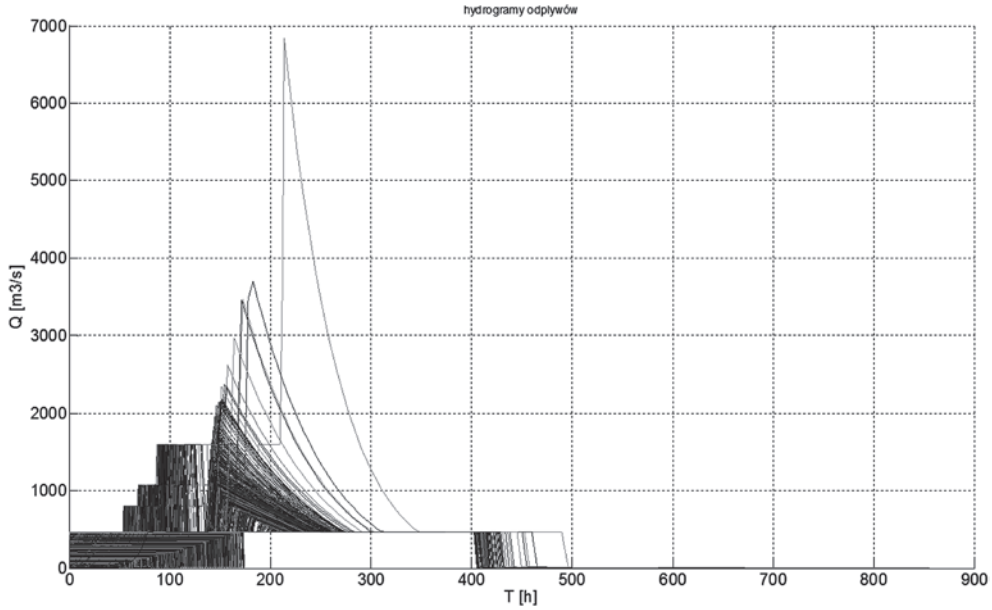

Fig. 14. Hydrographs of wave outflows from the Racibórz reservoir, 10 000 waves, a variable time of base flood elevation

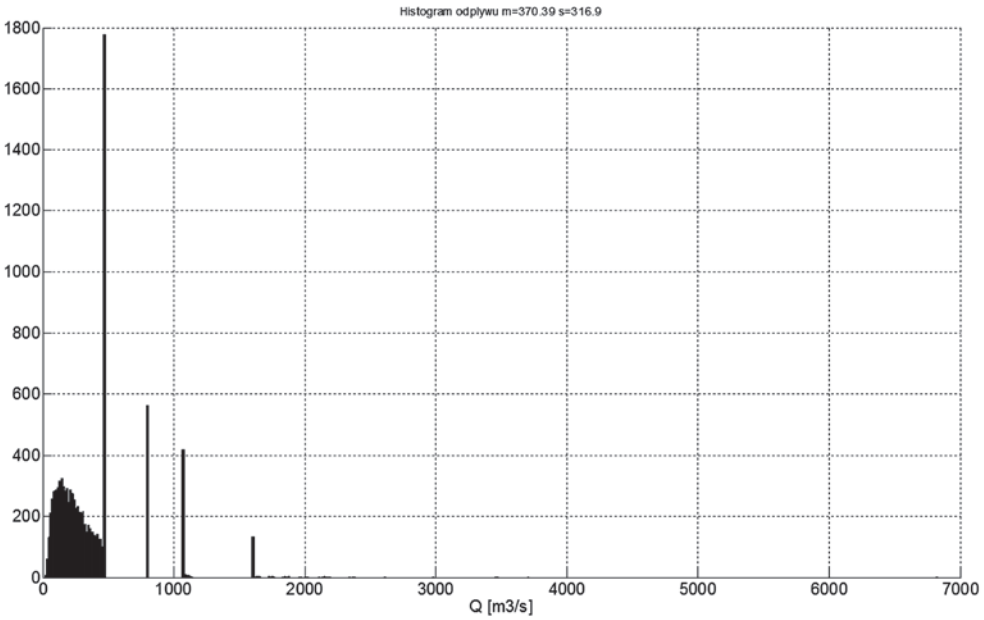

Fig. 15. A histogram of maximum outflow values, 10 000 waves, a variable time of base flood elevation

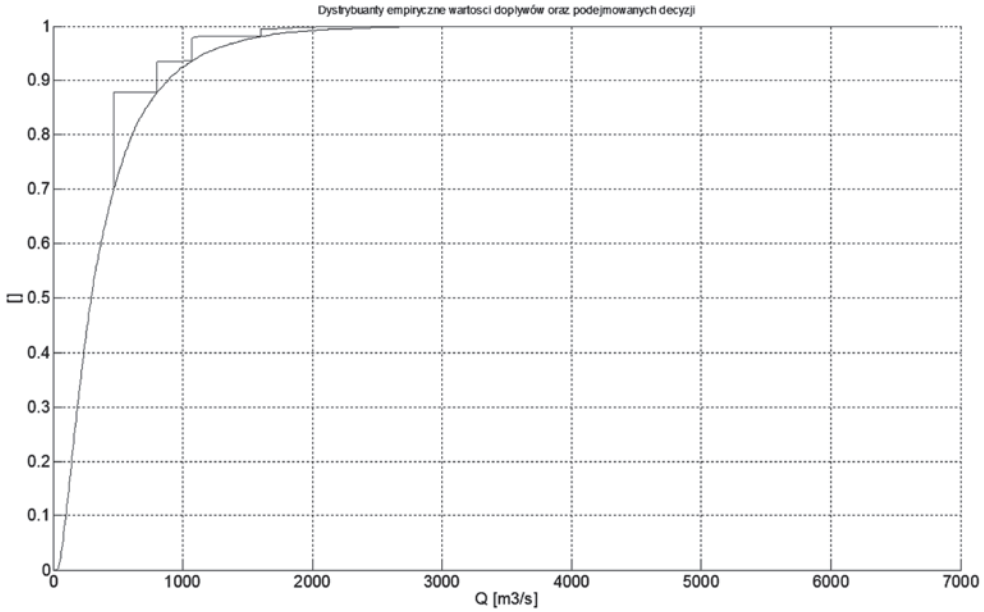

Fig. 16. Empirical cumulative distribution functions of maximum inflow values (blue) and maximum discharged outflows (red) in the reservoir, 10 000 waves, a variable time of base flood elevation

9.2. An analysis of Racibórz polder control for a population of hypothetical flood waves characterised by a constant time of base flood elevation

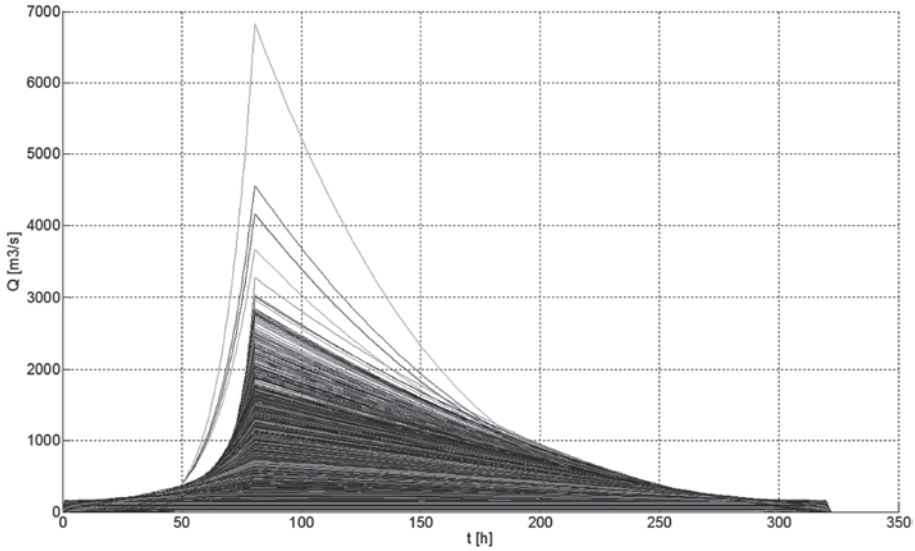

Fig. 17. Obtained hydrographs of flood waves based on the generated parameters, 10 000 waves, a constant time of base flood elevation

9.2.1. The case of fixed outflow control rule

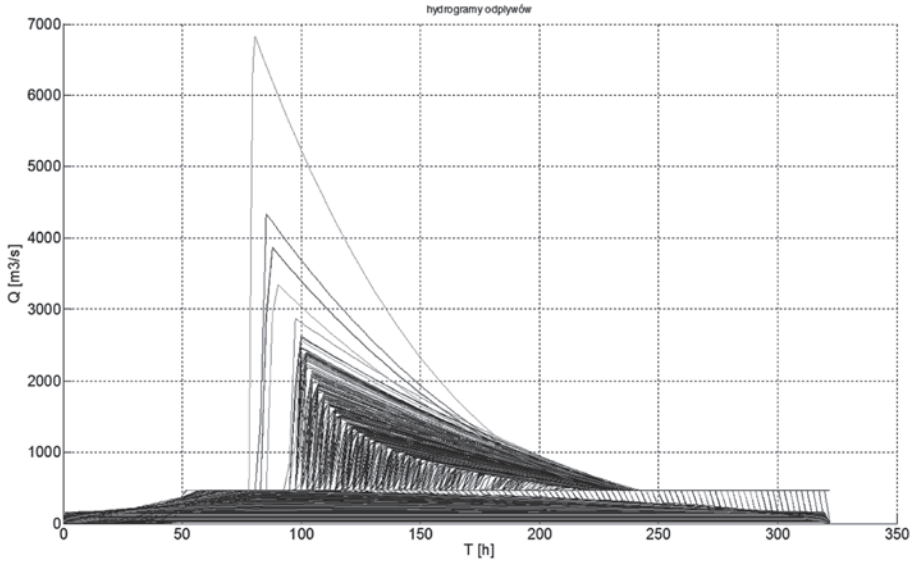

Fig. 18. Obtained hydrographs of outflows, 10 000 waves, a constant time of base flood elevation

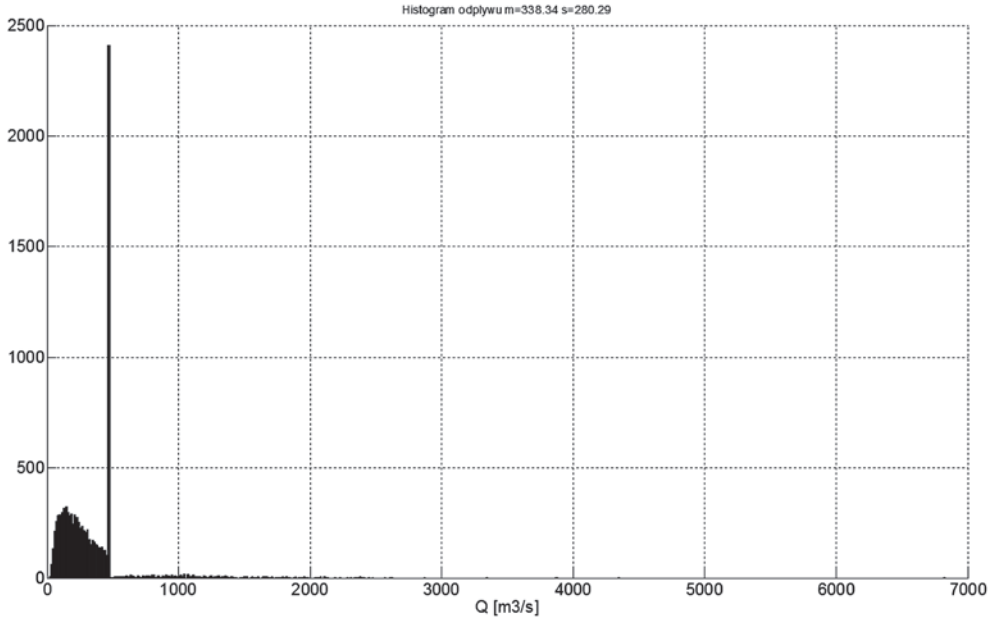

Fig. 19. A histogram of maximum outflow values, 10 000 waves, a constant time of base flood elevation

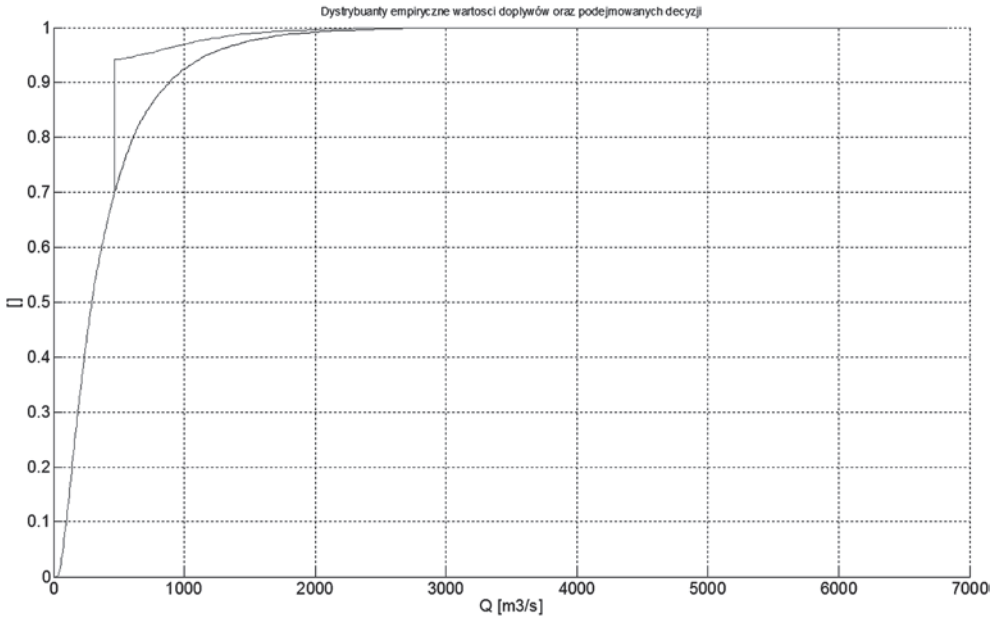

Fig. 20. Empirical cumulative distribution functions of maximum inflow values (blue) and maximum discharged outflows (red) in the reservoir, 10 000 waves, a constant time of base flood elevation

9.2.2. The case of semi-flexible outflow control rule

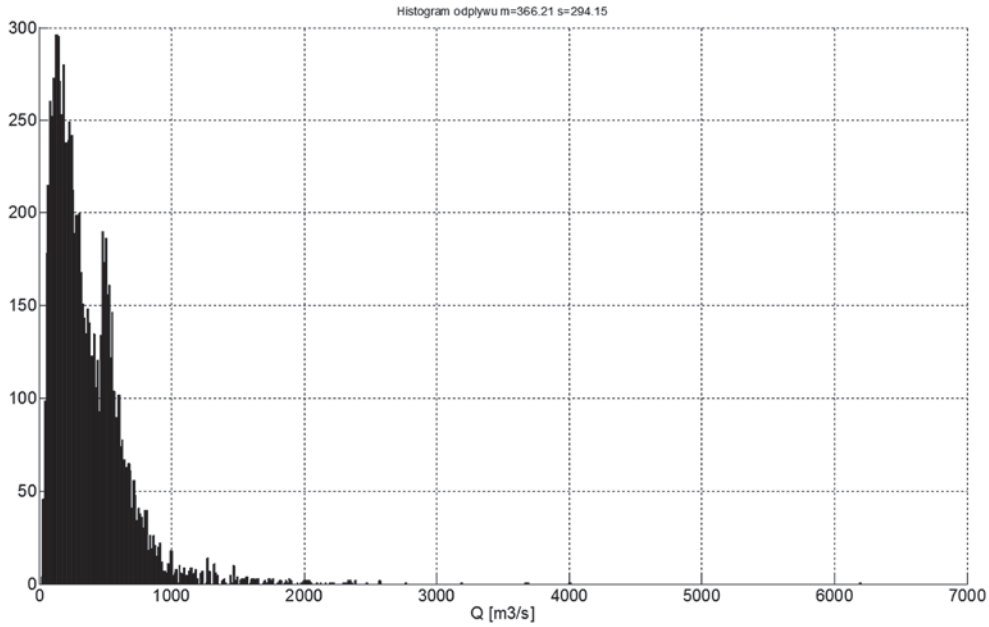

Fig. 21. A histogram of maximum outflow values, 10 000 waves, a constant time of base flood elevation

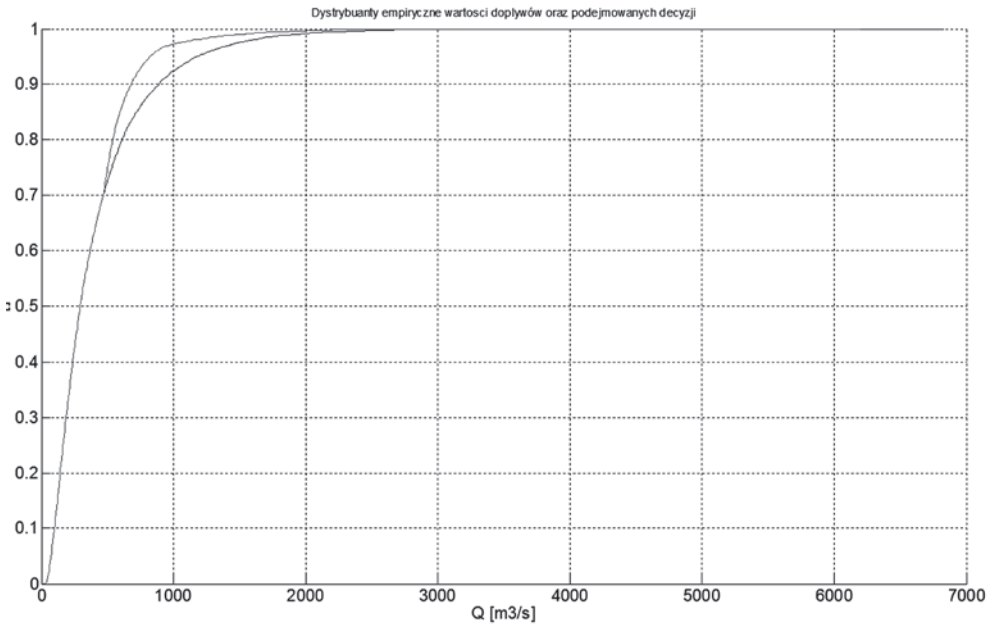

Fig. 22. Empirical cumulative distribution functions of maximum inflow values (blue) and maximum discharged outflows (red) in the reservoir, 10 000 waves, a constant time of base flood elevation

9.2.3. The case of step outflow control rule

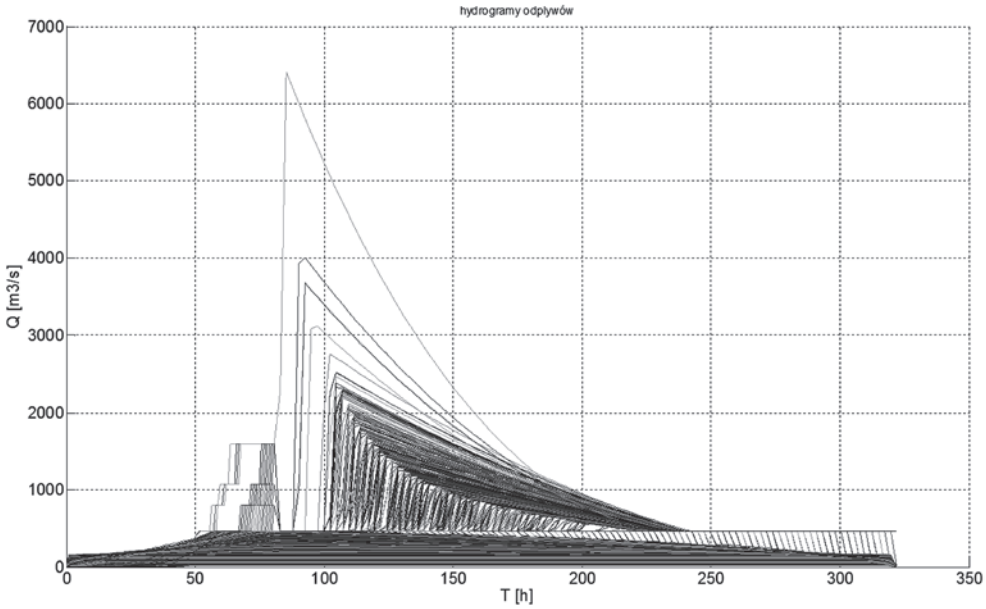

Fig. 23. Hydrographs of outflows, 10 000 waves, a constant time of base flood elevation

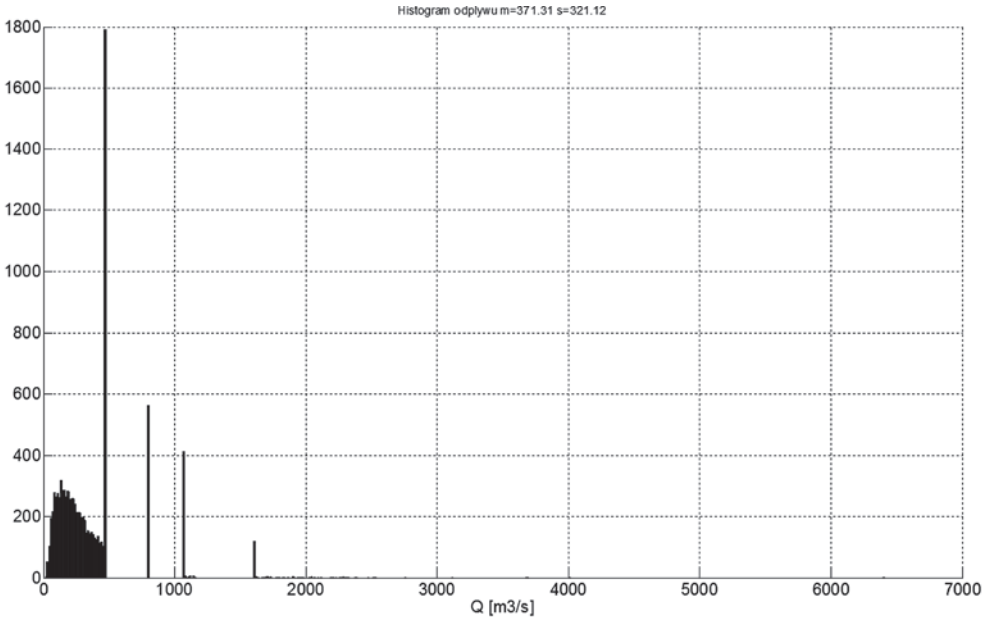

Fig. 24. A histogram of maximum outflow values, 10 000 waves, a constant time of base flood elevation

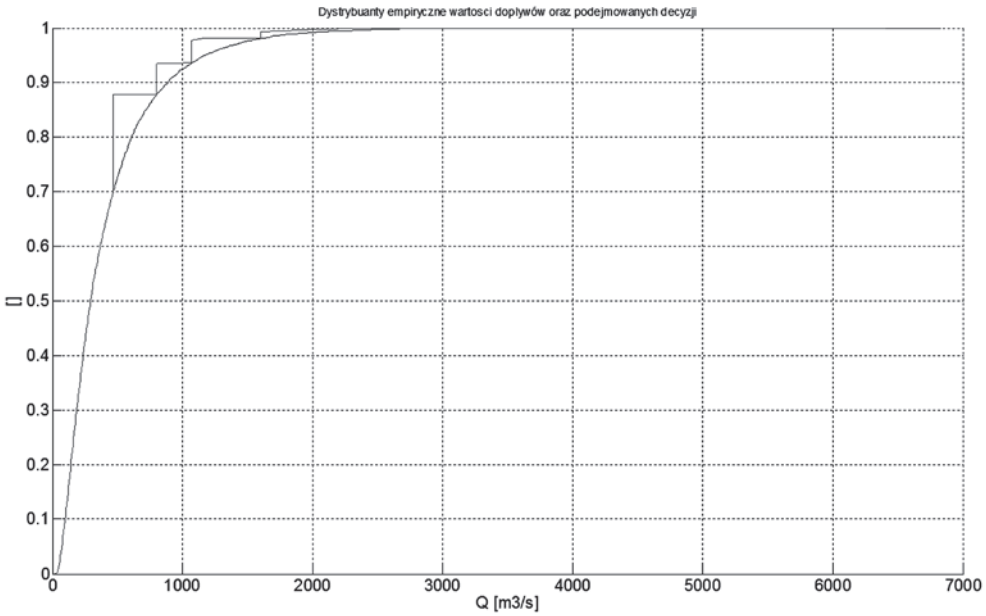

Fig. 25. Empirical cumulative distribution functions of maximum inflow values (blue) and maximum discharged outflows (red) in the reservoir, 10 000 waves, a constant time of base flood elevation

10. Conclusions

This study discusses the application of a method for determining characteristic flow values downstream of a retention reservoir and generating flood wave hydrographs using a Monte Carlo method, a two-dimensional copula function and power functions describing the hydrograph forms. The example discussed shows the interrelations between generated flood wave characteristics and hydrograph forms; the study also demonstrates the applicability of the results of this method in assessing the operation of a retention reservoir. A two-dimensional random number generator for peak values and volumes of flood waves was developed for the adopted Gumbel-Hougaard copula distribution. The forms of hydrographs of hypothetical flood waves were determined for a generated set of 10 000 two-element sets of flood wave characteristics, including the peak value and volume. The described operations were completed in order to perform an analysis of decisions made by staff managing a retention reservoir with the use of three control rules: fixed outflow, semi-flexible outflow and step outflow control. The analysis was performed for two types of populations of hypothetical flood waves, each consisting of 10 000 elements: with a variable and with a constant time of base flood elevation. All analyses were performed assuming a constant flood control capacity equal to 185 Mm^3.

The analyses performed clearly demonstrate that the reduction values of characteristic flows for a probability of exceedance of 1% reach a maximum value up to about 920 m^3/s in the control regimes analysed. Calculations were also performed for larger waves (a lower

probability of exceedance, peak, volume), but conclusions concerning the value of reduction of larger waves are affected by a larger error due to the level of precision in the analyses performed. About 2% points per generated population represent a set without correct solutions of the proposed equations. This absence of solutions results from the relation between the random variable of volume and the product of random variables of time and peak value. The problem may be solved by introducing truncated distributions that will be discussed in a separate study. The indicated points are concentrated principally in the areas of relatively small peak values and very large volumes.

A comparison of results for the populations with a variable time and a constant time of base flood elevation represents another important component of the analyses performed. In the analysis with a constant time value, an average value of wave duration was adopted. It may be concluded that the results of both analyses are almost identical with an accuracy of 5% (Fig. 34). This results principally from the time of base flood elevation being expressed as a function of wave volume (or vice versa, the volume as a function of time, this is irrelevant for calculation results), as a natural consequence of the relation between time and volume, and from a correlation analysis. This consistency would not exist if time was expressed as a function of peak value. There are no obstacles (except the limited number of elements in historical sequences) that would prevent generation of three numbers (Q, V, T), but such an approach extends calculation time, and consequently it is more reasonable to use the time–volume relationship. Assumptions for the indicated alternative approach and examples of analyses were presented in another study [3]. It should also be emphasised that the statistical independence of random variables Q and V was assumed in the analyses which limits the upper values of reduction in a justified manner.

Table 4

A statement of characteristic flow values and calculated reduction values for the Racibórz reservoir, Racibórz cross-section, flood control capacity of 185 Mm^3, the method with a variable time of base flood elevation

Probability of exceedance	Racibórz-Miedonia water-level gauge	Fixed outflow rule	Reduction – fixed outflow rule	Semi-fixed outflow rule	Reduction – semi-fixed outflow rule	Step outflow rule	Reduction – step outflow rule
0.5	293.5	294.4	–0.9	294.4	-0.9	294.4	-0.9
0.4	368.1	368.6	–0.4	368.6	-0.4	368.6	-0.4
0.3	469.1	469.8	–0.6	469.8	-0.6	469.8	-0.6
0.2	623.0	470.0	153.0	540.5	82.5	470.0	153.0
0.1	923.3	470.0	453.3	680.3	243.0	800.0	123.3
0.05	1277.8	708.5	569.3	820.1	457.7	1070.0	207.8
0.03	1578.0	1017.6	560.3	953.9	624.1	1070.0	508.0
0.02	1841.9	1181.8	660.1	1139.5	702.4	1119.9	722.0

Table 4 cont.

0.019	1877.0	1213.8	663.3	1170.8	706.3	1600.0	277.0
0.018	1914.4	1225.1	689.4	1180.8	733.6	1600.0	314.4
0.017	1954.5	1260.7	693.8	1214.7	739.8	1600.0	354.5
0.016	1997.5	1270.5	727.0	1223.4	774.1	1600.0	397.5
0.015	2043.9	1305.9	737.9	1257.3	786.6	1600.0	443.9
0.014	2094.2	1318.1	776.1	1268.4	825.8	1600.0	494.2
0.013	2149.1	1357.7	791.4	1305.8	843.3	1600.0	549.1
0.012	2209.3	1381.6	827.7	1354.3	855.1	1600.0	609.3
0.011	2276.0	1445.4	830.6	1415.8	860.2	1600.0	676.0
0.01	2350.4	1489.6	860.8	1432.8	917.6	1600.0	750.4

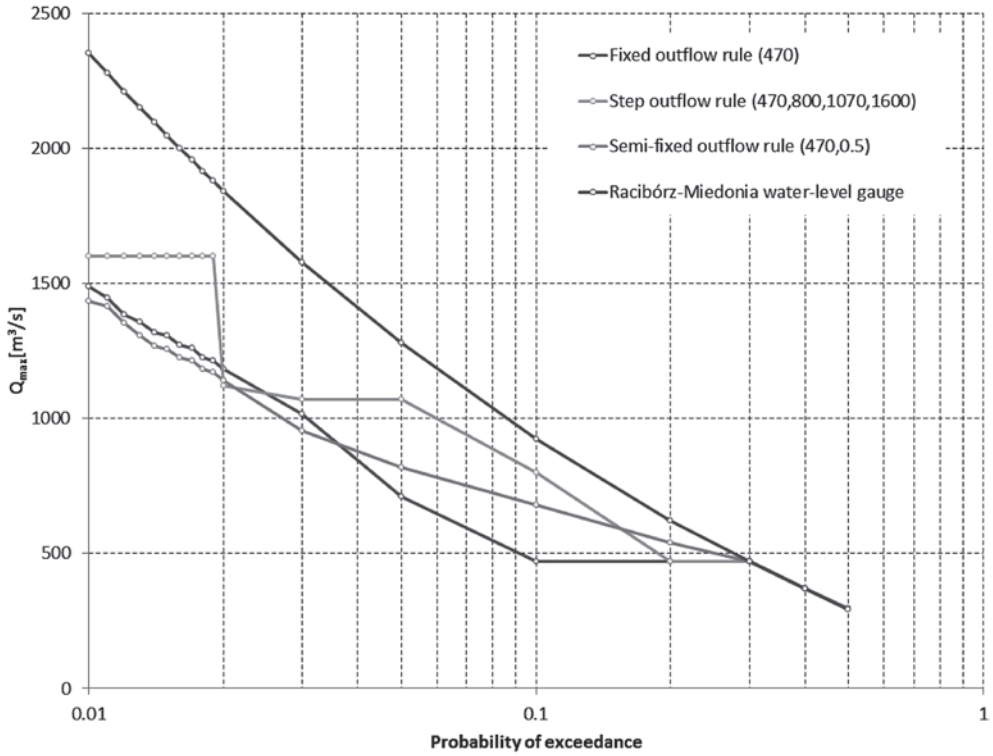

Fig. 26. Characteristic flow values downstream of the Racibórz reservoir for the analysed control rules, 10 000 waves, a variable time of base flood elevation

Table 5

A statement of characteristic flow values and calculated reduction values for the Racibórz reservoir, Racibórz cross-section, flood control capacity of 185 Mm^3, the method with a constant time of base flood elevation

Probability of exceedance	Racibórz-Miedonia water-level gauge	Fixed outflow rule	Reduction – fixed outflow rule	Semi-fixed outflow rule	Reduction – semi-fixed outflow rule	Step outflow rule	Reduction – step outflow rule
0.5	293.5	294.4	–0.9	294.4	–0.9	294.4	–0.9
0.4	368.1	368.6	–0.4	368.6	–0.4	368.6	–0.4
0.3	469.1	469.8	–0.6	469.8	–0.6	469.8	–0.6
0.2	623.0	470.0	153.0	540.5	82.5	470.0	153.0
0.1	923.3	470.0	453.3	680.3	243.0	800.0	123.3
0.05	1277.8	653.1	624.7	820.1	457.7	1070.0	207.8
0.03	1578.0	1014.9	563.1	967.2	610.8	1070.0	508.0
0.02	1841.9	1206.4	635.5	1162.3	679.6	1152.4	689.5
0.019	1877.0	1242.5	634.5	1184.5	692.5	1600.0	277.0
0.018	1914.4	1277.3	637.2	1219.2	695.3	1600.0	314.4
0.017	1954.5	1299.8	654.7	1237.8	716.7	1600.0	354.5
0.016	1997.5	1323.9	673.6	1269.2	728.3	1600.0	397.5
0.015	2043.9	1347.0	696.9	1283.6	760.3	1600.0	443.9
0.014	2094.2	1364.2	730.0	1321.4	772.8	1600.0	494.2
0.013	2149.1	1404.4	744.7	1338.2	810.9	1600.0	549.1
0.012	2209.3	1456.0	753.3	1393.4	815.9	1600.0	609.3
0.011	2276.0	1512.1	763.9	1463.9	812.1	1600.0	676.0
0.01	2350.4	1554.9	795.6	1480.8	869.6	1600.0	750.4

Table 6

A statement of differences between characteristic flows according to the methods with a variable and with a constant time of base flood elevation for the Racibórz cross-section, flood control capacity of 185 Mm^3

Probability of exceedance	Fixed outflow rule	Semi-fixed outflow rule	Step outflow rule
0.5	0	0	0
0.4	0	0	0
0.3	0	0	0
0.2	0	0	0
0.1	0	0	0

Table 6 cont.

0.05	55	0	0
0.03	3	–13	0
0.02	–25	–23	–33
0.019	–29	–14	0
0.018	–52	–38	0
0.017	–39	–23	0
0.016	–53	–46	0
0.015	–41	–26	0
0.014	–46	–53	0
0.013	–47	–32	0
0.012	–74	–39	0
0.011	–67	–48	0
0.01	–65	–48	0

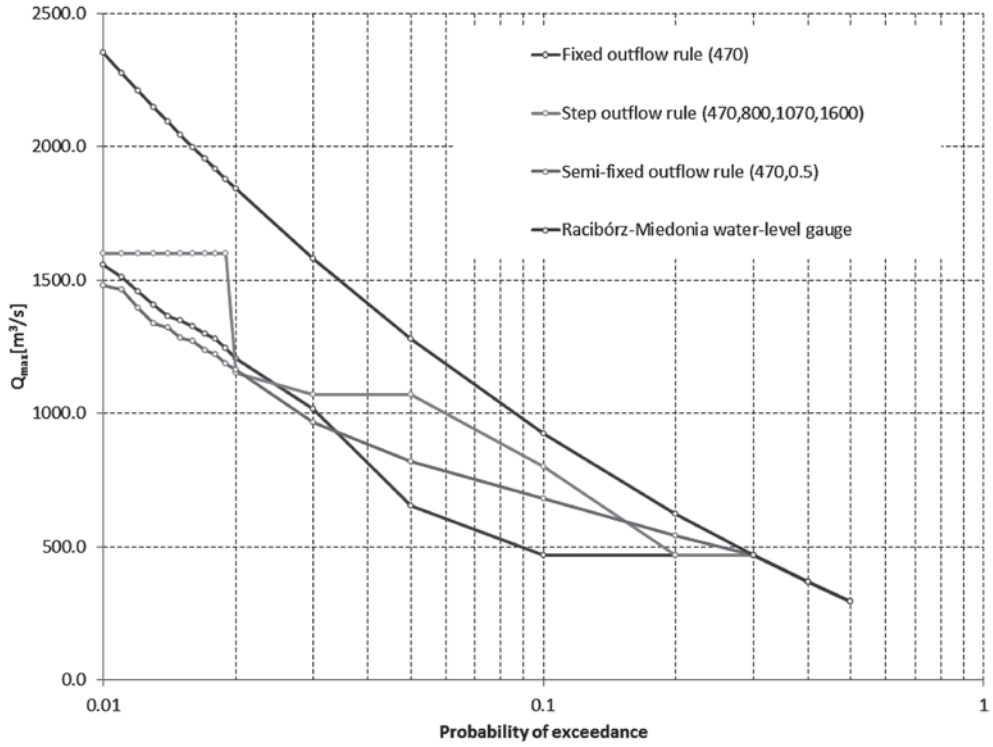

Fig. 27. Characteristic flow values downstream of the Racibórz reservoir for the analysed control rules, 10 000 waves, a constant time of base flood elevation

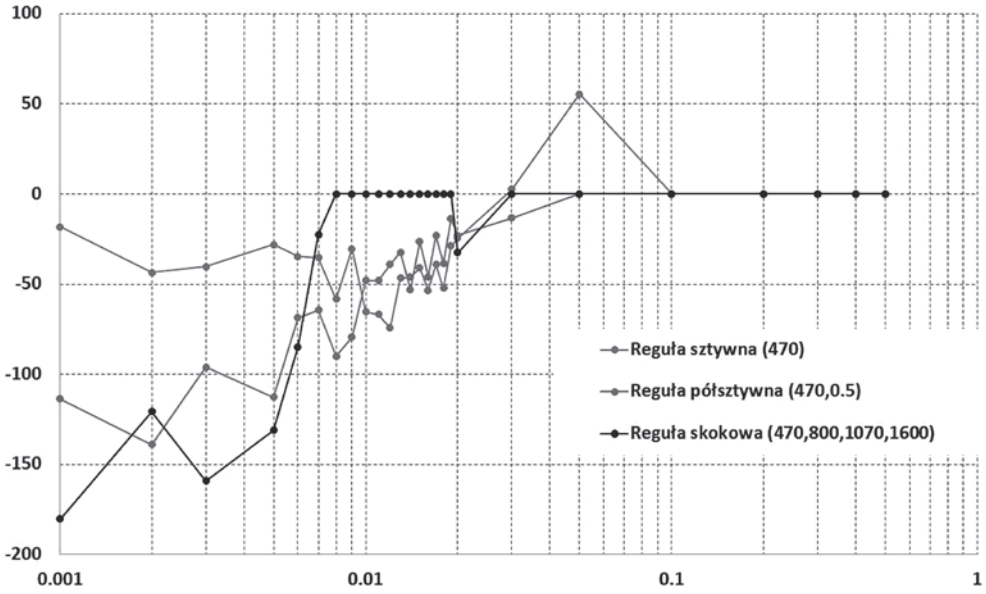

Fig. 28. A statement of differences between characteristic flows according to the methods with a variable and with a constant time of base flood elevation

The method proposed provides an alternative tool that may be used in testing or stochastic optimization of retention reservoir parameters and control rule parameters under flood conditions. Due to the possibilities offered by the copula function, as used in this study, the proposed method of generating hydrographs and testing reservoir parameters provides invaluable material for simulations, characterised by theoretical marginal distribution functions consistent with empirical marginal distribution functions.

The possibilities of the proposed use of MC methods are not limited to generating flood waves and analyses of retention reservoir operation. The method discussed gives freedom in designing and testing structure and equipment parameters that are dependent on certain random, statistical values. The effectiveness of MC methods in the area of application described is enhanced by the use of the copula function in generating multivariate distributions of a random variable with various, freely selected marginal distributions.

References

[1] Twaróg B., *Application the Monte Carlo method in generating flood wave hydrographs using the copula function*, Czasopismo Techniczne z. 2-Ś/2007.

[2] Twaróg B., Application of the copula function in generating probability multivariate distributions of random variable defined for a set of flood wave characteristics, Czasopismo Techniczne z. Ś-10/2006.

[3] Twaróg B., *Selected aspects of risk assessment in environmental engineering. Part II. Application of copula functions*, 6th National Seminar on Environmental Hazards, Paszkówka, October 2005, IMGW Monographs, Warsaw 2005, 68–89.

[4] Twaróg B., *Selected aspects of risk assessment in environmental engineering. Part I. Application of the Gumbel mixed model*, 6th National Seminar on Environmental Hazards, Paszkówka, October 2005, IMGW Monographs, Warsaw 2005, 90–110.
[5] *Calculation of maximum flows characterised by probability of exceedance p=0.3% and p=1% for the Oder river at the Koźle water-level gauge cross-section*, Institute of Meteorology and Water Management – National Research Institute, Kraków Branch, Hydrological Forecast Bureau in Kraków, Hydrological Documentation Team in Kraków, January 2015.
[6] *A concept of protection of the Oder river valley against floods, km 66+144, Kędzierzyn Koźle land district: A technical description and calculations*, HART S.C., Wrocław, August 2000.
[7] *A concept of flood protection of Kędzierzyn-Koźle and Reńska Wieś township: A technical description and calculations*, HART S.C., Wrocław, August 2000.
[8] Stodolak R., *Environmental aspects of water management in a dry flood control basin – a case study of the planned Racibórz reservoir*, Infrastruktura i Ekologia Terenów Wiejskich, No. 9/2008, Polish Academy of Sciences, Kraków Branch, 171–180.
[9] Stodolak R., A *study of flood wave reduction in 2010 by the Racibórz reservoir and Buków polder*, Infrastruktura i Ekologia Terenów Wiejskich, No. 3/III/2012, Polish Academy of Sciences, Kraków Branch, 235–244.
[10] *Water Management Instructions, water use assessment including instructions for water management in periodic processes of impoundment and retention of water from the Oder river in the Buków polder*, RZGW, Gliwice 2014.
[11] *Water use assessment including instructions for water management in periodic processes of impoundment and retention of water from the Oder river in the Buków polder*, RZGW, Gliwice 2014.
[12] Regulation by the Minister of Environment on technical conditions for hydraulic engineering structures and their locations, dated 20 April 2007 (Journal of Laws Dz.U. No. 86, item 579).
[13] Regulation by the Minister of Infrastructure and Development amending the Regulation on technical conditions for public roads and their locations, dated 17 February 2015 (Journal of Laws Dz.U. of 2015 item 329).
[14] Regulation by the Minister of Transport and Marine Economy on technical conditions for road engineering structures and their locations, dated 30 May 2000 (Journal of Laws Dz.U. No. 63, item 735).
[15] POIG.07.01.00–00–025/09, Raport z wykonania map zagrożenia powodziowego i map ryzyka powodziowego, projekt ISOK – raport z zakończenia realizacji zadania 1.3.2 – przygotowanie danych hydrologicznych w zakresie niezbędnym do modelowania hydraulicznego [*Report on completed flood hazard and flood risk maps, ISOK project – a report on completed task no. 1.3.2 – preparing hydrological data necessary for hydraulic modelling*], IMGW PIB, 2009.
[16] *Atlas of floodplains for concepts with and without capital expenditure projects, considering the existing and planned flood control infrastructure for the Oder river stretch between the planned Racibórz reservoir and the Brzeg Dolny water-level gauge*, CES GmbH, 2011.
[17] Regulation by the Minister of Environment, Minister of Transport, Building Industry and Marine Economy, Minister of Administration and Digitization and the Minister of Home Affairs concerning development of flood hazard and flood risk maps, dated 21 December 2012 (Journal of Laws Dz.U. of 2013 item 104).

TECHNICAL TRANSACTIONS | CZASOPISMO TECHNICZNE
ENVIRONMENTAL ENGINEERING | ŚRODOWISKO
2-Ś/2015

ALEKSANDER URBAŃSKI*, ŁUKASZ MICHALSKI**

FINITE ELEMENT ANALYSIS OF LATERAL EARTH PRESSURE ON A LAGGING IN SOLDIER PILE WALLS

ANALIZA NUMERYCZNA PARCIA BOCZNEGO GRUNTU W UKŁADACH TYPU „ŚCIANKA BERLIŃSKA”

Abstract

The main aim of this article is to show how different ways of modelling a construction process of soldier pile walls influence the development of the computational lateral earth pressure in this type of structure. Moreover, the paper includes an analysis of soldier pile systems designed in both traditional (Coulomb, Rankine etc.) and numerical approaches. In order to analyse the above problems, several numerical models of soldier pile walls were built and the results obtained were then compared.

Keywords: excavation, soldier pile wall, FEM

Streszczenie

Głównym celem artykułu jest odpowiedź na pytanie, w jaki sposób różne sposoby modelowania technologii realizacji ścianek berlińskich wpływają na rozwój obliczeniowego parcia czynnego w tego typu konstrukcjach oporowych. Ponadto praca zawiera analizę porównawczą projektowania ścianek berlińskich zarówno w ujęciu tradycyjnym, jak i numerycznym. W celu analizy powyższych problemów zbudowano kilka modeli numerycznych, a uzyskane z nich wyniki porównywano.

Słowa kluczowe: wykop, ścianka berlińska, MES

DOI: 10.4467/2353737XCT.15.234.4620

* Prof. DSc. PhD. Aleksander Urbański, Institute of geotechnics, Faculty of Environmental Engineering, Cracow University of Technology.

** MSc. Łukasz Michalski (PhD. student), Faculty of Environmental Engineering, Cracow University of Technology.

1. Introduction

Soldier pile and lagging walls are commonly used systems for supporting excavations in urban environments, where property lines or roads prohibit sloped or benched excavations. The soldier pile and lagging walls can be more economical and faster to construct than many other secure systems of excavations. In the past, they were used as elements of military fortifications.

The main components of the considered systems are steel H-piles placed vertically with spacing ranging from 1.2 m to 3.0 m, with the lagging placed between the piling to retain the soil. The lagging may be rough sawn timber, metal decking or even precast concrete planks. H-piles can be installed by driving, vibrating or by drilling a hole and wet-setting the pile in a grout column at the bottom of the excavation. Figure 1 shows the sort of the soldier pile walls which are discussed in this paper [1], [4].

The paper discusses only non-anchored soldier pile wall systems, which are used for a limited excavation depth, (in practice, $h < \sim 4.0$m). For these systems, correct evaluation of the earth pressure is of particular importance.

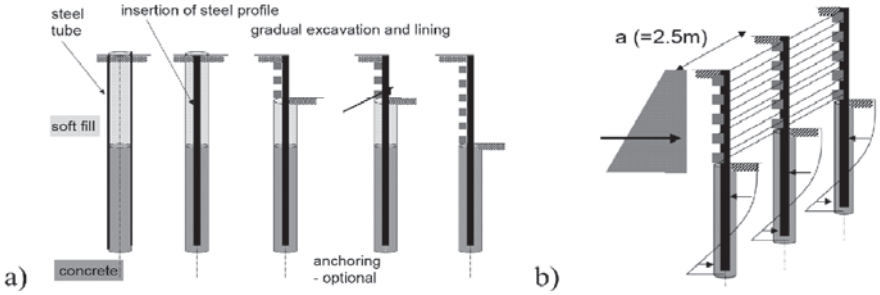

Fig. 1. Soldier pile wall („Berlin" type): a) phases of construction, b) load action

In continuous rigid earth retention systems, such as sheet pile walls, the lateral earth pressure and the displacement are generally assumed to be constant along the length of the wall (this is the one of the basic rules of analysis in the plane strains – PS). In the soldier pile and lagging systems, the lagging is often significantly less stiff than the steel soldier piles. As the lagging deflects, the soil tends to bridge between the stiffer elements resulting in a lower pressure on the lagging [2, 4].

The main aim of this article is to show how different ways of modelling the construction process of soldier pile walls influence the development of the computational lateral earth pressure in this type of structure. Moreover, the paper also discusses an analysis of the soldier pile systems designed in both traditional (Coulomb, Rankine, etc.) and numerical approaches. In order to analyse these problems, several numerical 3D models of the soldier pile walls from Figure 1 were built.

The article is the first part of wider research work devoted to creating a design algorithm for soldier wall systems based on computer modelling. However, the main subject of this research are problems regarding the bearing capacity of the underground part of the structure, and the recognition of lateral loads such as earth pressure will also be an important issue.

2. Geometry, material and load model of the soldier pile wall

A detailed geometric model of the soldier pile wall used in this case study is shown in Figure 2. The structure of the wall consists of:
– steel profiles IPE 360, length 8.0 m placed vertically at 2.5 m, E = 210 GPa, ν = 0.3,
– concrete piles Ø 0.5 m, length 4.0 m, E = 30 GPa, ν = 0.2 (under the bottom of the excavation),
– timber lagging 0.25 m × 0.10 m, E = 11 GPa, ν = 0.25.

The described secure system of excavation represents the case of a cantilever wall where anchoring is not required.

Two classes of soils were used in the analysis: cohesive soils and cohesionless soils. No additional load is assumed above the wall.

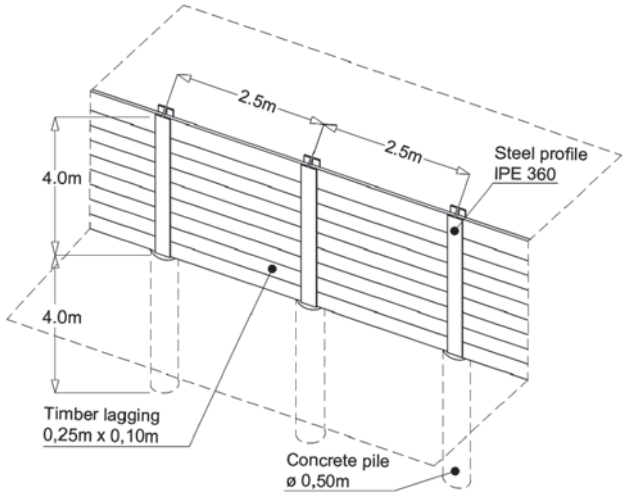

Fig. 2. Geometric model of the soldier pile wall

Four modelling scenarios of the construction process of a soldier pile wall were analysed. The process consists of two first steps which are common in all scenarios: 1 – drilling the hole, 2 – pouring the concrete and placing the steel profile. For the further phase of the construction, different scenarios are as follows (see Figure 3):
– first modelling scenario (in one stage): 3 – excavation to the required level (–4.0 m), 4 – placing the lagging with use of a controlled unloading algorithm,
– second modelling scenario (in four stages – lagging immediately after the excavation): 3, 4, 5, 6 – simultaneous excavation and placing the lagging,
– third modelling scenario (in four stages – excavation then lagging in next step): steps 3, 5, 7, 9 – excavation, steps 4, 6, 8, 9, 10 – placing the lagging,
– fourth modelling scenario (in sixteen stages): steps 3 to 31 – excavation, steps 4 to 32 – placing the lagging.

Deactivation of a certain part of the numerical model (corresponding to the excavation zone) is required in order to model the process of excavation. For this purpose, Zsoil 2012 Student v12.19 software was used. This allows instability problems occurring in the numerical solution due to unbalanced internal forces to be avoided by applying the partial relaxation technique.

First modelling scenario (in one stage)

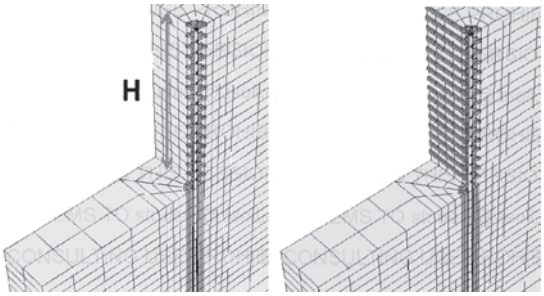

Second modelling scenario (in four stages – lagging immediately after excavation)

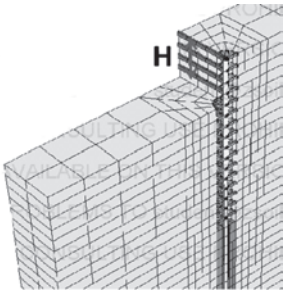

Third modelling scenario (in four stages – excavation then lagging in next step)

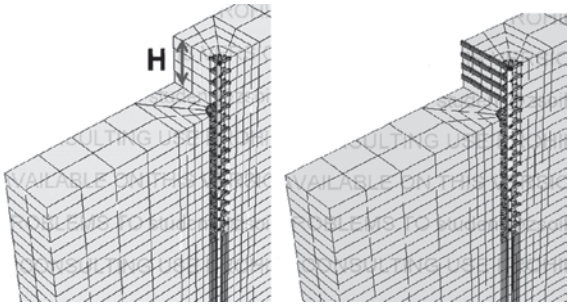

Fourth modelling scenario (in sixteen stages)

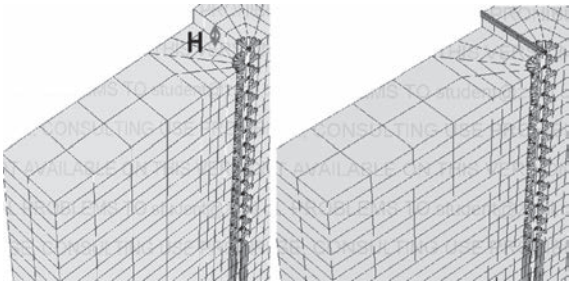

Fig. 3. Considered modelling scenarios of the construction process of the soldier pile wall – step of the excavation and lagging placement

The principle of operation is based on the deactivation of the elements (its stiffness) at the part of the numerical model corresponding to the excavation zone while the resultant internal forces (equivalent to stresses) are preserved in the deleted elements. These forces are in the following incremental steps gradually reduced to zero. At the edge of the remaining area, the difference between internal forces at the deleted and remaining elements is a load (tending to zero), which facilitates the convergence of the iterative process. Figure 4 shows the process of controlled unloading by using the LTF function (Load Time Function).

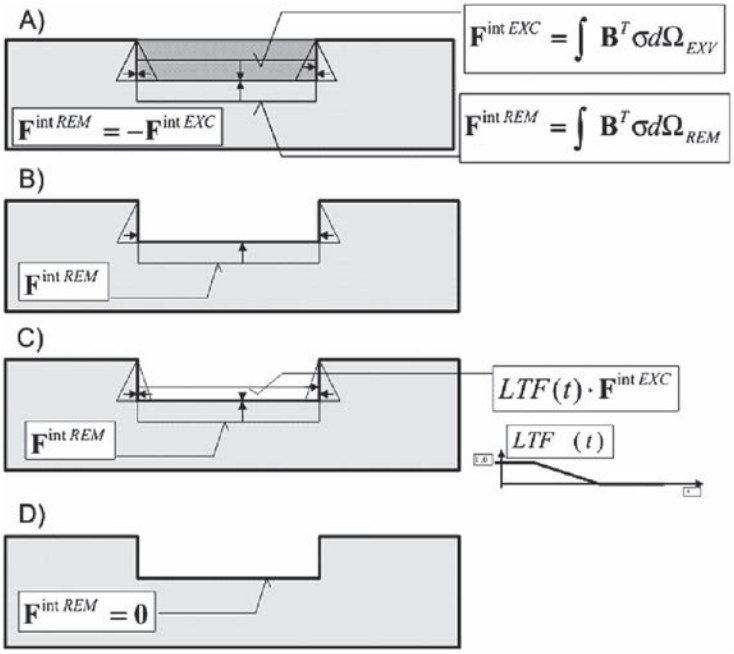

Fig. 4. The process of controlled unloading:
a) equilibrium state before excavation, b) forces after excavation without controlled unloading, c) forces after excavation with controlled unloading, d) the final state of equilibrium after unloading

3. FE models of the soldier pile wall

For analysing the problem of lateral earth pressure on the lagging in a soldier pile wall, 3D FE models were built (see Figure 5), and named as follows:

– "shell model",
– "beam-shell model",
– "beam model".

Detailed description of each of the FE models can be found below.

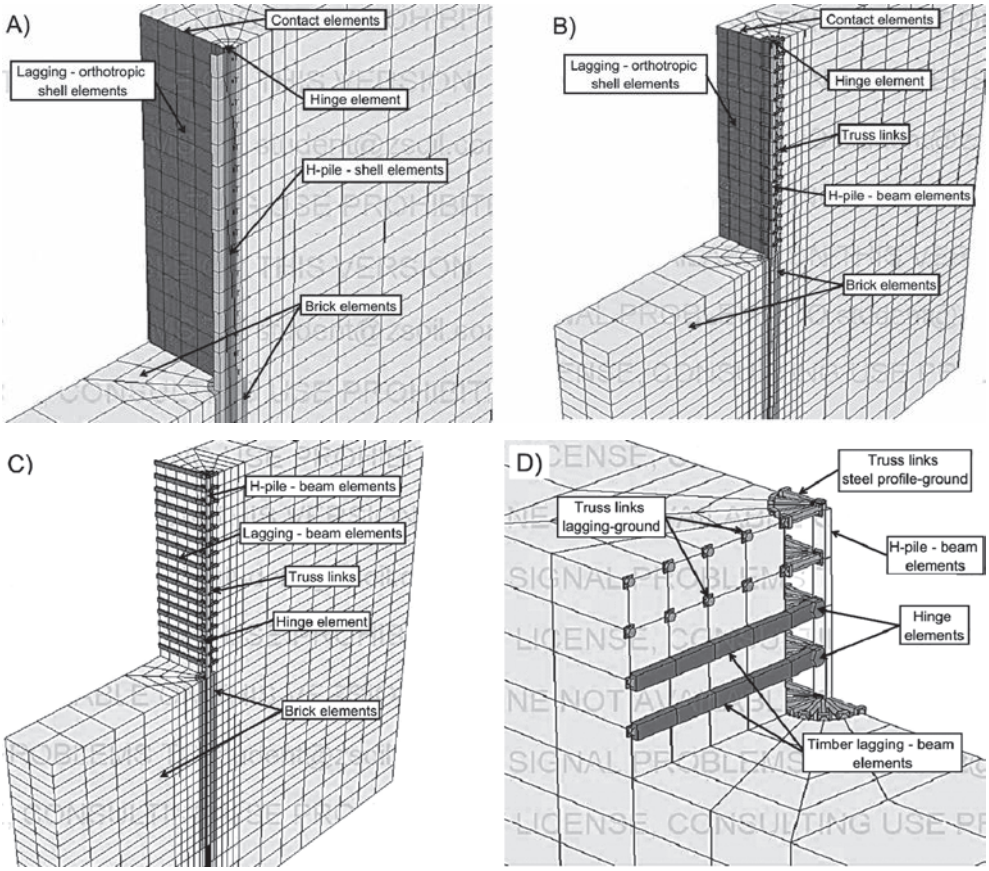

Fig. 5. FE models of the soldier pile wall: a) "shell model", b) "beam-shell model", c) "beam model", d) detail of the "beam model"

As can be seen in Fig. 5, the FE models were built based on the symmetry of the analysed problem. The elastic-plastic Mohr-Coulomb model of soil with the following parameters: E = 100 MPa/20 MPa, $\nu = 0.3$, $\psi = 0°$ (there is only one layer of soil) was applied in each of the cases. Structural elements of the wall were made of elastic materials. The results are compared for cohesive and cohesionless soils.

Figure 5a shows the model where the steel profile and the lagging were described as shell and orthotropic shell elements (Q4 plane elements), respectively – "shell model". The concrete part of the pile was modelled as B8 brick elements. In order to diversify vertical displacements of the soldier pile wall and the adjacent soil, interface (contact) elements were applied between these parts of the model.

The "beam-shell model" is shown in Figure 5b. The main difference between this model and the model described earlier is in the use of beam elements for the steel profile and truss elements for its connection with the soil. The truss links have a compressive strength ($f_c \neq 0$) and no tensile strength ($f_t = 0$). The lagging and the concrete pile have the same numerical structures as in the "shell model".

The "beam model" is shown in Fig. 5c and 5d. In this situation, both the steel profile and the lagging are the beam elements connected with the soil by truss links. The truss links were divided at the links connecting steel profile – soil and links connecting the lagging – soil (see Fig. 5d). These truss links have different parameters of strength and stiffness [1, 3].
In this way, unilateral constraints between the soil and the lagging were modelled in two equivalent fashions:
– in the "shell-beam model" and the "shell model" by frictionless contact interface elements,
– in the "beam model" by no tension truss links.

4. Results of the numerical analysis

While comparing the displacements and forms of deformation among the "shell model", "beam" and "beam-shell model", a good agreement of these was noticed. Therefore, this section describes only the results from numerical analysis of the "beam" and "beam-shell model". These two models are easier and faster to visualise the numerical results and to compare with the traditional approach. The first results are shown for the second modelling scenario of the construction process of the soldier pile wall (in four stages – lagging immediately after the excavation).

4.1. Cohesionless soils

The subject of the analysis were cohesionless soils with a variable value of friction angle from 24º to 46º with an increment of 2º. The values of cohesion and a Young's modulus were adopted: ~0 kPa and 100 MPa, respectively. Fig. 6 shows the results for both the "beam model" and the "beam-shell model" for the soil with $\phi = 36º$. Fig. 7 shows a comparison of an active pressure for numerical and traditional approaches. Good agreement between the computations was reported.

4.2. Cohesive soils

The subject of the analysis were cohesive soils with variable values of the friction angle ranging from 6º to 22º with an increment of 2º and cohesion ranging from 15 kPa to 31 kPa with an increment of 2 kPa. The value of Young's modulus $E = 20$ MPa was adopted. Fig. 8 shows the results for both the "beam model" and the "beam-shell model" for the soil with $\phi = 16º$ and $c = 25$ kPa. Fig. 9 shows a comparison of an active pressure for the numerical and the traditional approaches.

The non-physical phenomena could be seen when analysing the results for cohesive soils from Fig. 8. The Fig. 8c, 8e, 8g and 8h show the bending moments in the steel profile from the excavation site and in the lagging from the ground site while the soldier pile walls are not anchored. Besides this, Fig. 8h shows the arching effect well. Active pressure resultants E_a in the numerical and the traditional approaches are different as shown in Fig. 9 [5].

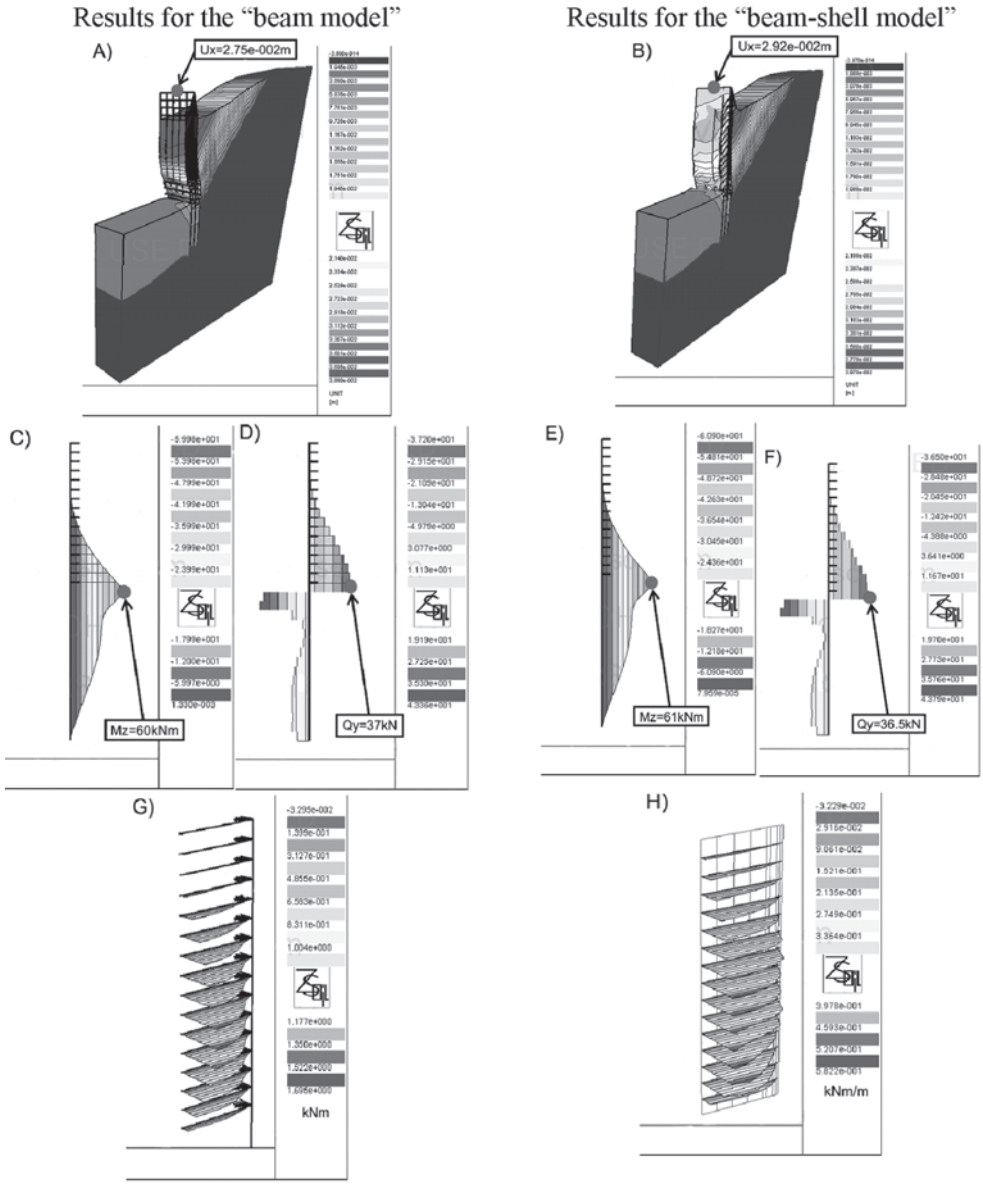

Fig. 6. Comparison of the numerical results for the "beam model" and the "beam-shell model", the cohesionless soil $\phi = 36^{o}$: a), b) displacements and forms of deformation, c), e) bending moment for the steel profile, d), f) shear force for the steel profile, g), h) bending moment for the lagging

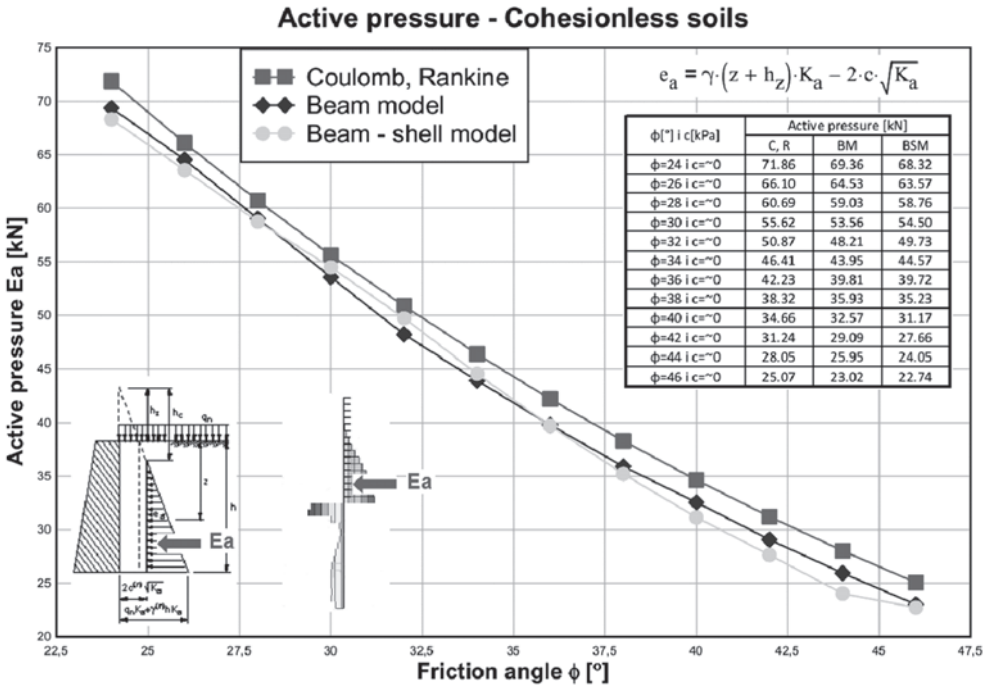

ϕ[°] i c[kPa]	Active pressure [kN]		
	C, R	BM	BSM
ϕ=24 i c=~0	71.86	69.36	68.32
ϕ=26 i c=~0	66.10	64.53	63.57
ϕ=28 i c=~0	60.69	59.03	58.76
ϕ=30 i c=~0	55.62	53.56	54.50
ϕ=32 i c=~0	50.87	48.21	49.73
ϕ=34 i c=~0	46.41	43.95	44.57
ϕ=36 i c=~0	42.23	39.81	39.72
ϕ=38 i c=~0	38.32	35.93	35.23
ϕ=40 i c=~0	34.66	32.57	31.17
ϕ=42 i c=~0	31.24	29.09	27.66
ϕ=44 i c=~0	28.05	25.95	24.05
ϕ=46 i c=~0	25.07	23.02	22.74

Fig. 7. Comparison of an active pressure for the "beam model", the "beam-shell model" and the traditional approach, cohesionless soils

5. Results of the numerical analysis after upgrade

Non-physical bending moments in the soldier pile wall are related to the poor way of describing the unloading of the ground in the Mohr-Coulomb soil model, resulting in too large a displacement (vertical and horizontal) on the excavated side. Figure 10 shows the influence of the excavation on the development of the bending moments in the wall. It can be seen that, in modelling, the effect of beam curvature due to excavation prevails on effects of lateral loads.

In order to remove the non-physical bending moments from the steel profile and the lagging, the parameters of the truss links were changed (reduced values of stiffness). Additionally, a third class of truss links (see Fig. 11) was introduced. These links separate the adjacent ground from the steel profile (in reality, bentonite is between the adjacent soil and the steel profile). Besides these treatments, the other ways of modelling the construction process of the soldier pile wall were analysed: the first modelling scenario (in one stage), the third modelling scenario (in four stages – excavation then lagging in next step) and the fourth modelling scenario (in sixteen stages). The detailed results below are shown for the "beam model" only and for the example of soil with the following parameters: $\phi = 16^{o}$ and c 25 kPa (see Fig. 12, 13, 14).

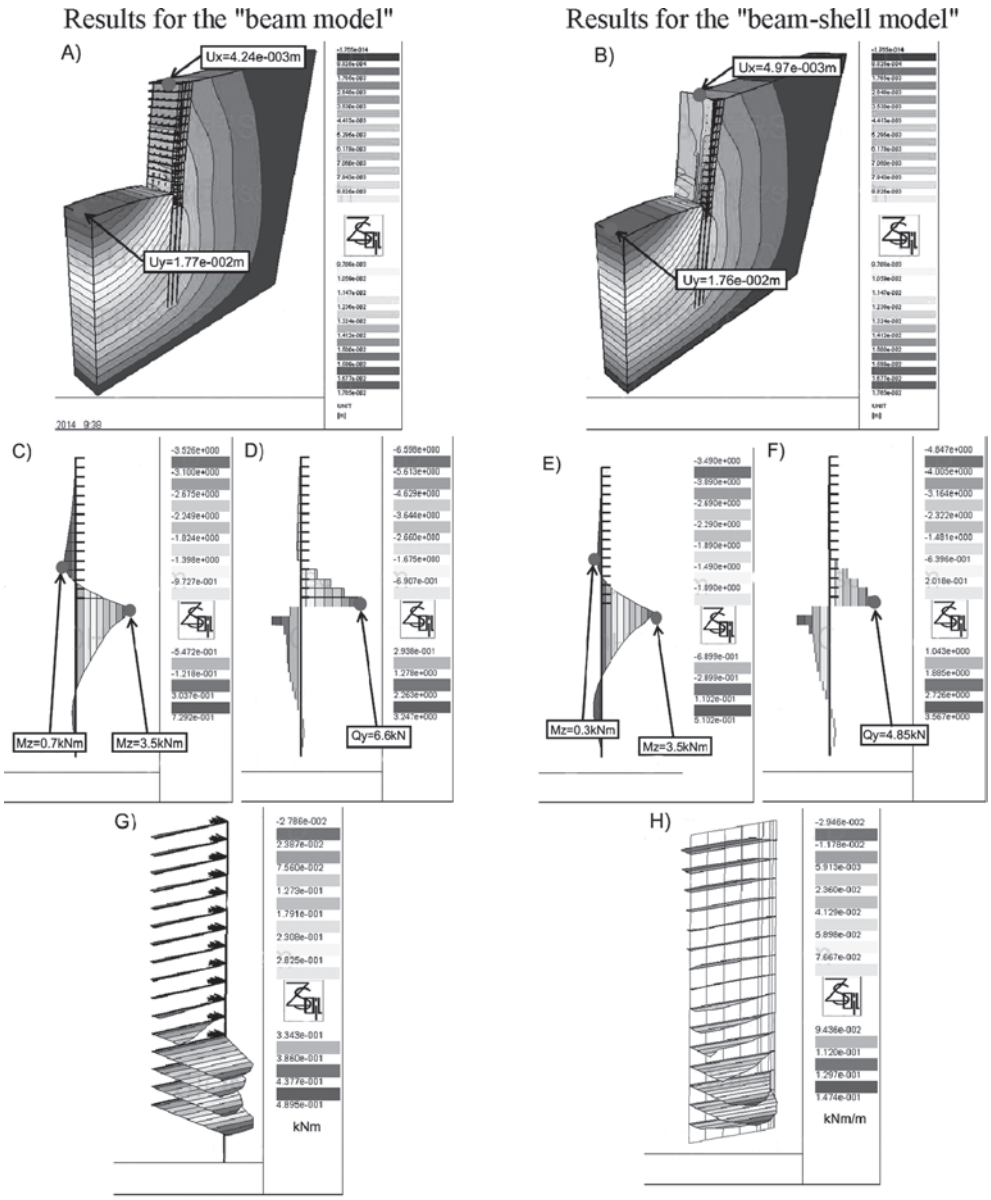

Fig. 8. Comparison of the numerical results for the “beam model” and the “beam-shell model”, the cohesive soil $\phi = 16^{o}$ and $c = 25$ kPa: a), b) displacements and forms of deformation, c), e) bending moment for the steel profile, d), f) shear force for the steel profile, g), h) bending moment for the lagging

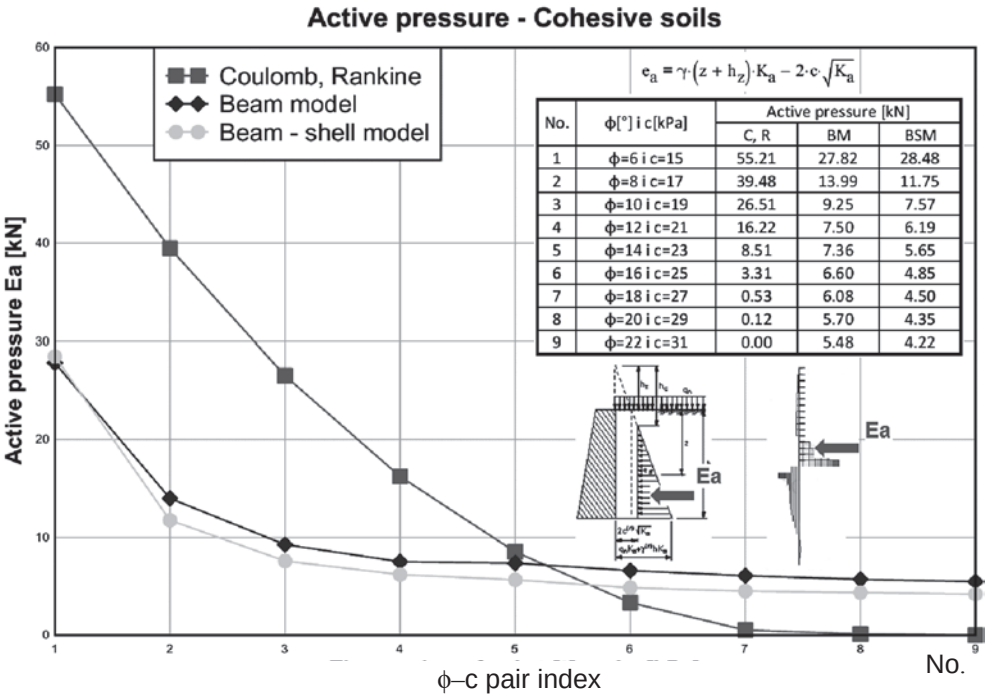

No.	ϕ[°] i c[kPa]	Active pressure [kN]		
		C, R	BM	BSM
1	ϕ=6 i c=15	55.21	27.82	28.48
2	ϕ=8 i c=17	39.48	13.99	11.75
3	ϕ=10 i c=19	26.51	9.25	7.57
4	ϕ=12 i c=21	16.22	7.50	6.19
5	ϕ=14 i c=23	8.51	7.36	5.65
6	ϕ=16 i c=25	3.31	6.60	4.85
7	ϕ=18 i c=27	0.53	6.08	4.50
8	ϕ=20 i c=29	0.12	5.70	4.35
9	ϕ=22 i c=31	0.00	5.48	4.22

Fig. 9. Comparison of an active pressure for the "beam model", the "beam-shell model" and the traditional approach, cohesive soils

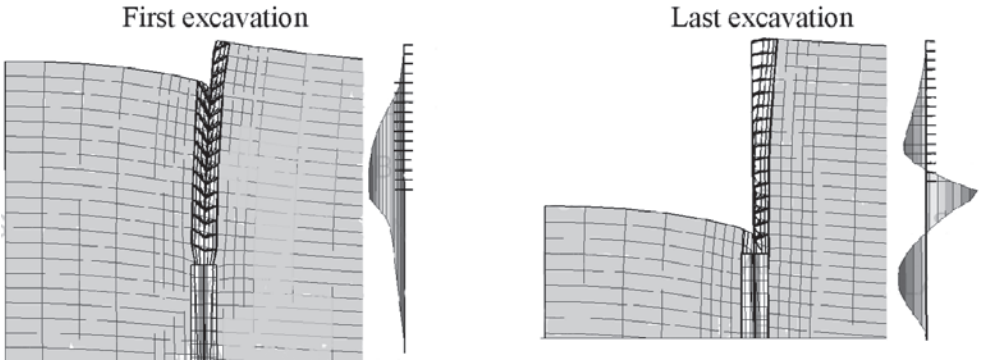

Fig. 10. Influence of the relaxation of the ground on the bending moments in the soldier pile wall

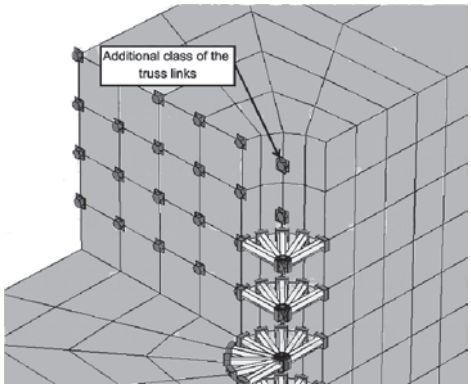

Fig. 11. An additional class of the truss links

As can it be seen in Fig. 12a, the bending moments in the steel profile from the excavation site still exist. In the case of the third and the fourth modelling scenarios of the construction process, the correct moment graphs for the cantilever wall can be seen (see Fig. 13a, 14a). Furthermore, it seems that the bending moment in the lagging for the fourth modelling scenario best reflects the real distribution of the lateral earth pressure in the lagging (see [5]). In reality, the single timber lagging is placed one after another during digging (Fig. 14c). The influence of cohesion on the lateral earth pressure in the soldier pile wall can be seen in Fig. 15.

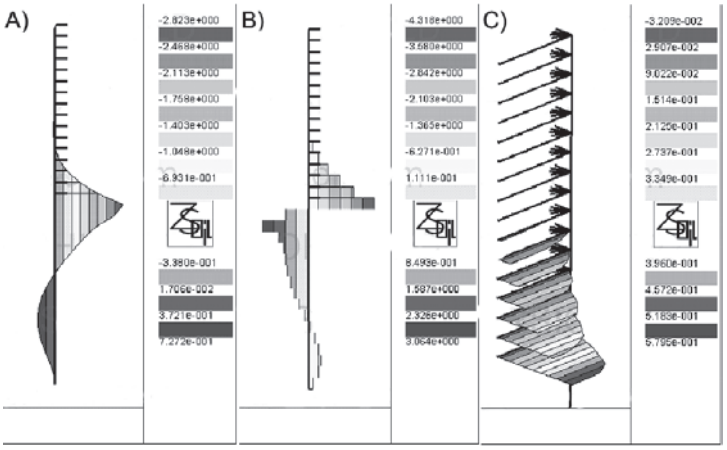

Fig. 12. The results for the first modelling scenario (in one stage) of the construction process of the soldier pile wall, the "beam model", the cohesive soil $\phi = 16^{\circ}$ and $c = 25$ kPa: a) bending moment for the steel profile, b) shear force for the steel profile, c) bending moment for the timber lagging

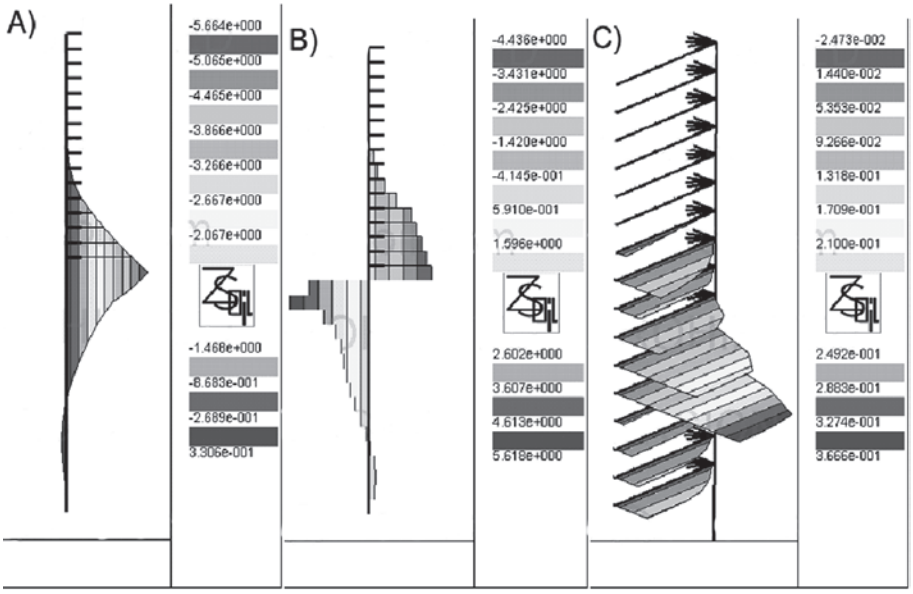

Fig. 13. The results for the third modelling scenario (in four stages – excavation then lagging in next step) of the construction process of the soldier pile wall, the "beam model", the cohesive soil $\phi = 16^{o}$ and $c = 25$ kPa: a) bending moment for the steel profile, b) shear force for the steel profile, c) bending moment for the timber lagging

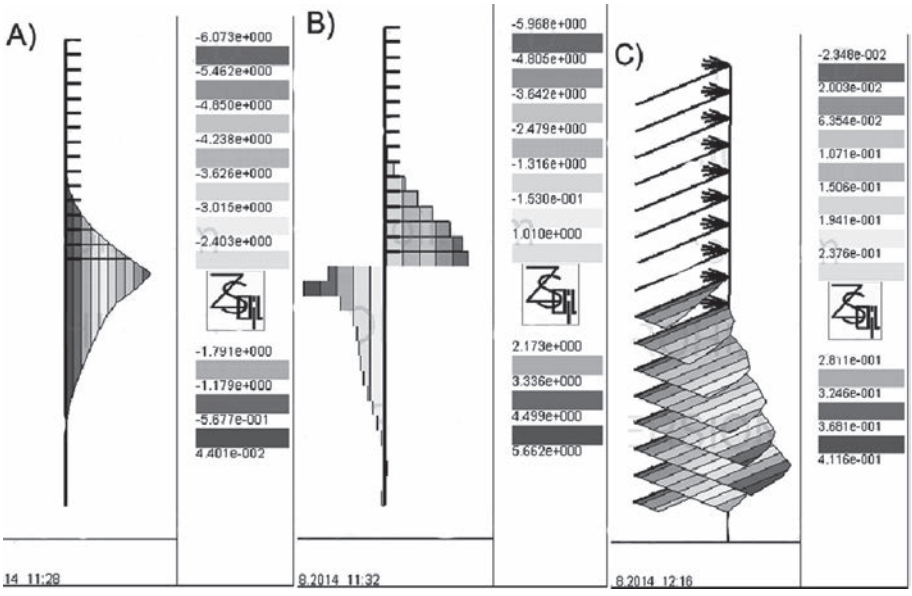

Fig. 14. The results for the fourth modelling scenario (in sixteen stages) of the construction process of the soldier pile wall, the "beam model", the cohesive soil $\phi = 16^{o}$ and $c = 25$ kPa: a) bending moment for the steel profile, b) shear force for the steel profile, c) bending moment for the timber lagging

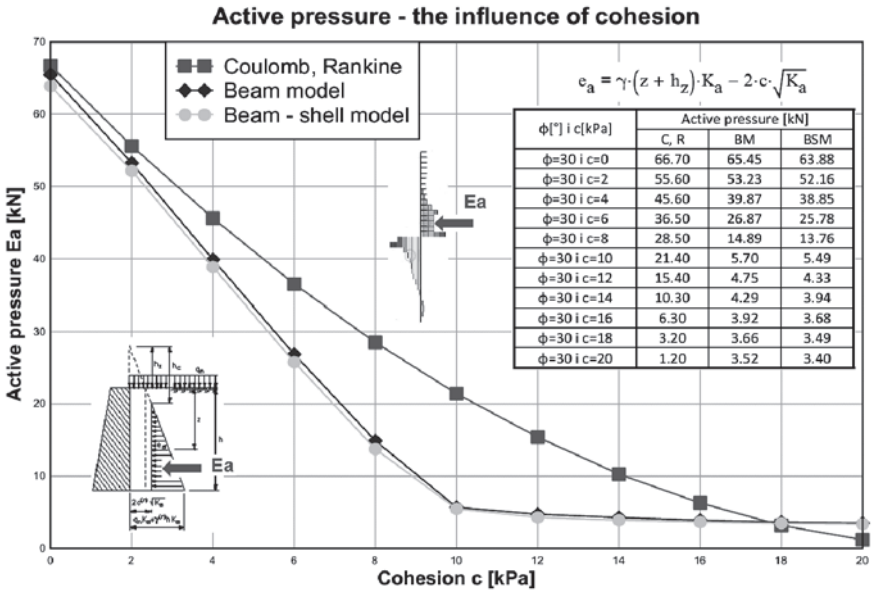

ϕ[°] i c[kPa]	Active pressure [kN]		
	C, R	BM	BSM
ϕ=30 i c=0	66.70	65.45	63.88
ϕ=30 i c=2	55.60	53.23	52.16
ϕ=30 i c=4	45.60	39.87	38.85
ϕ=30 i c=6	36.50	26.87	25.78
ϕ=30 i c=8	28.50	14.89	13.76
ϕ=30 i c=10	21.40	5.70	5.49
ϕ=30 i c=12	15.40	4.75	4.33
ϕ=30 i c=14	10.30	4.29	3.94
ϕ=30 i c=16	6.30	3.92	3.68
ϕ=30 i c=18	3.20	3.66	3.49
ϕ=30 i c=20	1.20	3.52	3.40

Fig. 15. Comparison of an active pressure for the "beam model", the "beam-shell model" and the traditional approach, the influence of cohesion

6. Conclusions

The article discusses the issue how development of the lateral earth pressure in the soldier pile walls depends on: the type of soil, and the modelling scenario of the construction process of the excavation. In addition, its dependence on the parameters of the numerical model was analysed. Internal forces for the "beam" and the "beam-shell model" were compared in this article. The paper also contains an analysis of the soldier pile systems designed in both the traditional (Coulomb, Rankine etc.) and the numerical approach.

As was shown, the so called "beam model" of the soldier pile wall is easier and faster in visualisation and analysis of the internal forces. They can be used directly for the design of the wall. The correct choice of the parameters of the truss links, which are defined in the "beam model", is of crucial importance. Incorrectly assumed parameters (stiffness) of these truss links may cause non-physical phenomena such as the bending moments in the steel profile from the excavation and in the lagging from the ground.

The modelling scenario of the excavation in the soldier pile wall should be focused on the distribution of the lateral earth pressure in the lagging. The presented modelling scenarios of the excavation clearly show the differences in the internal forces of the soldier pile wall (mainly in the lagging). It seems that the bending moment in the lagging for the fourth modelling scenario (in sixteen stages) best reflects the real distribution of the lateral earth pressure in these elements of the wall – in practice, the single timber lagging is placed one after another during digging.

The added truss links in the "beam model" easily allow a comparison of the lateral earth pressure with the traditional approach. For cohesionless soils, good agreement between computations was observed. In the case of cohesive soils, deeper analysis is necessary.

The paper also shows how different ways of modelling and their details may have an influence on important results in soil structure interaction problems.

Recognition and establishment of a way to realistically describe load action on the soldier pile wall (cantilever schema) was an introductory part of a wider research project devoted to practically deriving design formulae based on FEM analysis of these geo-structures. Its main issue, i.e. analysis of the underground part of the soldier pile wall, will be the subject of the future studies.

References

[1] Urbański A., Łabuda A.*, A modeling method 2d/3d of a deep excavation supported by a soldier pile wall* (in Polish), Technical Transactions v. 1-B/2004, Cracow University of Technology Press.

[2] Urbański A., Grodecki M., *Analysis of a breakdown of a deep excavation supported by soldier pile wall* (in Polish), Technical Transactions v. 1-B/2004, Cracow University of Technology Press.

[3] Urbański A., A *simplified computational model for a periodic system of horizontally loaded piles*, Third international symposium on computational geomechanics (ComGeo III), Cracow, Poland, August 2013, 516–524.

[4] Perko H. A., Boulden J. J., *Lateral earth pressure on lagging in soldier pile wall systems,* DFI Journal Vol. 2 No. 1, November 2008.

[5] Vermeer P.A., Punlor A., Ruse N., *Arching effects behind a soldier pile wall*, Computers and Geotechnics, January 2001, 379–396.

[6] *Z_Soil.PC, Theoretical Manual*, ZACE Services Ltd., Lozanna 2007.

TECHNICAL TRANSACTIONS | CZASOPISMO TECHNICZNE
ENVIRONMENTAL ENGINEERING | ŚRODOWISKO
2-Ś/2015

ALEKSANDER URBAŃSKI*, LESZEK OPYRCHAL**

ANALYSIS OF MECHANICAL EFFECTS OF LOW- AND HIGH-FREQUENCY TEMPERATURE CHANGES IN A MASSIVE CONCRETE DAM

ANALIZA WPŁYWU WOLNO- I SZYBKOZMIENNYCH PÓL TEMPERATURY NA STAN MECHANICZNY MASYWNEJ ZAPORY BETONOWEJ

Abstract

The numerical simulation of time evolution of thermal and mechanical fields in a selected section of a massive concrete dam was undertaken by means of the Finite Element Method (FEM) using 3D modelling. Low- (i.e. with time period – year) and high frequency (i.e. with time period – day) cycles of environment temperature variation were considered. The results of the computation confirmed the hypothesis of the vulnerability of the structure to thermal influences and explained the mechanism of the structural defects observed.

Keywords: thermo-mechanical effects, massive concrete dam, FEM

Streszczenie

W pracy przedstawiono symulacje numeryczne dotyczące efektów termo-mechanicznych w masywnej zaporze betonowej. Zastosowano trójwymiarowe modelowanie metodą elementów skończonych niestacjonarnego w czasie pola temperatury i pól mechanicznych. Rozpatrzono zarówno wpływ zmian temperatury otoczenia w cyklu rocznym, jak i w cyklu dobowym. Wykazano, że mogą być one przyczyną zaobserwowanych uszkodzeń na powierzchniach betonu.

Słowa kluczowe: *efekty termo-mechaniczne, masywna zapora betonowa, MES*

DOI: 10.4467/2353737XCT.15.235.4621

* Prof. DSc. PhD. Aleksander Urbański, Institute of Geotechnics, Faculty of Environmental Engineering, Cracow University of Technology.

** DSc. PhD. Leszek Opyrchał, AGH University of Science and Technology, Faculty of Mining Surveying and Environmental Engineering, Department of Environmental Management and Protection.

Symbols

T – temperature [K]
ι – time [day]

1. Introduction

The dam is located in the southwest Poland. The reservoir area is 32 ha and water volume is 2 mln m^3. The total length of the dam is 306.0 m. Its central part is split into 12 sections of buttress type concrete dam with variable height, ranging from 15.0 to 34.5 m in the middle.

In the year 1998 [3], i.e. after 34 years of exploitation, cracks and fissures in the buttress and transition zones of the highest sections of the dam (nr 6 and 7), as shown in Fig. 1, were noted during a technical inspection. In the year 2013 surface cracking of the concrete was also detected on the head surfaces of the buttress. An explanation for the observed phenomena has become vital for the safety assessment of the dam and design of the rehabilitation procedure. The crack pattern indicates that the possible reason for cracking is the influence of the thermal stress field.

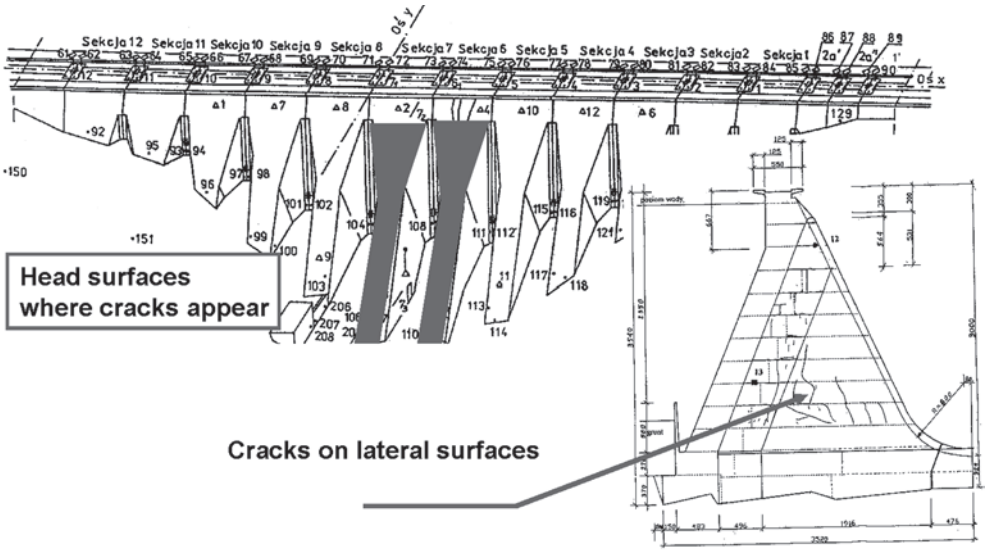

Fig. 1. a) View of the dam from the downstream site b) View of the right wall of the buttress of the 6-th section of the dam with cracks, after [3].

Typical cracks appearing on the head surface of the buttress are shown in Fig. 2.

Fig. 2. Crack on the head surface

2. Numerical modelling of the thermal process and its mechanical effects in a massive concrete structure

As an initial investigation of the observed cracks points to a thermal stress field as the most probable cause, numerical simulation of the time evolution of thermal and mechanical fields in the highest central section of the dam was undertaken using the Finite Element Method (FEM).

As a software tool, the Z_SOIL.PC system was chosen [2, 4], because of its ability to take into account in a fully automated way the interaction between: temperature evaluated in a transient heat transfer problem, pore pressure field developed in filtration analysis with materially nonlinear and/or rheological static analysis of the concrete dam and its foundation.

Due to the generic tri-dimensionality of the dam section, a full 3D FEM simulation has been created. The strategy for the analysis was adopted as summarized below. Firstly, thermal analysis of yearly (low-frequency) environmental temperature variation was undertaken. Its results, i.e. temperature space and time distribution $T(\mathbf{x},t)$, consist of an entry to the analysis of mechanical fields (displacements, strains and stresses). These analyses were run for a total period of 10 years, what is necessary to remove the effects of an improperly set thermal initial condition (as it is *a-priori* unknown). A time step of $dt1 = 10$ days was assumed, thus only low-frequency (winter-summer) environmental temperature variation could be taken into account.

Secondly, the influence of a high-frequency, i.e. daily (night-day) cycle of environmental temperature variation and its mechanical effects were analysed separately, for the fragment of the structure close to the cracked head surface, for a period of 1 year with time stepping $dt2 = 0.1$ day. Of course, this analysis takes into account (as initial and boundary conditions) the temperatures obtained in the first, low-frequency analysis.

For both cases an incremental mechanical analysis is run, taking into account the increments of the imposed thermally induced strains. Note that these strains, in general, do

not fulfil the Saint-Venant compatibility equations, and as so are the source of self-equilibrate stresses.

As numerical evaluation of all integrals over a finite element (for stiffness or force vector) requires values at integration (Gauss) points, temperature increments at these points are interpolated from values previously evaluated at the nodes of the FE mesh used in the heat problem. Notice that the FE meshes used in both thermal and mechanical analyses do not need to be identical; the same holds for time step implementation, see [2] for details.

In this way, using the described two-stage analysis it was possible to explain all the mechanisms of observed cracks in the structure. The analysis of high-frequency temperature changes for the full model of the section, which also requires much denser FE discretisation, is currently not feasible on standard PC computers, due to the numerical size of the job.

The mechanical material parameters of the concrete were assumed as follows, marked with (*) basing on the measurements done on core samples (diameter 75 mm, length 150mm): Young's modulus: E = 21.2 GPa (*), Poisson's ratio: $\nu = 0.19$(*), tensile strength: ft = 3.000MPa(*, Brazilian test), compressive strength fc = 30.000 MPa(*), thermal dilatancy coefficient: $\alpha = 1.13 \cdot 10^{-5}$ [1/K].

For the concrete elastic-perfectly plastic model due to Menetrey and Willam (MW) [1], with limit surface tri-elliptic in axiatoric and parabolic in deviatoric section, identified from uniaxial tensile (ft) and compressive strength (fc) was applied.

2.1. Thermal and mechanical analysis of yearly (low-frequency) environmental temperature variation

The first problem to be solved is to find the space distribution and time evolution of the temperature field $T(\mathbf{x}, t)$ in the concrete dam section and its surroundings due to the annual cyclic variation of climatic conditions described by the Fourier equation (1):

$$\left(\lambda\left(T_{,i}\right)\right)_{,i} = c\dot{T}\,, \tag{1}$$

where: heat conductivity λ = 155/259 [kJ/(m · day · K)] for concrete/bedrock and heat capacity c = 2016 / 1800 [kJ/(m^3 · K)], respectively, were assumed.

In the analysis, all 3 types of boundary conditions (BC) were used (Fig.3a):

1. Known temperature BC (1st kind), $T(\mathbf{x},t) = \bar{T}(h,t)$ at the dam upstream surface. Starting from the measured water temperature profiles as a function of the depth h in winter $T_W(h)$ and in summer $T_S(h)$, assuming sinusoidal time variability in the temperature during the yearly cycle the relation is used, (t = 0 set for 1st of January):

$$\bar{T}(h,t) = \frac{T_S(h)+T_W(h)}{2}\left(1-\frac{T_S(h)-T_W(h)}{T_S(h)+T_W(h)}\cos\left(2\pi t/365\right)\right), \quad t[\text{days}]\,; \tag{2}$$

2. Adiabatic BC (2nd kind) $q_n = 0$ on vertical planes Z = 6.0, $X = \pm 50.0$;

3. Convective BC (3rd kind), i.e.: $q_n = \alpha_c(T - T_e)$ at the remaining surfaces, with ambient temperature $T_e(t) = T_A(1 - \Delta T / (2T_A)) \cdot \cos(2\pi t / 365))$, where T_A = 8 [°C] is the yearly average temperature, ΔT = 18 [°C] is the amplitude of monthly averaged temperatures and α_c = 2000 [kJ/(m^2 · day · K)] is the convection coefficient (concrete wall – air).

Fig. 3 shows the FE model (rough mesh is shown) with BC used in the 3D analysis of heat problem and the resulting temperature distribution in [°C] in winter [W] and in summer [S].

In Fig. 4 the histograms of the temperature in points laying on the surface and in the midst of the buttress are shown. A temperature difference of up to ΔT_1 = 7°C appears between the interior and the side surface of the pillar due to the high thermal inertia of the system, related to large dimension of the structure ($L_{\min}$ = 5.0 m). Moreover, the gradients of these strains in the transversal directions are not constant. This explains the main source of thermal stresses and, in consequence, cracking on the lateral surfaces. As a result of subsequent mechanical analysis, the principal stress distributions are shown in Fig. 5 (compression-blue, tension-red). Due to the symmetry, only half of the pillar is considered.

Note, however, that the above low-frequency thermo-mechanical analysis does not indicate any reason for cracking in the head surfaces of the buttress. In this zone, both in summer and in winter, only compressive stresses appear, reaching the value $\sigma_n \cong 1$ MPa, in the direction tangent to the slopes of the pillar.

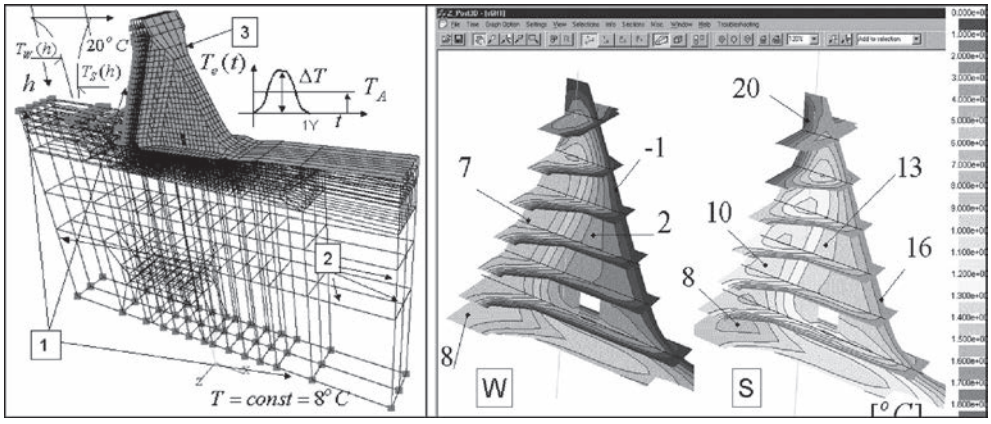

Fig. 3. a) Heat transfer BC. b) Temperature distribution in winter [W] and summer [S]

The temperature field shown in Fig. 3b and Fig. 4 was obtained during the first computational analysis of the dam, conducted by the first author of this paper in 2002 and reported in [5, 6]. In the present analysis, the FE mesh was densified, see Fig. 5, giving however practically the same output.

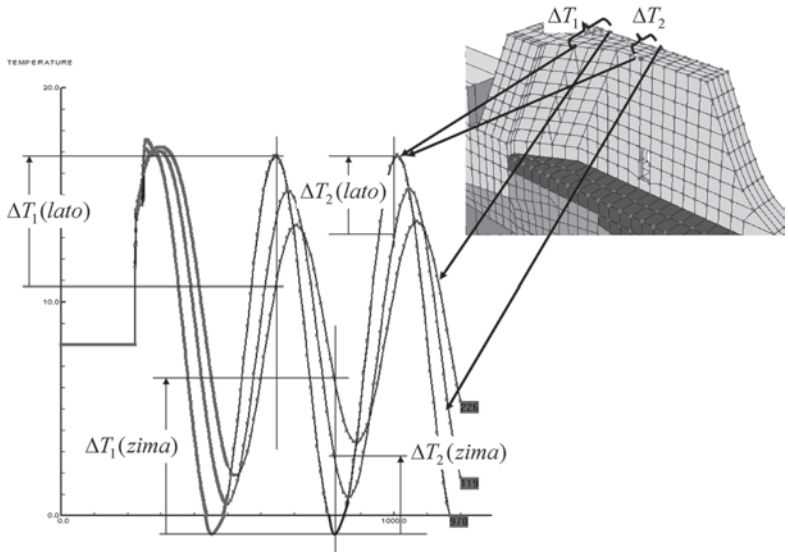

Fig. 4. Histograms of the temperature at selected points

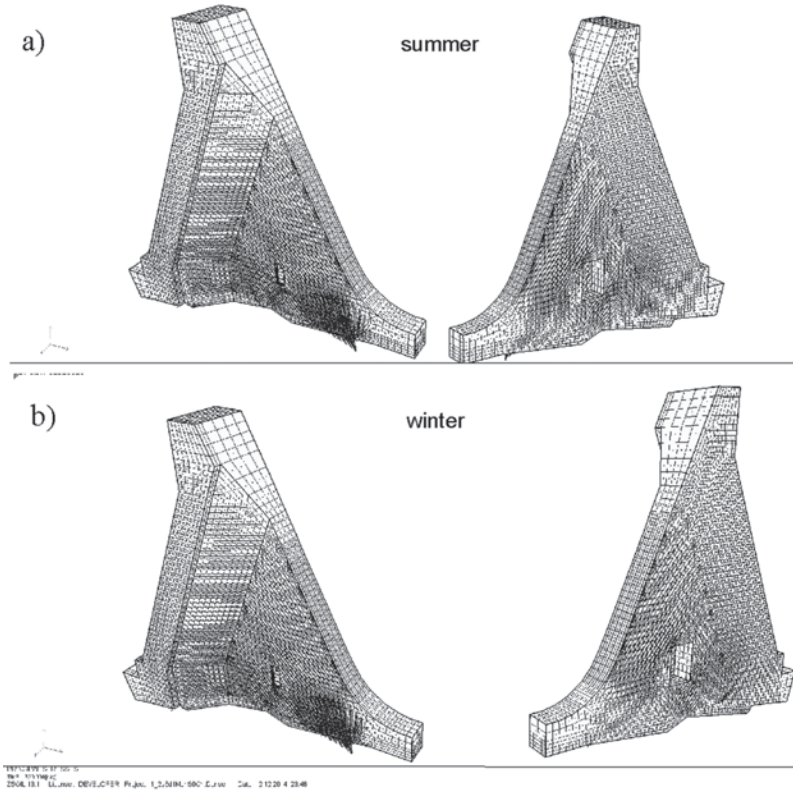

Fig. 5 Principal stresses a) in a summer b) in a winter

2.2. Thermal analysis of diurnal (high-frequency) environmental temperature variation and its mechanical impact

In attempting to explain the origin of the multiple cracking of the concrete appearing on the head surface of the buttress, which cannot be result of the yearly temperature cycle, an analysis of daily (high-frequency) environmental temperature variation was undertaken. This is set in the 3D/2D domain which is representative of the whole region close to the head surface. This is shown in Fig. 6. An analysis of high-frequency temperature changes for full model of the section requires also a much denser FE discretisation (estimated size of element in near-surface zone ~10 cm) and time stepping $dt2 = 0.1$day (10 steps per day). These would result in an unacceptably long computation time (few days). Therefore an approximate procedure has been chosen.

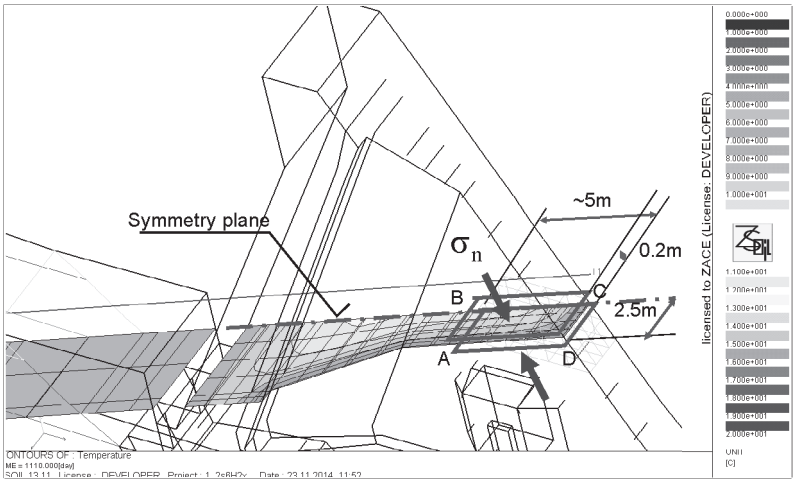

Fig. 6. Localization of the domain for high-frequency thermal and mechanical analysis

Boundary conditions for thermal analysis for the fragment of the dam were adopted as follows:

- along the segment AB – 1-st type of BC, by adopting nodal temperatures as a function of time obtained from the low-frequency solution;
- along the segment BC, on the symmetry plane, 2-nd type of BC (adiabatic, $q_T = 0$);
- along the segments CD and AD, 3-rd type of BC (convection). The function of ambient temperature $T_{eHF}(t)$ describes diurnal variability throughout the year, with yearly averaged temperature $T_A = 8$°C and $\Delta T = 18$°C being the amplitude of daily averages. A term describing the diurnal fluctuation has been added.

$$T_{eHF} = \underbrace{(T_A - \Delta T/2)\cdot \cos(2\pi t/365) + (5\text{-}2.5\cdot\cos(2\pi t/365))}_{\text{low-frequency}} \cdot \underbrace{\sin(2\pi t)}_{\text{high-frequency}}$$

They vary with the seasons, maximum daily amplitude $\Delta T_{dS} = 15$°C (in the summer) and minimum $\Delta T_{dW} = 5$°C (in the winter) were assumed based on meteorological data. The diurnal

cycle was adopted in the form of a sine wave. The ZSoil screen with the function $T_{eHF}(t)$ is shown in Fig. 7 with high-frequency variability lasting for one year, from the $t_1 = 555d$ till $t_2 = 920d$.

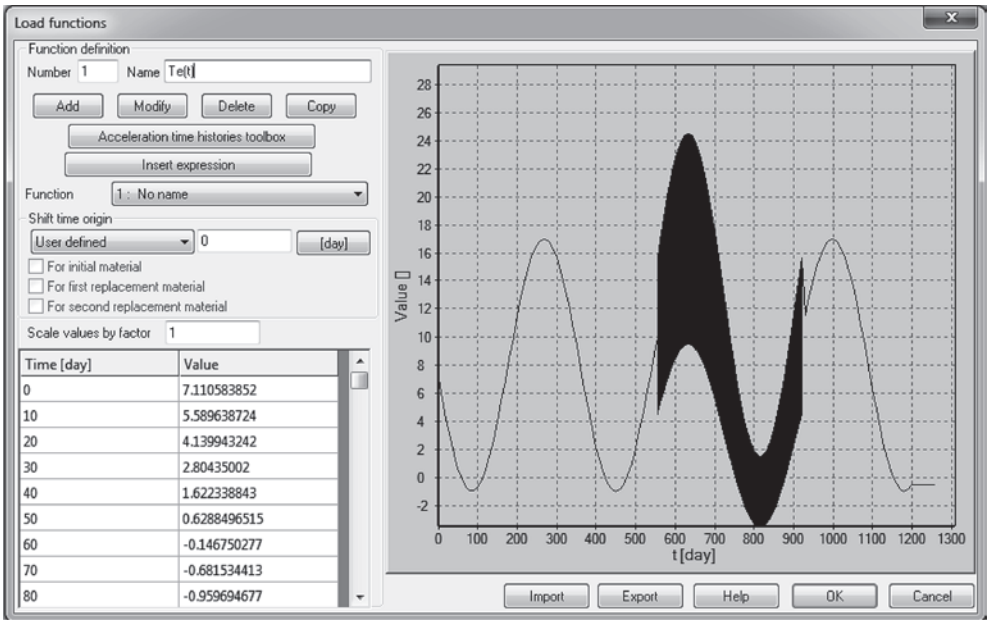

Fig. 7. Ambient temperature function, with high-frequency part $T_{eHF}(t)$

The following results from thermal and subsequent mechanical analysis for high-frequency temperature variation are shown in Fig. 8: map of the temperature field, principal stress crosses, map of maximum tensile stresses. They are given in 5 selected time instances ($t + 0.0d$, $t + 0.2d$, $t + 0.4d$, $t + 0.6d$, $t + 0.8d$), during one selected day ($t = 640d$) in summer. For that day the maximum of diurnal temperature fluctuation has been reached ($\Delta T_{dS} = 15°C$).

These results explain the essence of the observed phenomena in the following way: the maximum daily temperature zone shifts from the outer surface into the depths of the massif, temperature gradients reach the value ~4°C/0.5 m near the surface. The accompanying thermal strains increments $\Delta\varepsilon^{o}_{ii}(x, y, z) = \alpha\Delta T(x, y, z)$ have a spatial distribution which do not conform to the compatibility equations (are not-kinematically allowed). As the final deformation must satisfy the compatibility equation, the difference between this and the deformation related to imposed thermal strains is the source of a thermal stress field.

In the present case, these stresses reach values close or equal to the tensile strength of the concrete ($ft = 3.00$ MPa). These may be one cause of the cracks at the surface zone. The extent of these cracks is about 0.5m in the depth of the massif.

3. Final conclusions

The analysis of the thermal and mechanical state in the massive pillar of the dam indicates that there are 2 different mechanisms causing the appearance of cracks in the structure. Both are strongly connected to environmental temperature variation.

The first mechanism concerns cracking in the central zone of the pillar, which may be explained by temperature differences in the internal points, which remain almost constant during the year, and the temperature and lateral surfaces on the pillar which vary in an annual, low-frequency cycle (winter-summer).

The second, i.e. cracking on the head surfaces, are high-frequency (diurnal) temperature fluctuations (night-day), particularly intensifying in the sunny area, in accordance with the mechanism described in p. 2.2.

These phenomena are stable, they are the consequence of the massiveness of the structure and appear inevitable in a massive concrete structure, but do not threaten its security.

The phenomena of thermal cracking, however, can coexist with other conditions which cause gradual degradation of the structure, such as chemical corrosion of the concrete or frost phenomena. It is noted that penetration of water and its freezing in the already cracked concrete may have a particularly adverse effect on the durability of the structure.

In the long term, the phenomena of thermal cracking may be an important factor influencing the durability of massive concrete dam structures, and proper actions must be undertaken to minimize its effects.

a) temperature field (10÷20)°C	b) principal stress crosses (tension, compression)	c) σ_1 (0÷3.0) [MPa] + deformation (×400)
t = 640.0d		
t = 640.2d		
t = 640.4d		

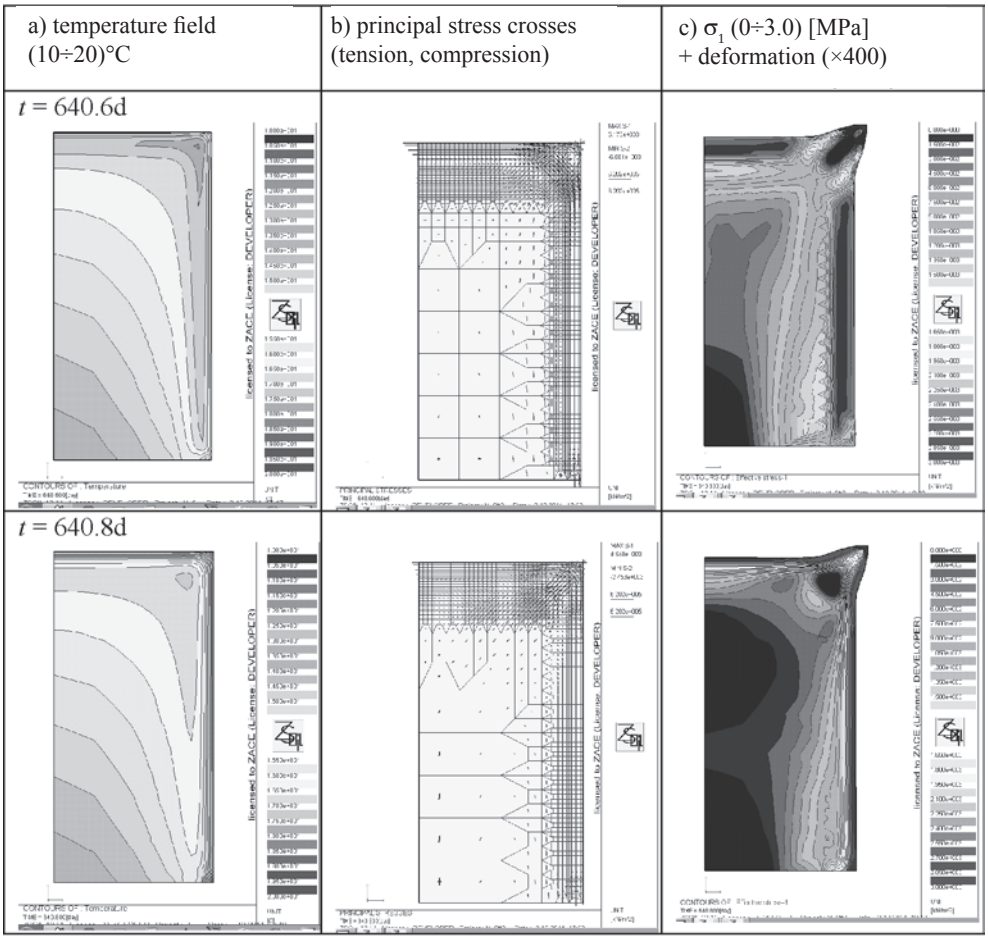

Fig. 8. High-frequency temperature fields and thermal stresses in one daily cycle

References

[1] P. Menetrey, *Numerical analysis of punching failure in reinforced concrete structures,* Ph.D. Thesis, EPFL, Lausanne 1994.

[2] *Z_Soil.PC, Theoretical Manual,* ZACE Services Ltd., Lausanne 2007.

[3] W. Hrabowski, *Interpretation of the measurement results and evaluation of the safety state of the dam Zatonie* (in Polish), "HRABOWSKI-consulting", 1998.

[4] A. Urbański, *Numerical modeling of thermal, filtrational and mechanical phenomena in a selected section of a gravity dam*, Proc. of Numerics in Geotechnics & Structures Symposium, Lausanne 2010.

[5] A. Urbański, W. Hrabowski, J. Hrabowska*, Trójwymiarowe modelowanie numeryczne i analiza in-situ pól termicznych, filtracyjnych i mechanicznych w wybranej sekcji zapory betonowej w Zatoniu*, Materiały Konferencji TKZ Kielce 2003.

[6] W. Hrabowski, A. Urbański, J. Hrabowska, *Analiza porównawcza pracy najwyższych sekcji zapory w Zatoniu w świetle wyników obserwacji i modelowania komputerowego*, Materiały XIV Konferencji Naukowej – Korbielów' 2002, Wyd. PK 2002.

TECHNICAL TRANSACTIONS | CZASOPISMO TECHNICZNE
ENVIRONMENTAL ENGINEERING | ŚRODOWISKO
2-Ś/2015

BOGUSŁAW ZAJĄC*

LABORATORY TESTING OF TRANSIENT HEAT FLOW IN CONCRETE

BADANIE LABORATORYJNE NIEUSTALONEGO PRZEPŁYWU CIEPŁA W BETONIE

Abstract

The article is a description of the laboratory testing of transient heat flow in small-size samples of concrete and analysis of the impact of spacers made of a polyurethane material to the flow and the temperature distributions in the sample. This problem affects the working of concrete structural members exposed to a wide range of temperatures, and the thermal stresses generated in them, especially when the heat flow is analysed by a combination made of a flexible connection. The results can be used in issues related to the durability of concrete elements and their connections.

Keywords: transient heat flow, concrete, temperature

Streszczenie

Przedmiotem artykułu jest opis badania laboratoryjnego nieustalonego przepływu ciepła w małogabarytowych próbkach betonowych oraz analiza wpływu przekładki wykonanej z materiału poliuretanowego na przepływ i rozkłady temperatury w próbce. Zagadnienie to ma wpływ na pracę betonowych elementów konstrukcyjnych poddanych działaniu szerokiego zakresu temperatury oraz generowanych w nich naprężeń termicznych, zwłaszcza gdy analizowany jest przepływ ciepła przez ich połączenie wykonane ze złącza podatnego. Wyniki badań mogą być wykorzystane w zagadnieniach związanych z trwałością elementów betonowych oraz ich połączeń.

Słowa kluczowe: nieustalony przepływ ciepła, beton, temperatura

DOI: 10.4467/2353737XCT.15.236.4622

* PhD. Bogusław Zając, Institute of Structural Mechanics, Faculty of Civil Engineering, Cracow University of Technology.

Symbols

Φ – diameter
A – surface area
l – length
T – temperature
ρ – density
α – thermal expansion coefficient
E – Young's modulus

1. Introduction

Concrete structures under conditions of use and operation are exposed to the impact of variable temperatures. These changes in diurnal and annual cycles cause dimensional changes which in turn leads to stress. Additional components made of other materials with other heat conductivities and other thermal capacity significantly impact on the temperature distribution in the whole structure creating additional stresses. These changes, combined with the influence of moisture and other factors have an important influence on the durability and longevity of the structure. Thermal stresses in the boundary area depend on the coefficients of thermal expansion (CTE) and the Young modulus of adhesive and bonded materials. Knowledge of all the parameters affecting the mechanical properties at the interface between different materials, and the environmental impact [1–3] and soil on them, allows for efficient numerical analysis [4] and design [5]. Polyurethane materials were used in vibration damping systems [6], and repair of historic structure [7] and concrete elements.

One of the latest methods for repairing and strengthening of concrete structures (Fig. 1) is the Flexible Joint Method, developed at the Cracow University of Technology, and is based on polyurethane polymers used as adhesive layers in the bonding of different engineering materials and FRP composites to concrete and masonry substrates [8]. Analysis of the work of flexible connections in a wide temperature range is a further development of this method.

2. Experiments

2.1. Measurement of a transient heat flow in concrete

Two concrete slabs 100 × 100 × 500 mm were prepared for testing. Samples were made two years ago for a series of other endurance tests. As surplus to requirements they remained unused in the research and were kept in a dry warehouse. It was decided to use them in a study of temperature. To place the thermometers in the samples, holes were made with a depth of 50 mm and diameter of 6 mm along the axis (Fig. 2, cross-section α-α) with a distance of 30, 50, 75, 100, 150, 200, 250, 300 and 400 mm from the top of the sample. Next, holes with a depth of 20 [mm] were made at a distance of 100 and 200 mm (Fig. 2, cross-section β-β). Thermometers mounted in the cross section α-α were used to measure the

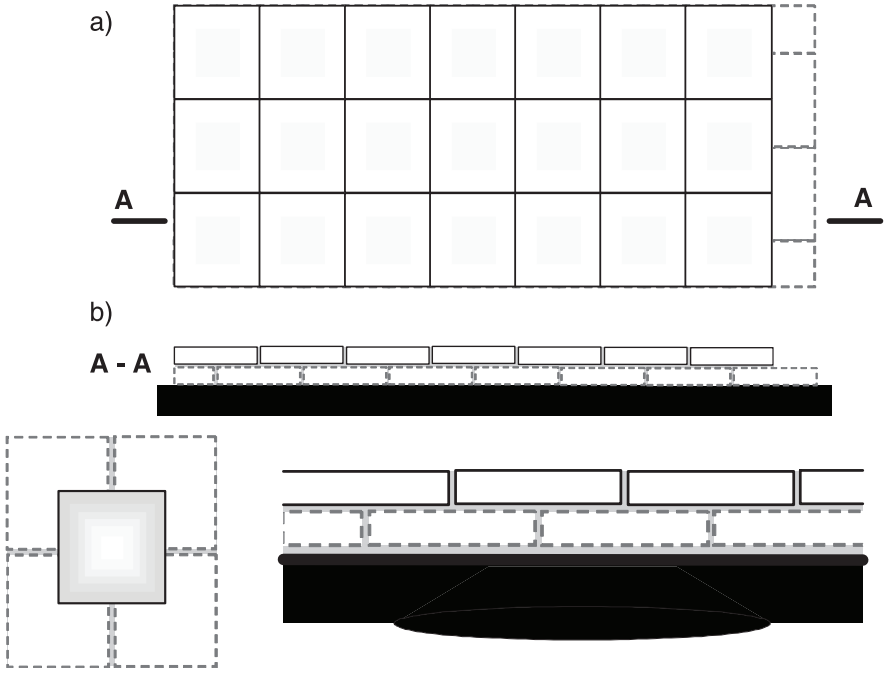

Fig. 1. Schematic diagram of laying concrete panels using the Flexible Joint Method – after [8]

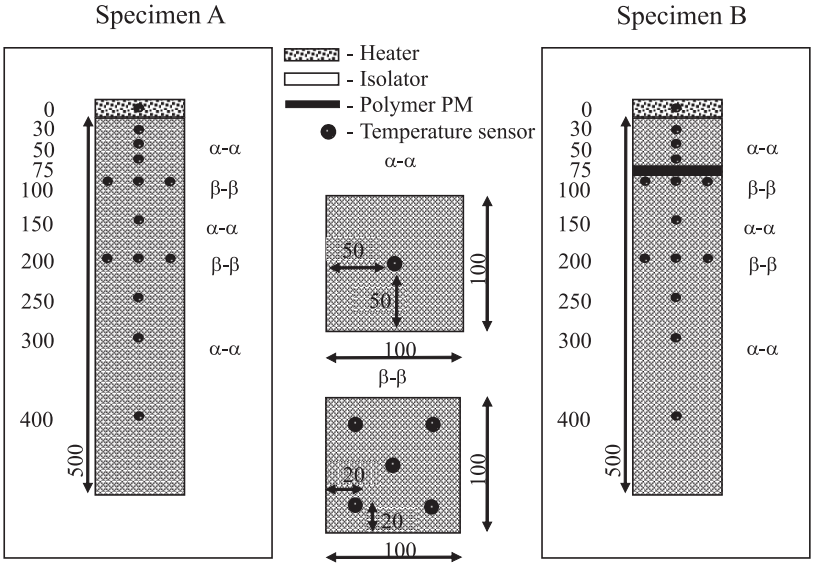

Fig. 2. Schematic arrangement of thermometers in the test samples, sample A – reference, sample B – with polymer PM layer

temperature distribution along the axis of the sample, and an additional four thermometers in cross section β-β were used to verify the differences in the temperature distribution in the analysed cross section. The first sample remained to test as a whole, while sample B was cut at a distance of 87.5 mm from the beginning. An intersection was introduced with a 10 mm layer of polyurethane PM. The two-component polyurethane PM was properly prepared in accordance with the recommendations of the manufacturer's data sheet. In liquid form, it was introduced into the void 10 mm between the transected pieces of concrete sample B. After hardening the whole sample received polymer spacer again. To determine the temperature distribution DS18B20 (Maxim Dallas Semiconductors) in TO-92 a package were used as thermometers. The DS18B20 digital thermometer provides Celsius temperature measurements with an operating temperature range of –55°C to +125°C and is accurate to ± 0.5°C over the range of –10°C to +85°C. Each DS18B20 has a unique 64-bit serial code, which allows one microprocessor to be used to control many DS18B20s distributed over a large area [9]. They were placed in the holes and covered with cotton isolation material. The temperature was measured continuously at two second intervals. As the heating element an aluminium plate with dimensions of 100 × 100 × 5 mm was used. Heat was generated by power transistors fixed to the aluminium plate controlled by a thermoregulation unit. The samples were placed in 100 mm thermal insulation made of polystyrene foam (Fig. 2).

2.2. Measurement of basic mechanical properties of polymer PM

The basic mechanical properties of the polyurethane PM in tension and compression were measured using a ZWICK 1450 universal testing machine and digital extensometer at room temperature according to EN ISO 527-1 [10] and are presented in Table 1.

Table 1

Basic mechanical properties of polyurethane PM determined during laboratory static tests at room temperature, according to ISO 527-1 [11]

Material	Young's modulus [MPa]	Tensile strength [MPa]	Elongation [%]	Coefficient of thermal expansion (CTE) [10^{-6}/ºC]
PM	4	1.4	140	150

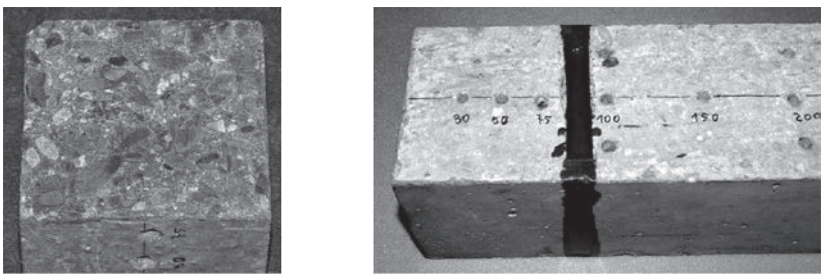

Fig. 3. Cross-section of the concrete sample and general view of sample B with the layer of polyurethane PM

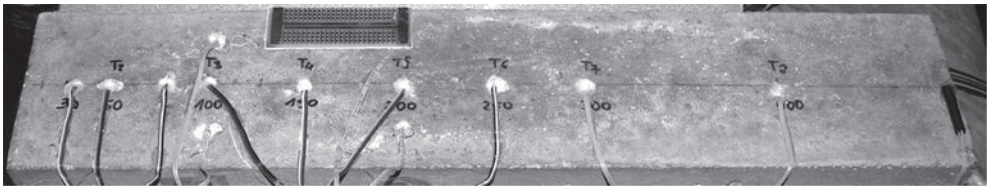

Fig. 4. General view of sample A

2.3. Heating testing program:

- Heating up to 40ºC and constant 40ºC for 1 hour,
- Heating up from 40º to 60ºC and constant 60ºC for 1 hour,
- Heating up from 60º to 80ºC and constant 80ºC for 1 hour,
- Cooling to start temperature approx. 16 hours.

3. Results

3.1. Temperature displacement

Figure 5 presents a diagram of the temperature distribution in sample A without the polymer spacer as a function of time. Fig. 6 presents the temperature distribution in sample B with the polymer spacer.

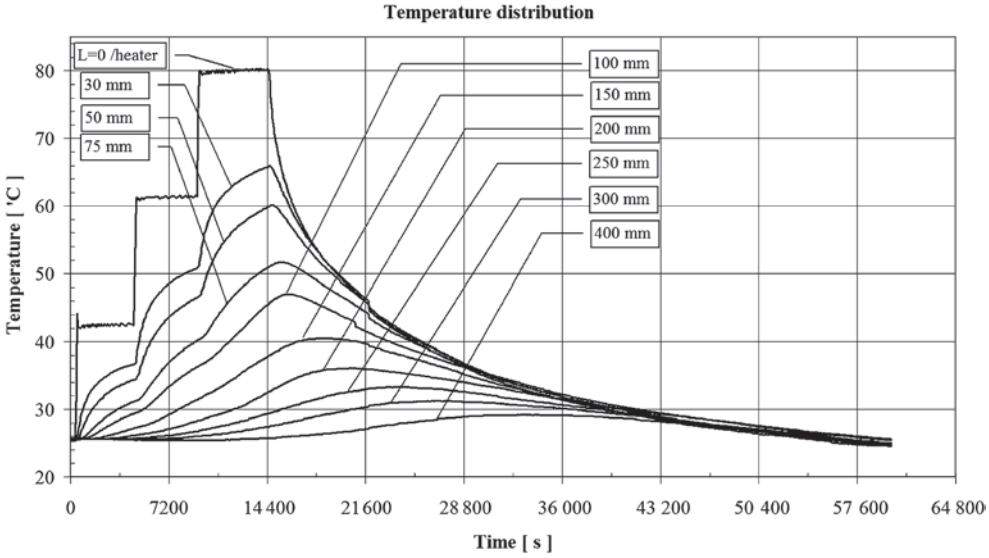

Fig. 5. The temperature distribution in concrete specimen A as a function of time

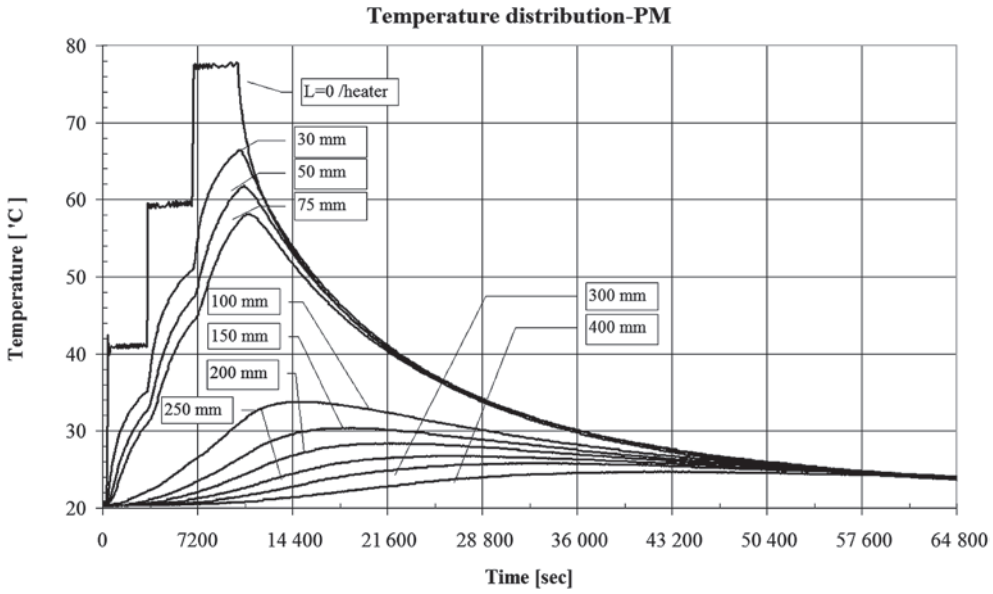

Fig. 6. The temperature distribution in concrete specimen B with polymer PM spacer as a function of time

For sample A the temperature distribution is related to the thermal conductivity and specific heat of the concrete. There is a time shift in the maximum temperature of the sample length. For a length of 400 mm, this is about 10 hours after the end of heating. The sample returns to the starting temperature after about 18 hours.

For sample B there is a significant effect of the polyurethane spacer on the distribution of the temperature in the length of sample. The upper section of sample B heats up more than the part beyond the polyurethane spacer. The polyurethane spacer of 10 [mm] caused a temperature difference of 25ºC due to its low thermal conductivity. The sample returns to the starting temperature after about 26 hours.

4. Conclusions

The study showed that:

- Research has shown uniform heat flow through the sample,
- A homogeneous temperature distribution within the cross section,
- Polyurethane PM spacer is a thermal transition barrier,
- Increased delay to achieve a maximum temperature of the sample length,
- Polyurethane PM spacer increases the temperature inertia of the system.

The numerical data of the laboratory testing was used for numerical modelling by Grodecki M. presented in another paper in this monograph.

Symbol: **PM** (and others, not mentioned in this paper) is a name of two component polyurethane applied in the Flexible Joint Method, developed at a Institute of Structural

Mechanics of the Cracow University of Technology. Various technologies using the Flexible Joint Method, applied in civil engineering, are protected by patents PL207028 (B1), PL214295 (B1) and PL384411 (A1).

References

[1] Dębska D., *Wpływ środowiska ciekłego na trwałość betonu cementowego z kruszywem dolomitowym*, Ochrona przed Korozją (Corrosion Protection), SIGMA-NOT, 56, 4, 2013, 134–143.

[2] Dębska D., *The impact of liquid environments containing* Mg^{2+} *and* SO_4^{2-} *ions on the durability of cement concrete with limestone aggregates*, Ochrona przed Korozją (Corrosion Protection), SIGMA-NOT, 57, 4, 2014, 124–128.

[3] Dębska D., *Wpływ siarczanu sodu i magnezu na trwałość betonów z kruszywem węglanowym*, Przegląd Budowlany, 5, 2014, 14–17.

[4] Truty A., *Sztywność gruntów w zakresie małych odkształceń. Aspekty modelowania numerycznego*, Czasopismo Techniczne z. 3-Ś/2008.

[5] Grodecki M., Truty A., Urbański A., *Modelowanie numeryczne ścianek szczelnych*. Kwartalnik AGH Górnictwo i Geoinżynieria, r. 27, z. 3–4, 2003, 297–303.

[6] Kwiecień A., Chełmecki J., Zając B., *The inertancy function in dynamic diagnosis of undamaged and damaged structures*, XXV Konf. Nauk. Metody Komputerowe w Projektowaniu i Analizie Konstrukcji Hydrotechnicznych, Korbielów 2013.

[7] Falborski T., Kwiecień A., Strankowski M., Piszczyk Ł., Jankowski R., *The influence of temperature on properties of the polymer flexible joint used for strengthening historical masonries,* Structural Analysis of Historical Constrictions – Jerzy Jasieńko (ed), DWE, Wrocław 2012, 816–822.

[8] Kwiecień A., *Polimerowe złącza podatne w konstrukcjach murowych i betonowych.* Monografia nr 414, Wydawnictwo Politechniki Krakowskiej, Seria Inżynieria Lądowa, Kraków 2012.

[9] Maxim Integrated Products, Inc.: DS18B20 Programmable Resolution 1-Wire Digital Thermometer. Maxim Integrated Products Inc. 2008 http://datasheets.maximintegrated.com/en/ds/DS18B20.pdf

[10] EN ISO 527-1 (1993) Plastics-determination of tensile properties – Part 1: General principles.

CONTENT

TREŚĆ